DOE/ET/20426-1

LINE FOCUS SOLAR THERMAL CENTRAL RECEIVER RESEARCH STUDY

Final Report, April 30, 1977—March 31, 1979

By
Daniel G. Di Canio
William J. Treytl
Frank A. Jur
C. Don Watson

April 1979

Work Performed Under Contract No. EY-76-C-03-1246

FMC Corporation
Engineered Systems Division
Santa Clara, California

U.S. Department of Energy

Solar Energy

DISCLAIMER

NOTICE

DOE/ET/20426-1
Distribution Category UC-62d

LINE FOCUS SOLAR THERMAL CENTRAL RECEIVER RESEARCH STUDY

FINAL REPORT
FOR PERIOD APRIL 30, 1977 – MARCH 31, 1979

DANIEL G. DI CANIO
WILLIAM J. TREYTL
FRANK A. JUR
C. DON WATSON

APRIL 1979

FMC CORPORATION
ENGINEERED SYSTEMS DIVISION
P. O. BOX 450
SANTA CLARA, CALIFORNIA 95050

PREPARED FOR THE
U. S. DEPARTMENT OF ENERGY
SOLAR ENERGY
UNDER CONTRACT DE-AC03-76ET 20426

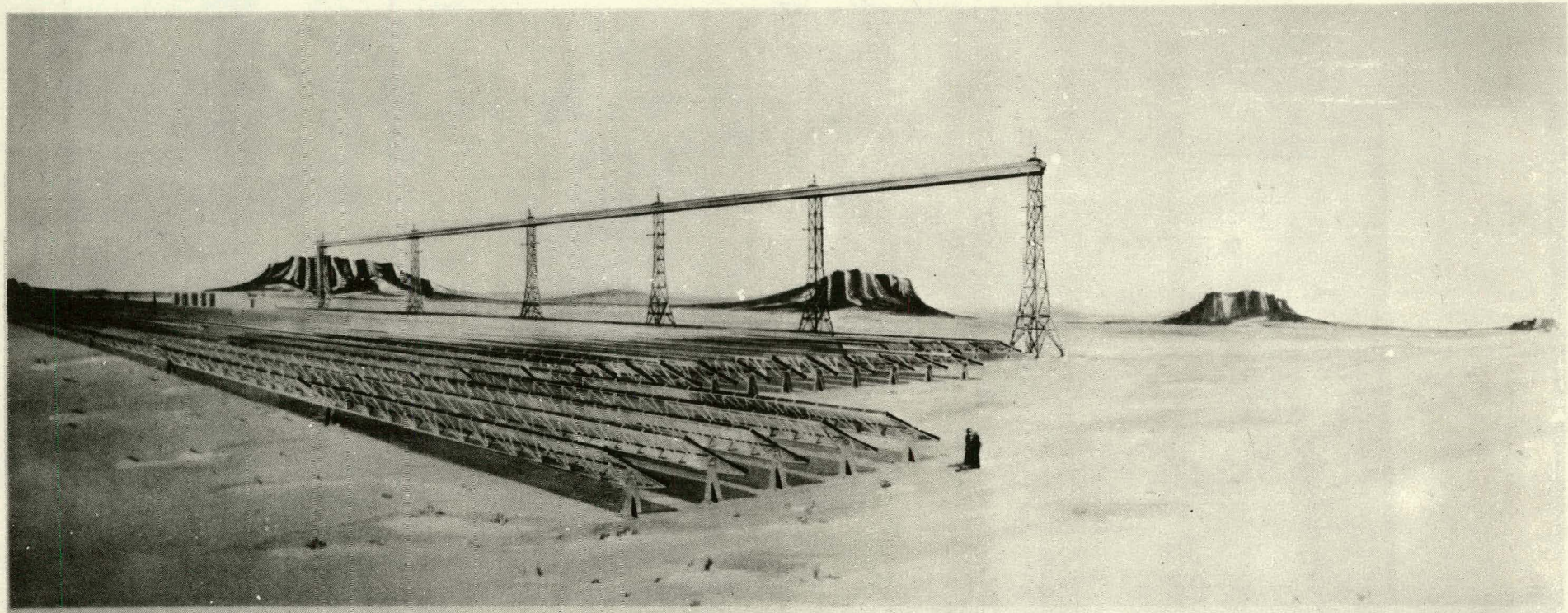

FMC LINE FOCUS CONCEPT IN 2.5 MWe CONFIGURATION

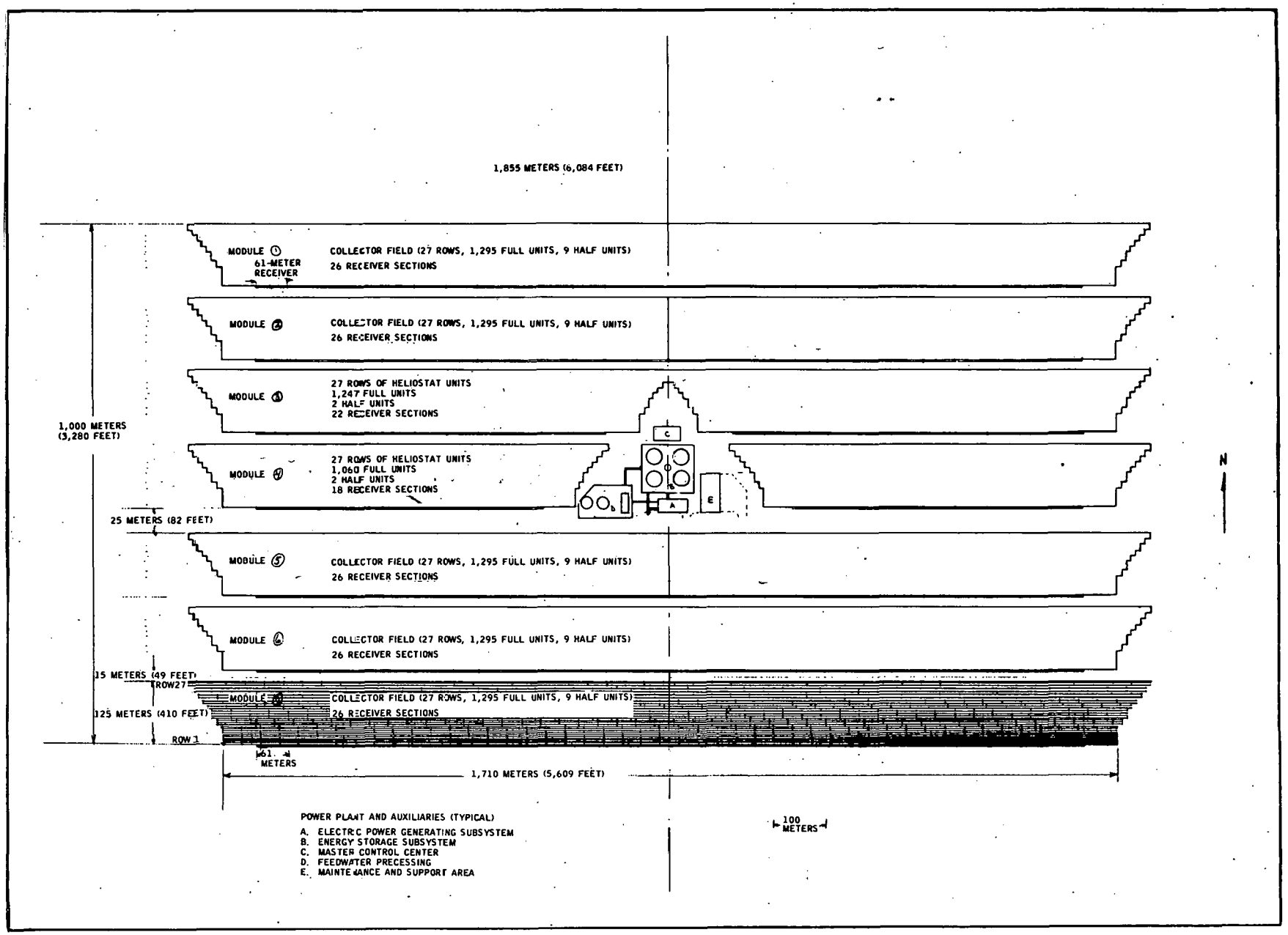

FMC LINE FOCUS CONCEPT IN 100 MWe CONFIGURATION

PREFACE

This report contains the results of work performed by FMC Corporation under Department of Energy (DOE) Contract DE-AC03-76ET-20426, "Line Focus Solar Thermal Central Receiver Research Study." The work was performed between 30 April 1977 and 31 March 1979 by members of the FMC Engineered Systems Division. Members of SRI International served as team members in the analysis phase of the project.

The project was funded as part of the DOE Solar Thermal Power program, the prime goal of which is to stimulate research and development activities leading to commercially feasible systems for generating electricity with solar energy. The prime thrust of the DOE program is centered on the point focus, central tower concept for conversion of solar energy to useful thermal energy. The point focus concept uses parabolic (dish) heliostats, arranged in a circular field about a central tower, and controlled in azimuth and elevation to focus the solar image on a receiver mounted at the top of the tower.

The FMC line focus concept uses parabolic cylinder (trough) heliostats arranged in rows on an East-West axis and controlled in elevation to focus on linear cavity-type receivers mounted on steel lattice towers. FMC proposed the line focus concept as an alternative to the point focus concept because of several attractive features, including:

- System modularity (same heliostat, receivers, and towers for any size plant)
- Low towers, based on existing designs for transmission line towers
- Single-axis control of a relatively large reflecting area per heliostat
- Adaptability of heliostat, receiver, and tower to automated factory production, transport on existing common carriers, and installation with standard construction equipment
- Maximum usage of land area and adaptability to different site configurations
- Linear field symmetry to allow automated cleaning of reflector surface and minimize maintenance logistics.

These features prompted DOE to fund FMC for an effort to establish feasible design concepts for the heliostat, heliostat control, and receiver, and to examine the performance and economics of typical power plant configuration based on the line focus alternative. The results of these efforts support the position that the line focus concept is a feasible and competitive alternative for solar thermal generation of electric power.

CONTENTS

CONTENTS (continued)

ILLUSTRATIONS

ILLUSTRATIONS (continued)

ILLUSTRATIONS (continued)

ILLUSTRATIONS (continued)

ILLUSTRATIONS (continued)

ILLUSTRATIONS (continued)

1.0 EXECUTIVE SUMMARY

This report contains the results of a study undertaken by FMC Corporation to examine the line focus central receiver alternative for solar thermal generation of electric power on a commercial scale. The project was sponsored by the Department of Energy as a result of a concept proposed by FMC for the Central Receiver Solar Thermal Power System study.

1.1 CONCEPT DESCRIPTION

The baseline concept consists of the following elements (Figure 1-1):

- A solar collector (heliostat) whose geometry is the equivalent of a focused parabolic cylinder. The heliostat reflecting surface is composed of an array of flexible rectangular mirror panels supported along their long edges by a framework which rotates about an axis parallel to the ground plane. The mirror panels in one section (18.3 meters by 3.05 meters (60 feet by 10 feet)) are defocused in unison by a simple mechanism under computer control to achieve the required curvature. Two sections (110 meters^2(591 feet^2)) are controlled and driven in elevation by one control/drive unit.
- A linear cavity receiver, composed of 61-meter (200-foot) sections supported by towers at an elevation of 61 meters (200 feet). Each section receives feedwater and produces turbine-rated steam. The cavity is an open cylinder 1.83 meters (6 feet) in inside diameter, with a 1.22 meter (4 foot) aperture oriented at 45 degrees to the collector field.
- Heliostat control, consisting of a local controller at each heliostat module which communicates with a master control computer to perform elevation tracking and focal length adjustment. The control logic is open-loop, with sun position computed by the master computer with an algorithm. Image sensors, mounted above and below the receiver aperture, are used to monitor the collector field and provide feedback to the master computer for detection of misaligned heliostats.

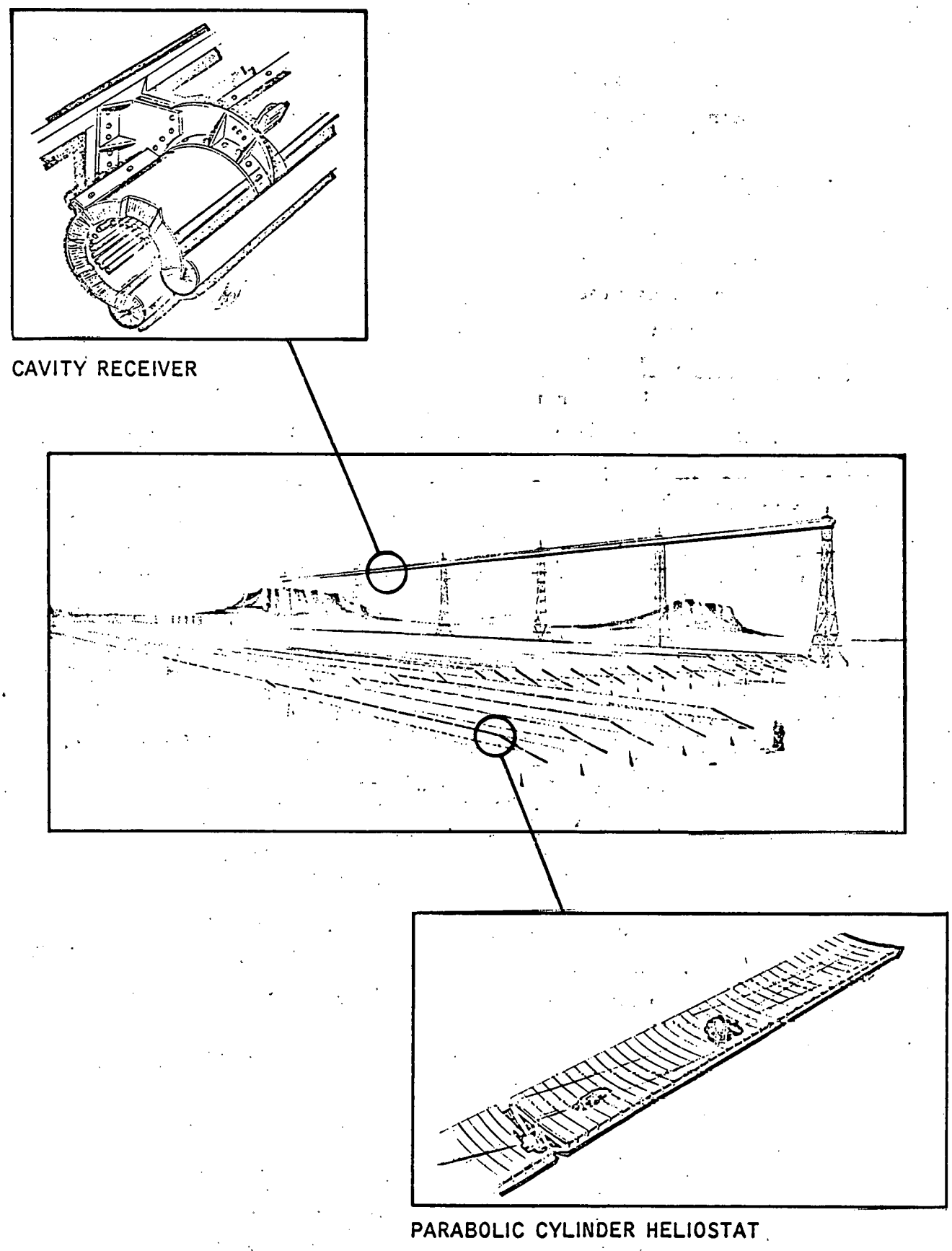

Figure 1-1. FMC LINE FOCUS CONCEPT ELEMENTS.

The underlying rationale behind the choice of a line focus concept for solar thermal power generation is the favorable balance between performance and cost for a given system capacity. Inherently, a line focus system is less efficient than a point focus system. More than balancing this, however, is the lower life cycle cost derived from the modularity and field symmetry of a line focus system. Specific advantages are as follows:

- Modularity
  The heliostat/receiver configuration has been designed for interconnecting in a "building block" manner for scaling to necessary plant sizing requirements.
- Simplicity of Control
  Single-axis control is inherently simpler and more reliable than two-axis tracking. All heliostats in a given row track at the same angle, while the tracking angle of each row is offset by fixed increments relative to each other.
- Efficient Land Use
  Rows of end-to-end heliostats permit high-density field coverage. Blocking and shading are not concerns in the axial dimension. Linear systems can be installed in strips, utilizing land unusable by nonlinear systems.
- Stigmatic Focus
  Because cylindrical optics focus in one plane, it is possible to systematically compensate for off-axis incidence resulting in essentially stigmatic focus, using a unique variable curvature feature.
- Favorable Concentration
  Depending on field configuration, aperture concentrations of up to 100 suns can be obtained, although more typically a concentration of 60 to 80 suns is to be expected. This concentration level is suitable to produce steam at the rated temperature and pressure, but not sufficient to pose a danger of catastrophic damage to the receiver or towers.
- Heliostat Cost
  The linear heliostats are suitable for high-efficiency mass production using automated methods and standardized materials.
- Installation
  Heliostats are low profile and require less substantial installation pedestals. The basic design should permit rapid, low-cost field installation. Receiver towers are modified utility transmission line towers.

- Reliability and Maintainability

  Because of the low profile and rugged one-axis mounting, the heliostats are less susceptible to wind and other environmental effects than are higher-profile systems. The row arrangement is conducive to efficient cleaning, and the heliostats can be stowed in an overturned position for protection from the elements when not in use.
- Monitoring and Adjustment

  The field is automatically monitored for tracking and focus fidelity.
- Fail-Safe Protection

  In case of power failure, or failure of receiving updated tracking information, a mechanical system is activated to defocus and stow the affected heliostat.

1.2 PROJECT OBJECTIVES

The objectives of the project were to (1) analytically evolve the baseline concept into a feasible configuration for solar thermal power generation, and (2) experimentally verify the predicted performance of the baseline heliostat. Efforts to accomplish the objectives were performed within the constraints of baseline sizings for heliostat and receiver sections. These sizings were established early in the project as reasonable choices to (1) maximize adaptability to automated factory production, (2) permit transport and installation with standard equipment and processes, and (3) configure a wide range of plant capacities with a single set of basic components. Section 2.0 contains a more detailed description of the rationale used for baseline sizing.

Rigorous optimization of component sizings require a level of detail design that was outside the project scope. The estimates of plant performances presented in Section 6.0 and Appendix D should not be significantly affected by alternate choices of baseline sizes because in a linear system, (1) solar to thermal conversion efficiency is essentially independent of the unit lengths of heliostat and receiver, and (2) total collector area required for a given power level is independent of unit collector size. Analyses to support the feasibility of the baseline sizings are presented in Sections 2.0 and 3.0, and Appendices D and E.

1.3 RESULTS OF CONCEPT ANALYSIS STUDIES

1.3.1 Collector Field Studies

Initial analytic efforts centered on establishment of requirements for receiver aperture size and requirements for heliostat optical control, based on assumed maximum errors of:

- 2 mrad mirror surface dispersion error *
- 2 mrad focus control error
- 2 mrad tracking control error.

Based on these errors, an optimum width of 1.22 meters (4 feet) and orientation of 45 degrees were established for the receiver aperture on the basis of maximum collected energy at the receiver aperture plane (Section 2.2).

Heliostat focus control requirements were then determined (Section 2.3), based on the optimized aperture size. The results of this analysis were used to establish design parameters for the focusing mechanism (Section 3.1) and the heliostat local controller (Section 5.2). One important result of the analysis was the establishment of a maximum deflection requirement of 20mm (0.79 inch) for mirror deflection at the heliostat centerline.

The results of the initial optical analysis were used to develop a rigorous model (Appendix A) for examining and optimizing collector field sizing. A series of field sizing and performance analyses were undertaken. A winter solstice design day was chosen to provide a basis for comparison with point focus, central tower concepts. The collector field model was used to compare optimum field sizing for a number of alternative configurations, including:

- North/South versus East/West orientation
- Noon versus 2:00 p.m. design points
- Flat field versus sloped field.

Primary optimization parameters were the number of rows and minimum row spacing to achieve a fixed level of intensity at the receiver aperture plane and eliminate shading and blocking.

---

* 1.2 mrad error measured for one mirror panel (Appendix F).

The analysis resulted in the selection of a flat, North collector field (South-facing heliostats aligned on an East-West axis) as the baseline for further analyses. Subsequent comparisons of a 10 MWe plant configuration using North fields versus a configuration using North and South fields verified this choice (Section 1.3.3.1 and Appendix D).

The analysis also indicated that a sloped field offered significant improvement in performance over a flat field. However, the flat field was chosen for subsequent analyses based on relative design simplicity.

1.3.2 Receiver Studies

Two concepts for steam generation were evaluated for use in the baseline receiver envelope. One concept is a once-through-to-superheat design using loops of tubes oriented along the centerline of the receiver cavity. The second concept is a natural convection design using a double screen of vertical tubes mounted in the aperture plane of the receiver. Figure 1-2 shows the baseline concepts.

Both concepts were carried forth through parametric evaluation to establish feasible sets of design parameters for production of turbine-rated steam at nominal working pressure of 6.9 MPa (1,000 psia).

Two alternatives were examined in the analysis of the once-through concept. In the flat plate design alternative the boiler/superheat tubes are mounted in the receiver aperture plane. In the other alternative (cavity design) the tube loops are distributed along the inner circumference of the receiver cavity. Comparative performance analysis indicated that the cavity design exhibited superior performance over a wide range of flow rates and radiation properties, primarily because locating the tubes well within the receiver cavity reduces losses due to reradiation to the surroundings. Based on these results, the cavity design was selected as the baseline once-through-concept.

A model of the baseline once-through concept was developed (Appendix B) for more detailed analysis of tube sizing and performance, using the incident flux distributions generated by the collector field model. The results of this analysis led to the selection of an eight-pass configuration containing 108

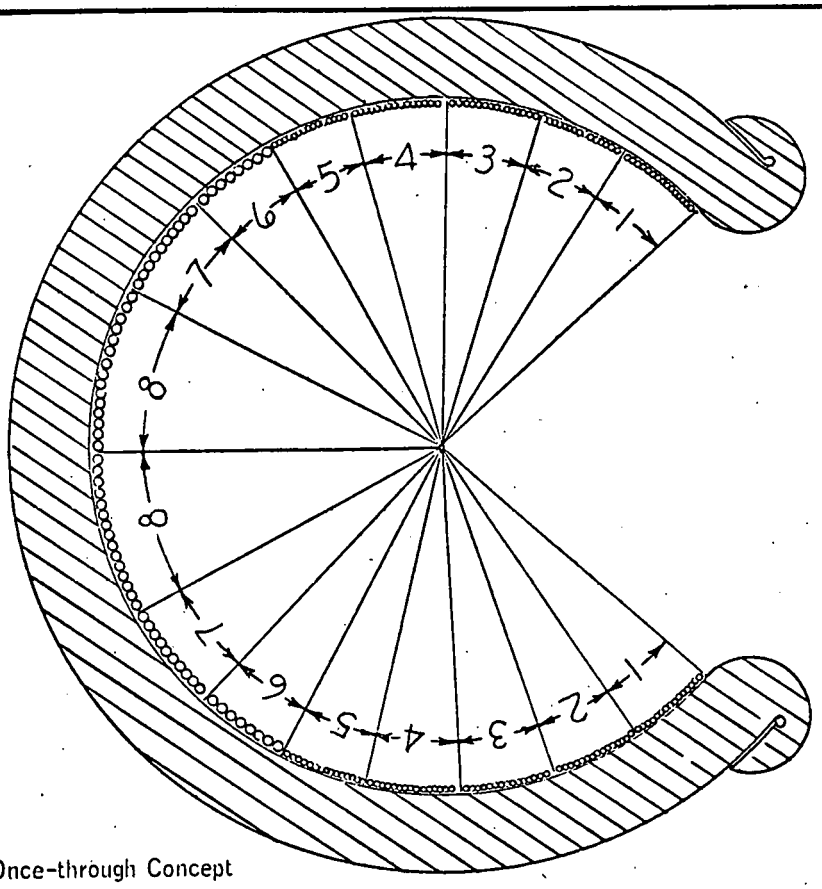

PASS	TUBING I.D. (INCHES)	NUMBER OF TUBES IN BOTH SECTIONS
1 (1)	0.5	30
2	0.5	30
3	0.5	30
4	0.5	30
5	0.5	30
6	0.9	16
7	0.9	20
8 (2)(3)	0.9	30

(1) FEEDWATER (2) SUPERHEATER
(3) STAINLESS STEEL; OTHERS MILD STEEL

Once-through Concept

SS: SATURATED STEAM
SH: SUPER HEAT

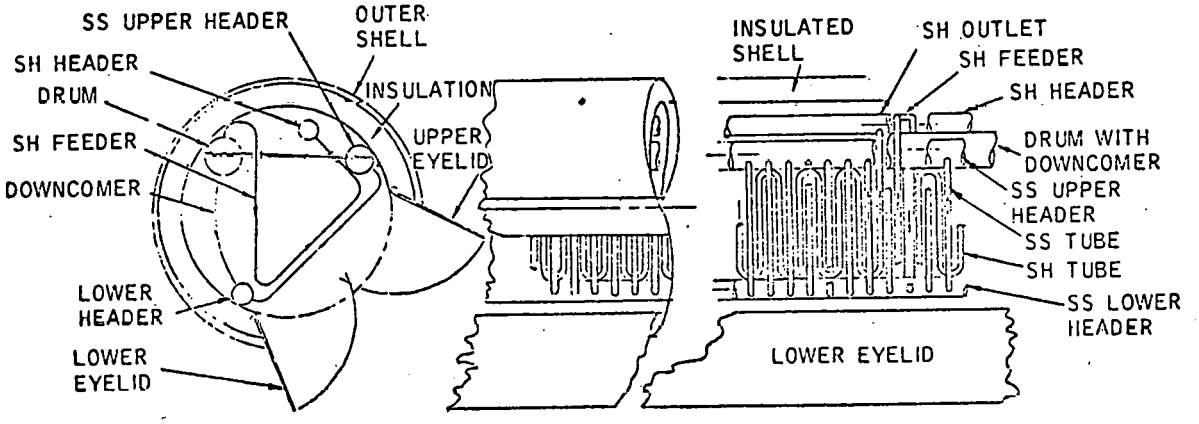

Natural Convection Concept

Figure 1-2. BASELINE STEAM GENERATOR CONCEPTS

tubes in each half of the receiver cavity (Figure 1-2). Each pass runs the length of the cavity. Feedwater enters the tubes in pass 1 and traverses each pass in countercurrent flow. Preheat and boiling occur in the first seven passes, superheating in the eighth pass.

The analysis of the natural convection concept led to the selection of the design shown in Figure 1-2. The design consists of a double screen of vertical tubes mounted in the aperture plane of the receiver. There are 800 tubes in each row. Nominal tube diameter is 9.2 millimeter (0.375 inch). Feedwater enters the tubes in the front row, where saturation boiling occurs. Saturated steam passes to a separation drum which feeds vapor to the rear row for the superheat pass.

Table 1-1 contains a comparison of estimated performances of each concept at design point sizings for generation of 510°C (950°F) steam.

Table 1-1 COMPARISON OF RECEIVER PERFORMANCES

Concept	10 MWe Plant Sizing 1400 Winter Solstice (26.9 kw/m^2)* 0.71 kg/s per receiver section Thermal Efficiency	100 MWe Plant Sizing 1200 Equinox (34.0 kw/m^2) 1.39 kg/s per receiver section Thermal Efficiency
Once-through	0.78	0.86
Natural convection	0.72	0.77

* Average intensity from collector field at receiver aperture plane.

The once-through concept was selected for use in sizing of baseline plant concepts, primarily because of higher thermal efficiency and lower cost (Appendix E). However, both concepts must be subjected to further detail evaluation, both analytically and experimentally, before a final choice can be made.

1.3.3 Plant Sizing Studies

The baseline elements of the line focus concept were used to size baseline concepts for electric generation plants.

Two concepts were generated. The concepts, a 10 MWe pilot plant and a 100 MWe commercial plant, were based on (1) requirements used by Phase I contractors for the Point Focus Central Receiver Solar Thermal Power

System, and (2) the thermal-to-electric power conversion cycles evolved by the McDonnell Douglas Astronautics Company (MDAC). The MDAC power conversion cycle was selected because the flow rates and steam conditions required by the MDAC thermal storage and electric power generating subsystems best matched the FMC receiver concept.

1.3.3.1 10 MWe Pilot Plant

Two concepts were evaluated. The first concept was based on North and South collector fields, optimized for 2:00 p.m. winter solstice design point (Section 2.2) The second concept contained only optimized North collector fields. Appendixes D and E contain details of the sizing computations.

Field sizing was based on early data for the MDAC 10 MWe concept which specified turbine operation at 477°C (890°F) 10 MPa (1,450 psia) input steam, 56.7°C (135°F) 0.16 MPa (2.5 psia) exhaust steam. These conditions differ from the final MDAC specifications, but do not significantly change the comparative significance of analysis. Table 1-2 contains a summary of the configuration, performance, and cost of each concept.

Table 1-2 CHARACTERISTICS OF 10 MWe BASELINE SYSTEMS

Subsystem characteristic	North/south system	North-only system
Number of heliostats	1,010	782
Number of 61-m receivers	10 (double)	20 (single)
Number of 61-m towers	11	21
Collector area (km^2)	0.121	0.094
Annual energy (MWeh)	30,900	31,000
Design point operation (hours)		
10 MWe	4.0	5.0
7 MWe	3.9	3.4
Annual load factor	0.35	0.36
Relative Investment Cost	100	92
Relative Busbar Power Cost	100	96

1.3.3.2 100 MWe Commercial Plant

The plan view of the baseline concept, configured for a 3:00 p.m. equinox design point, is shown in the frontispiece. The collector field consists of 170 receiver sections arrayed in seven field modules. Each module contains 27 rows of south-facing heliostats. The plant contains 8,831 heliostats (8,782 full units (36-meter by 3.05-meter glass area), and 49 half units). The total glass area is 0.967 square kilometer (1.05 by 10^6 ft^2).

The 100 MWe configuration is essentially a scaling up of the 10 MWe concept constrained by realistic piping requirements, and sized for a different design point day. The same heliostats, receivers, and towers are used in both concepts.

The baseline receiver concept is a once-through-to-superheat design containing an eight-pass steam generator. The passes are arrayed circumferentially on the wall of the receiver cavity (Section 4.1). The feedwater and superheat passes in the receivers in one field module are manifolded to common headers and downcomers.

Each heliostat is controlled by a local control computer. The local controllers in each field module are directed by a field computer. Each of the seven field computers communicate with the master control computer. Section 5.0 contains a description of control logic.

The thermal storage subsystem and electric power generating subsystem are those specified for the MDAC commercial plant configuration. The thermal transport network has been sized for the inlet and outlet conditions specified for these subsystems.

Figure 1-3 and Table 1-3 show the performance of the configuration. Table 1-4 and Figure 1-4 show plant efficiencies and power flow at noon equinox for 950 w/m^2 insolation level with 96.5 percent of the heliostats in operation.

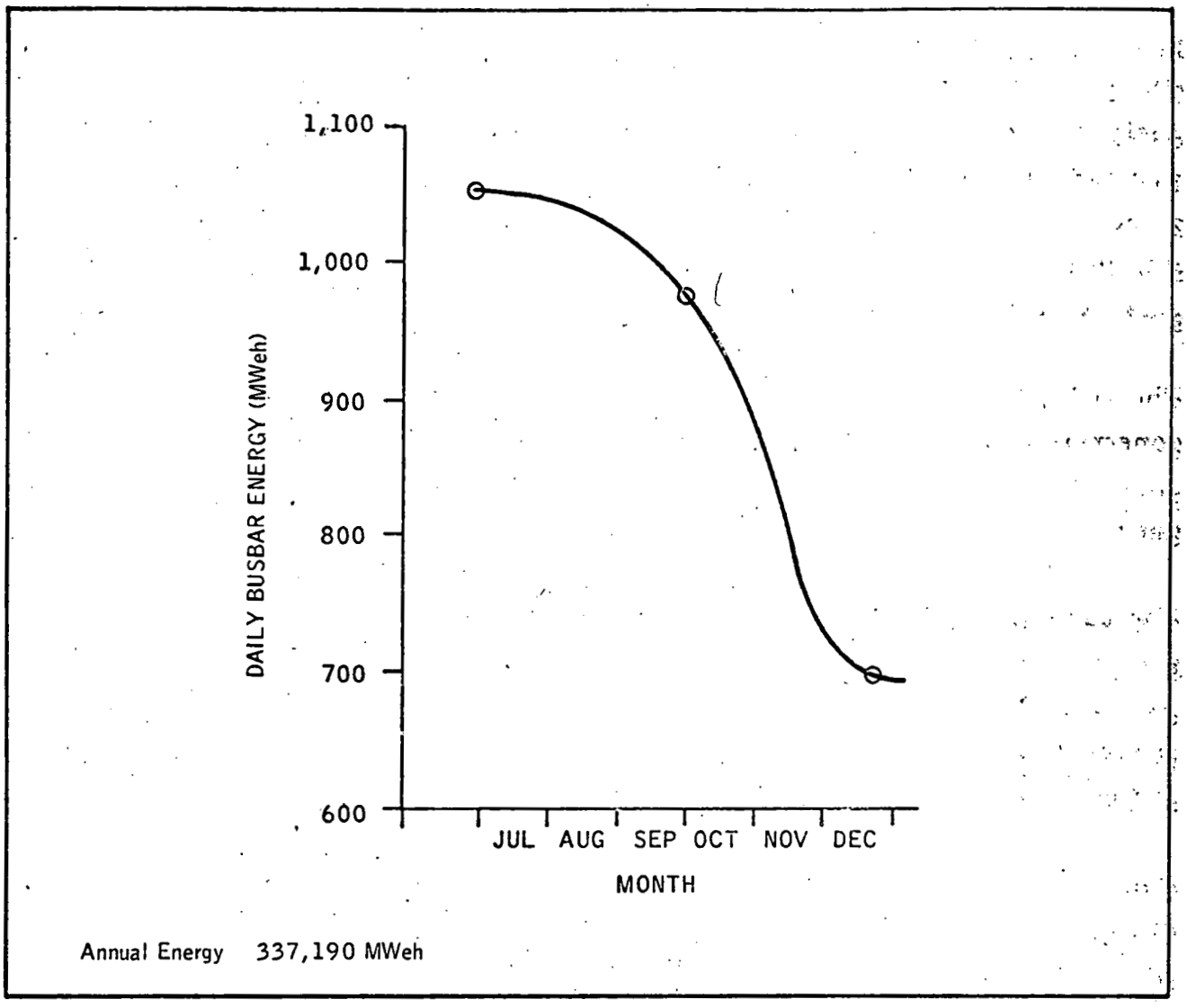

Figure 1-3 ANNUAL BUSBAR POWER OF 100 MWe CONFIGURATION

Table 1-3 SUMMARY OF DAILY PERFORMANCE OF 100 MWe CONFIGURATION

Day	Total energy to receivers (mwh-th)	Busbar energy (MWeh)		Hours of operation	
		Direct	From storage	100MWe	70MWe
Equinox (design day)	4,080	550	426	5.5	6.1
Summer solstice	4,439	600	454	6.0	6.5
Winter solstice	2,846	500	218	5.0	3.1

Table 1-4 100 MWe PLANT EFFICIENCIES AT NOON EQUINOX

Efficiency	Direct from receivers	Direct from storage
Collector	0.712	0.712
Receiver	0.860	0.860
Piping	0.970	0.970
Storage	–	0.940
Turbine	0.377	0.268
Parasitic	0.89	0.92
System	0.20	0.14

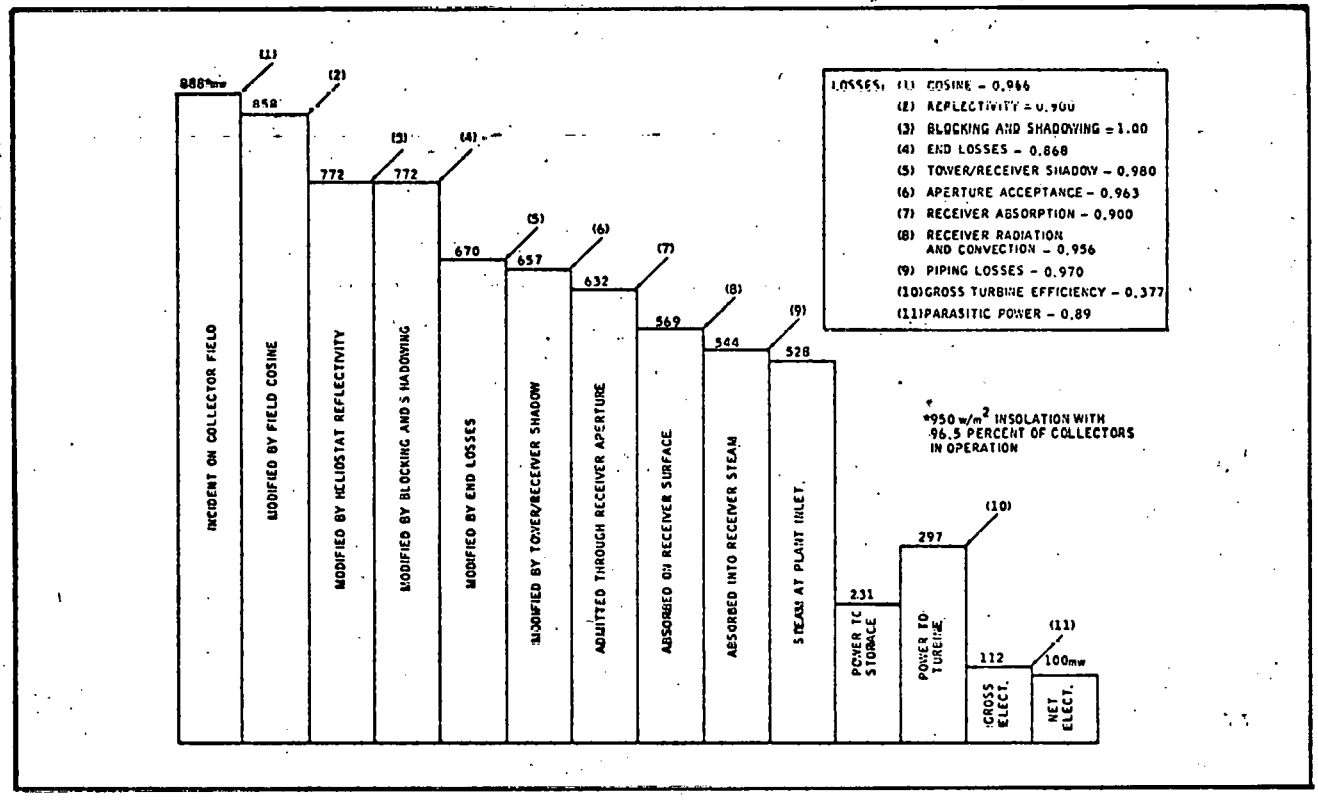

Figure 1-4 POWER FLOW FOR 100 MWe CONCEPT (EQUINOX NOON)

Estimates of plant investment and operational costs were based on estimates made for the 10 MWe concept, with adjustments for differences in production volumes. Appendix E contains the detail cost computations for the collector, receiver, thermal transport, and control subsystems. Costs for the remaining subsystems are those of the MDAC 100 MWe concept. Figure 1-5 shows the distribution of capital cost among the plant subsystems. Table 1-5 contains a summary of annual service cost, as computed with the JPL/EPRI economic model.

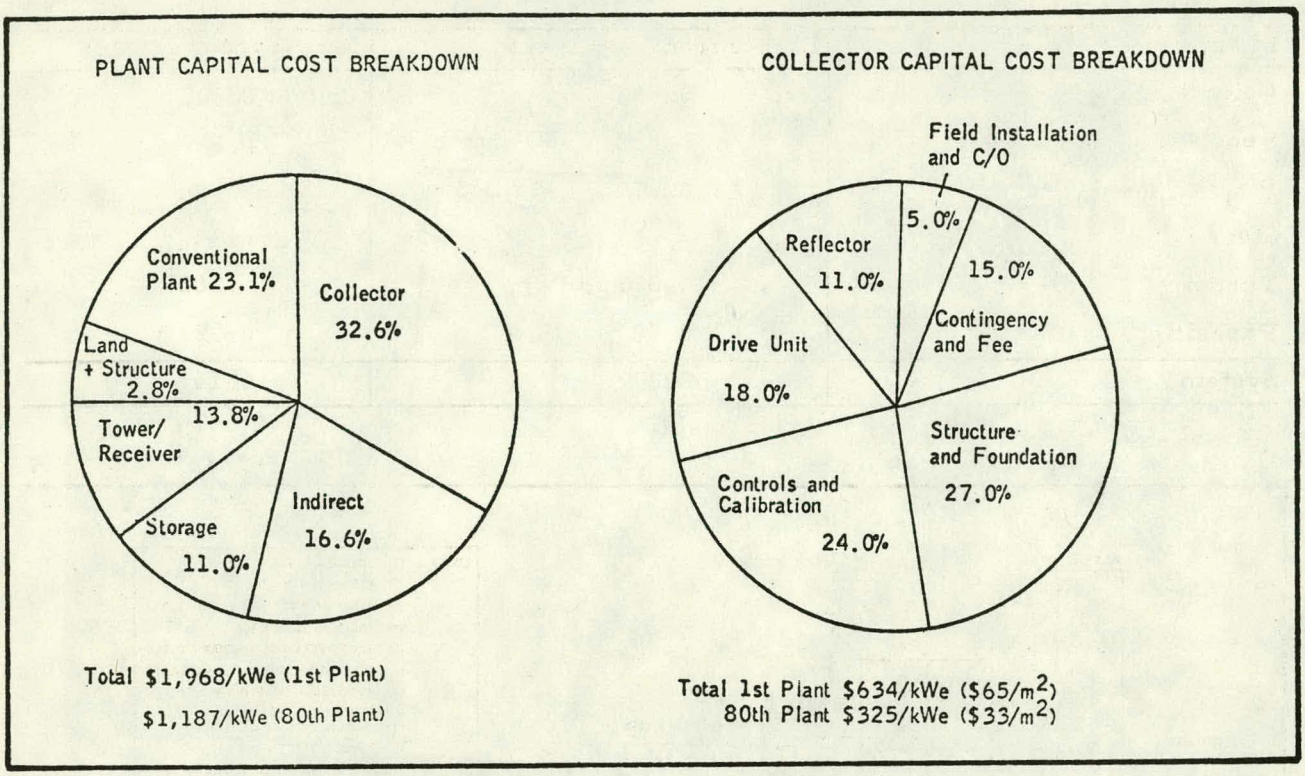

Figure 1-5 DISTRIBUTION OF CAPITAL COSTS OF 100 MWe CONCEPT

Table 1-5 COST OF SERVICE FOR 100 MWe CONCEPT

Factor	Value
Plant unit	80th
System life	30 years
Base year	1978
First year of operation	1990
Capital cost	$1,187/kWe
Annualized system resultant cost	$254/kWe
Levelized busbar energy cost	71 mills/kWeh

1.4 RESULTS OF HELIOSTAT TESTS

Two experimental-model heliostat sections were fabricated. One model, shown in Figure 1-6, was a jury rig which contained four mirrors in a support frame which simulated the structure of a full-sized section. The jury rig was used to debug the concept for mirror focus control, and verify that the focus mechanism performed as required.

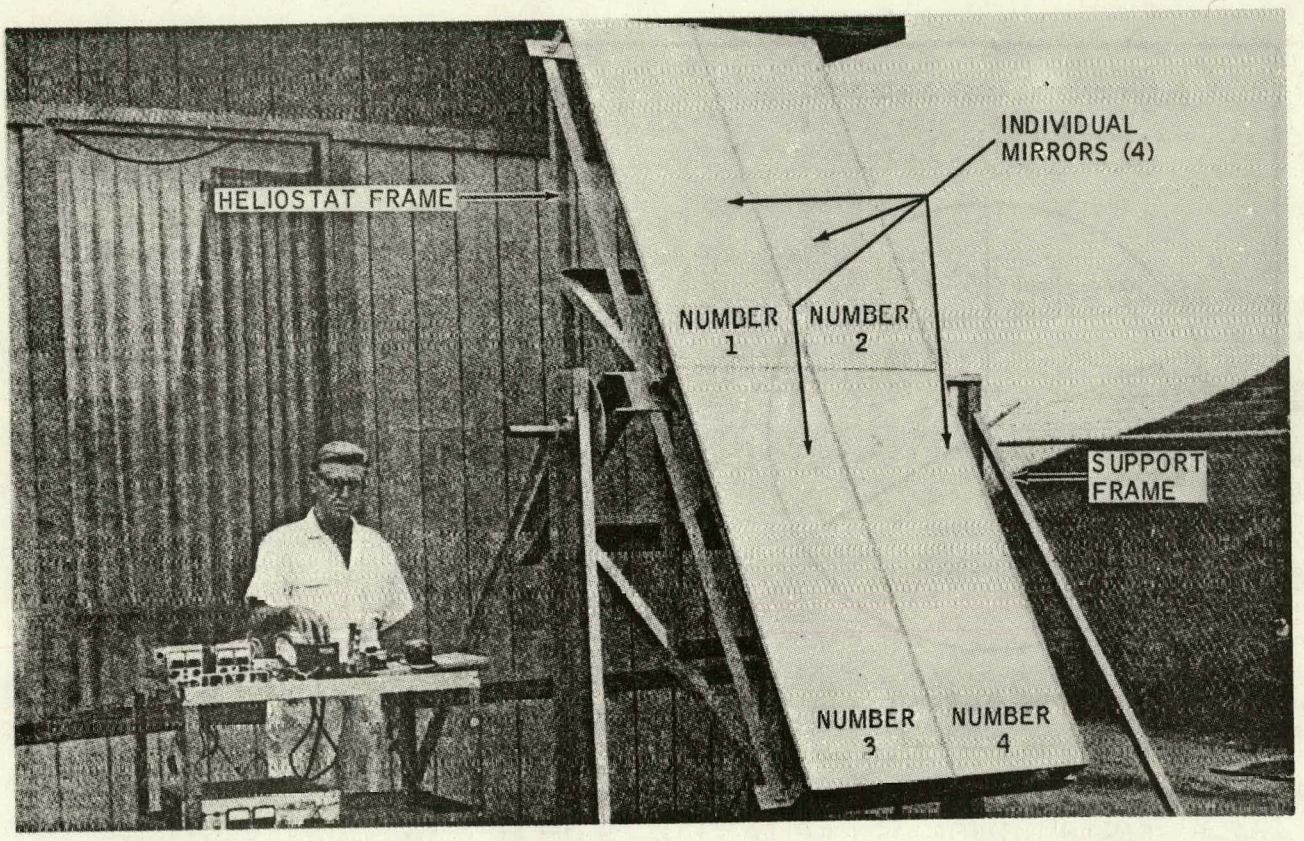

Figure 1-6 JURY RIG HELIOSTAT MODEL

The second model, shown in Figure 1-7, was a full-sized heliostat section with focus elevation drive, and a local control system. The heliostat section was 17.92 meters by 3.05 meters (58.5 feet by 10 feet), containing 51.1 meters^2 (550 feet^2) of exposed mirror area. The section was slightly shorter than concept design length to accommodate a commercially available mirror.

The section contained 70 mirror panels. Each panel was 152.4 centimeters long by 50.8 centimeters wide (60 inches by 20 inches), composed of 2.29 millimeters (0.09 inch) thick second-surface float glass. The reflecting surface was silver/copper flash covered by black organic paint and protected by a 3.3 millimeter (0.13 inch) thick layer of polystyrene foam. Each panel was enclosed in a metal frame.

One panel was sent to Sandia Laboratories for reflectance measurements. The results of these measurements (Appendix F) indicate that the mirror panels have an average specular reflectance of 0.85 and an RMS optical dispersion error of 1.2 mrad in the long dimension.

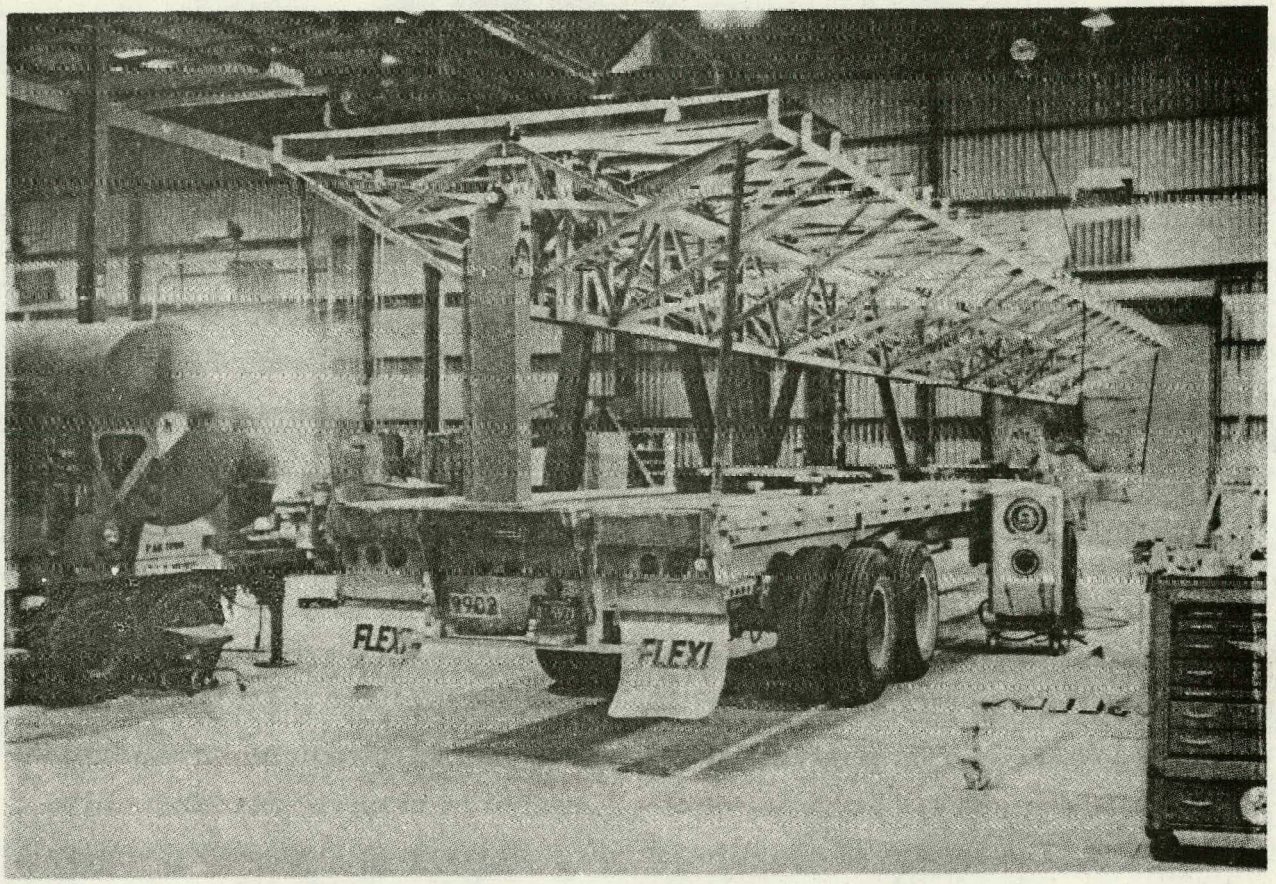

Figure 1-7 FULL SIZE HELIOSTAT SECTION

The heliostat was assembled on a flat bed trailer and was to be used in a field experiment to verify predicted performance of the control system and to measure collector efficiency. The field experiment was deleted from the project scope at the request of DOE. Appendix C contains a description of the tests planned during the field experiment.

Functional tests were performed during the project to verify that the heliostat concept performed as required. The results of these tests (Section 3.3) are summarized below:

- Image Focusing

  The jury rig model was used to focus the sun image on a target at a slant range of 61 meters (200 feet), which is the minimum heliostat-to-receiver range. The mirror focus mechanism successfully focused the solar image from all mirrors into a vertical band 1.22 meters (4 feet) wide.

The field experiment model heliostat was set up at the ESD facility for a series of tests to measure the size of the reflected image from 15 rows of mirror panels. Figure 1-8 shows the test setup. A series of tests was conducted between March 12 and March 20, 1979. Figures 1-9 and and 1-10 show the images obtained during tests conducted on March 20.

The tests demonstrated that the field experiment heliostat focused the solar image to within a 1.22-meter (4-foot) width at a range of 61 meters (200 feet). Based on the results of the tests, it was estimated that the field configuration used for the 100 MWe plant concept (Section 6.0) would achieve an efficiency of about 0.9 in concentrating reflected flux within a 1.22-meter receiver aperture at a noon equinox design point. This is lower than the efficiency of 0.963 predicted from the plant performance analysis.

This lower-than-predicted efficiency was due to misalignment and distortions in the mirror surface which prevented attainment of maximum focus control. The causes of the misalignment and distortions were identified, and can be eliminated by (1) rework of mirror support structure, and (2) fabrication of a fixture to perform alignment of mirror panels under controlled conditions.

- Emergency Defocus
  The full-scale section was focused to maximum deflection, and power was then interrupted to simulate a malfunction. The mirror surfaces returned to a defocused position in 0.2 second, well within required safety limits.
- Elevation Drive
  The full-scale section was run through functional testing to verify operation of the elevation and stow drive. All test results were within 1 percent of design requirements.

The tests satisfied part of the objectives and demonstrations planned for the field experiment. All of the specific tests described in Appendix C, except measurement of image intensity, were accomplished with the heliostat in a manual operation mode. Most important, the ability of the focusing concept to repeatedly achieve a 1.22-meter (4-foot) image size in a full-scale heliostat configuration was successfully demonstrated.

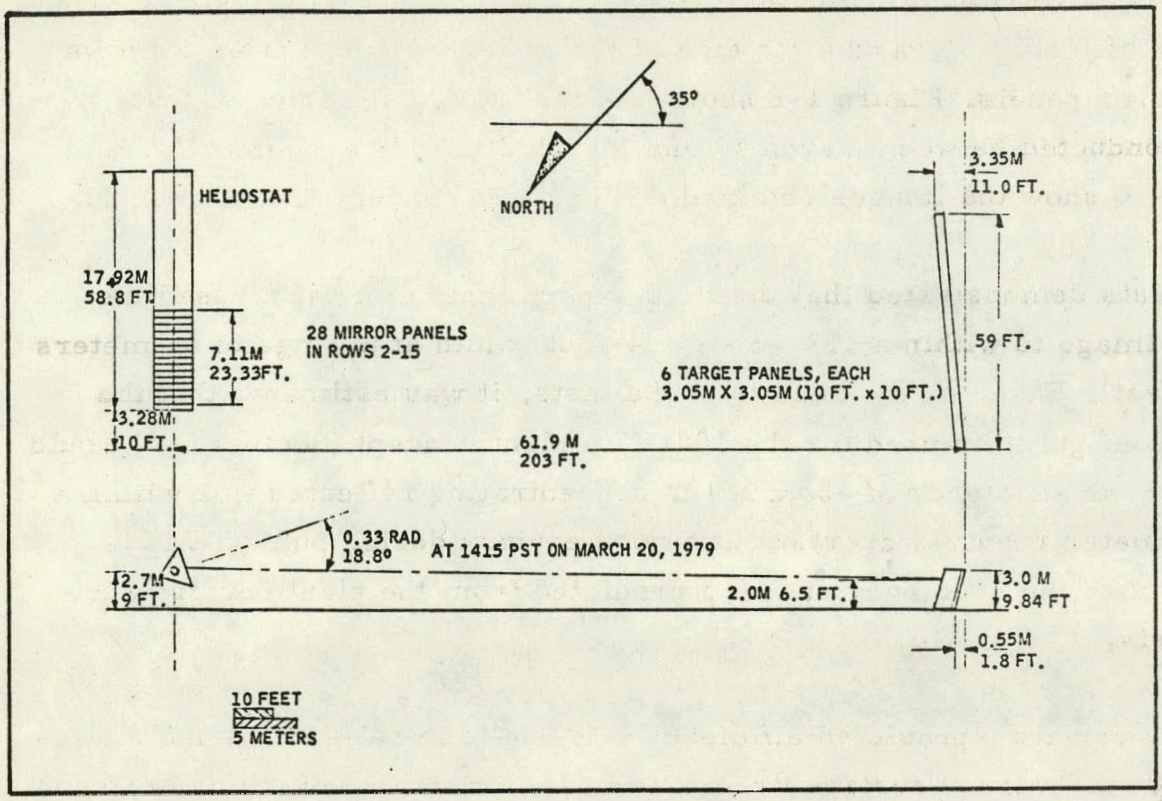

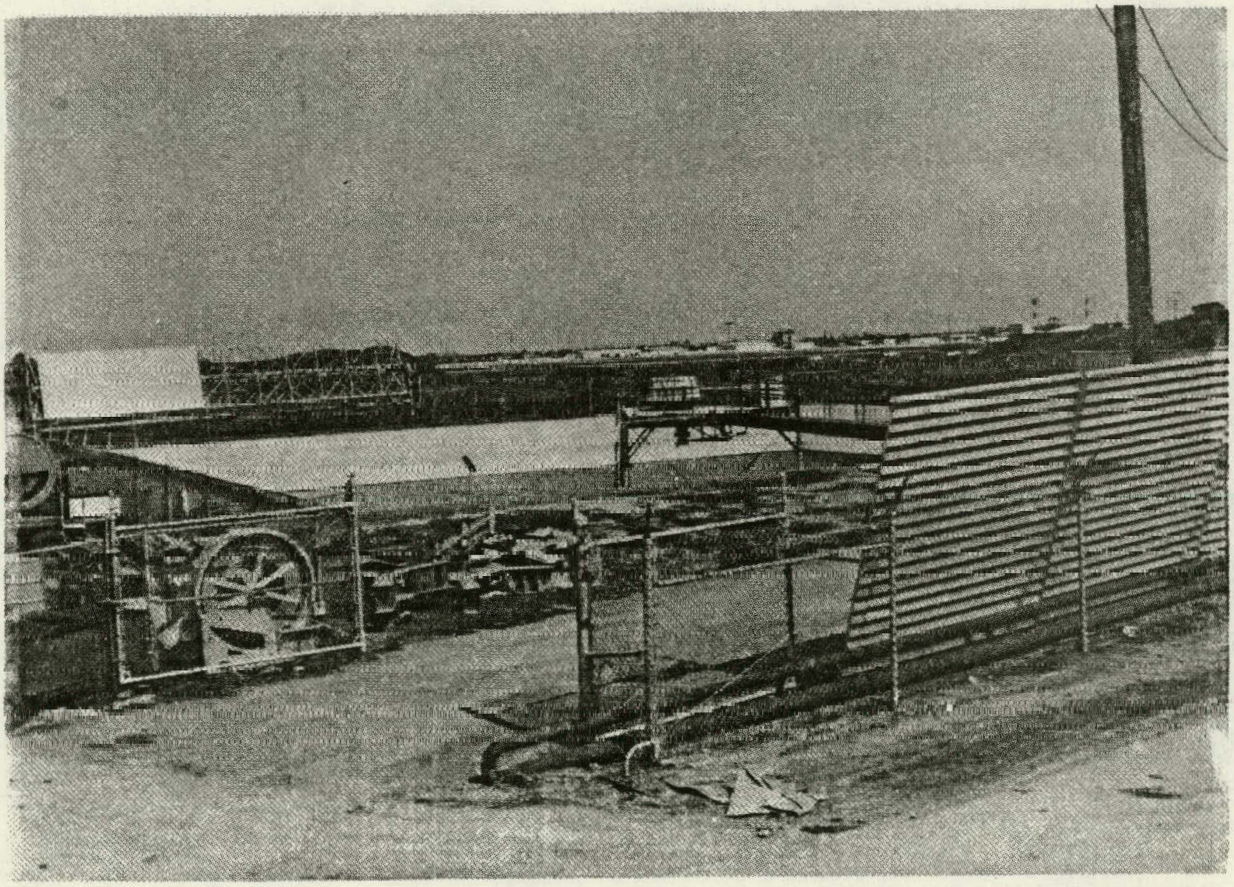

Figure 1-8 TEST OF IMAGE SIZE FROM FIELD EXPERIMENT HELIOSTAT

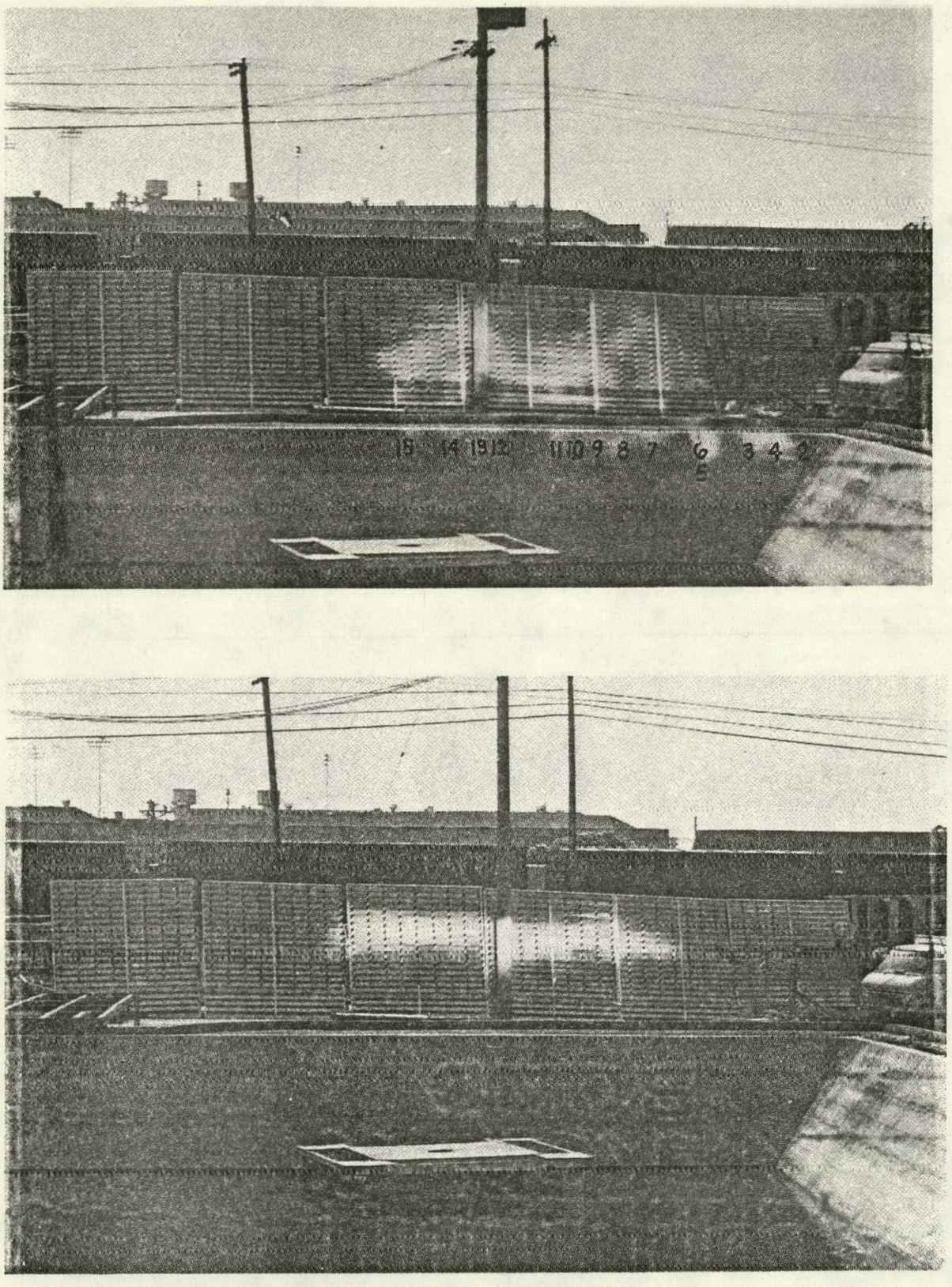

Figure 1-9 HELIOSTAT IMAGES OBTAINED IN TEST OF 20 MARCH 1979

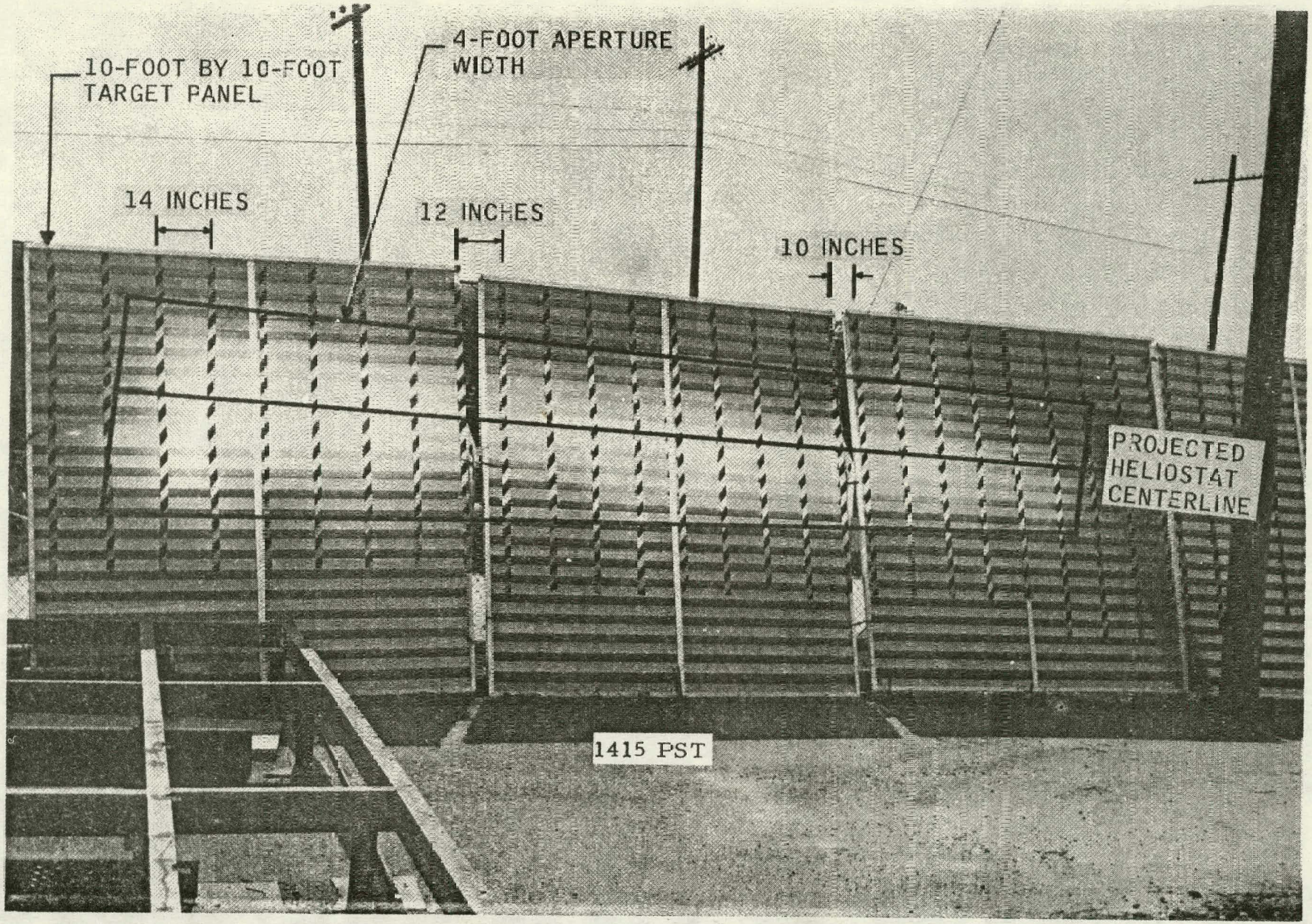

Figure 1-10 DETAIL OF FOCUSED IMAGE OBTAINED IN TEST OF 20 MARCH 1979

THIS PAGE

WAS INTENTIONALLY

LEFT BLANK

2.0 CONCEPT CONFIGURATION ANALYSES

The primary purpose of the analysis phase of the project was to evolve the fundamental concept of line focus solar energy conversion into feasible system configurations for electric power generation. Analytical objectives evolved from those established by the Department of Energy (DOE) for the Central Receiver Solar Thermal Power System (STPS) program. The objectives of the program were to (1) configure solar thermal power plants with rated capacities of 10 MWe (pilot scale) and 100 MWe (commercial scale), (2) analytically establish the cost effectiveness of the commercial scale plant, and (3) perform subsystem research experiments to verify analytical predictions. Plant configurations were to be based on conventional water/steam cycle plants, with solar energy as the source of fuel.

FMC adopted the objectives of the STPS program, but limited the scope to detailed analysis of the collector, receiver, and control subsystems. Within this scope, specific analytical efforts were performed to optimize collector field sizing and receiver configuration for specific design points, and to establish feasible conceptual designs for the receiver and for control of the collector field. The results of these analytical efforts were then used with data from the STPS program to configure and evaluate cost/performance of 10 MWe and 100 MWe plants. Specifically, the power cycle concepts (thermal storage and conventional plant) generated by each of the contractors involved in the Phase I STPS study were evaluated, and the concept which best matched the estimated performance of the FMC receiver was used to configure plant concepts.

2.1 BASELINE ASSUMPTIONS

Several baseline assumptions about physical characteristics of the line focus heliostat and receiver were made at the beginning of the project. These assumptions were developed from the philosophy that, to compete with other forms of power generation, solar-to-thermal energy conversion must be

accomplished with one set of modular components which can be (1) used for any plant capacity, (2) fabricated and assembled in a factory, (3) shipped in completed form on existing common carrier equipment, and (4) installed with standard construction equipment.

The assumptions described below were carried forth through the analysis phase of the project without rigorous examination of the effects on performance or cost of alternate assumptions because the purpose of the analysis was to establish feasibility.

2.1.1 Heliostat Dimensions

An 18.3 meter by 3.05 meter (60 foot by 10 foot) size was selected as the basic unit of controllable collector area because (1) this is the maximum size which can be shipped on a standard truck trailer or rail flatcar, (2) standard processes and equipment can be used to mass produce the support structure, and (3) the unit can be shipped as a completed assembly, ready for installation.

There are relationships between unit collector size, optical performance, and system economics which could influence the choice of an optimum collector size. Some of the more important relationships were qualitatively examined on the basis of a fixed level of energy collection from a field of heliostats.

Since a field of heliostats is, in effect, the fresnel equivalent of a single parabolic concentrator with a much larger concentration ratio than a single heliostat, decreasing the width of a heliostat, and increasing the number of rows could result in an increase in field collector efficiency and a decrease in the total collector area required for a fixed level of energy collection. Balancing this is an increase in the number of (smaller) heliostats and attendant control units. Conversely, increasing the width of a heliostat would reduce the number of control units, but add complexity to fabrication and handling of heliostat sections, and increase design requirements for heliostat support structure and drive units.

Field efficiency is relatively unaffected by variations in the length of a collector unit, since individual units reflect as plane mirrors along the axial dimension. The primary trades involving unit collector length are

(1) the economic relationships between the number of drive and control units, the cost of the units, the number of control points in a field, the fraction of field concentration lost due to malfunction, and (2) the modularity and transportability requirements discussed above.

There are other factors which can influence the choice of unit collector size such as, the trade between optimum spacing between rows and minimum access requirements for maintenance and cleaning vehicles.

The qualitative examinations supported the choice of the baseline unit collector size. Further analyses (Section 3.1 and 5.2) showed that two sections could be driven in elevation and controlled in common, so the effective unit controllable area is doubled while the advantages of the 18.3 meter by 3.05 meter section size are retained.

2.1.2 Receiver Section Dimensions

The nominal dimensions of a receiver section were fixed at 61 meters (200 feet) in length by 61 meters (200 feet) in height. Again, these dimensions were selected primarily on the basis discussed above. It is envisioned that receiver and support towers will be factory-fabricated in unit sections which would be transported on standard common carrier equipment to the field for installation.

The receiver unit section length of 61 meters was derived from calculations made early in the project to estimate steam flow rate required to generate 1 MWe busbar power, using a three-pass-to-superheat, horizontal-tube steam generator concept. These early computations used optimistic estimates for incident solar energy and turbine cycle efficiency. More realistic data were used in subsequent computations of plant sizings (Section 6.0 and Appendix D). These computations indicate that 17-20 sections per 10 MWe of busbar power are required, depending on design point conditions.

There is some qualitative argument to indicate that a longer unit section length would result in more optimal plant configurations on an economic basis, since receiver performance is independent of section length. From a plant design standpoint, increasing receiver unit length to 73 meters (length of two heliostat

modules), could result in a slight reduction in the number of heliostats required for a given plant capacity, and would reduce the number of support towers, but would increase tower structural requirements.

There is little support for unit receiver lengths greater than 73 meters. Some reduction in thermal transport piping would be realized, but intermediate support towers would be required, so it is doubtful that any economic advantage would be realized.

Decreasing unit section length to 55 meters (length of 1.5 heliostat modules) would reduce design requirements for the support towers, and for receiver sections, since the flow rate per section would be less for a given plant capacity. However, more receivers, support towers, and thermal transport piping would be required.

Further in-depth quantitative analysis is required to verify that a 61 meter section length is an optimum choice. However, there is sufficient data at this point to support the choice as feasible from the standpoints of performance and structural requirements. Additionally, the nominal sizing of 0.5 MWe per section offers the flexibility of (1) configuring plants over a wide range of power levels, and (2) increasing the generating capacity of large plants in time-phased increments to optimally match the increase in load demand.

A nominal height of 61 meters was selected for the towers because (1) standard designs for utility transmission towers (which reach heights of 61 meters) can be used, and (2) erection of towers and receivers can be performed with standard construction cranes. Structural requirements for a support tower were generated during the project based on a 61-meter receiver section. Appendix F contains the computations.

2.1.3 Collector Field Design Point

The collector field optimization analysis was based on a winter solstice design point which was the design point specified by DOE for the central receiver 10 MWe pilot plant. Consequently, all of the receiver performance data used to size plant concepts are based on this design point, although parametric relations were developed to use the receiver data with performance data for an optimized equinox field.

It is important to note that the winter solstice design point led to the discarding of the South collector field and the twin-receiver (North and South-facing) concept in favor of North-only field design (Appendix D, Section D.1). However, further analysis (Section 6.5) tends to support the reinstatement of the South field for an equinox design point. Further examination of this point is warranted because of the economic advantages of the twin-receiver concept.

2.2 RECEIVER CAVITY APERTURE OPTIMIZATION

The effect of the solar divergence angle on the unsymmetrical mirror field distribution is that a progressively larger cavity aperture is required as the mirror field moves away from the receiver. Tilting the receiver to make the plane of the aperture more normal to incident flux increases recovery from the outboard mirrors at the expense of reduced intensity from the inboard mirrors. The best tradeoff will maximize recovery and intensity at minimum aperture width.

The results of this analysis are shown graphically in Figure 2-1, with the best case indicated that leads to minimum receiver aperture. Aperture width of 1.34 meters (4.4 feet) and receiver orientation of 45 degrees were initially selected as nominal design points.

The initial optimization analysis was based on an approximation of the incident intensity reflected from a collector field. Further analysis was performed to verify the original results with the collector field optimization model (Appendix A).

The distribution of solar intensity at the focal plane of a receiver was computed as a function of aperture width and orientation. Figure 2-2 shows the results, which support the original selection of nominal receiver parameters. However, the results indicated that the aperture area between 2.0 and 2.2 feet admitted less than 1 percent of total incident energy, but accounted for 10 percent of the aperture area. It was concluded that reducing the nominal aperture width to 1.22 meters (4 feet) would improve overall receiver efficiency by reducing the energy losses from reradiation and convection. This reduction would more than offset the small decrease in energy admitted through the aperture.

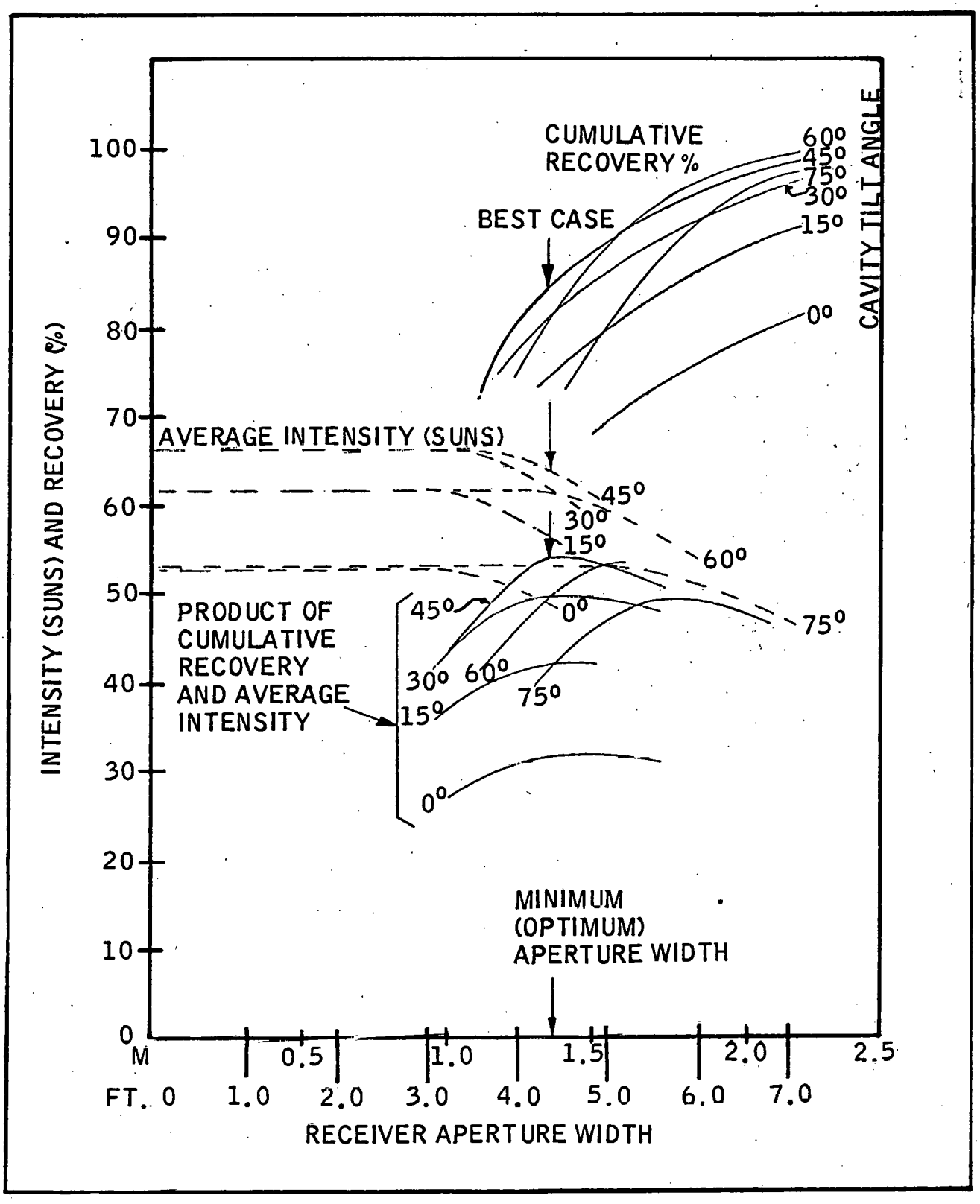

Figure 2-1 RECEIVER CAVITY APERTURE OPTIMIZATION

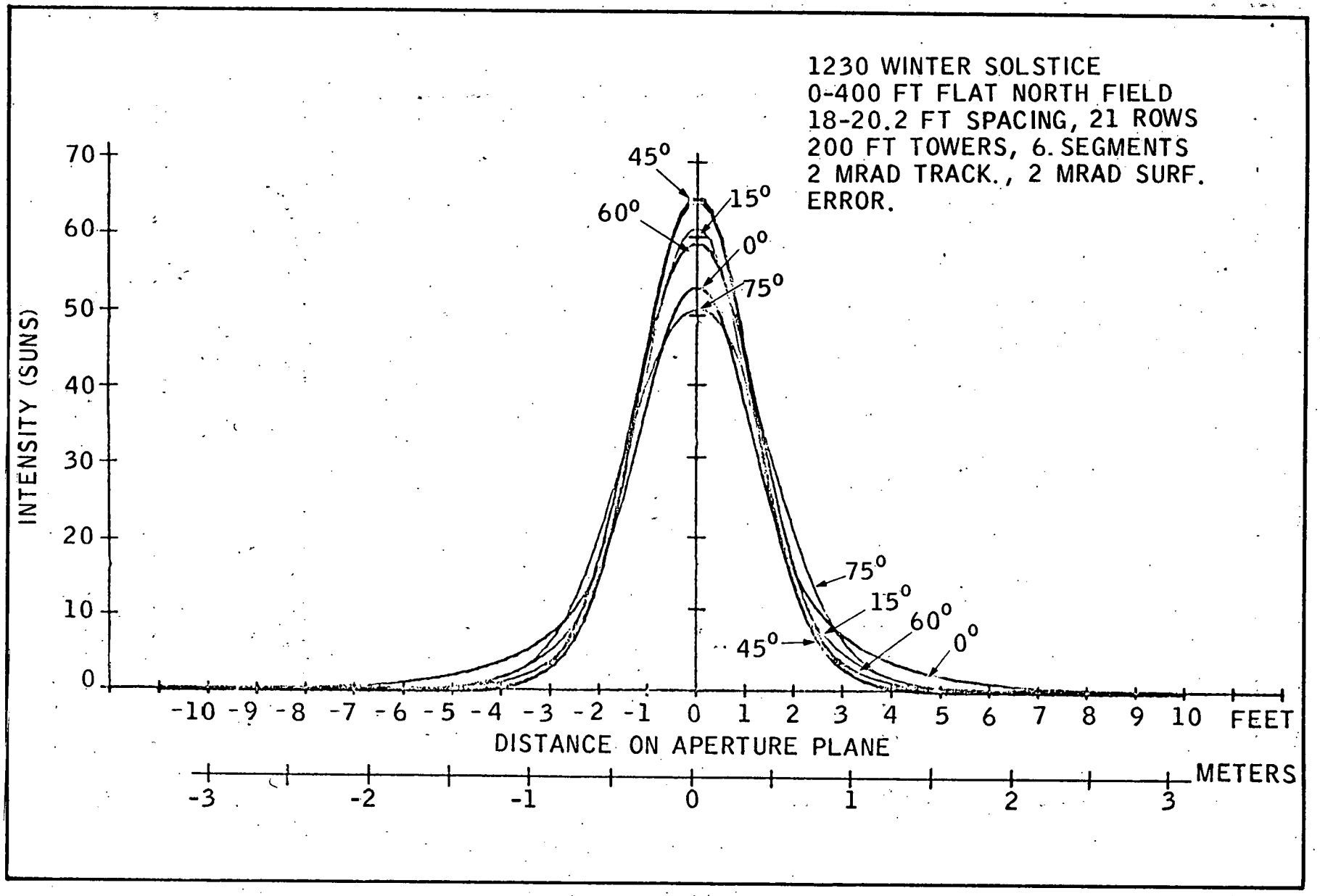

Figure 2-2 FLUX DISTRIBUTION FOR VARIOUS RECEIVER TILT ANGLES

The effect of varying the aperture plane angle has been calculated for a flat North field 400 feet wide and configured for solar noon at winter solstice. Figure 2-3 shows the peak intensity and average intensity over a 4-foot-wide aperture plotted against aperture angle.

These curves indicate that intensities exhibit maxima, and that peak intensities are increased over a horizontal aperture plane by 23 percent and 19 percent for peak and average intensities, respectively. It is interesting to note that the maxima do not occur at the same angle. Highest peak intensity occurs at 35 degrees, while the maximum average intensity is obtained at 45 degrees. Because a 4-foot aperture is to be employed, the 45-degree aperture plane angle selection appears near optimum.

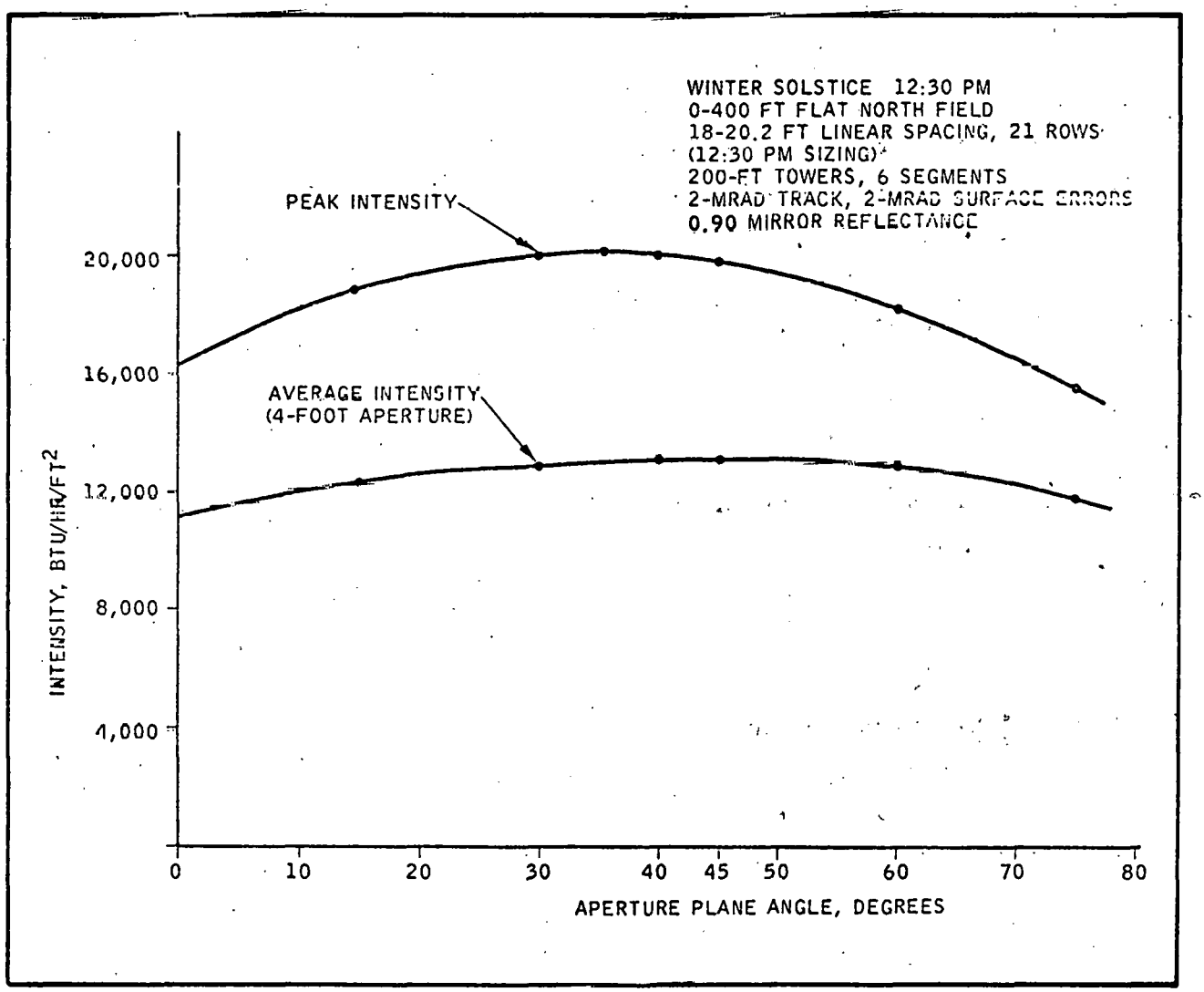

Figure 2-3 EFFECT OF APERTURE PLANE ANGLE ON APERTURE FLUX INTENSITY

2.3 COLLECTOR FOCUSING ANALYSIS

A significant advantage of a cylindrical mirror over a spherical mirror is the ability to bring the light to a sharp focus. Illumination is generally off axis, and consequently off-axis astigmatism is introduced. In the case of spherical mirrors, two focal planes, the sagittal and the tangential, are formed, which increase in separation as the illumination angle increases. The working focal plane is taken as the plane of least confusion, which is located between the two foci. In contrast, cylindrical mirrors illuminated off axis in the present manner have infinite radius of curvature in the sagittal plane and therefore focus only in the tangential plane. It follows that a cylindrical mirror with adjustable radius of curvature can be brought to a linear focus at any off-axis illumination angle, and can be considered astigmatic.

2.3.1 Focusing and Solar Position

If a cylindrical mirror of radius of curvature R is illuminated off axis with a projected angle, A, in the plane of curvature, the tangential focal length is

$$F_t = (R \cos A)/2. \tag{1}$$

For a pure circular curvature, R is related to the chordal height, h,

$$h^2 - 2Rh + c^2 = 0 \tag{2}$$

where c is one-half the aperture width (1.52 meters). If $h \ll c$, a valid condition in this case,

$$h = c^2/2R. \tag{3}$$

This approximation introduces an error of less than 0.004 percent. Substituting and rearranging,

$$h = (c^2 \cos A)2F_t. \tag{4}$$

The focal length, F_t, is equal to the optical path length of the ray from collector to receiver

$$F_t + d = (y_i^2 + H^2)^{1/2} \tag{5}$$

where y_i = horizontal distance from receiver axis and H = receiver height.

Using the sign convection that angles are positive when the rays approach the receiver, angle A can be written

$$A = \alpha + \phi \text{ (or } \psi) \tag{6}$$

where α is the tracking angle, and ϕ (or ψ) is the incident angle of the sun, projected in the plane perpendicular to the heliostat axis.

Combining the above equations, the chordal displacement for a north or south field (east-west axis) can be written

$$h = c^2 \left(\cos\left[\tan^{-1}\left(\cos\beta / \tan\theta\right)\right] + \tan^{-1}\left(y_i/H\right)\right)/2 \sqrt{y_i^2 + H^2} \tag{7}$$

The expression for North-South axis fields can be similarly derived. Equation (7) gives the chordal height of each mirror explicitly as a function of solar azimuthal (β) and elevation (θ) angles, and the horizontal row distance (y_i). Because the relationship between β and θ with time is known, the chordal height can be plotted against time. This has been done for representative mirror rows in Figures 2-4 through 2-6.

2.3.2 Focusing Errors

The relation between focusing error and chordal height error must be known to assign realistic tolerances to the focusing mechanism. The convergent half angle, γ, of the rays coming to a focus from a mirror is

$$\gamma = \tan^{-1}\frac{c}{F_t} \approx c/F_t \tag{8}$$

for small angles. Combining Equations (4) and (8)

$$\gamma = \frac{4h}{c \cos A} \tag{9}$$

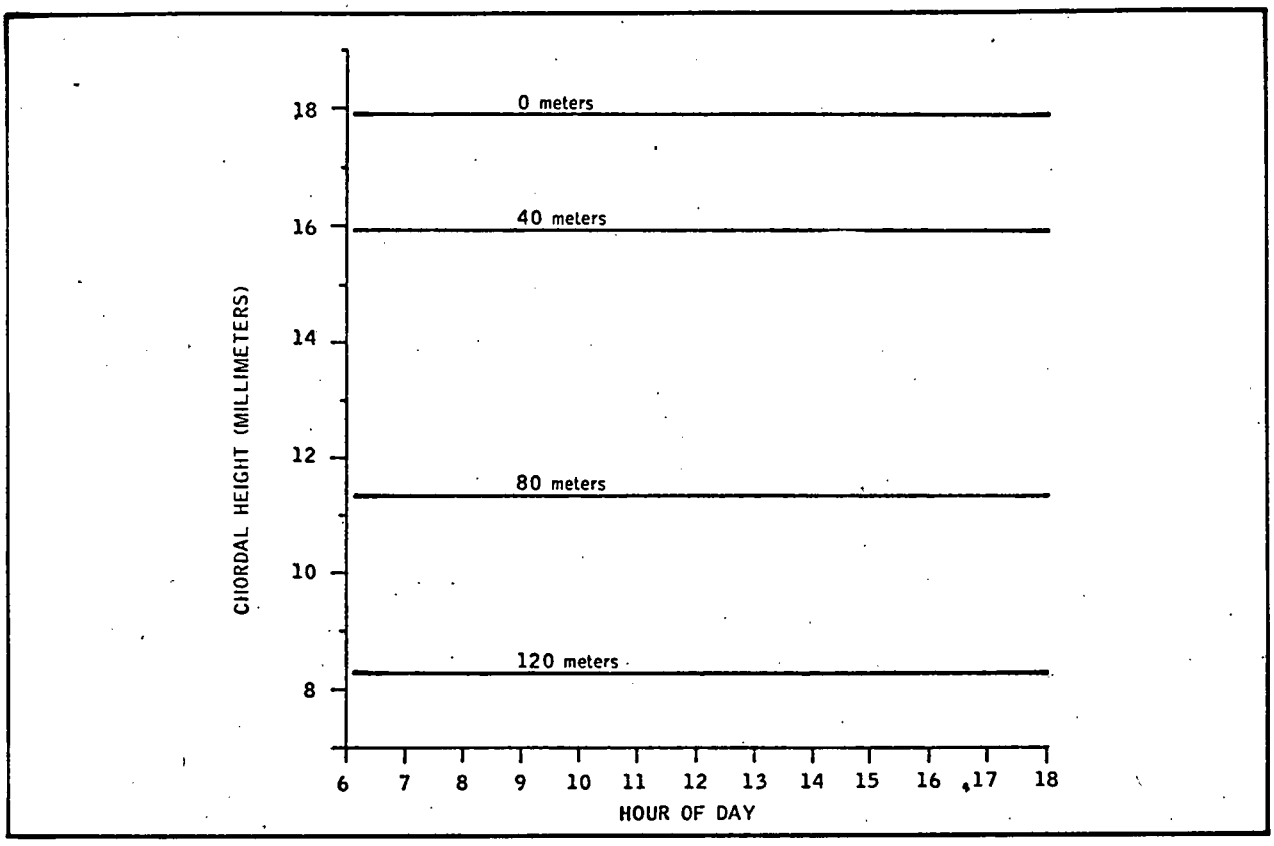

Figure 2-4 HOURLY FOCAL ADJUSTMENTS FOR REPRESENTATIVE ROW DISTANCES FROM RECEIVER TOWER IN METERS; EQUINOX

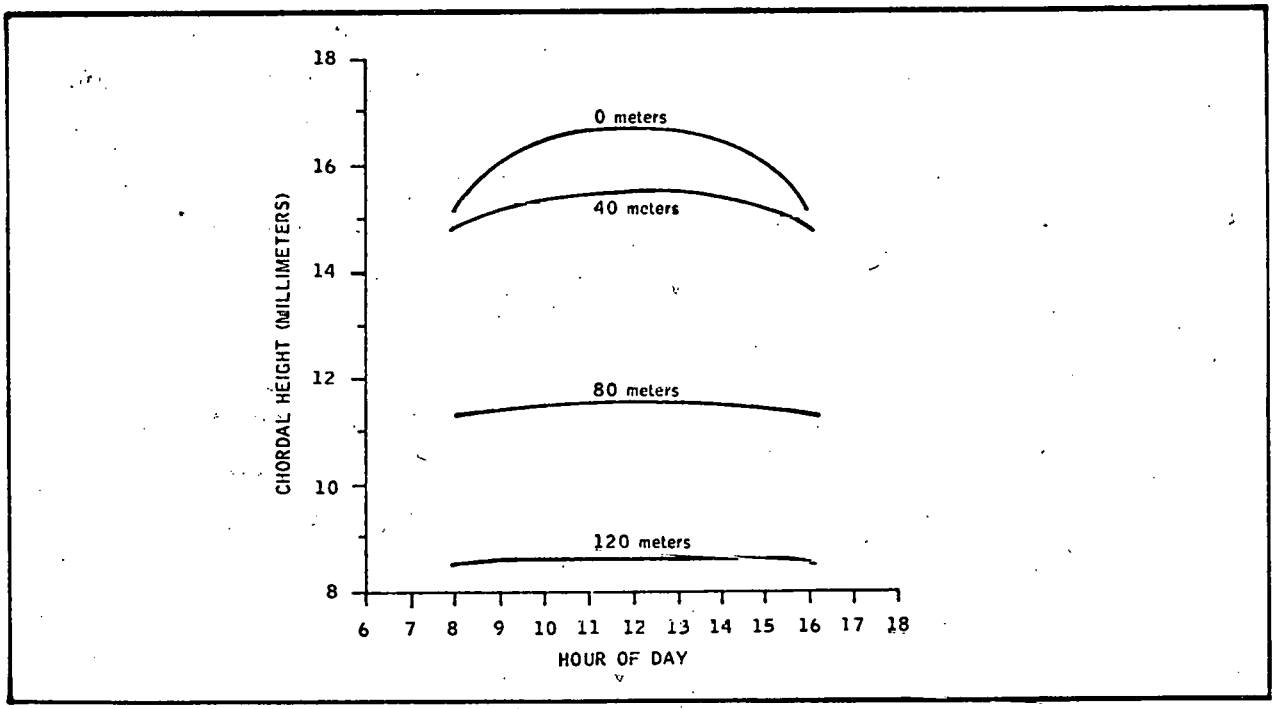

Figure 2-5 HOURLY FOCAL ADJUSTMENTS FOR REPRESENTATIVE ROW DISTANCES FROM RECEIVER TOWER IN METERS; WINTER SOLSTICE

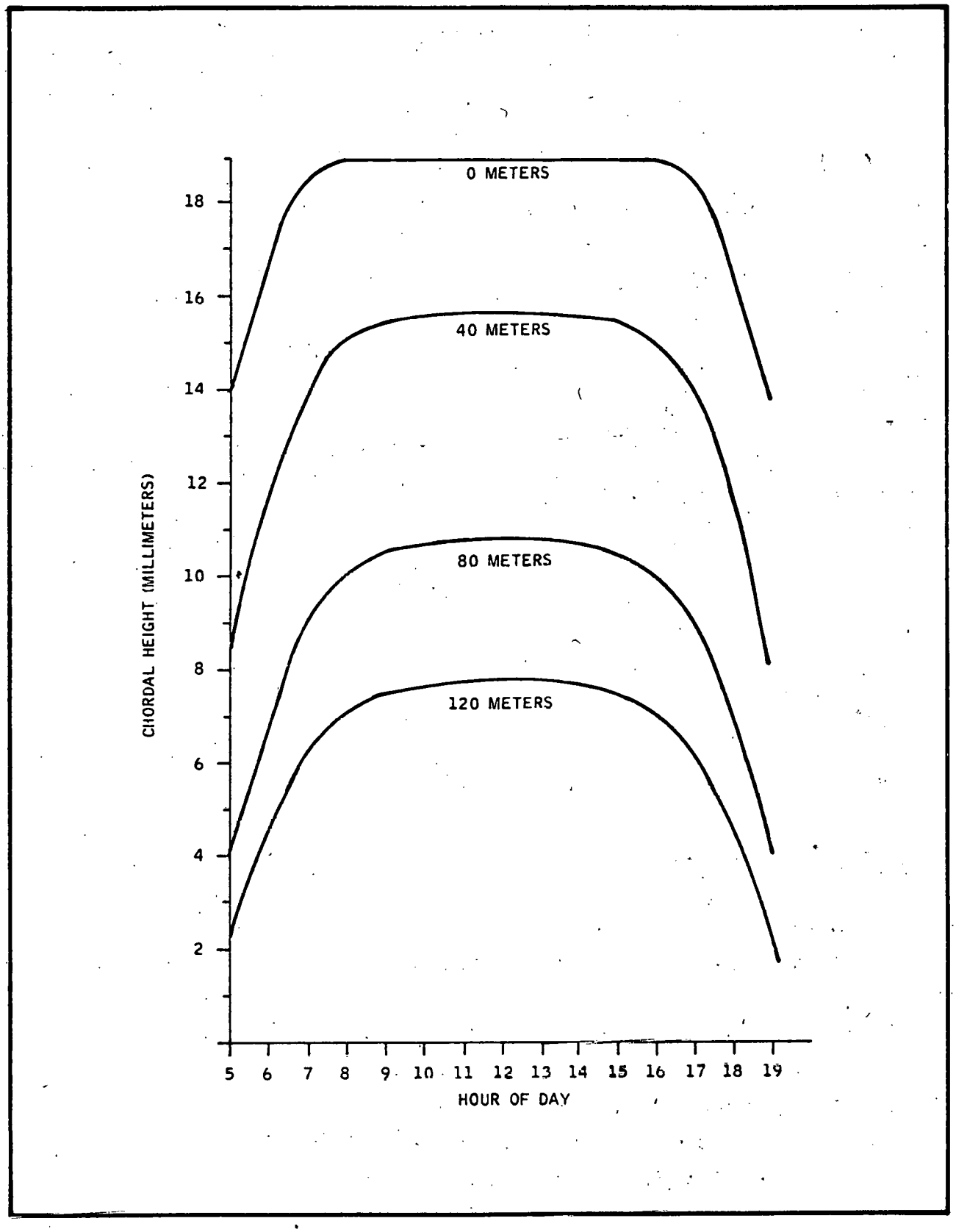

Figure 2-6 HOURLY FOCAL ADJUSTMENTS FOR REPRESENTATIVE ROW DISTANCES FROM RECEIVER TOWER; SUMMER SOLSTICE

if h varies by Δh, then γ will vary by $\Delta\gamma$

$$\gamma + \Delta\gamma = \frac{4}{c \cos A} (h + \Delta h) \tag{10}$$

Let the fractional errors be defined:

$$E = \frac{\Delta\gamma}{\gamma}, \quad \delta = \frac{\Delta h}{h}$$

Then (10) becomes

$$\gamma(1 + E) = \frac{4}{c \cos A} h(1+\delta) \tag{11}$$

Dividing (11) by (9) gives the result

$$E = \delta. \tag{12}$$

Then

$$\frac{\Delta\gamma}{\gamma} = \frac{\Delta h}{h} \tag{13}$$

Substituting (9) into (13) and rearranging,

$$\Delta\gamma = \frac{4}{c \cos A} \Delta h \tag{14}$$

Taking $\Delta\gamma = 0.002$ radians as maximum permissible error, 60 degrees as the maximum off-axis angle, and $c = 1.52$ meters,

$$\Delta h = \frac{0.5(1.52)}{4} (0.002) = 0.38 \text{ mm.} \tag{15}$$

Holding the chordal height to a tolerance of 0.015 inch will meet the required 2-milliradian focus error requirement. At smaller off-axis angles, larger tolerances are allowed, the maximum being 0.76 millimeter at normal incidence.

2.3.3 Effect of Curvature Irregularities on Focal Size

Irregularities in the mirror curvature introduce an angular divergence, δ', of the reflected ray equal to twice the angular value of the irregularity. If the value is small, this is equal to the difference of the tangent of the irregularity and the tangent of the ideal parabolic curve at that point. Assuming these errors have a nearly normal distribution, the effect of such error sources on the focal line width has been treated in the derivation of the divergence angle distribution (Appendix A). The calculations indicate that these errors should be held to less than 2 milliradians.

The initial proposed mirror arrangement consisted of a central loading of the surface with edge support to provide curvature. The curve so produced is not a true radius, but a curve with a slope of:

$$\theta = 12kw^2 c(1-c) \tag{16}$$

where c is related to the position along the surface, $x = cw$, $0<c<0.5$, and k is a system constant,

$$k = y_{max}/w^3 \tag{17}$$

y_{max} being the central displacement.

The parabolic slope, in the same units, is

$$\theta_p = \frac{cw}{2F} \tag{18}$$

F being the focal length. The difference between θ_p and θ is Δ. It can be shown that, for w = 10 feet,

$$\delta' = 2\Delta = 2c\left[\frac{5}{F} - 1200k(1-c)\right] \tag{19}$$

δ' will vary between $\pm \delta_{max}$, when $k = 0.007113/F$. (20)

At F = 200, $\delta = \pm 3.67$ milliradian, which is unacceptably high.

If the surface were pulled down at three equally spaced points,

$$\delta' = c\left[\frac{2.5}{F} - 300k(1-c)\right] \qquad (21)$$

with k = 0.0142/F. At F = 200, δ = 1.83 milliradian, a more acceptable value. The error can be reduced further by additional pull downs. Alternately, other designs such as edge-applied bending torque could be employed. This would give a constant radius over the width of the mirror.

The current concept uses 153 centimeters by 51 centimeters by 3.3 millimeters (60 inches by 20 inches by 0.09 inch) glass panels supported at the edges. Such an unsupported plate should sag approximately 3 millimeters (0.12 inch) in the center due to gravity, resulting in a 10.3-milliradian error. However, this error is longitudinal, and therefore contributes primarily to an approximate 3-meter (10-foot) increase of focal line length, and any loss occurs only at the ends of the receiver.

2.4 COLLECTOR FIELD PERFORMANCE ANALYSIS

Field sizing calculations in Subsections 2.4.1 and 2.4.2 are based on the computer model described in Appendix A.

2.4.1 Flat Field

Calculated aperture flux profiles for a winter solstice day obtained from a north field with an east/west axis is shown in Figure 2-7. The mirror row spacing was adjusted to obtain an approximate maximum intensity/mirror ratio at solar noon. Peak intensity of 64 suns is obtained, assuming 2-milliradians tracking and 2-milliradians surface error contributions, a 400-foot-wide field, and a 45-degree-aperture plane angle. The field contains 21 mirror rows, for a total field coverage of 52.5 percent, which corresponds with the field cosine value for that day of 51.5 percent. The field has also been spaced for 2:30 p.m. on the same day, requiring 19 mirror rows. The hourly intensity for the two configurations is shown in Figure 2-8. The two configurations are compared in Table 2-1.

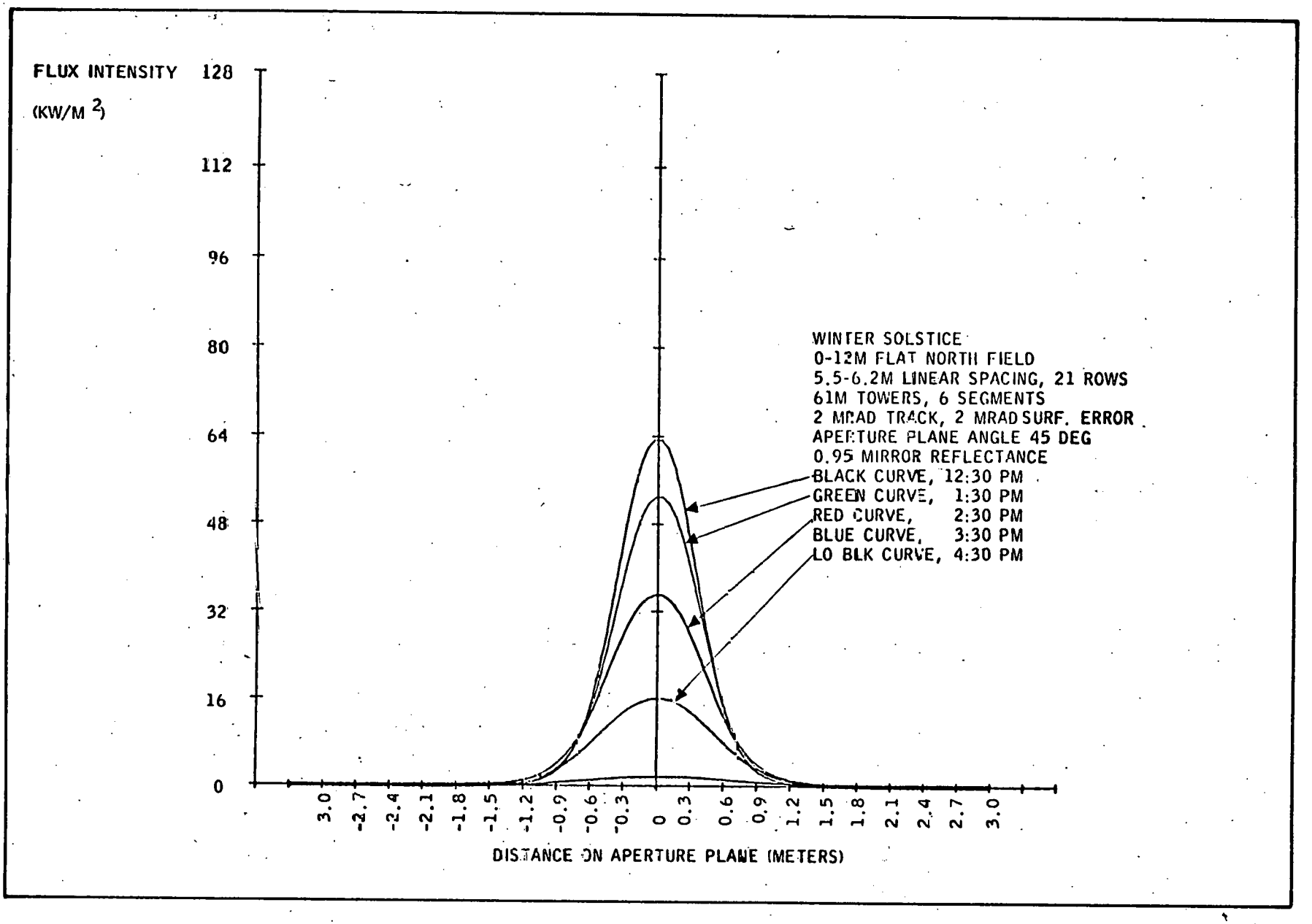

Figure 2-7 APERTURE FLUX INTENSITY PROFILES FOR FLAT NORTH FIELD

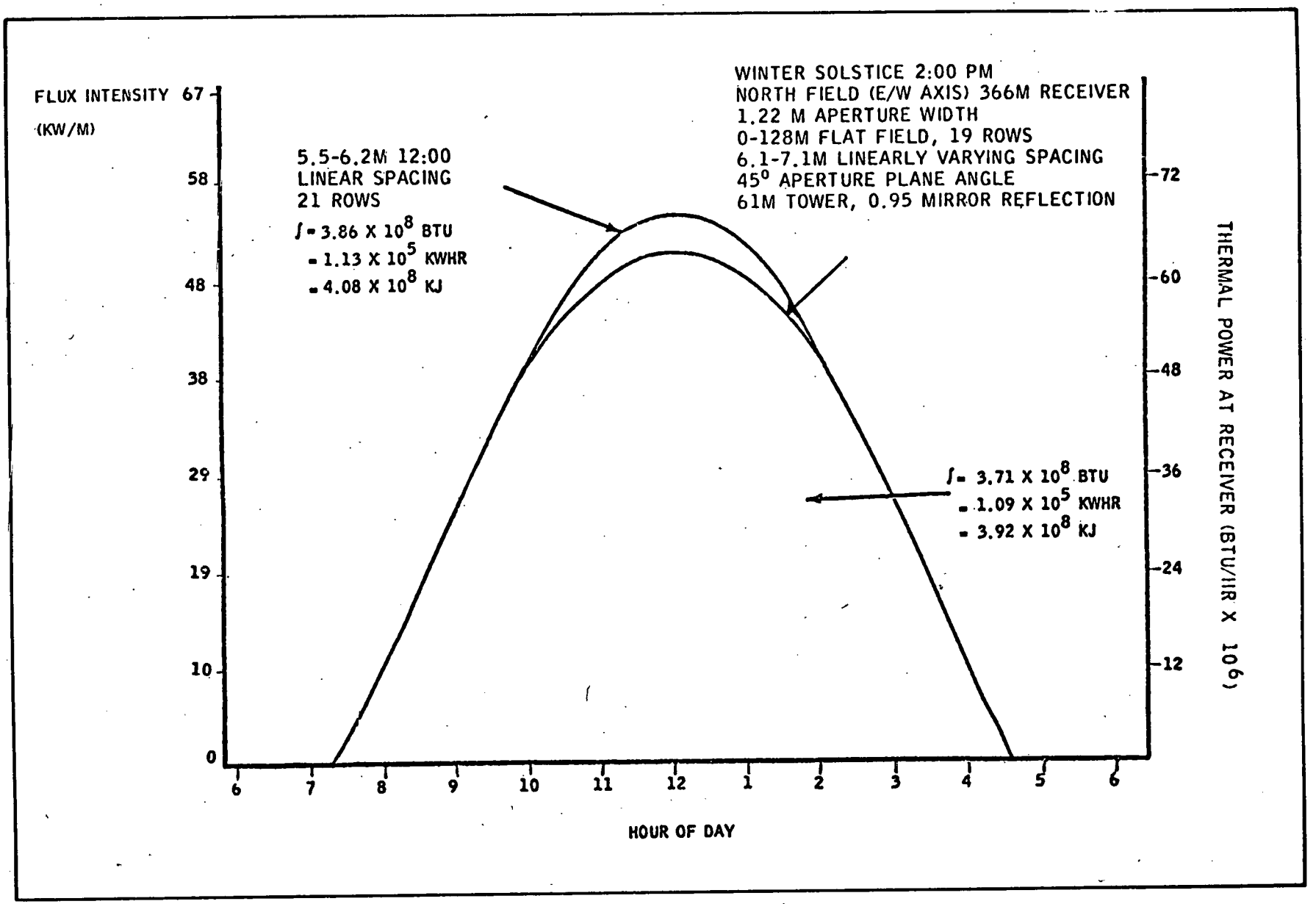

Figure 2-8 HOURLY FIELD PERFORMANCE — NORTH FIELD

It should be noted that a field sized for 2:00 p.m. winter solstice yields an output that is nearly independent of season.

Table 2-1 COMPARISON OF FIELDS SIZED FOR 12:30 and 2:30 WINTER SOLSTICE

Item	12:30 Sizing	2:30 Sizing
Number of rows	21	19
Maximum intensity (suns)	64.0	58.0
Average intensity (4-foot aperture at 2:30 p.m.)	26.9 KW/m^2	26.9 KW/m^2
Total daily energy (4-foot aperture)	3.3×10^5 KJ/Ft	3.10×10^5 KJ/Ft
Average intensity/row (4-foot average at 12:30 p.m.)	3.13 KW/Row	2.99 KW/Row
Energy/row (4-foot aperture, 9:30-2:30)	1.03×10^4 KJ/Ft/Row	1.08×10^4 KJ/FT/Row

Similar calculations for a South (east/west axis) field and an East (north/south axis) field have been performed. To obtain equivalent output at winter solstice, a South field of 29 rows is required.

Figure 2-9 shows the hourly peak intensity of an east field at winter solstice. Conditions included a constant 12-foot spacing (34 rows). The shape of the curve is explained by the fact that the northward axial displacement is greatest at midday, resulting in nearly doubled path lengths. The morning sun is incident on the mirrors at a greater angle with the mirror normals. As a result, the mirrors are more nearly normal to the sun in the afternoon and are individually more effective. The 12-foot spacing permits the sun to "see" the gaps between the mirrors during the middle hours of the day. Therefore, during these unshadowed hours, the heliostats behave as isolated collectors, performing more effectively in the afternoon and resulting in the asymmetric distribution. A west field would give peak output in the morning.

2.4.2 Sloped Field

As part of the checkout process for the various capabilities of the collector field program, the performance of a 35-row north field situated on an 11-degree slope was performed. The output was strikingly improved from

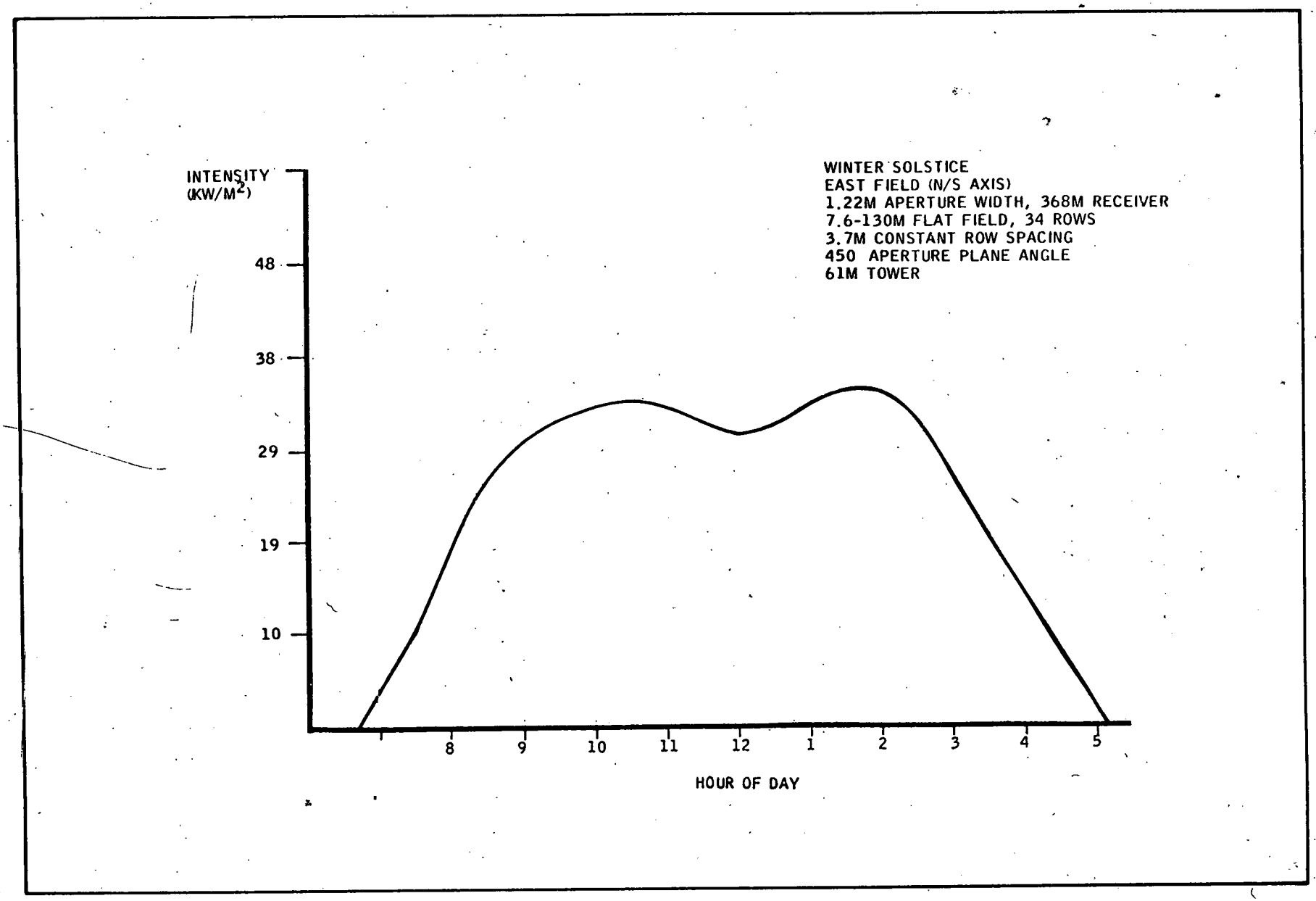

Figure 2-9 HOURLY FIELD PERFORMANCE — EAST FIELD

65 to 90 suns peak concentration (Figures 2-7 and 2-10). No field size optimization was performed. Shading and screening factors indicate that the field density is about 15 percent high; therefore, equivalent performance could be obtained from an appropriately spaced field containing five fewer rows. Conversely, a steeper terrace should yield higher concentration, approaching 100 suns.

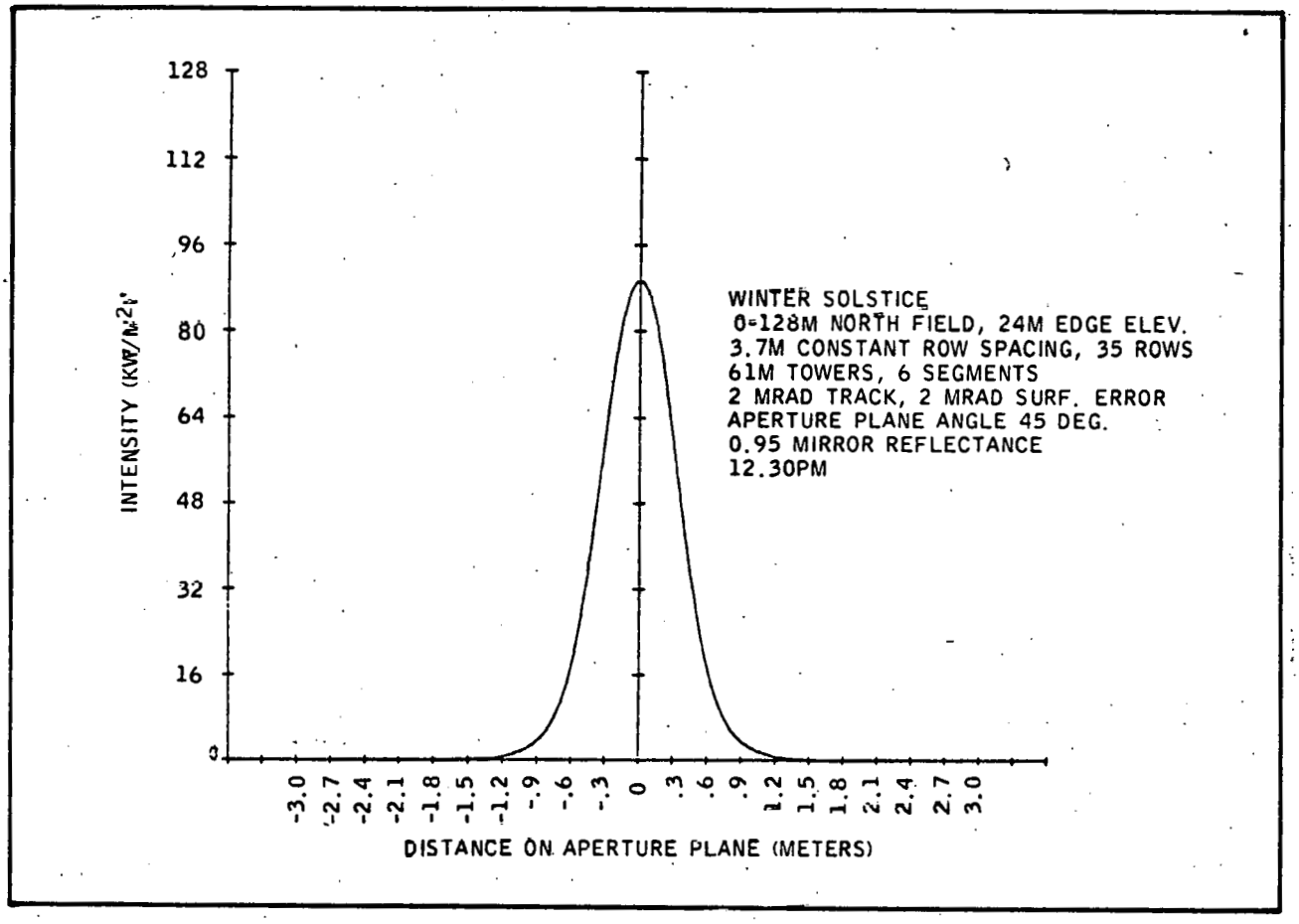

Figure 2-10 APERTURE FLUX INTENSITY FOR SLOPED NORTH FIELD

This increased solar concentration is attractive. The increased flux would permit the receiver to operate more efficiently for a longer operating day. For a North field, the optical pathlength is reduced, and, therefore, the length of the butterfly end section is reduced, in the case calculated, by 10 percent. A South field can also be installed in a downward slope. However, the increased optical pathlength and screening should partially offset the increased collection power. The output of an unoptimized 35-row South field sloped 11 degrees (about 20-percent slope) was calculated (Figure 2-11). A 74-sun concentration was obtained. Shading and screening factors indicate that some further increase could be obtained with an increased row density.

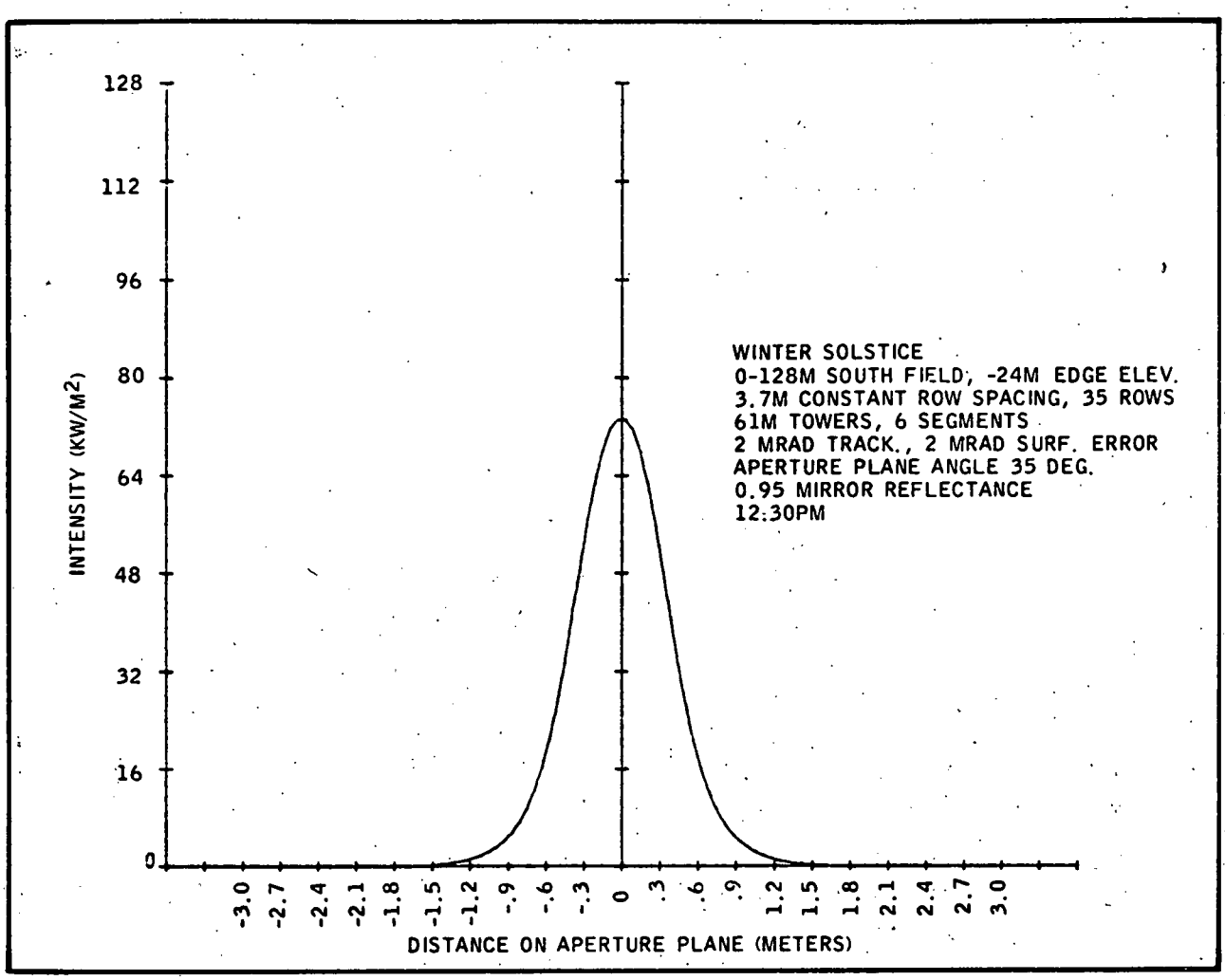

Figure 2-11 APERTURE FLUX INTENSITY FOR SLOPED SOUTH FIELD

Additional calculations were performed to describe a more nearly optimized sloped field configuration. Slope angles and mirror spacings were varied to obtain maximum output and peak concentration per row. Noon winter solstice was chosen for these calculations. Peak performance from a north field was obtained from a field on a 30-percent (16.7-degree) slope, containing 30 heliostat rows spaced in parabolically varying intervals from 12 feet at the inside to 20 feet at the outside of the field. The projected maximum horizontal width was maintained at 425 feet. Peak intensity of 99.5 suns was obtained with a concentration ratio of 3.32 suns per row. Best output from a south field was obtained with 37 rows spaced 10.5 feet to 13 feet apart on parabolically varying intervals and placed on a -30-percent (-16.7-degree) slope. Peak intensity was 78.5 suns, and the concentration ratio was 2.28 suns per row. These data are plotted in Figures 2-12 and 2-13.

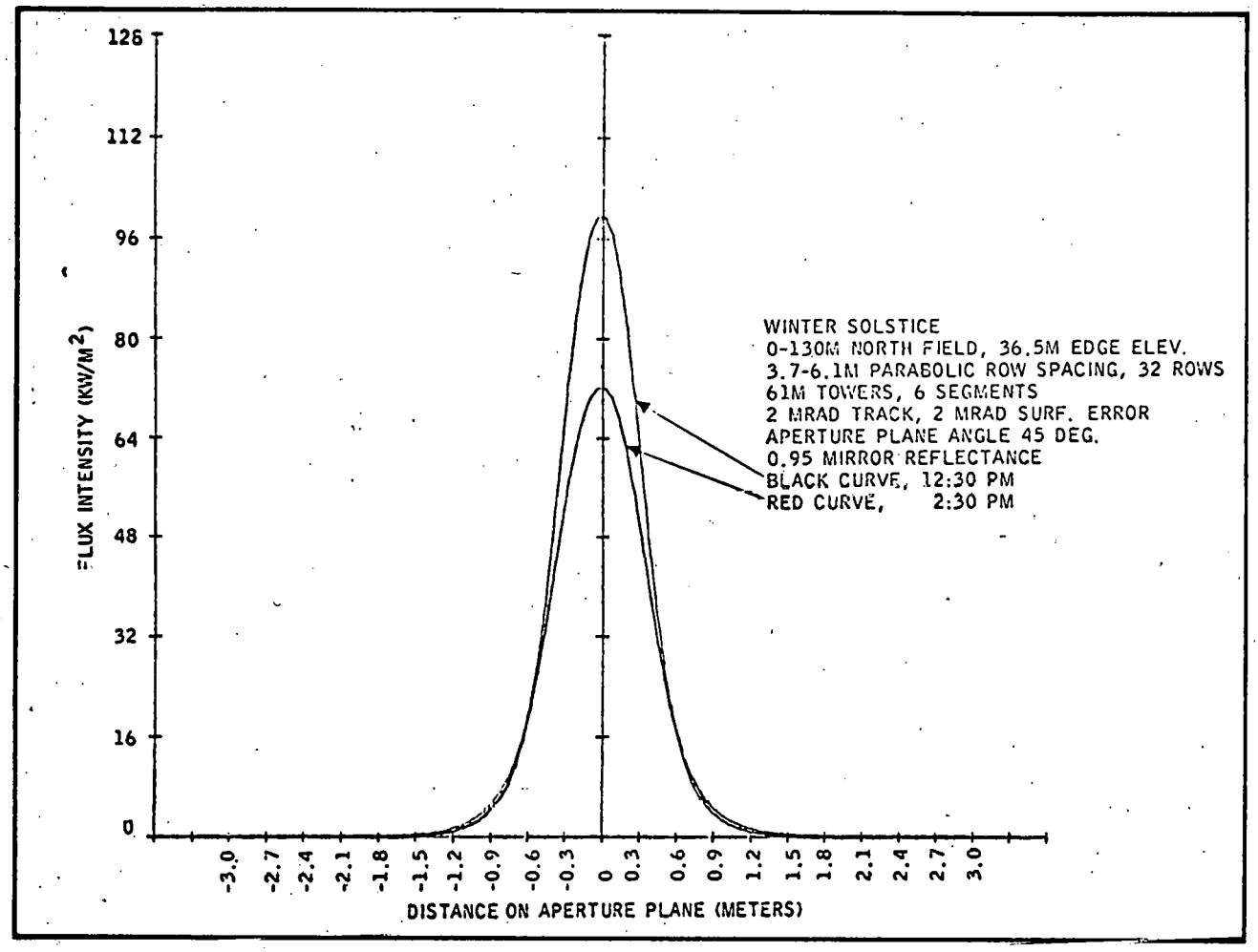

Figure 2-12 APERTURE FLUX INTENSITY PROFILE FOR OPTIMIZED SLOPED NORTH FIELD

Comparison between the optimized sloped north field and an optimized flat north field is shown in Table 2-2.

Table 2-2 COMPARISON OF FLAT AND SLOPED NORTH COLLECTOR FIELDS

Parameter	Sloped North Field	Flat North Field
Horizontal width, meters	130	130
Slope, degrees	16.7	0
Number of rows	30	21
Aperture angle, degrees	45	45
Tower height, meters	61	61
Peak concentration, suns	99.5	64
Concentration, suns per row	3.32	3.05

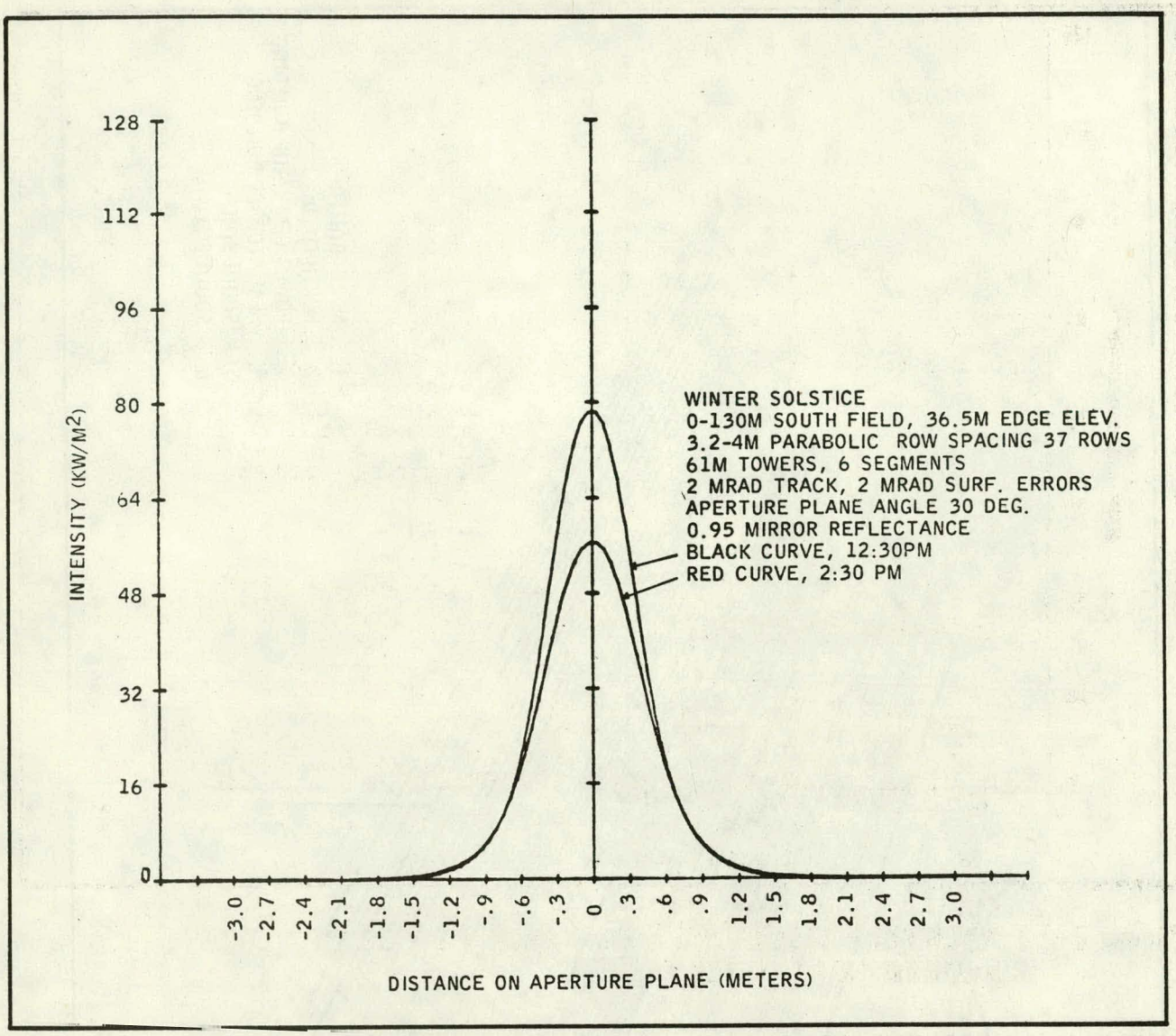

Figure 2-13 APERTURE FLUX INTENSITY PROFILE FOR SLOPED SOUTH FIELD

The linear collector system is essentially a long, narrow concept utilizing a strip of land 900 feet wide and 1,200 feet long for a 10 MWe plant. Collector fields and receivers for longer plants could be laid out, like ribbons, on available southward-facing slopes. Moreover, the linear nature of the concept permits the system to follow local topological features. That is, the receiver and collector field need not be perfectly straight, but can tolerate a reasonable degree of serpentining. This feature can substantially increase the availability of suitable flat or sloped installation sites. An artist's rendition of an installation on a slope is included in Figure 2-14.

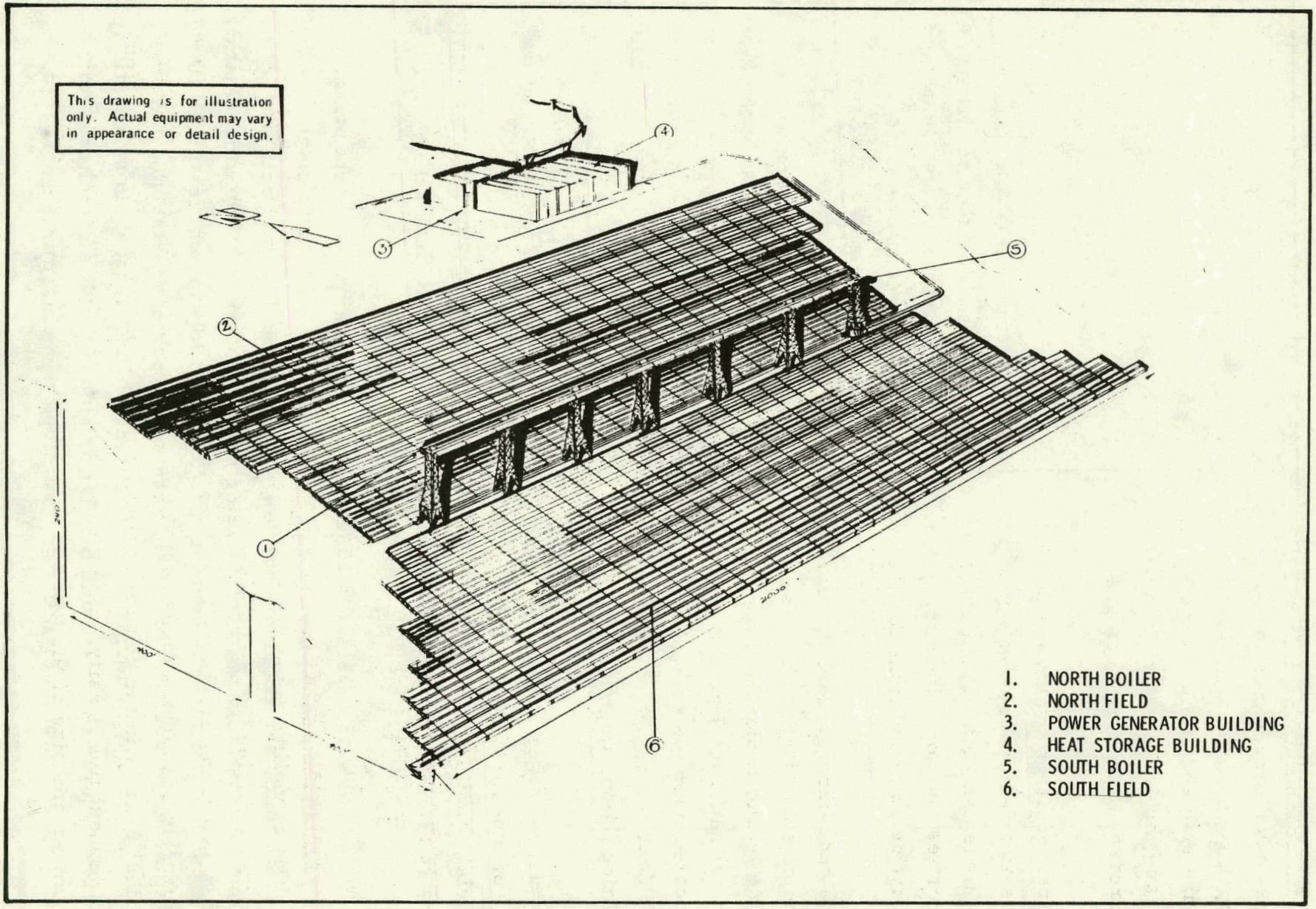

Figure 2-14 SLOPED FIELD SYSTEM

2.5 EVALUATION OF ONCE-THROUGH DESIGN CONCEPTS

First-order procedures for evaluating the thermal performance of once-through receiver designs were developed to investigate design variables such as tube size and number under a variety of operating parameters such as flow rate and insolation. The procedure was applicable to both the subcritical and supercritical pressure designs.

The performance evaluation procedure divided the receiver into a series of sequential receivers over which the fluid properties and flow and heat-transfer conditions can be assumed constant. The procedure calculated the change in properties and conditions across the section and produced a revised set of properties and conditions for the subsequent section.

In the once-through design, tubes run down and back a modular length, assumed about 50 feet for ease of transport and erection. The program calculates the radiant and convective losses, and takes into account the distribution of radiation flux across the aperture. The cooler tubes are assumed to be located near the edge of the aperture where the flux is lowest and the hotter tubes near the center where the intensity is greatest. Steady-state operating conditions from stagnation through all others of interest were determined.

Two basic designs were considered; one in which the boiler consists of a plane of tubes mounted in the focused region and backed by a refractory material, another in which the tubes are mounted on the inside of a circular cavity of refractory material with an aperture at the position of the focus plane.

2.5.1 Flat-Plate Design

Computer modeling of the flat-plate receiver considered the full hydraulic performance using the properties of water, and included conduction and convection heat transfer, as well as radiation. The coolest fluid flows down the tubes on the edge of the focus region and returns in the next bank of tubes. The final pass is in the central portion of the aperture plane, in the region of the highest flux density. The number of passes, the length of the passes, the number and size of the tubes in the passes, the emissivity, the local

temperature, and the local wind velocity are among the input variables to the program. Typically we consider that the fluid flows down a 200-foot length before being turned and flowing in the opposite direction. This distance corresponds to the distance between support towers.

These calculated fluid properties at any point in the reciever, including velocity and Reynolds number, can be used to assist during the boiler design phase. Given restraints, we achieve a design which optimizes the availability function, where availability = $h - T_\infty s$

and h = enthalpy

T_∞ = ambient temperature

s = entropy.

The availability is an indicator of the specific work that can be extracted from the working fluid at the given ambient temperature. The advantage of considering availability rather than only enthalpy is that availability also accounts for the pressure drop through the receiver system. By looking at the availability, one can tell whether a sacrifice in enthalpy or in pressure is more expeditious.

Two design strategies have been used. In one strategy, a specified number of tubes has been assigned to each pass. The size of the tubes in each pass varies to accommodate increasing specific volume as heat is added and pressure drops. In the other design strategy, the size of the tubes in all loops is constant and the number of tubes is varied to accommodate the expansion. Within reasonable design limits, both designs appear to optimize to nearly the same performance.

Just past the design point of 1400 winter solstice, a flat-plate recciver efficiency of about 60 percent was estimated, with inlet conditions, at 204°C (400°F), and 6.9 MPa (1,000 psia) and exit temperature of 454°C (850°F). The comparable figure for 1230 winter solstice is about 75 percent. A wide range of operating pressures and temperatures were explored.

2.5.2 Cavity Design

A model was generated to compare the performance of the flat plate with the performance of cavity construction and to test the radiation analysis techniques applying to the cavity. The model was simple in that it did not consider the hydraulic aspects, or heat transfer effects other than radiation. The model used the flux data output from the collector field program. In the model, a 6-foot-diameter cavity was modeled by a nonagon 2 feet on a side, with two sides of the nonagon missing to simulate the aperture. The heat flux was made symmetrical to simplify calculations. The fluid was assumed to enter the panel near the aperture and exit from the highest flux panel opposite the aperture opening.

Typical performance graphs are shown in Figure 2-15. The curves indicate that at an output temperature of 454° C (850° F) the collection efficiency increases by 10 percent for high-emissivity tubes (emissivity = 0.95), a 14 percent increase for an emissivity of 0.8, and a 23 percent increase for an emissivity of 0.5. The simple model confirmed that a cavity design gives a significant efficiency advantage, especially for lower emissivities.

A complete performance model of the cavity, similar to that of the flat plate, was implemented on the computer using the radiation procedures developed in the simplified model. The model is described in Appendix B. Shown in Figure 2-16 are the results of a thermal analysis of 61-meter-long cavity type receiver using a once through boiler. The efficiency of the receiver and outlet temperature are plotted as a function of steam flow.

Figure 2-17 shows the results of a similar analysis for the flat-plate receiver. As can be expected, the cavity receiver shows a much better maximum efficiency (i.e., about 73 percent versus 56 percent for the flat-plate receiver at 1230, winter solstice).

It appears that the cavity receiver is capable of producing a steam outlet temperature of 450° C at 2,000 kilograms per hour at a near maximum receiver efficiency at 2:30 p.m., winter solstice. Shown in Table 2-3 are the effects of variation of tube absorptivity (α), emissivity (ϵ), and steam pressure on the boiler outlet temperature and efficiency at constant flow rate.

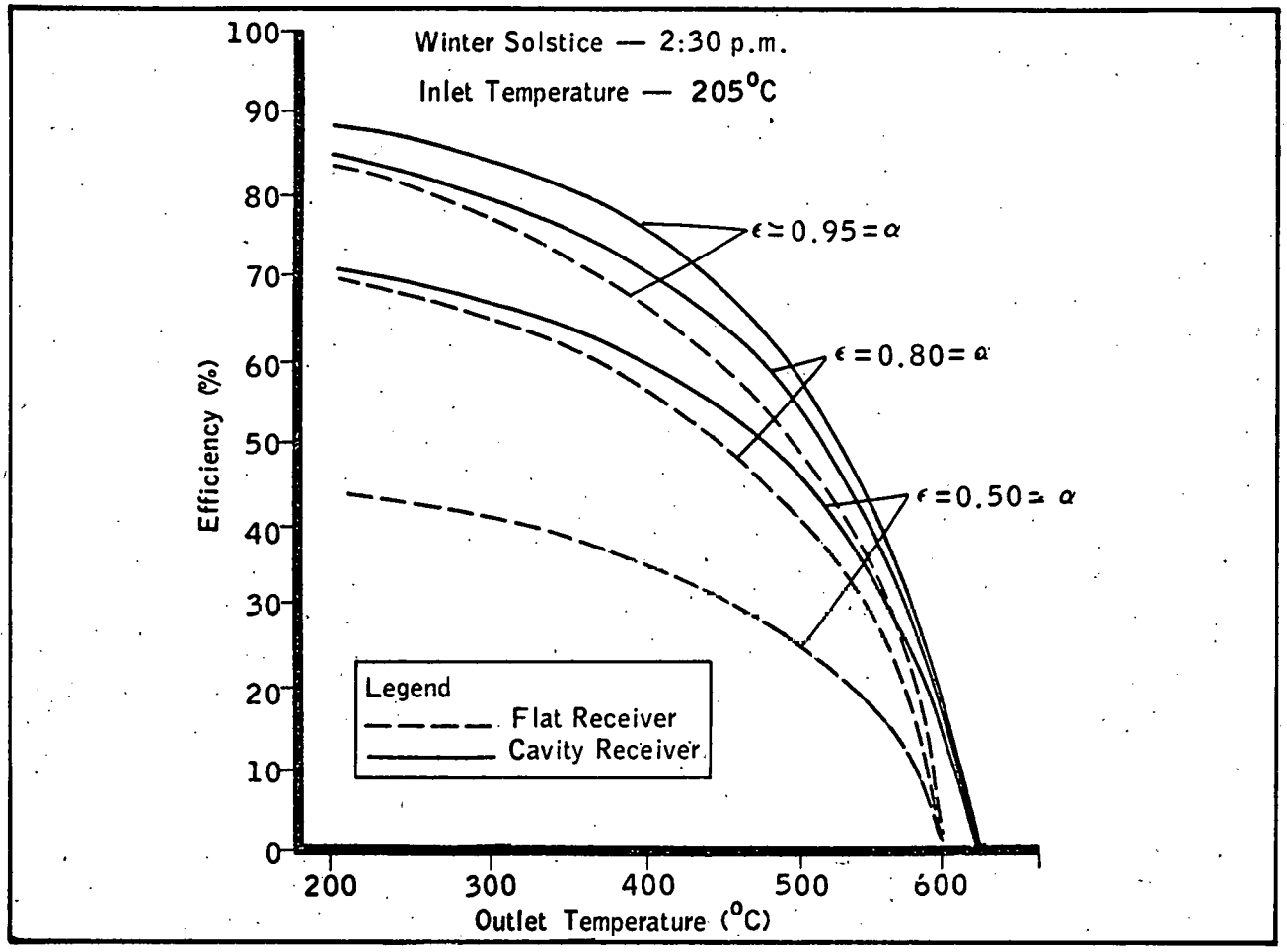

Figure 2-15 RECEIVER EFFICIENCY

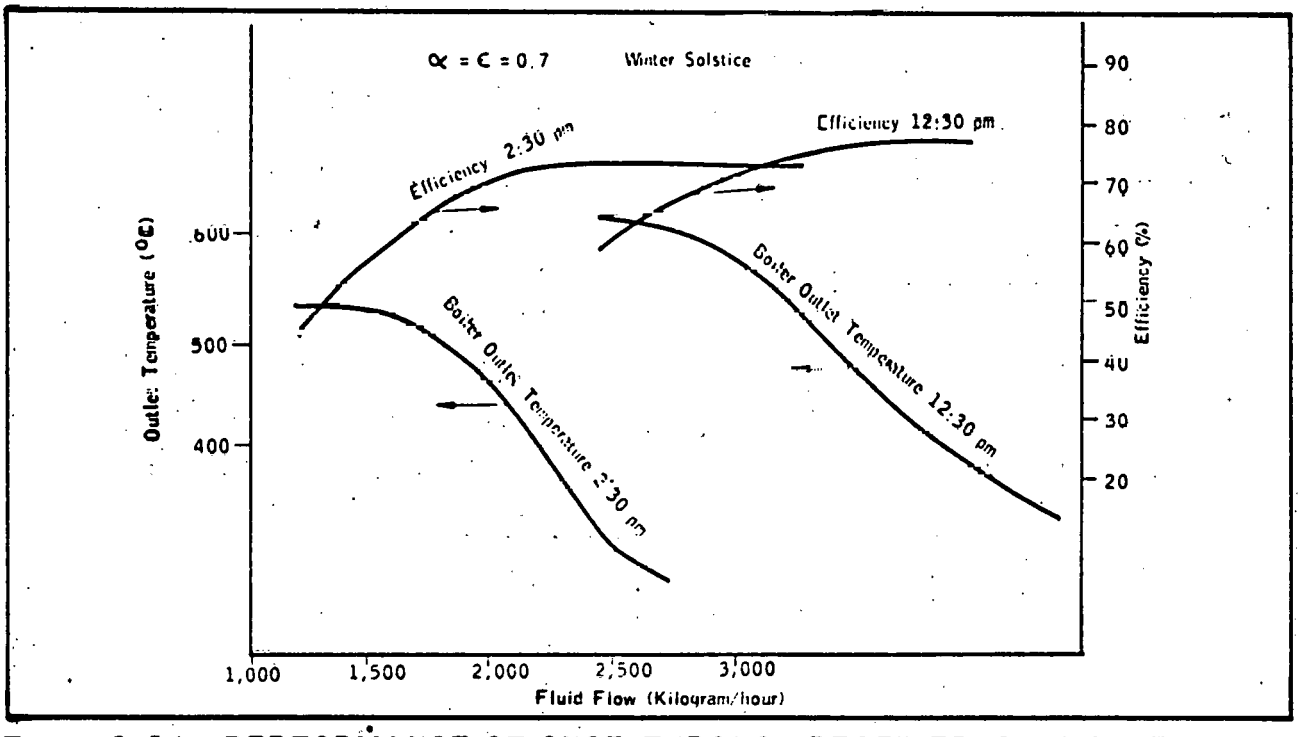

Figure 2-16 PERFORMANCE OF ONCE-THROUGH RECEIVER (CAVITY DESIGN)

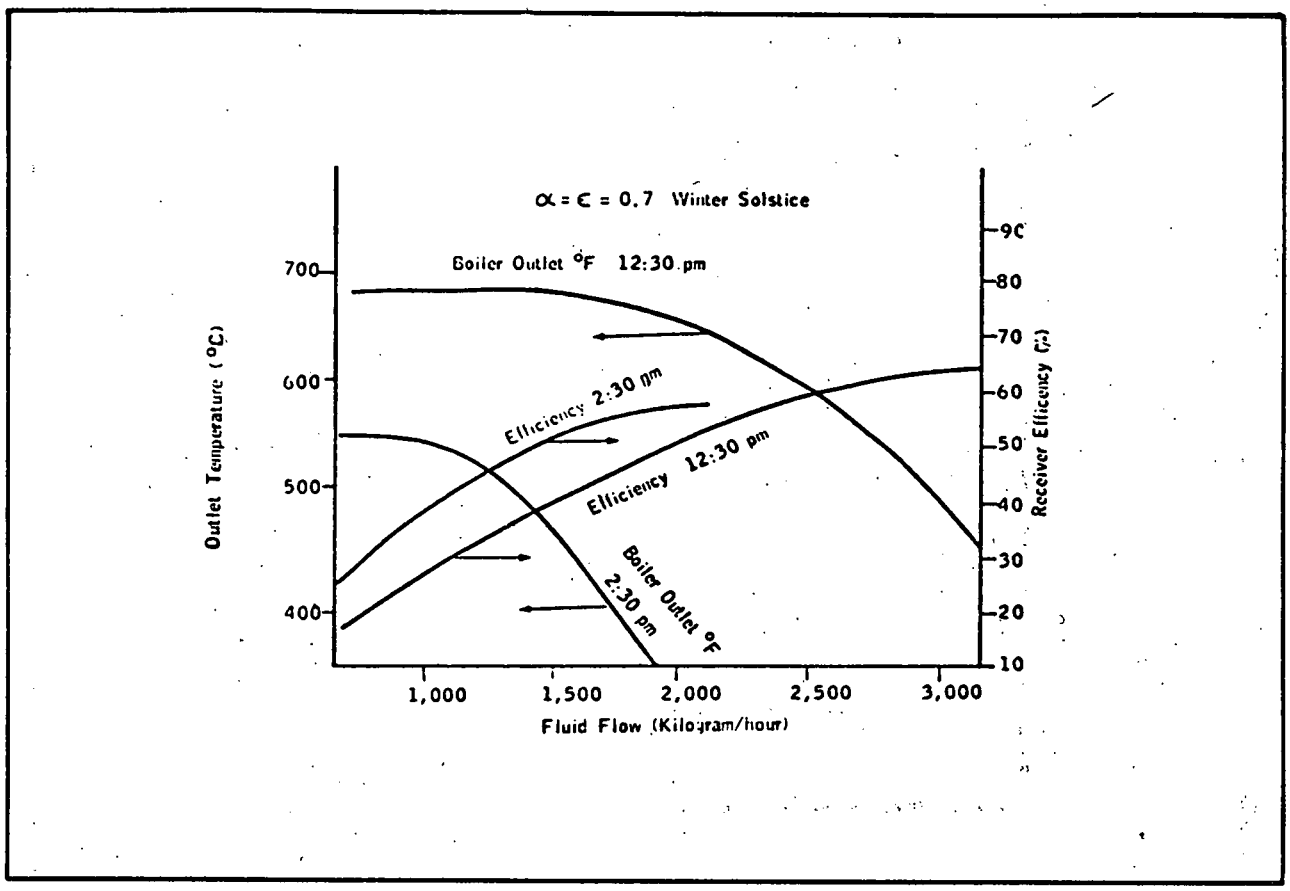

Figure 2-17 PERFORMANCE OF ONCE-THROUGH RECEIVER (FLAT PLATE DESIGN)

Table 2-3 61-METER CAVITY BOILER ONCE-THROUGH DESIGN

$\alpha = \epsilon$	Outlet Pressure MPa (Psi)	Outlet Temperature °C (°F)	Change in Enthalpy kg-cal/kg (btu/lb.)	Thermal Efficiency
0.7	6.9 (1,000)	498 (928)	551 (992)	0.66
0.7	6.9 (1,000)	499 (930)	552 (993)	0.67
0.75	6.9 (1,000)	506 (943)	556 (1,000)	0.67
0.8	6.9 (1,000)	507 (944)	557 (1,001)	0.67
0.7	4.8 (700)	502 (936)	558 (1,004)	0.68
0.7	2.8 (400)	507 (944)	563 (1,013)	0.69

Note: For constant steam flow of 1814 kg/hr (4000 lb/hr).

2.5.3 Effect of Selective Coating on Receiver Tubes

An analysis was made to study the effect on receiver efficiency of the use of boiler tubes with a selective surface. Original calculations were made using $\alpha = 0.9$ and $\epsilon = 0.7$. Sandia Laboratories has reported that Harshaw Chrome gives a stable coating with $\alpha = 0.95$ and $\epsilon = 0.25$ at 300°C. Calculations were made using $\alpha = 0.95$ and $\epsilon = 0.25$ and the results are compared in Figure 2-18. It can be seen that the maximum receiver efficiency is raised from 85 percent to 90 percent by the use of the selective surface, and that this type of receiver can benefit somewhat from the use of selective coatings on the boiler tubes. Unfortunately, Harshaw Black Chrome will not withstand the temperatures anticipated. Consequently, the more conservative values of tube absorption and emissivity were used for receiver performance estimates. However, in view of the potential performance improvements illustrated in Figure 2-18, it may be considered desirable to develop selective coatings for this type of central receiver.

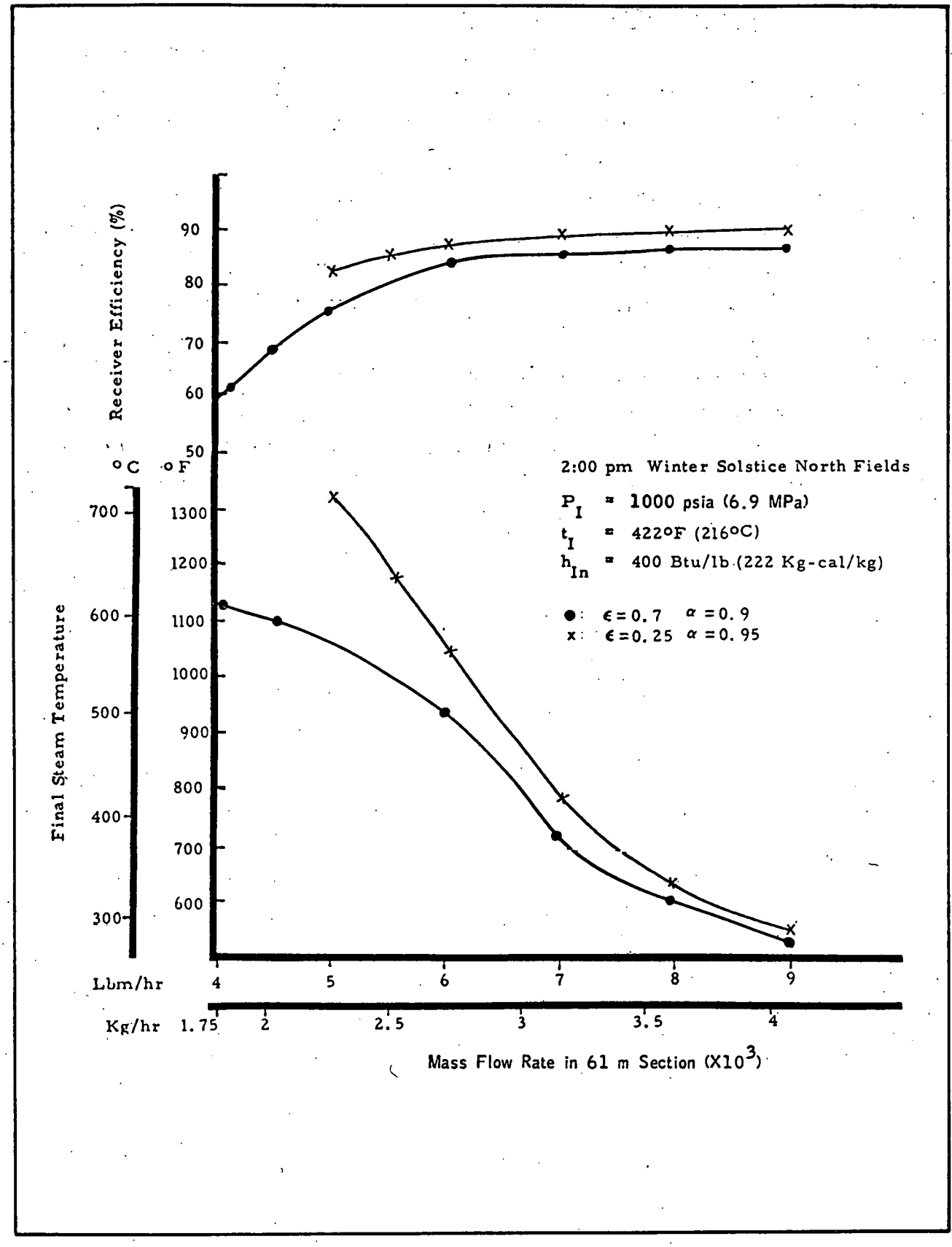

Figure 2-18 EFFECT OF SELECTIVE SURFACE ON RECEIVER PERFORMANCE

THIS PAGE

WAS INTENTIONALLY

LEFT BLANK

3.0 HELIOSTAT

The FMC heliostat is a parabolic cylinder, the reflecting surface of which is composed of an array of flexible, rectangular mirrors which can be focused into the fresnel equivalent of a parabolic surface. The reflecting surface rotates about its long axis. The combination of parabolic deformation and rotation of the reflecting surface enables concentration of the solar image along an elevated linear receiver throughout a solar day. The generation of turbine-rated steam is achieved by overlapping of the concentrated images from a field of heliostats.

The heliostat described in the following paragraphs is the first iteration in a design evolution to generate a low-cost, mass-producible line focus heliostat. The general characteristics of the design were dictated by the following goals:

- Permit factory-finishing of complete sections with automated fabrication and assembly techniques
- Maximize the area of reflecting surface controlled by one drive/control unit
- Permit complete sections to be shipped on existing common carrier equipment ready for field emplacement with existing construction equipment and techniques.

The heliostat section that was designed and built during the project reflects these goals, insofar as experimental hardware can. Further evaluation of the design toward a mass-producible state was not within project scope.

3.1 DESCRIPTION

Each heliostat consists of two mirror sections with a common elevation aim drive unit and local controller. Each mirror section is 18.3-meters (60 feet) long by 3.05-meters (10 feet) wide and contains a focus drive unit. Conceptually, each heliostat contains 110 meters^2 (1,181 feet^2) of reflecting area. Figure 3-1 shows one-half of a heliostat module.

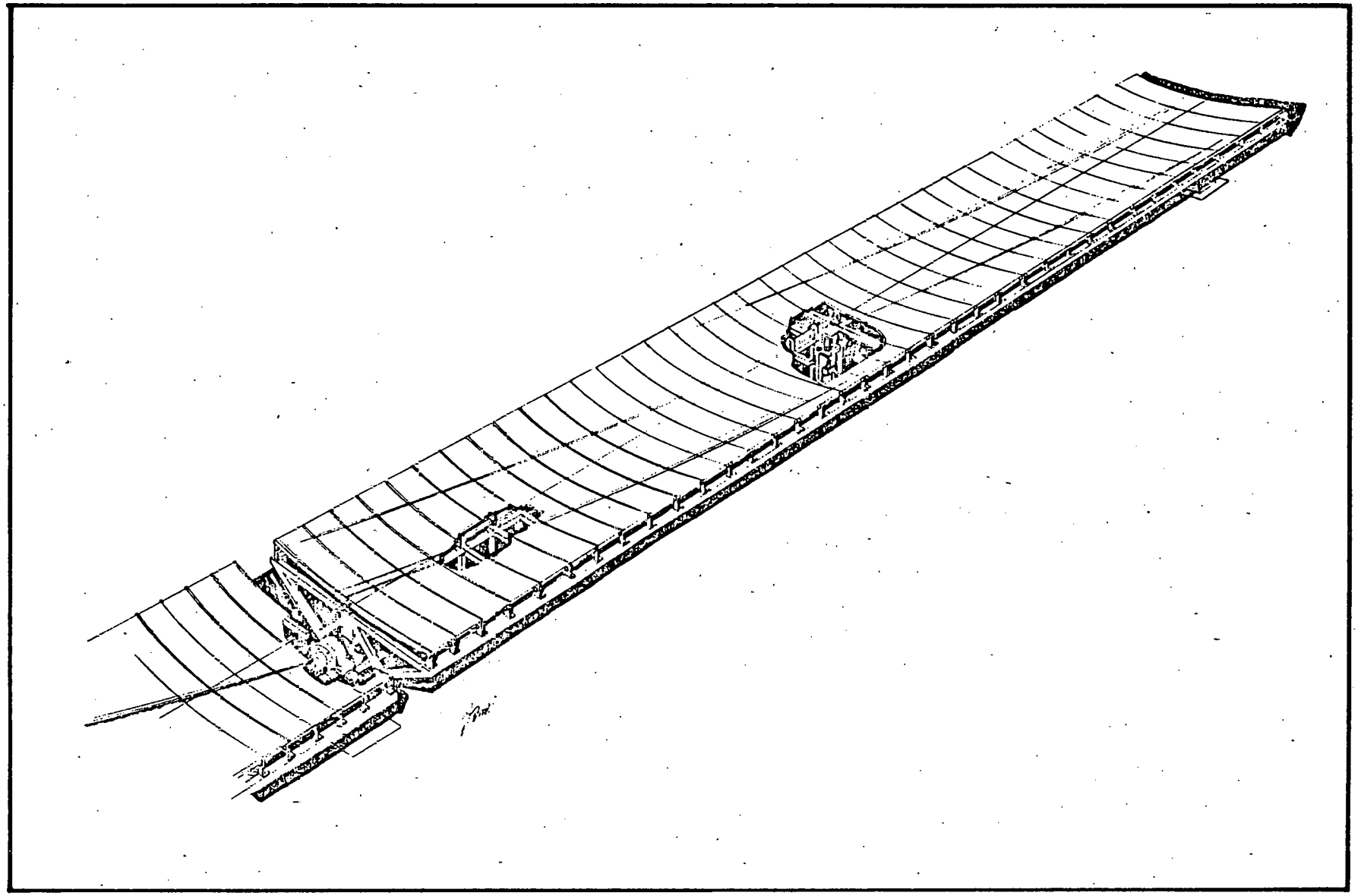

Figure 3-1 ONE-HALF HELIOSTAT MODULE

The reflecting surface is composed of mirror panels which slip into the support frame. The mirrors are supported along the long edges by flexible beams supported at the ends. The heliostat section fabricated during the project contained 70 panels. Each panel consisted of a second-surface, float glass mirror, 2.29 millimeters (0.090 inch) thick, fabricated by standard commercial techniques. The reflecting surface is a silver/copper flash protected by black organic paint and a 3.30-millimeters (0.13 inch) thick polystyrene foam backing, and enclosed by metal frames.

One mirror panel was sent to Sandia/Albuquerque to test reflectance and dispersion. The tests (Appendix F) yielded a specular reflectance of 0.85 and a surface dispersion of 1.2 mm in the long dimension.

The experimental heliostat section was slightly shorter (17.92 meters) than the conceptual design because the mirror manufacturer* was tooled to produce high quality float glass mirrors to a maximum width of 50.8 centimeters (20 inches). The design of the experimental section was modified to accommodate this width to avoid the cost of retooling. The completed section contained 51.1 meters^2 (550 feet^2) of exposed mirror area; roughly 93 percent of the conceptual design area of one mirror section.

Each mirror section is constructed of welded formed-steel sections. Formed-steel sections are lighter and less expensive than rolled sections. The bearings are mounted at the center of gravity so there will be no appreciable torsional deflections under no-wind conditions. Figure 3-2 illustrates the structure of a single section.

The section is supported at each end. On one end is a pillow-block sealed ball bearing. The other end is supported by the zero backlash worm gear-box output shaft. Figure 3-3 depicts the focus wedges and the focus rack-and-pinion drive system. The control logic used for elevation and focus control is discussed in Section 5.0.

---

* Mechanical Mirror Works, Inc., 661 Edgecombe Avenue, New York 10032.

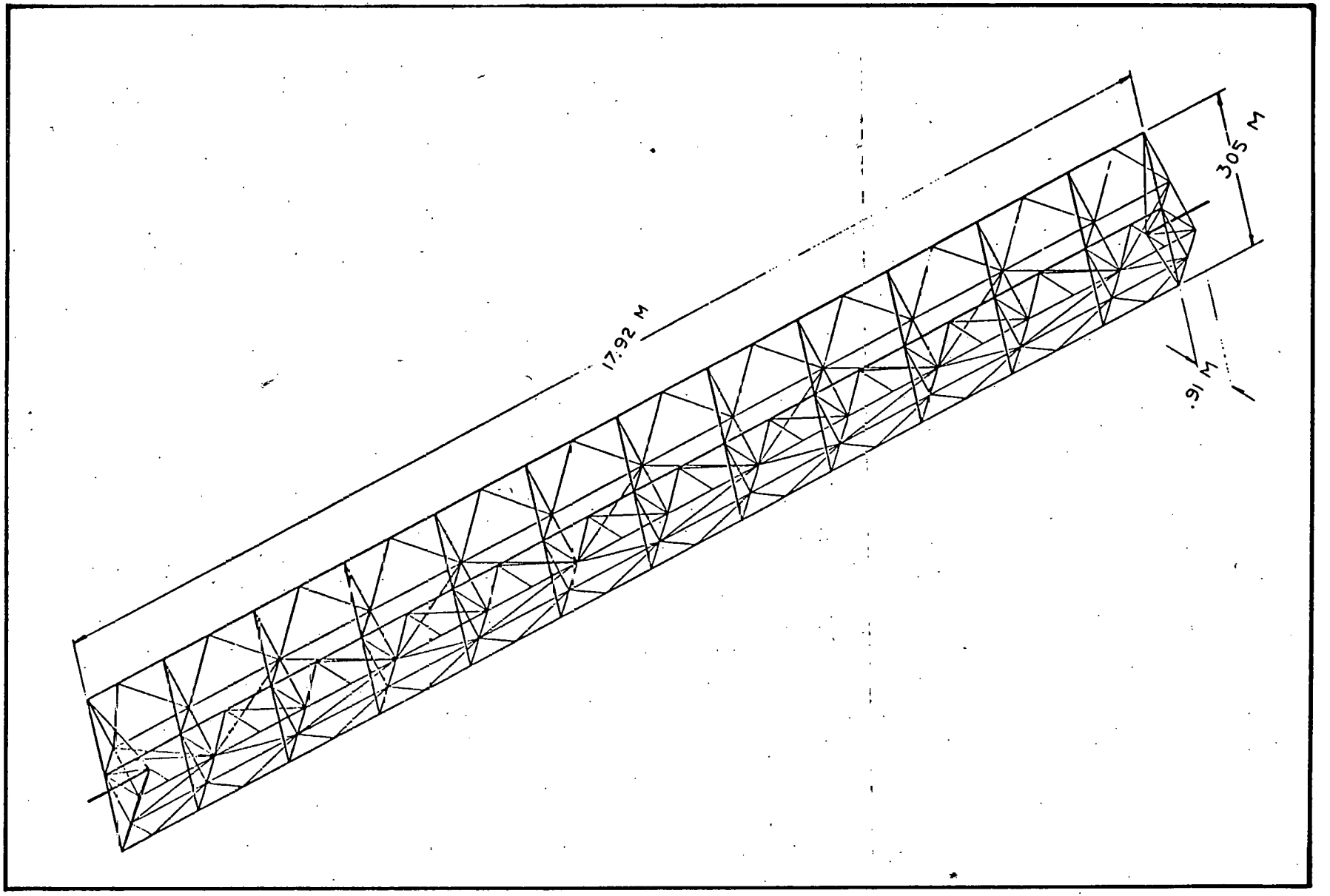

Figure 3-2 HELIOSTAT MIRROR SUPPORT STRUCTURE

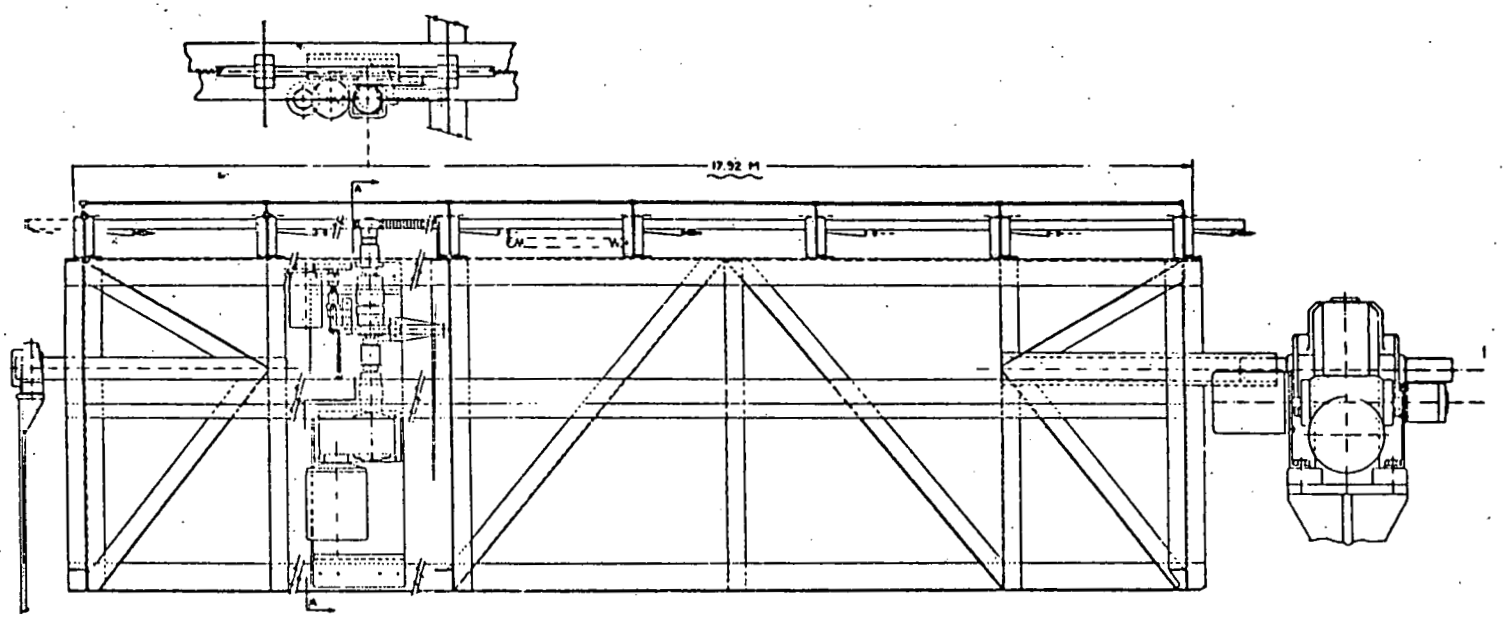

Figure 3-3 FOCUS WEDGES AND DRIVE SYSTEM

The operation of the focusing system (Figures 3-4 and 3-5) is described below. The mirrors are deflected by oilite shoes attached to the mirror deflection beams. The shoes ride on sloped cams. As the cams are forced past the shoes, the beams are deflected downward at the center. All the cams are actuated in unison by a rectangular cam shaft which is driven by a rack and pinion. The cam shaft return spring places the cam shaft in tension to return the mirrors to the defocus condition and to eliminate drive system backlash.

Defocusing operation is achieved by use of the defocusing clutch which couples the pinion shaft to the focus drive stepper motor and gearbox. When engaged, the clutch allows the focus drive stepper motor to move the cam shaft and hence have direct control of the mirror deflection. The defocus clutch is engaged by the defocus torque motor operating through its gear train and ballscrew/nut drive. This pulls the defocus clutch lever, moving the defocus clutch lower jaw, and engages the clutch. The defocus spring will pull the lever down, separating the jaws when disengaged. Applying power to the torque motor will wind up the ballscrew/nut against the defocus spring, thereby engaging the clutch. The torque motor can operate in continuous stall and will maintain the engagement of the clutch. When the power is removed, the defocus spring will pull the ballnut down on the ballscrew, lowering the clutch lever, and cause the torque motor drive to unwind. The clutch jaws separate, and the cam shaft return spring will return the mirrors to the defocus condition. A fail-to-safe condition is thereby obtained, where loss of control signal or power will automatically defocus the heliostat.

The MIT ICES computerized structural analysis was used to configure the frame shown in Figure 3-2. The analysis was based on a load equal to the weight of structure, mirrors and mirror supports for one heliostat section. In addition, a wind load of 24.4 kg/m^2 (5 lb/ft^2)* perpendicular to the mirror surface was included. Following is a summary of the results of the analysis:

- Total weight of the heliostat section: 2,209 kilograms (4,860 pounds).

---

* 99.9-percentile wind velocity with a gust factor of 1.4 (18.7 meters per second, 36.6 knots) (1).

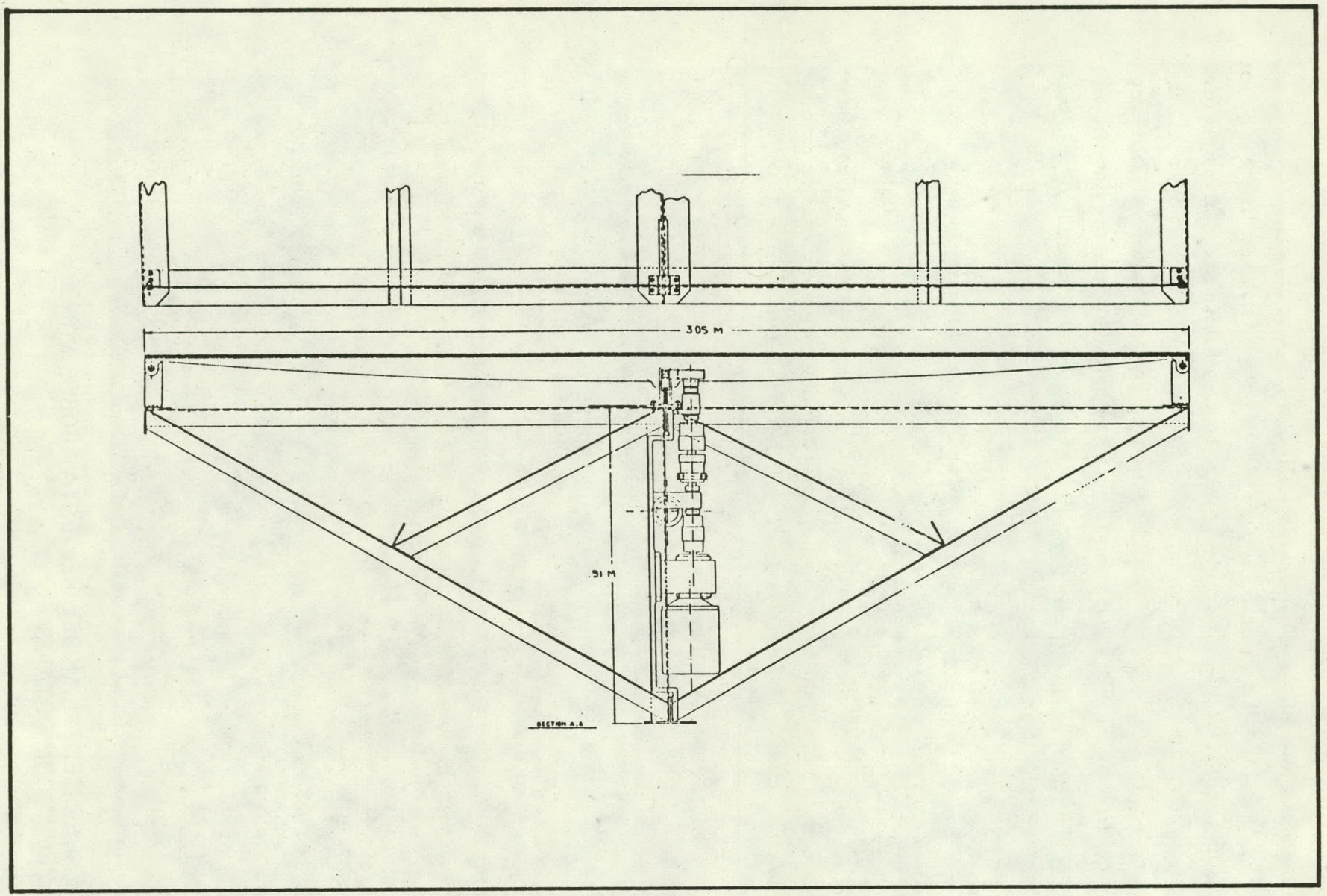

Figure 3-4 FOCUS DRIVE MECHANISM LAYOUT

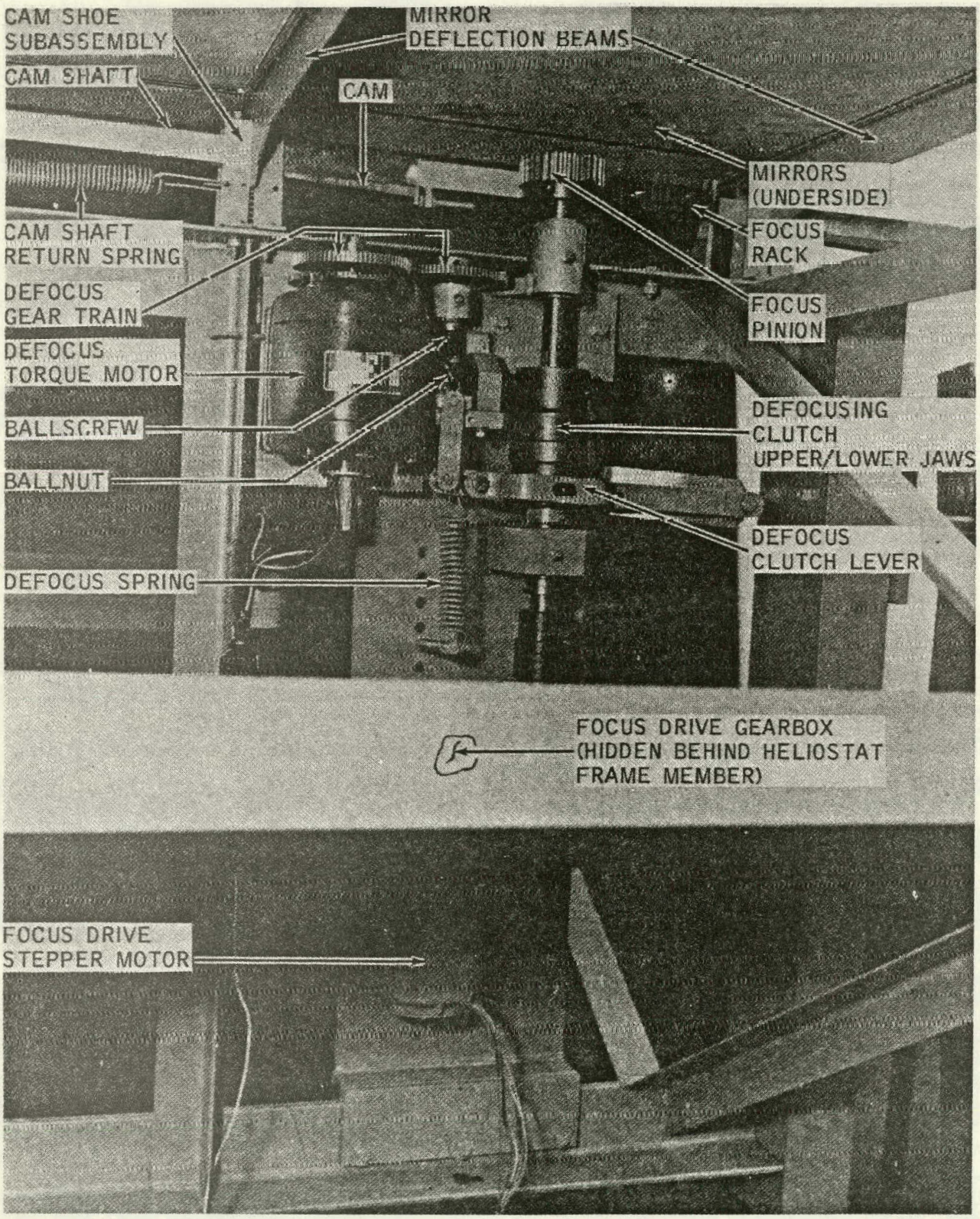

Figure 3-5 EXPERIMENTAL MODEL HELIOSTAT FOCUSING MECHANISM DETAILS

Heliostat Horizontal

- Deflection at center of the span due to weight only: 1.04 centimeters (0.41 inch).
- Deflection at center of the span due to weight and wind load: 1.73 centimeters (0.68 inch).
- Maximum stress, stub shaft support: 1,251 kg/cm^2 (17.8 kips/in^2).
- Maximum stress at center of the span: 562 kg/cm^2 (8.0 kips/in^2).

Heliostat Vertical

- Rotational deflection due to uniform distributed torque: 114 m-kg (825 ft-lbf) along the full length of the heliostat: 0.002 radian (0.113 degree).
- Deflection at center of the span due to weight only: 0.41 centimeter (0.16 inch).
- Deflection at center of the span due to weight and wind load: 0.84 centimeter (0.33 inch).
- Maximum stress at stub shaft support: 893 kg/cm^2 (12.7 kips/in^2).
- Maximum stress at center of the span: 485 kg/cm^2 (6.9 kips/in^2).

3.2 DEVELOPMENT WORK

Verification testing of the heliostat focusing mechanism was accomplished with a jury rig which simulated a 1-meter length of one heliostat section.

The same focusing mechanism was used for the jury rig and the field experiment model. The tests demonstrated that the focusing mechanism performed as predicted. Section 3.3 contains a description of the jury rig tests.

Fabrication of one heliostat section (17.92 meters by 3.05 meters) was completed. Figures 3-6 through 3-10 show the completed heliostat. This section, with the same focus drive mechanism used in the jury rig was mounted on a trailer for use in the field experiment. The following tests were planned:

- Measure reflected image intensity at ranges of 70, 110, and 150 meters.
- Test control logic for aiming and focusing.
- Verify emergency defocus and stowing logic.
- Evaluate heliostat and control system response to wind loading.

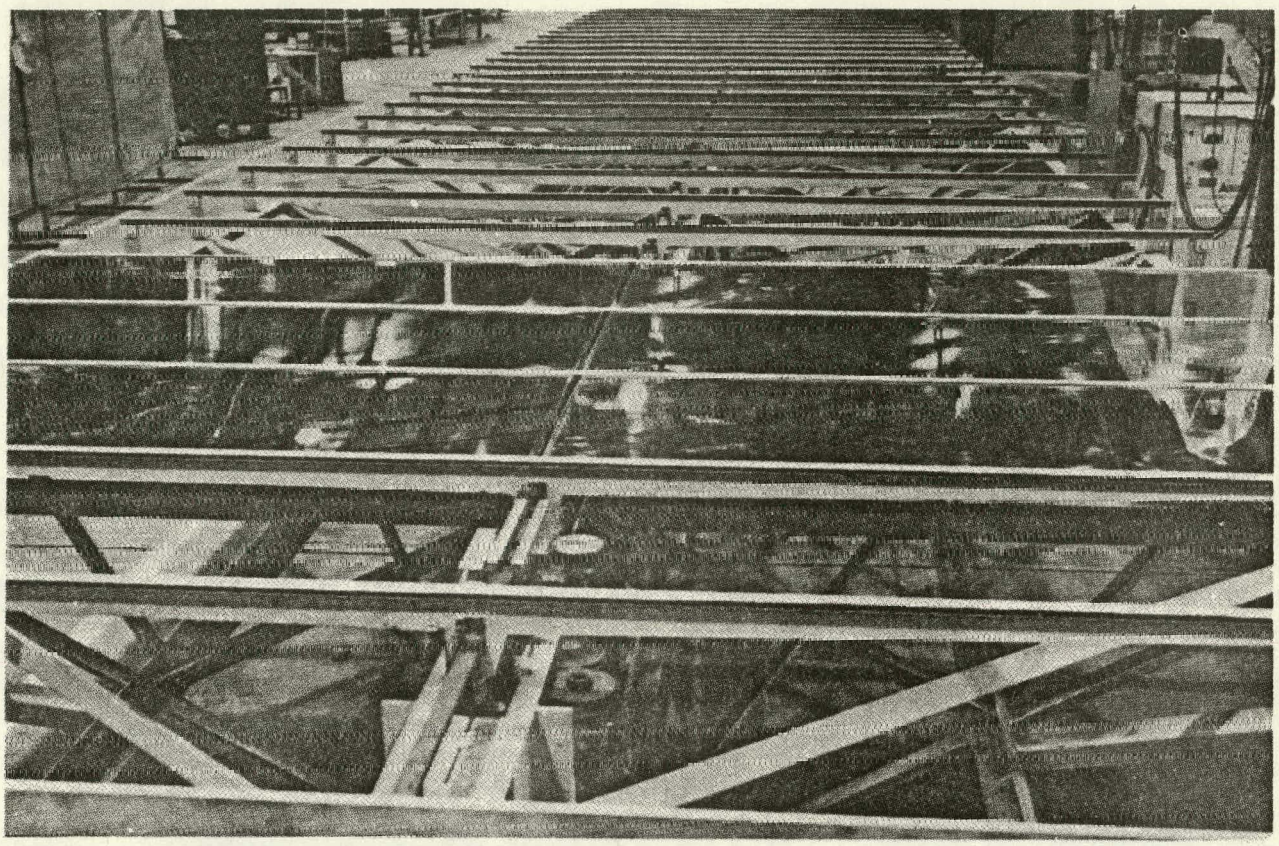

Figure 3-6 COMPLETED HELIOSTAT SECTION

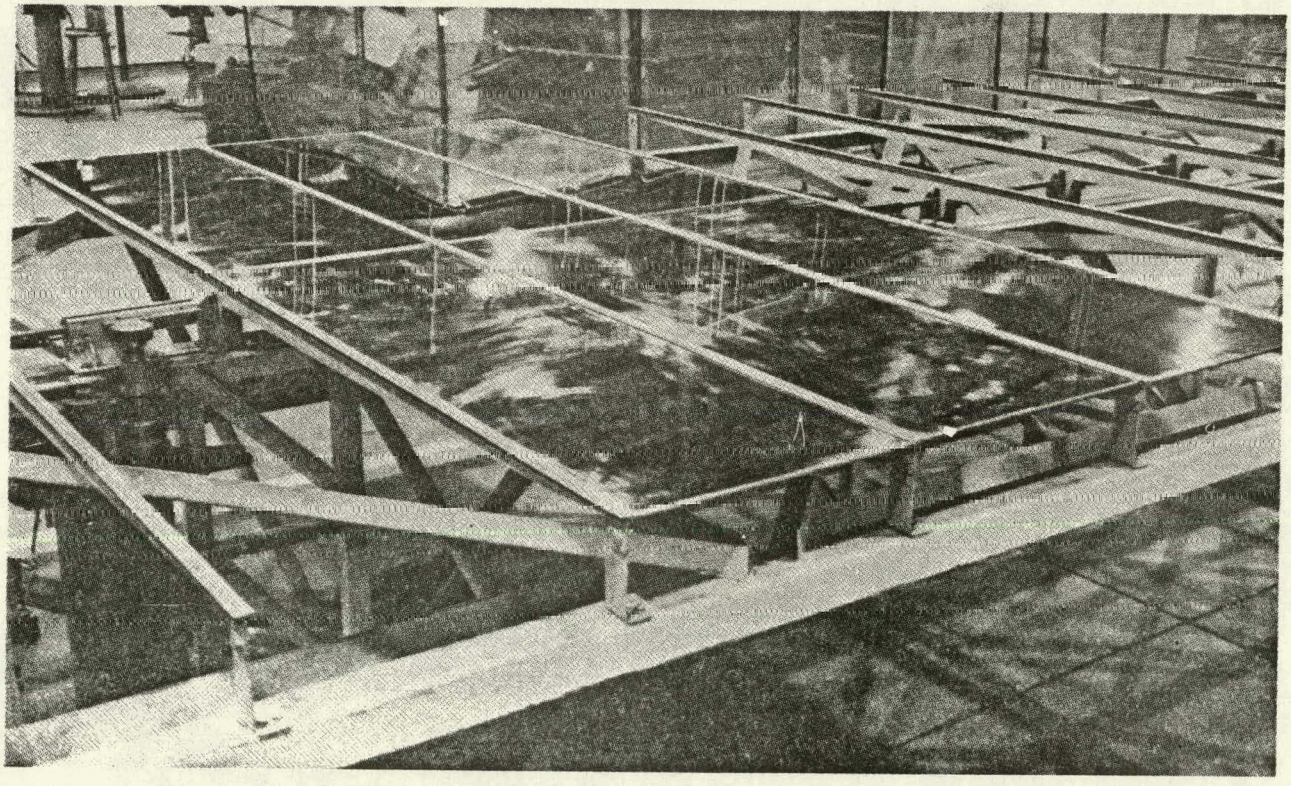

Figure 3-7 HELIOSTAT MIRRORED SECTION

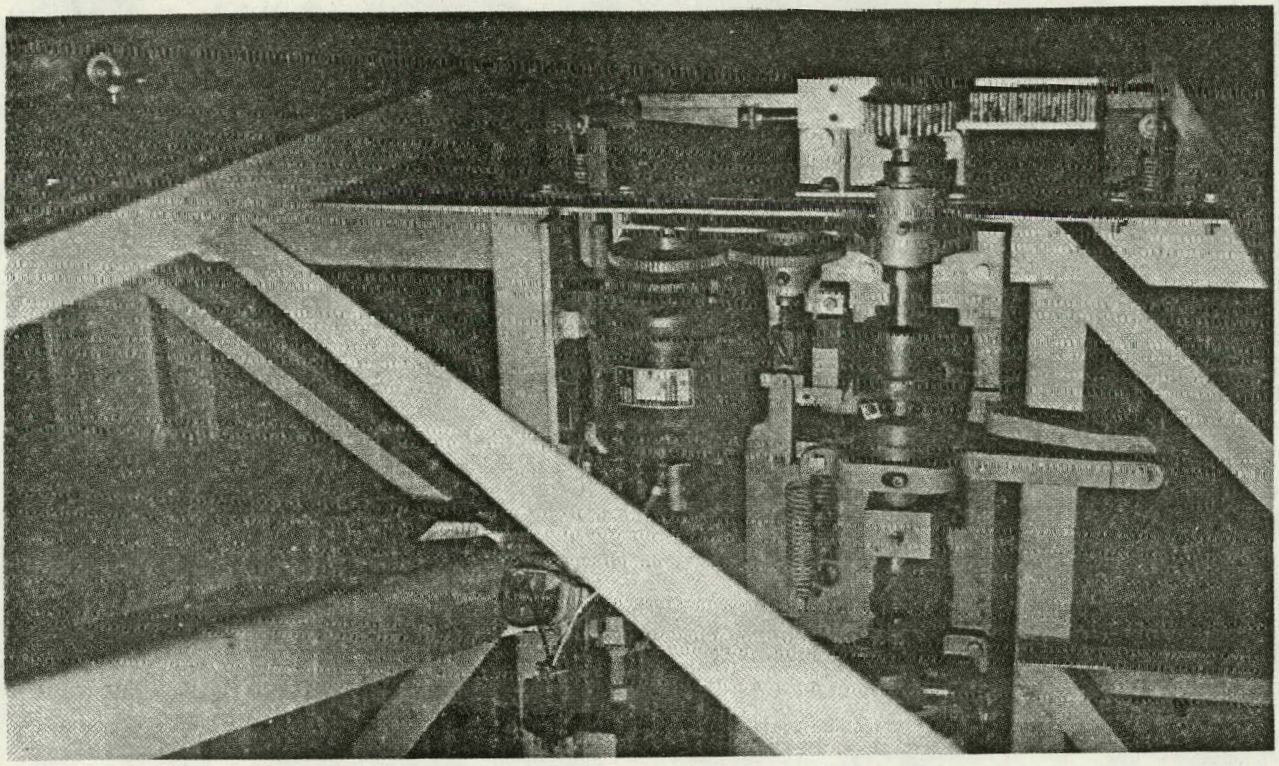

Figure 3-8 HELIOSTAT FOCUS DRIVE MECHANISM

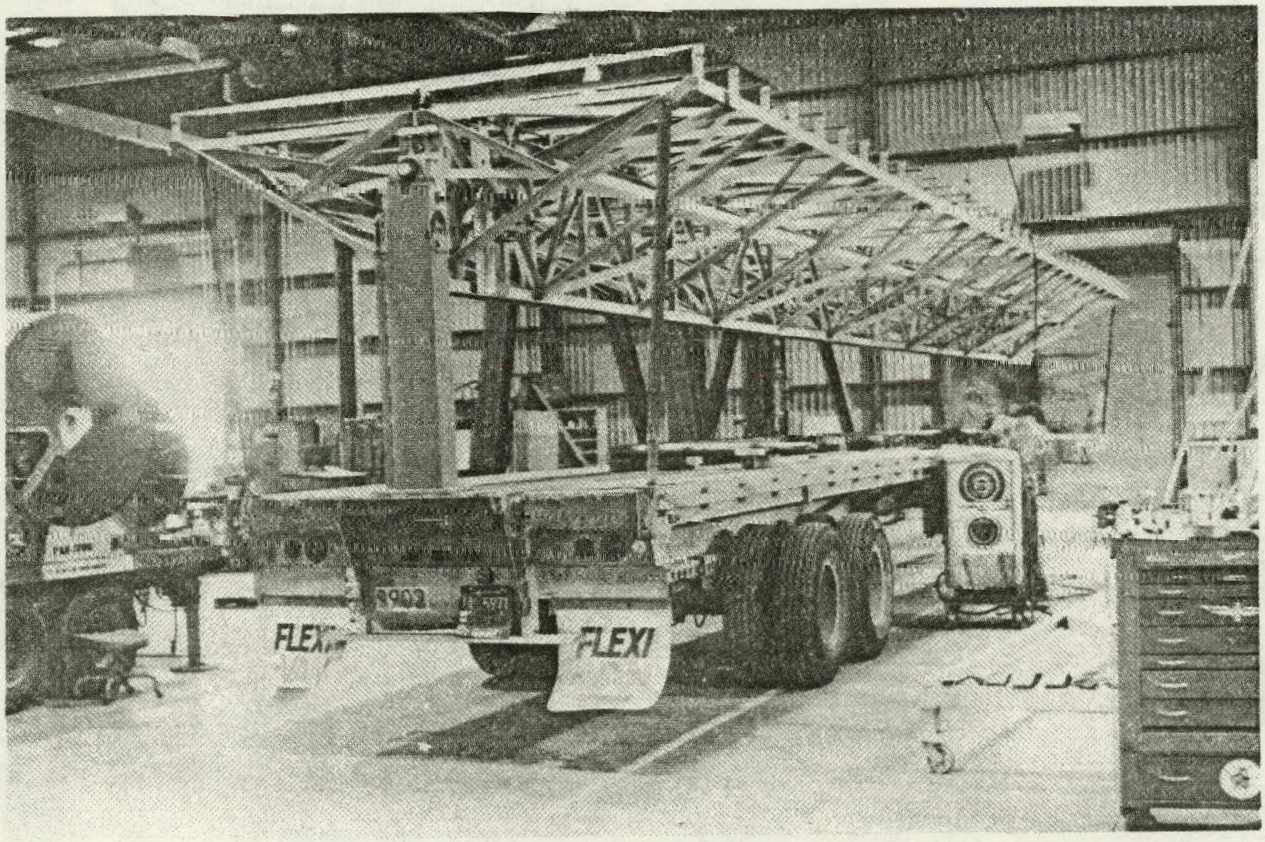

Figure 3-9 COMPLETED HELIOSTAT SECTION READY FOR TRANSPORT

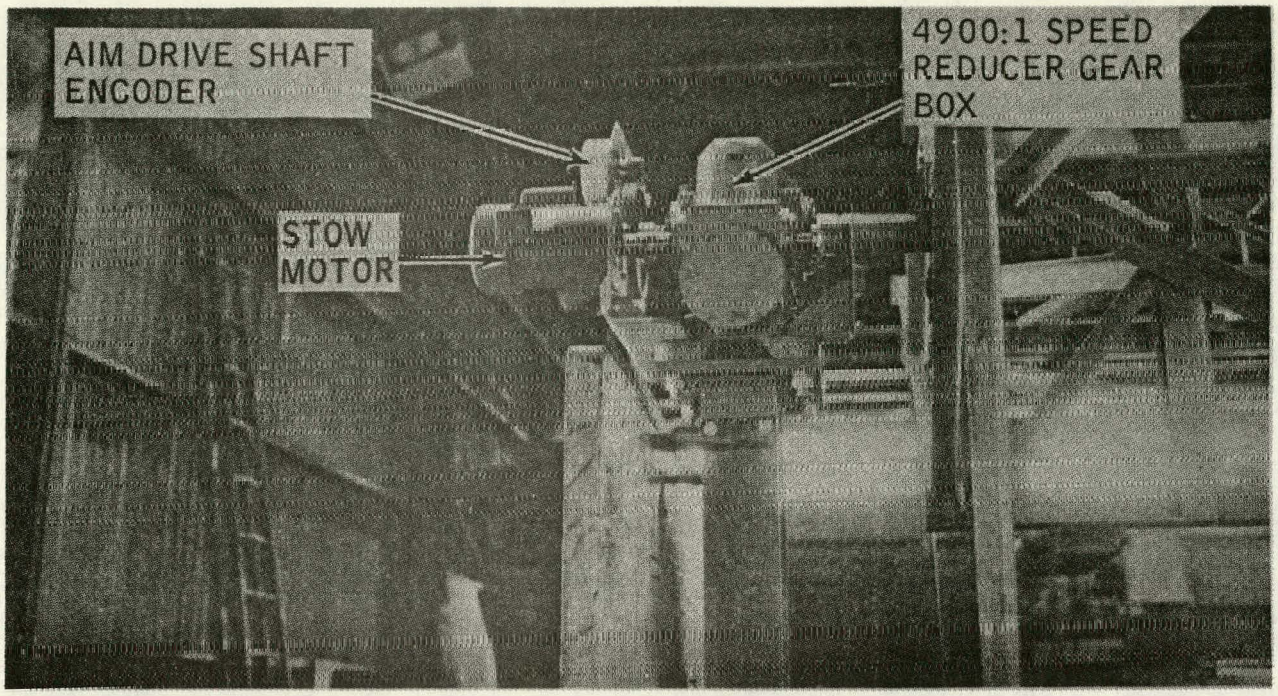

Figure 3-10 DETAIL OF ELEVATION AIM DRIVE MECHANISM

3.3 RESULTS OF TESTS PERFORMED ON FMC LINE FOCUS HELIOSTAT

This section contains the results of tests performed by FMC during the Central Receiver Research Study project.

3.3.1 Heliostat Jury Rig Model

The model of the heliostat (see Figure 3-11) employed the heliostat's basic triangular structure and width to accommodate four mirror panels. This setup allowed for an experimental determination of function and frictional forces in the mirror focusing mechanism and a preliminary observation of mirror imaging.

The model heliostat was mounted on a support frame to allow for elevation aiming. It also had a complete focus drive assembly and mirror focusing mechanism (see Figure 3-12). Figure 3-13 shows the control schematic used for focus control. The telephone dial simulated pulse commands from a central computer for operation of the focus drive stepper motor.

The defocusing mechanism was tested. The clutch as supplied from manufacturer's stock had rough cast iron jaws with square, castellated faces.

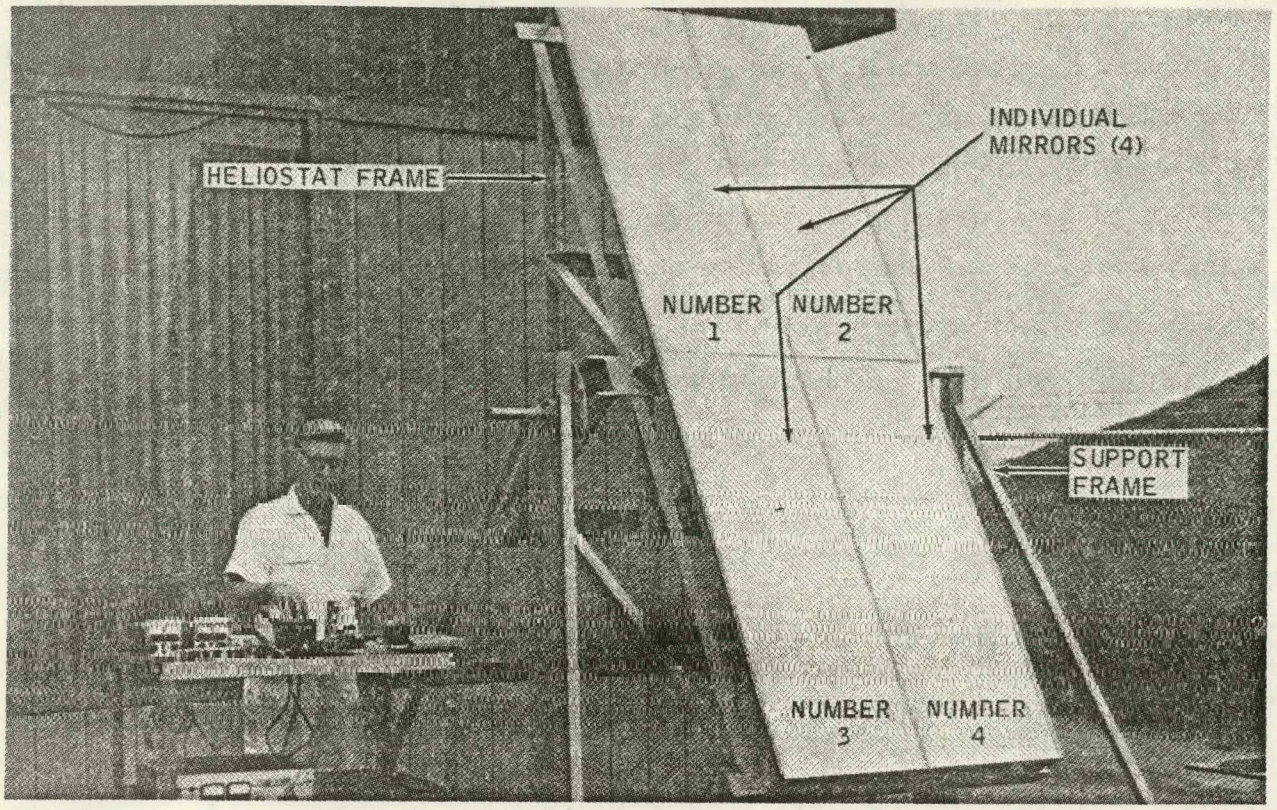

Figure 3-11 EXPERIMENTAL MODEL HELIOSTAT

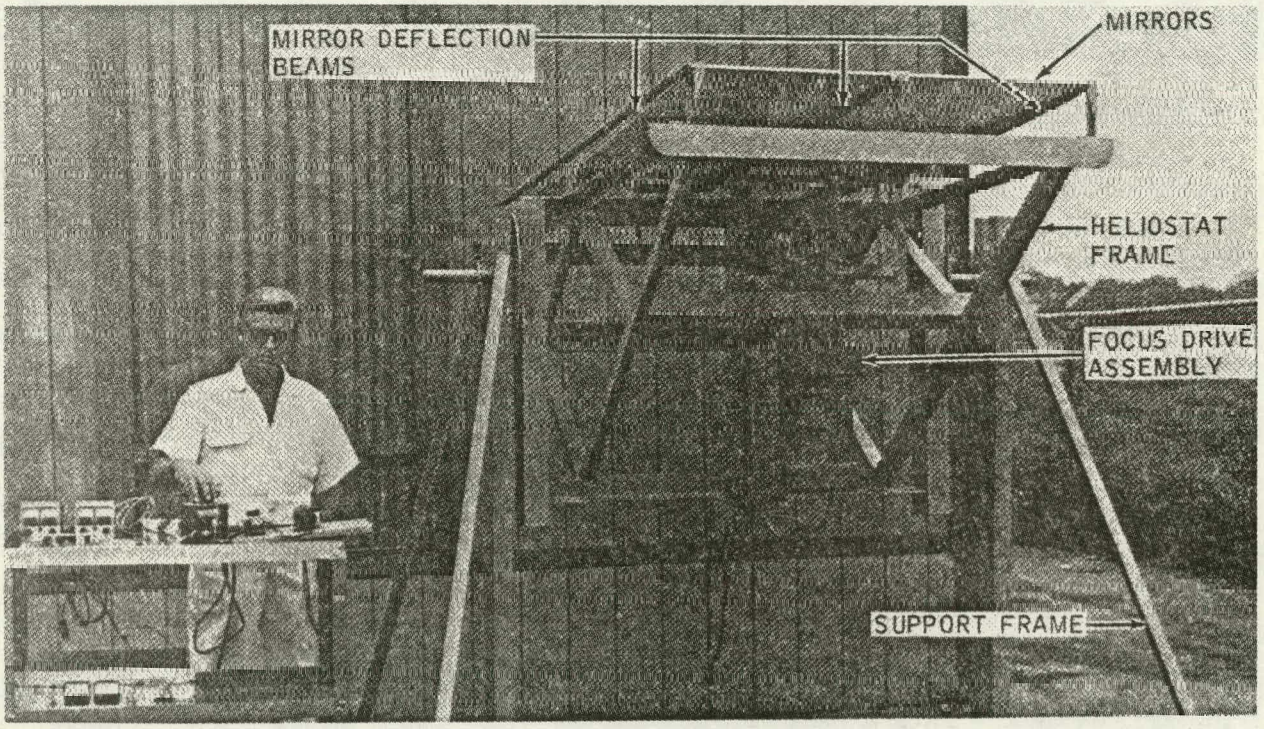

Figure 3-12 EXPERIMENTAL MODEL HELIOSTAT SHOWING FOCUSING MECHANISM

With any pressure applied to the faces the defocus spring was not sufficient to overcome the face friction and separate the clutch. A stronger defocus spring could not be used, as that would be beyond the torque limits of the torque motor. Therefore, a combination of face angles and facing materials was tried. The present configuration of a 45-degree face angle with nylon/polished cast iron faces appeared to separate under all operational condition of focus mechanism forces.

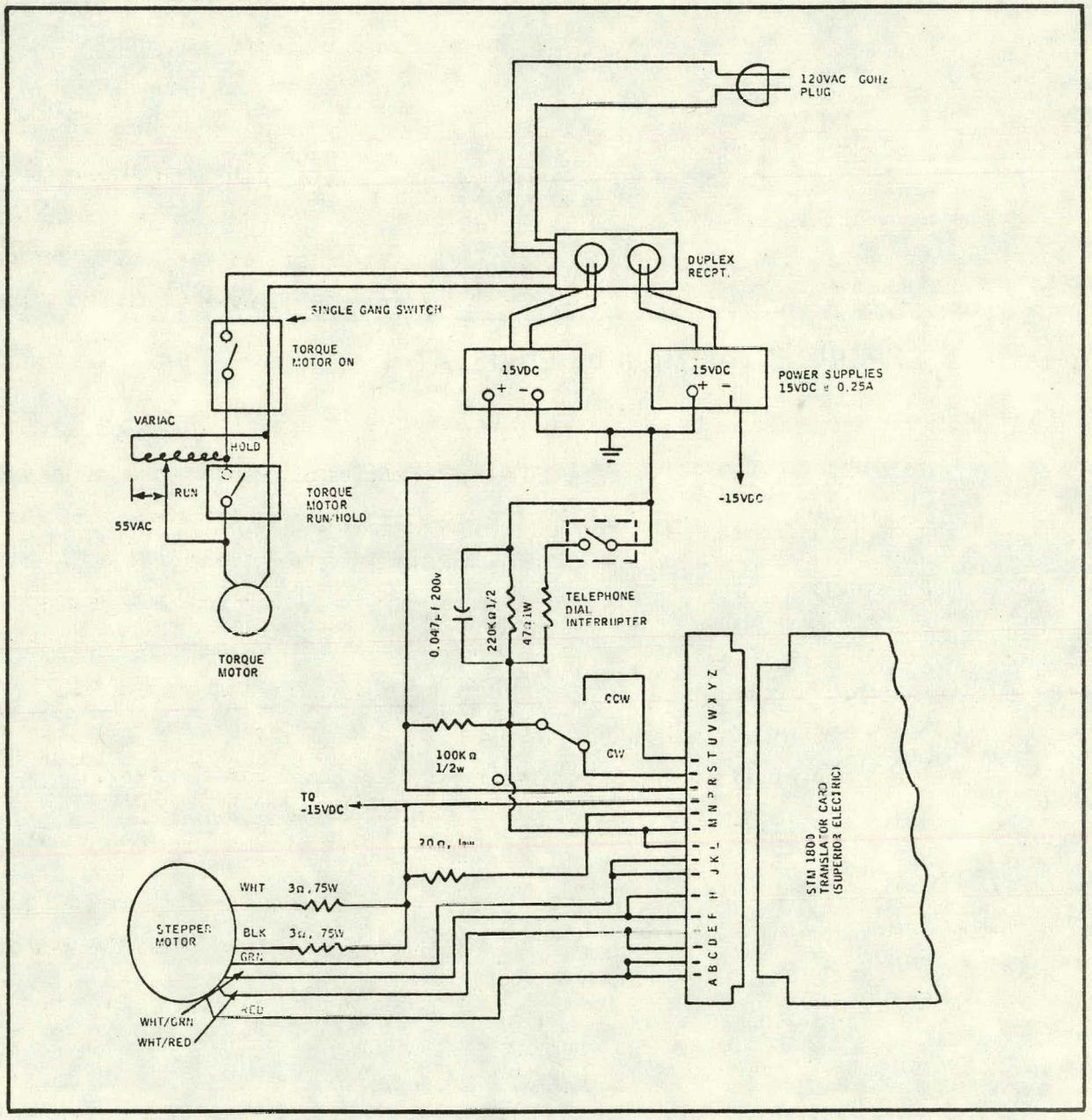

Figure 3-13 FOCUS JURY RIG TEST CONTROL

When the defocus clutch separated under the load, the return spring returned the cam shaft with a large impulse force. In an effort to absorb this shock, an air cylinder was mounted on the cam shaft. A needle valve regulates the admission and discharge of air into the cylinder. The returning cam shaft compresses the entrapped air in the cylinder which is then slowly released. The return shock is thereby absorbed and yet the mirrors are allowed to assume a slightly convex, defocused configuration.

Set outside the ESD facilities, the model was then used for mirror image tests (see Figure 3-14). The image of the sun was reflected onto the building wall. A target was placed in the vicinity of the image to provide height reference. Because of the facilities available at the time, the model heliostat optical axis was not normal to the reflecting wall. This condition produced the horizontal distortion of the image, but the vertical dimensions of the image were largely undistorted. The optical path length to the image was 200 feet -- the minimum heliostat-to-receiver distance encountered in the actual system.

Focusing tests were conducted on March 29, 1977, at about 1500 PST. Photographs were made of the image (see Figures 3-15 and 3-16) as the mirrors were being focused. The photographs enclosed in the report show the mirrors in the defocused and focused condition. The target gradations are at 1-foot intervals. It will be noted from Figure 3-15 that each mirror image appears to have two "hot" spots. These "hot" spots are caused by local mirror concavities which occurred during the mirror manufacturing process. In Figure 3-16 there appears to be an image splay on the upper "hot" spot of mirror number 1. This mirror was cracked but was still used for the test. The cracked portion was placed in the upper end of position number 1.

The tests with the experimental model have been valuable in determining final heliostat configuration. These tests have also demonstrated that the mirrors can be successfully focused and automatically defocused.

3.3.2 Field Experiment Model

The heliostat field experiment (Appendix C) was not accomplished, due to a reduction in the scope of work requested by DOE. All assembly work

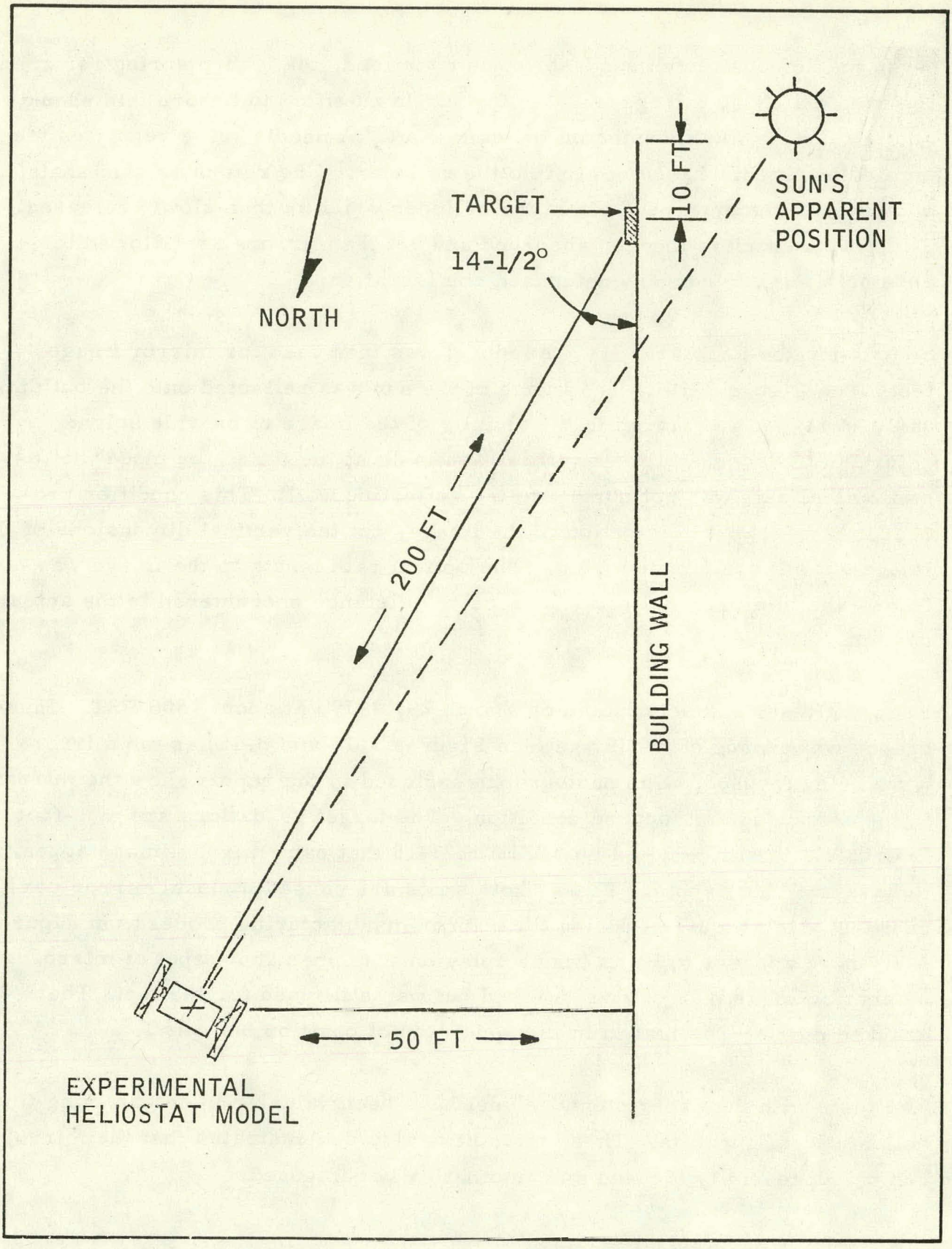

Figure 3-14 LAYOUT OF EXPERIMENTAL MODEL HELIOSTAT IMAGE TEST

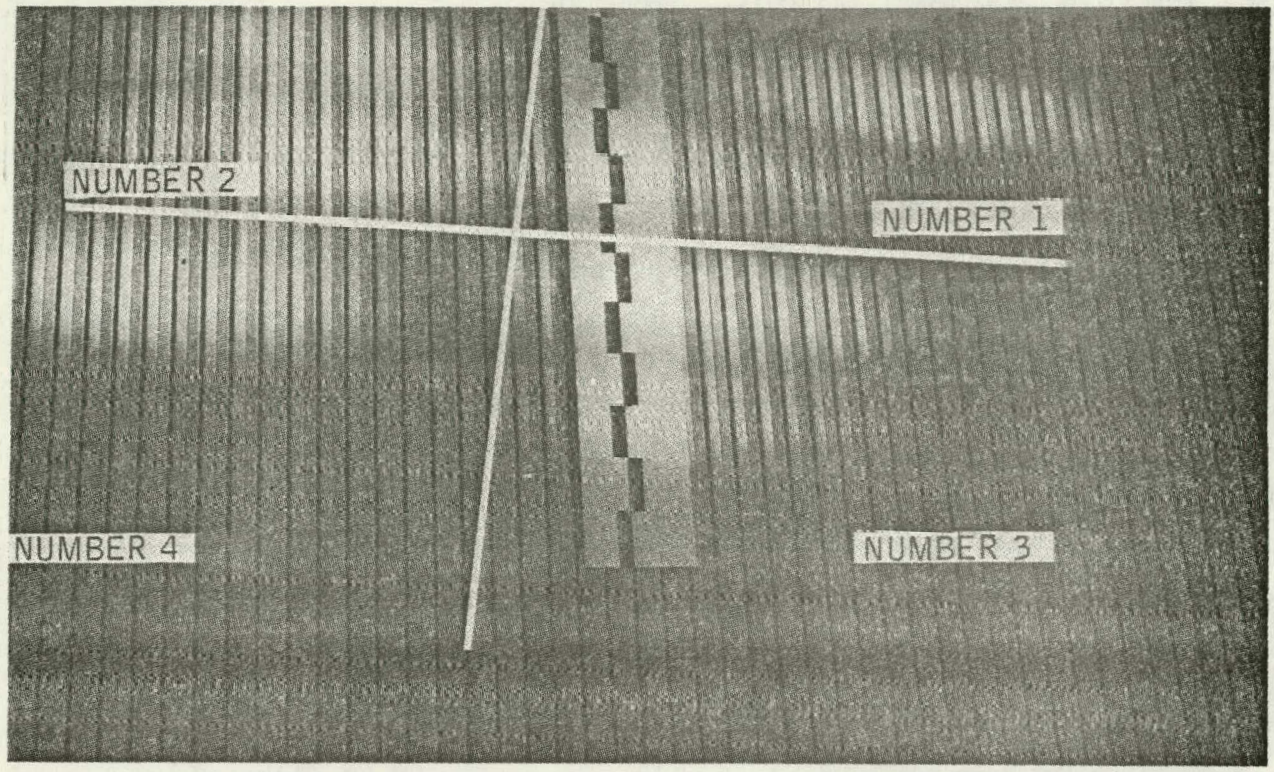

Figure 3-15 EXPERIMENTAL MODEL HELIOSTAT MIRROR IMAGE (DEFOCUSED)

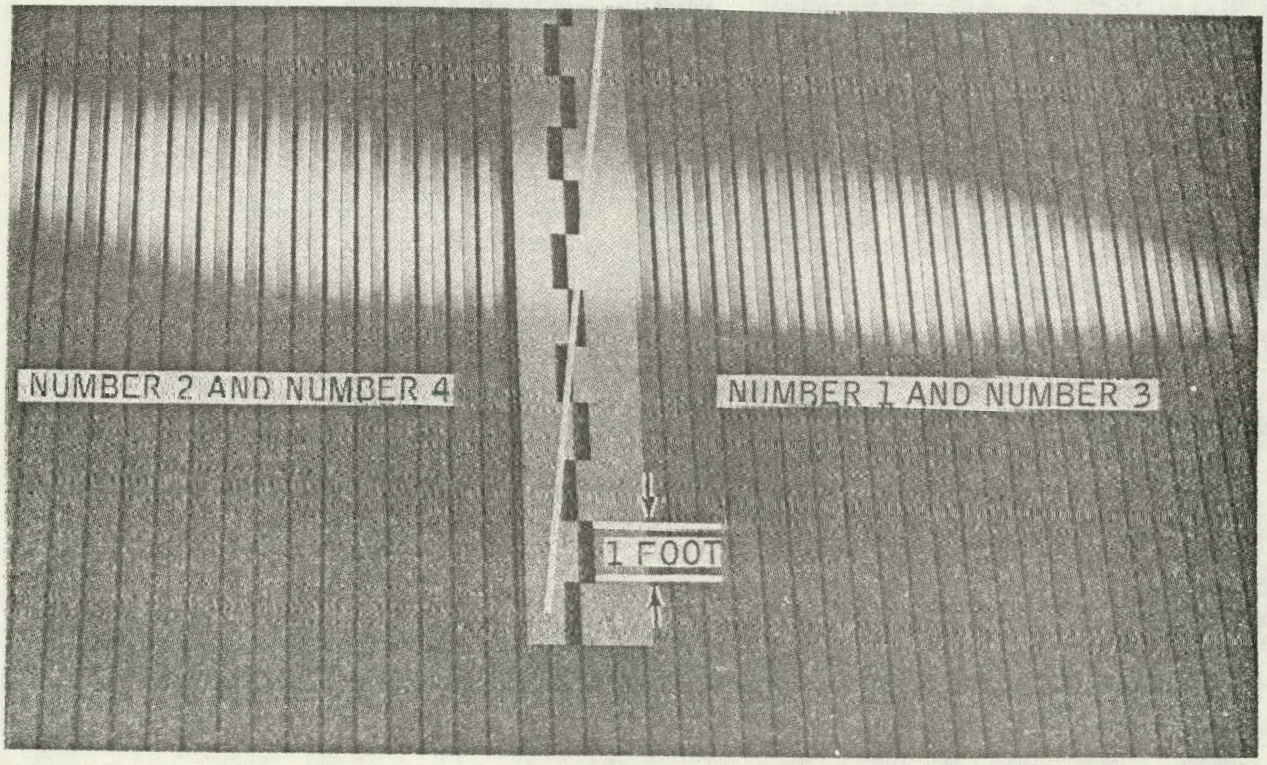

Figure 3-16 EXPERIMENTAL MODEL HELIOSTAT MIRROR IMAGE (FOCUSED)

on the field experiment model (Figures 3-7 through 3-10) was complete with the exception of wiring and programming of the local controller (Section 5.2). However, functional tests were performed with the completed field experiment model in the ESD shop to checkout and debug the heliostat prior to transport to the test site. The following functional tests were performed:

3.3.2.1 Focus Drive Mechanism

All mirror panels were installed in the heliostat (Figure 3-17). The focus drive control (Figure 3-13) was connected to the focus drive and the mirror surface was focused. Initial tests revealed that the mirror return springs called for in the design failed to produce a concave curvature in the mirrors in the full defocus position. The heliostat design specifications call for a minimum deflection of 1.6mm (1/16-inch) in full defocus position. The original springs (4.11 kg/cm (23 lb/in) compression constant) were replaced with stronger springs (24.11 kg/cm (135 lb/in) compression constant). Tests verified that the stronger springs produced the required defocus deflection.

Measurements of mirror deflection in focus mode were also performed. Design specifications call for a maximum convex deflection of mirror centerline of 20 mm (0.8 in) from neutral position (mirror undeflected).

Focus deflection measurements were made at 10-foot intervals along the mirror centerline after installation of the new mirror return springs. The measurements verified that maximum deflection requirements (Section 2.3.3) were achieved.

3.3.2.2 Emergency Defocus

The heliostat was focused to maximum centerline deflection, and power to the focus drive was then interrupted and the time required by the mirror surface to return to defocused position was measured. An average time of 0.2 second was obtained from several repetitions of the test. This is well within the safety criteria developed for point focus central receiver heliostats (2).

3.3.2.3 Elevation Drive

Jury rig power was applied to the elevation aim drive to exercize the aim drive stepper motor and stow motor, and to checkout the drive mechanism. Design specifications (Section 5.2) call for a maximum rotation speed of 0.048 mrad/sec (10 deg/hr) in tracking mode and 26.2 mrad/sec (0.25 rpm) in stowing mode.

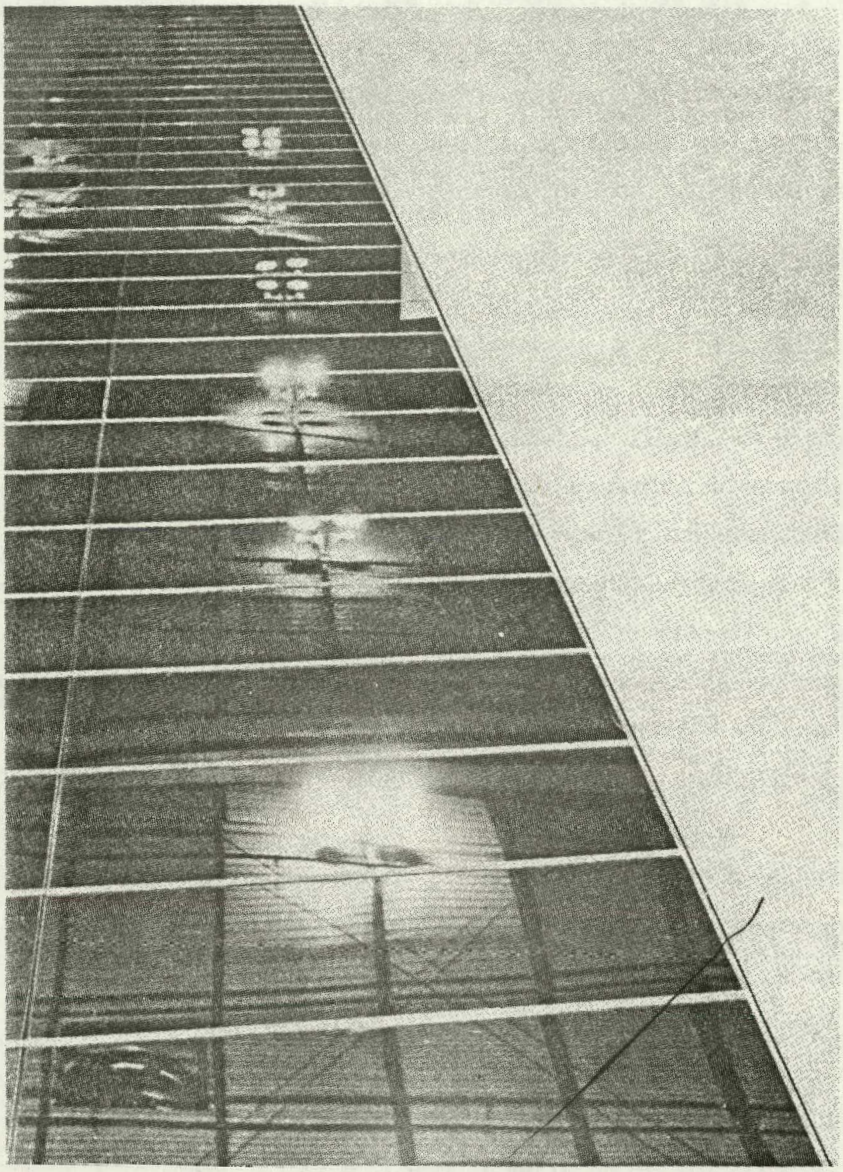

Figure 3-17 EXPERIMENTAL HELIOSTAT SECTION WITH MIRRORS INSTALLED

The heliostat was positioned to fully destowed criteria (mirrors horizontal, facing up) with the stow motor then rotated 180 degrees to a fully stowed position while time was recorded on a stopwatch. Stowing was completed in 118 seconds, within 2 seconds of design specification.

The heliostat was then positioned to a vertical orientation with the stow motor, and the stepper motor was then run through 20 steps while rotation time was recorded. The average time from several runs was 2.7 seconds (7.4 steps/second), which is within the design specification (0.159 rev/rad x 4.8 x 10^{-5}rad/sec x 200 motor steps/rev x 5000:1 gear ratio = 7.6 steps/sec), allowing for the fact that a 4900:1 ratio gearbox was used in the elevation drive.

3.3.2.4 Measurement of Image Size

The field experiment heliostat was used to obtain focused image size. The heliostat and 6 of the target panels built for the field experiment were set up behind the ESD facility as shown in Figures 3-18 through 3-20. The test area shown in Figure 3-18 was the only relatively flat, unobstructed area within proximity of the ESD facility (latitude 37°22', longitude 122°), where a mirror-to-target range of 61 meters (200 feet) could be obtained at a favorable orientation to the sun. The area in the background is a test track for armored vehicles, and was unsuitable as a test area. The view in Figure 3-18 is in an easterly direction. The normal to the centerline of the heliostat was 35 degrees west of true South.

Note that the distance from the centerline of the heliostat to the end of the top corner of the fence in the foreground of Figure 3-18 is 203 feet. An additional target panel was moved to this area after the photograph was taken.

The heliostat contained 28 mirror panels (2 mirror panels per row), located in Rows 2 through 15, counting from the end at which the focus drive mechanism is located. Row 1 was not used so that operation of the focus drive could be observed. Rows 16 through 35 were not used because the geometry of the test area prevented setup of more than 6 target panels. The geometry was such that 14 mirror rows and 6 target panels provided a time slot of about 20 minutes when the full image was on the target.

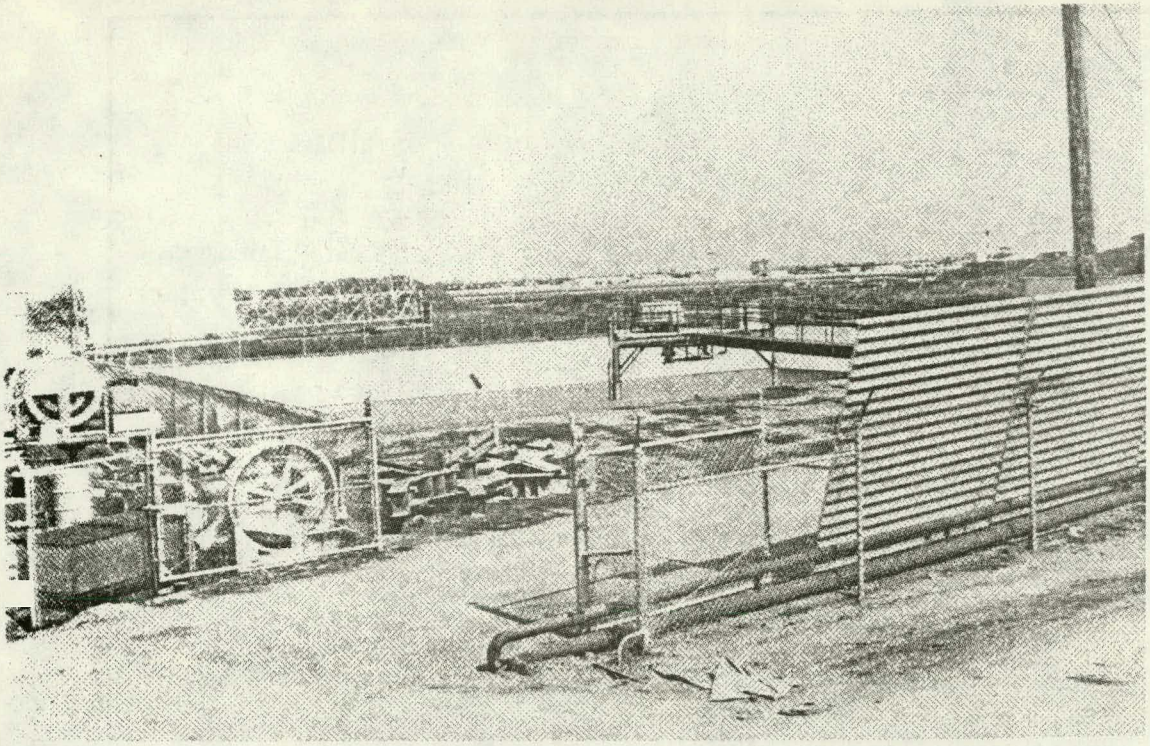

Figure 3-18 TEST SETUP FOR IMAGE SIZE MEASUREMENT

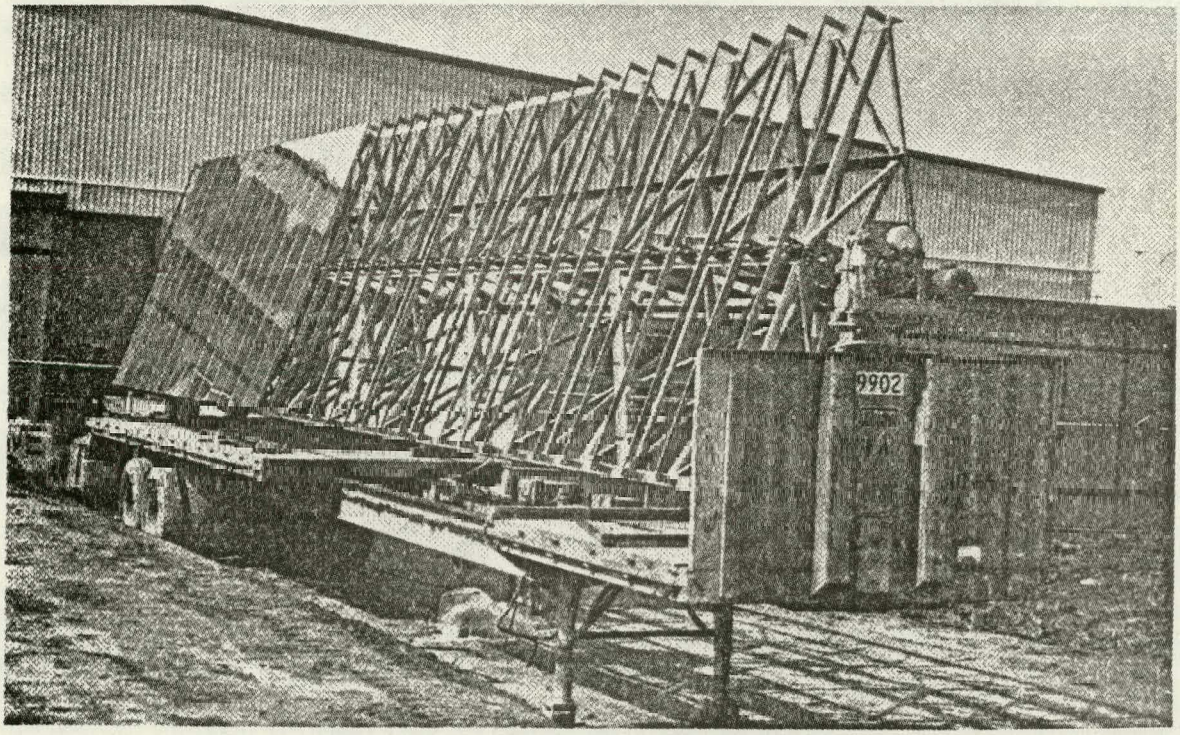

Figure 3-19 HELIOSTAT POSITIONED FOR IMAGE SIZE TEST

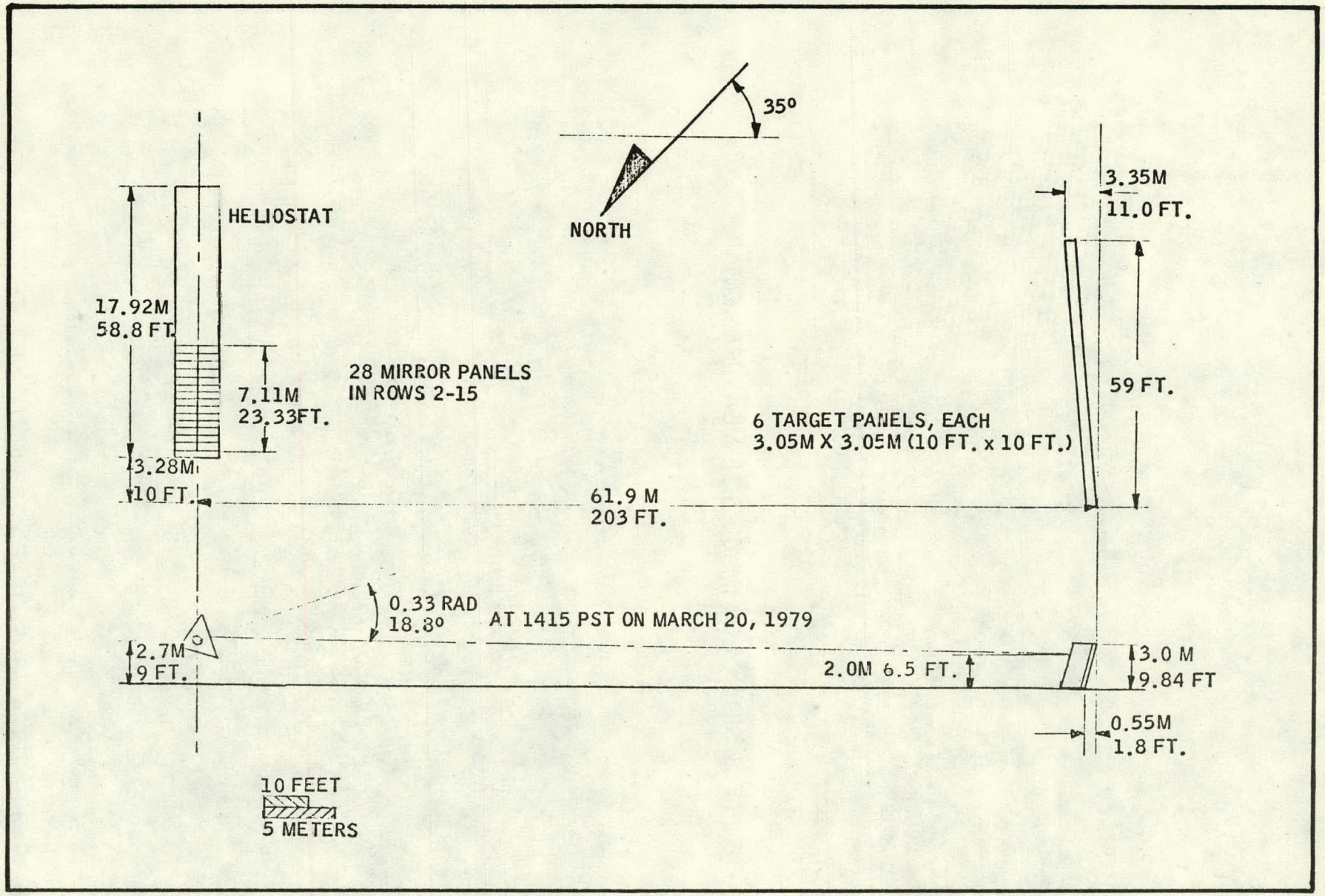

Figure 3-20 SCHEMATIC OF IMAGE SIZE TEST SETUP

Computations indicated that the sun would be in position for testing between 1330 PST and 1430 PST, at an elevation of about 0.66 rad (38 degrees) from horizontal at 1430 PST (1415 solar time) at 37° latitude on vernal equinox (3). At this elevation, a heliostat orientation of 19 degrees from vertical would project a beam parallel with the ground plane. Measurement of heliostat orientation verified these computations, as illustrated in Figure 3-20.

The length of the mirrored section (Figure 3-19) is 7.11 meters (23.22 feet). At a range of 61 meters (200 feet), the predicted length of the reflected image is 7.64 meters (25.1 feet), assuming that the direct normal component of solar radiation arrives at the earth's surface in an 8.73-mrad (0.5-degree) cone (4).

Heliostat elevation was controlled by operating the stow motor from the manual operation console built into the enclosure shown in the lower center of Figure 3-19. Mirror focusing was accomplished by turning the focus pinion gear (Figure 3-5) with a wrench after disengaging the defocusing clutch. This was necessary because the electrical connections between the focus drive and the manual operation console had not been completed.

Initial tests were conducted on March 12, 1979. Observations indicated that the sun would be in position to begin testing at about 1330 PST. At 1315 PST, the mirror section (unfocused) was elevated from a fully stowed position (mirrors down and on the horizontal) to a vertical orientation, so that the image was reflected on the ground immediately in front of the heliostat. When the position of the sun was correct, the mirror section was elevated until the top edge of the image was slightly below the top edge of the target. The mirror section was then focused until a minimum width image (determined by visual observation) was obtained.

Figure 3-21 shows the images obtained in the first test. The picture at the top of Figure 3-21 shows the focused image, which had an overall length of 7.61 meters (25.1 feet) and peak-to-peak width which varied from 0.76 meters (2.5 feet) to 2.0 meters (6.7 feet), with an average width of 1.4 meters (4.6 feet). Note that the orientation of the image is such that a plane containing the projection of the heliostat centerline is almost perpendicular to the vertical projection of the target plane, so the image is seen almost

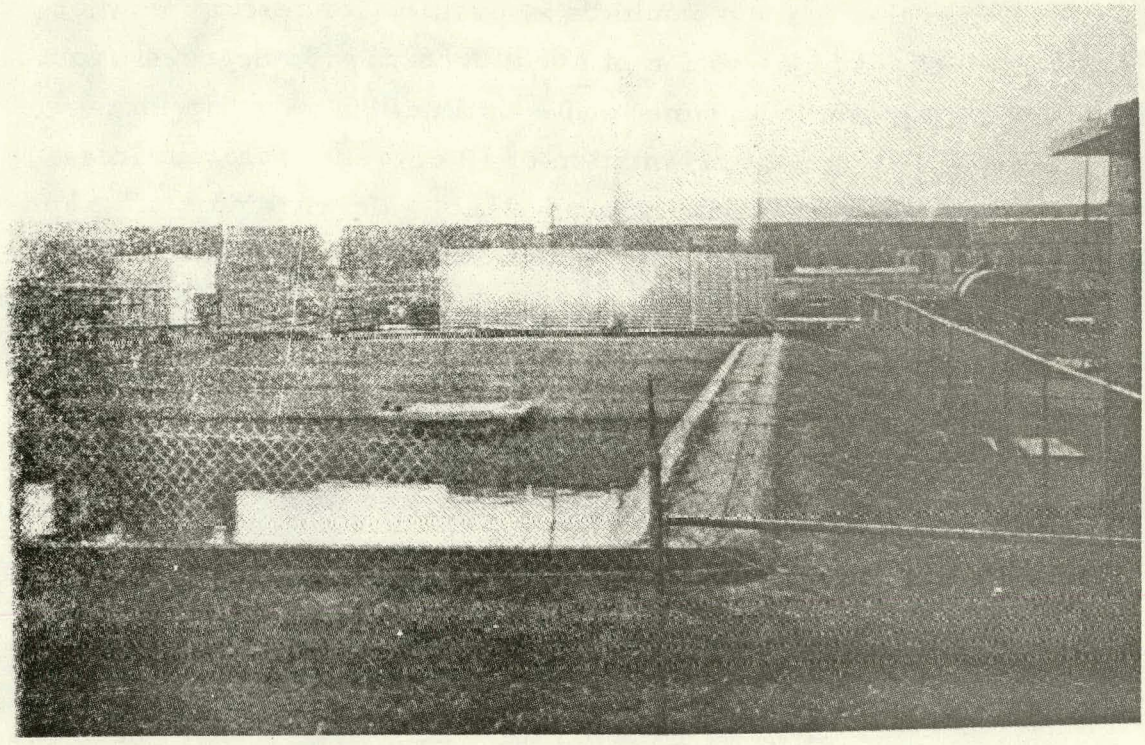

Focused Image (1405 PST)

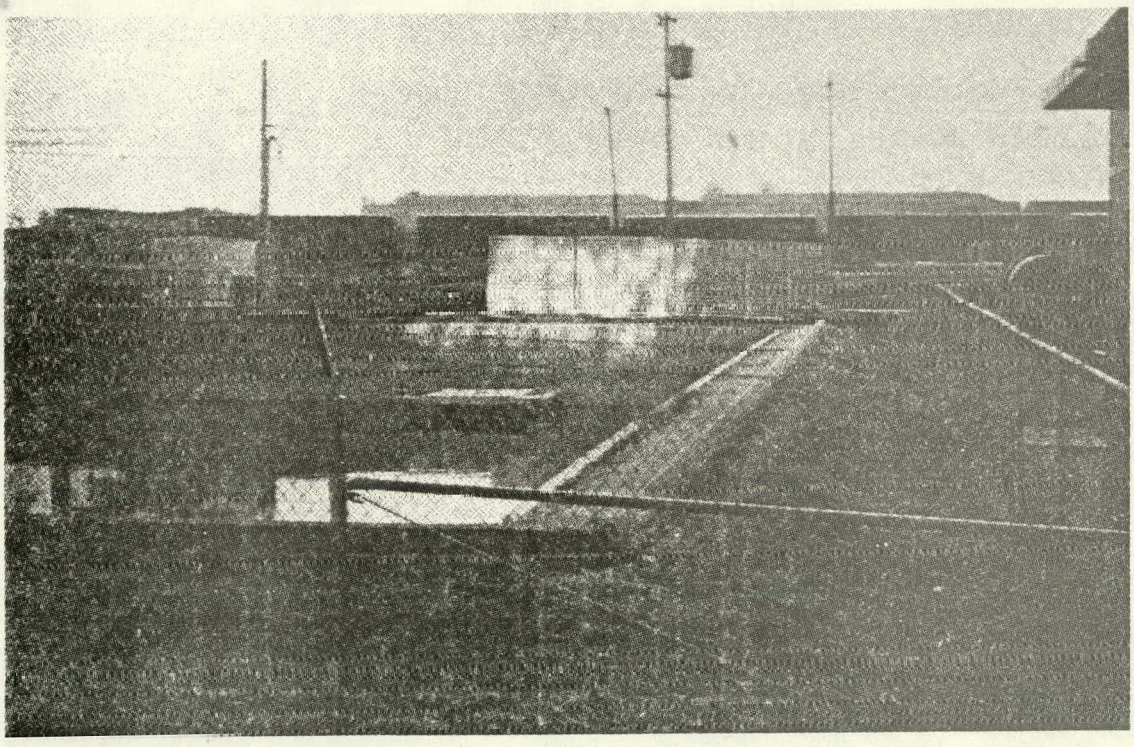

Defocused Image (1410 PST)

Figure 3-21 IMAGE SIZE TEST ON 12 MARCH 1979

undistorted by perspective. The peaks and gaps evident at several points in the image were due in part to misalignment of individual mirrors with respect to the plane of the mirror support structure, and in part to local distortions caused by the tight fit of some mirrors in their support frames.

The bottom picture in Figure 3-21 shows the image from the defocused mirror section, about five minutes after the top picture was taken. The width of the defocused image is about 3.66 meters (12 feet), which was expected because the mirror surface has a slight concave curvature in the fully defocused position. The apparent discontinuity of the image is caused by the lower part of the image being projected on the far wall of the test pond, which is about 14 meters (46 feet) closer to the heliostat than the target panels.

The initial test demonstrated that the heliostat focus mechanism was operating as designed, and that maximum focus was not attained because of mirror misalignments and distortions. The images obtained from the test were used to adjust the edge alignment of the mirrors and the focus cams which control the surface curvature of each mirror row. Edge alignment of adjacent mirrors was adjusted with the adjusting bolts at the ends of each deflection beam (see Figure 3-4). The focus cams of the mirror rows which caused the peaks in the focused image were adjusted to increase the deflection. Each cam can be moved independently so that the relative position of the cam with respect to movement of the focus rack can be different (see Figure 3-5).

Alignment and focus cam adjustments were completed prior to the second test, which was conducted on March 13. The same startup procedure used in the first test was followed. The focused image is shown in Figure 3-22. The picture at the top of Figure 3-22 was taken at 1355 PST. For reference, the tape strips on the target panels are 35.6 cm (14 inches) apart and 7.62 cm (3 inches) wide. (The two strips immediately to the right of the utility pole are 18 cm (7 inches) apart).

The image shown in Figure 3-22 is 7.35 meters (24.1 feet) in length, which is about 0.3 meters (1 foot) shorter than the image obtained in the March 12 test. It was determined that the shorter image was due to misalignment of the mirrors in Row 15 (extreme left in Figure 3-22), which crossed the image from Row 14.

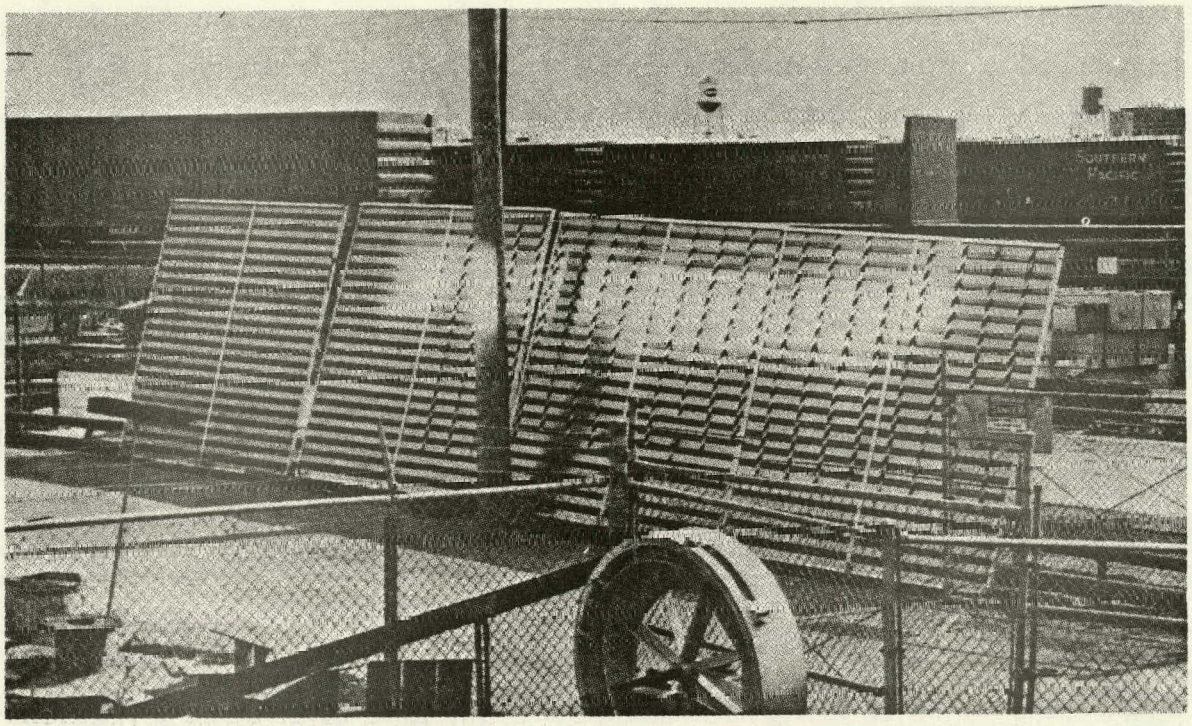

Focused Image at 1355 PST

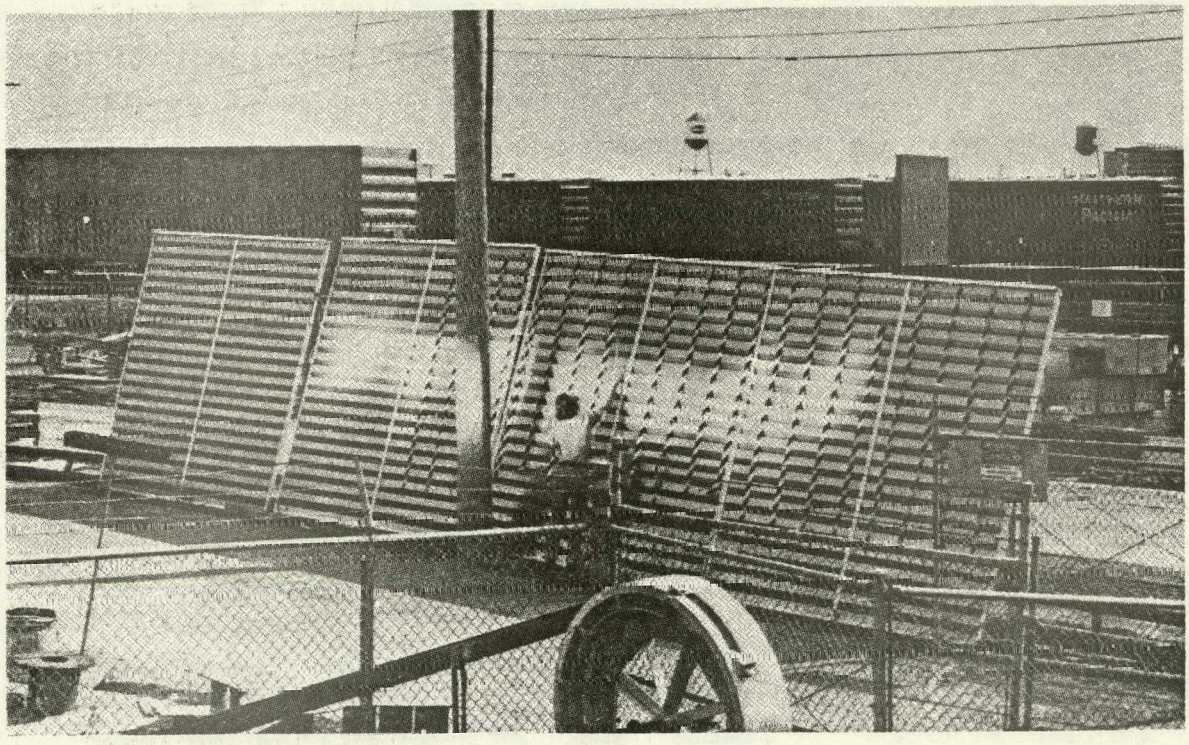

Focused Image at 1357 PST

Figure 3-22 IMAGE SIZE TEST ON 13 MARCH 1979

Image widths at several points along the image were determined by (1) scanning the image with a hand-held light meter along a vertical reference line, (2) marking the points where the light meter reading was equal to the reading for background illumination, and (3) measuring the distance between the marks. The average of five readings was 1.2 meters (3.8 feet).

The image in Figure 3-22 has fewer peaks and gaps than the image obtained in the March 12 test, and the average width is less than that obtained in the March 12 test. However, the width is larger than the target width of 0.61 meter (2 feet) which should be obtained from a properly aligned heliostat at a range of 61 meters (200 feet), to ensure that correct focus width is achieved at ranges up to 125 meters (410 feet), which is the maximum range in the field sizing for the 100 MWe plant concept (Figure 6-2).

Based on the results of the March 13 test, it was decided to attempt alignment adjustments while the heliostat was focused on the target. Several problems were encountered during this alignment work. Most significantly, it was discovered that several mirror panels were distorted to a wavy appearance because of a tight fit in the mirror support structure. These panels were replaced, but the problem persisted, apparently because the majority of the mirror panels were slightly oversize in width. Alleviation of this problem requires replacement of the metal frames which protect the edges cf the mirror panels with thinner frames.

The design chosen for alignment of the mirror deflection beams proved to be a problem because four mirrors are affected when one frame is moved (see Figure 3-7 for illustration). A deflection beam is adjusted by loosening the bolts which attach the ends of the beam to the heliostat structure, and adjusting the height of the beam. Dynamic alignment proved to be difficult because of the near-vertical orientation of the mirror surface and the short time in which the image was incident on the target.

Several attempts were made to improve alignment in preparation for a final test, which was conducted on March 20. Figure 3-23 shows the defocused and focused images obtained at the start of the test. The top picture shows

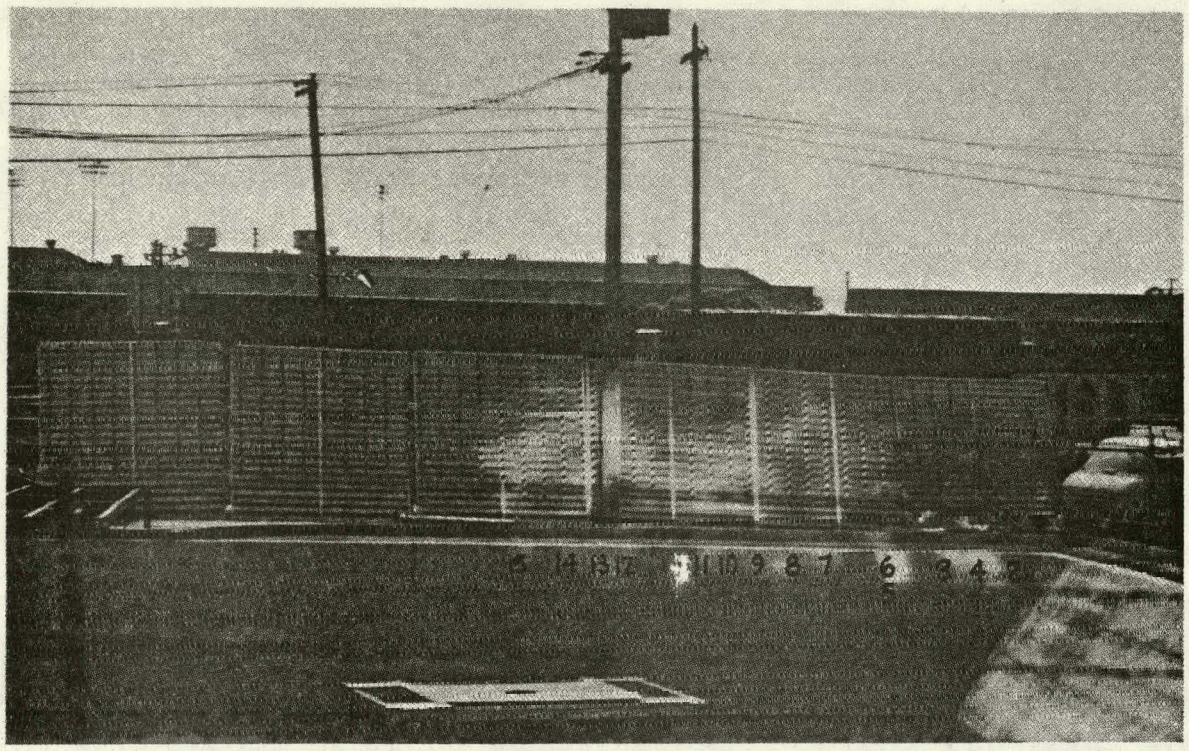

Unfocused Image (1345 PST)

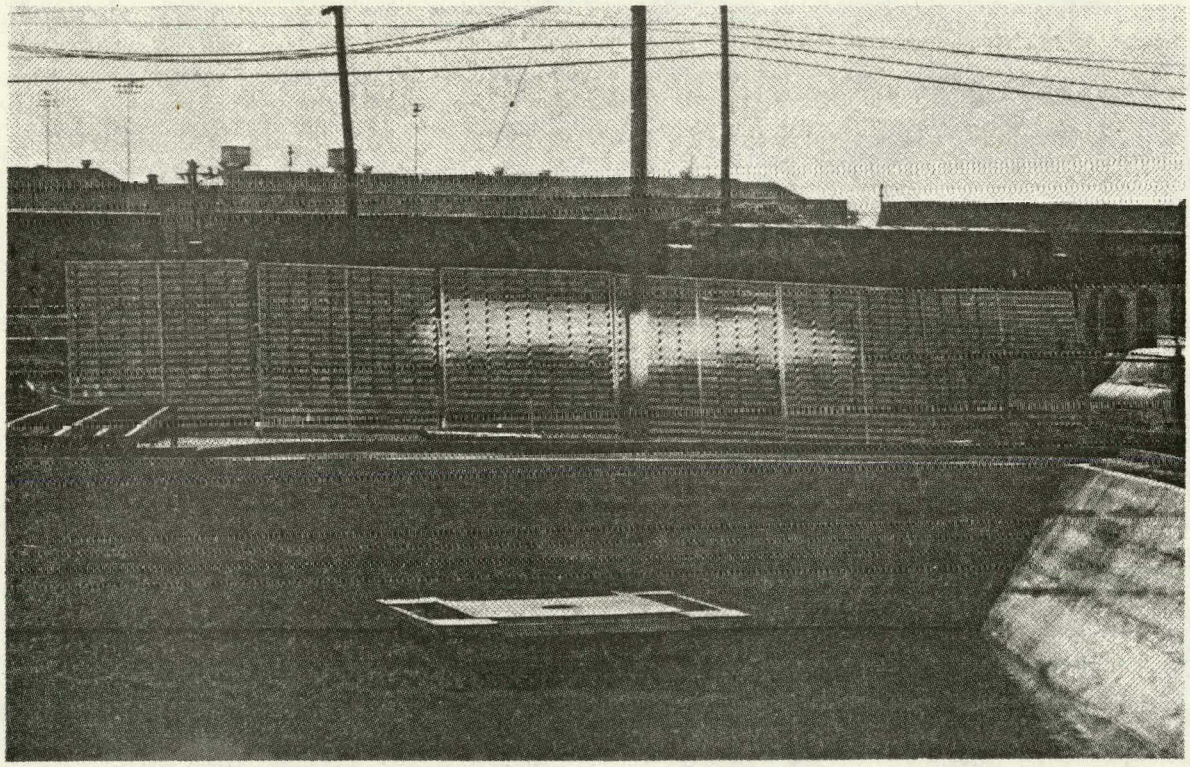

Focused Image (1353 PST)

Figure 3-23 INITIAL IMAGE SIZE IN 20 MARCH TEST

the unfocused image. Note that the image from mirror Row 3 crosses that of Row 4, and the images from Rows 5 and 6 and Rows 12 and 13 overlap, producing gaps and peaks.

The bottom picture shows the focused image. Note that the top edge of the image is from the lower half of the mirror section, which means that the focal line was slightly in front of the target plane when the picture was taken. This was done deliberately so that the images from individual mirrors could be seen when the mirrors were flexed by hand.

Comparison of the focused image in Figure 3-23 with that in Figure 3-22 shows more uniform alignment of the mirrors, and a more concentrated image. The peak in the upper right part of the image (between fifth and sixth tape strips from right edge of image) is due to misalignment of Row 5. The measured length of the focused image was 7.74 meters (25.4 feet).

Alignment adjustments to reduce the peaks and gaps were carried out, and image measurements were then obtained. Figure 3-24 shows the image at 1415 PST. A hand-held light meter was used to determine the following points along six tape strips within the image. The strips were located near the center and edges of each of the three illuminated panels shown in Figure 3-24.

- Points at the edge of image (light meter registered background brightness)
- Points where brightness was approximately 10 percent of maximum brightness reading.

These measured points were used in combination with the visual properties of the points, as seen in Figure 3-24, to map the focused image. Figure 3-25 shows the map, which is viewed in a vertical projection of the target plane (the target plane was tilted at about 11 degrees from vertical). Graphical integration of the map in Figure 3-25 shows that 95 percent of the overall image is within a 1.22-meter (4-foot) width. Additionally, the width of the image within the 10 percent brightness contour varies from 0.76 meter (2.5 feet) to 1.13 meters (3.7 feet), with an average width of 0.91 meters (3.0 feet).

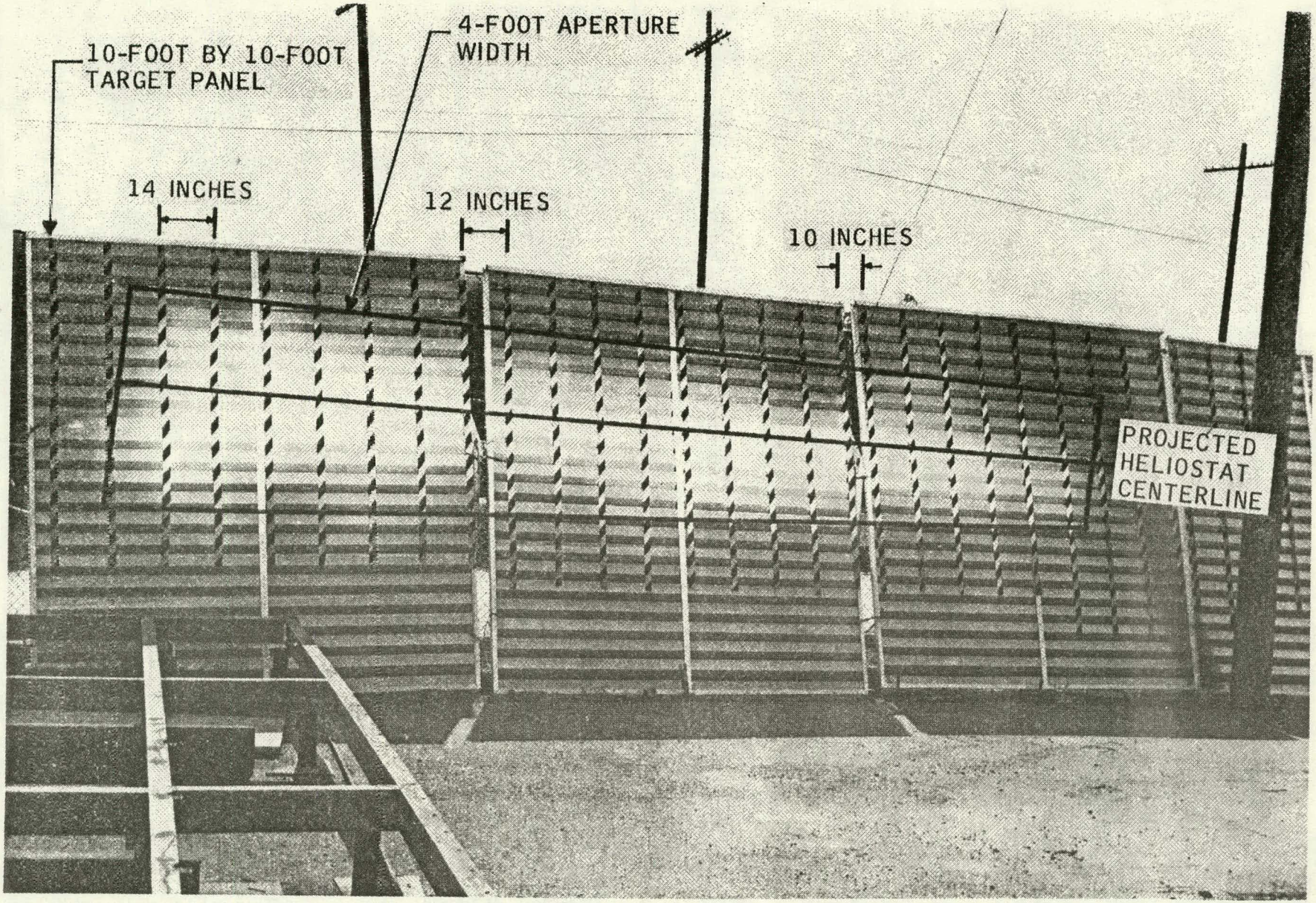

Figure 3-24 FOCUSED IMAGE AT 1415 PST ON 20 MARCH 1979

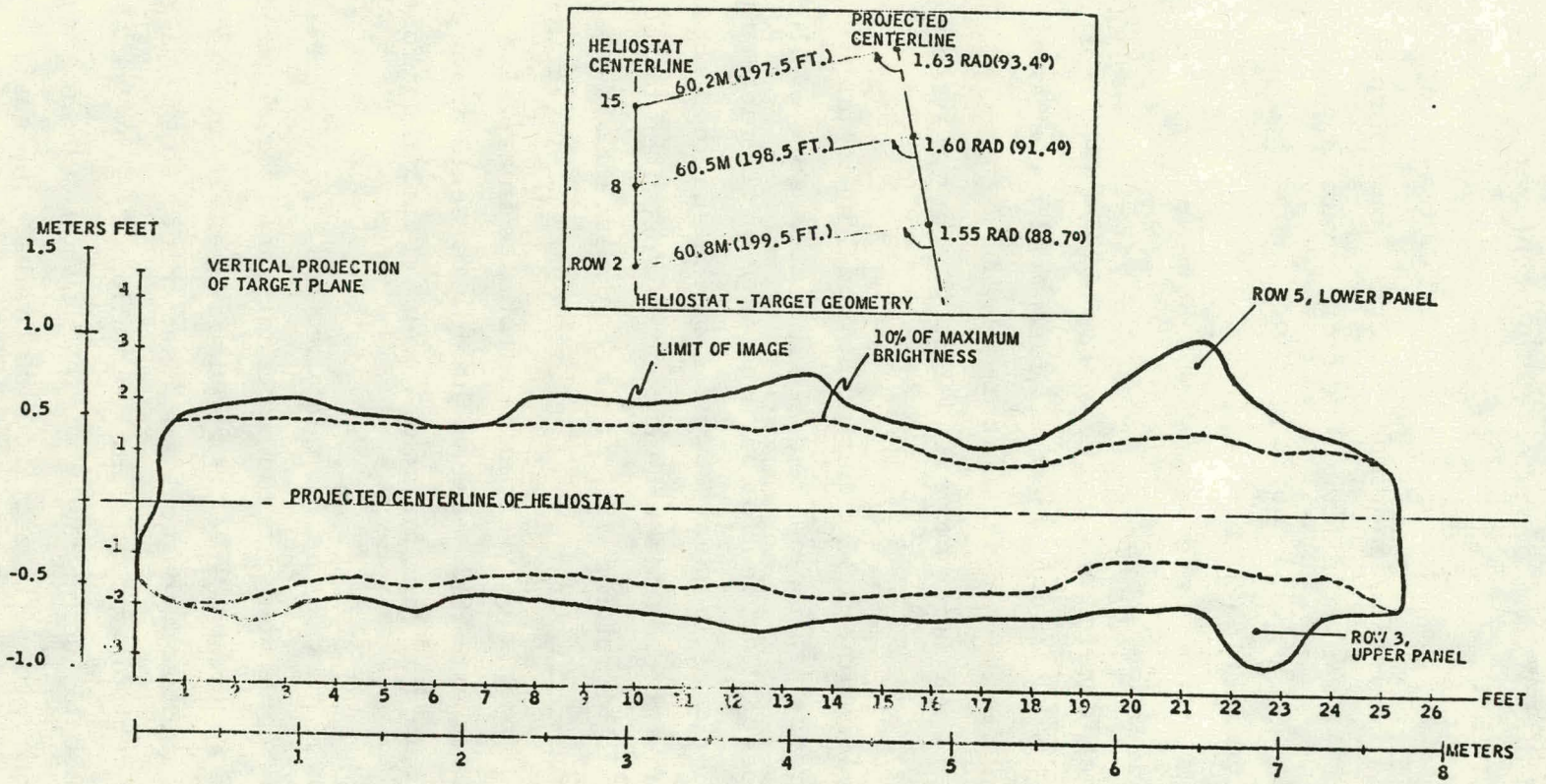

Figure 3-25 MAP OF FOCUSED IMAGE DURING MARCH 20 TEST

The fraction of reflected flux within a 1.22-meter (4-foot) aperture has been estimated as follows, based on the image shown in Figure 3-25:

- Assume normal distribution of reflected flux centered about the projected heliostat centerline.
- Average image half-width at a point where brightness (i.e., density) is 10 percent of maximum is 0.46 meter (1.5 feet). For a normal distribution, this point is at 2.15 standard deviations from symmetry axis. Thus, one sigma (σ) = 0.46/2.15 = 0.21 meter (0.7 foot).
- Half-width of 0.61 meter (2 feet) = 2.86 σ
- The normal distribution curve between $\pm$ 2.86 σ contains 99.6 percent of the total area under the curve.
- To achieve target focusing at a range of 125 meters (410 feet), the heliostat image must be about 0.61 meter (2 feet) at 61 meter range (200 feet). Image half-width of 0.305 meter (1 foot) = 1.43 σ
- 84 percent of the area under normal distribution curve is between $\pm$ 1.43 σ

Thus, it is estimated that the field experiment model heliostat would achieve at least 99 percent concentration of reflected flux at a range of 61 meters (200 feet), and about 84 percent concentration at a range of 125 meters (410 feet), for an average efficiency of 90 percent, based on the spacings showns in Figure 6-2. For comparison, the 100 MWe plant concept described in Section 6 is based on a collector field which concentrates 96.3 percent of reflected flux within a 1.22-meter aperture at a noon equinox design point (Figure 6-10). Thus, the concentration efficiency estimated from the image size test is lower than predicted. This is expected because the mirror section, as previously noted, was not accurately aligned for achievement of maximum focusing.

Further alignment work was not performed after the March 20 test was completed because it was concluded that the procedure used for alignment was inadequate to assure accuracy. What is required is an alignment fixture which incorporates a fixed light source such as a laser trace, so that alignment can be performed under controlled conditions. Additionally, rework of the mirror edge frames, and probably some rework of the deflection beams which support and bend the mirrors, is required to eliminate the surface distortions caused by tight fitting mirrors. Unfortunately, remaining project funds did not permit accomplishment of this work.

4.0 RECEIVER

The baseline receiver for the FMC Line Focus System consists of a 61-meter (200-foot) insulated cylindrical cavity oriented horizontally on an east-west axis. Movable doors or eyelids mounted on the aperture edges improve aperture collection efficiency in operation and conserve heat during periods of downtime. Each section is supported at an elevation of 61 meters (200 feet) by a steel lattice tower at each end. The towers are similar in design to those used by utilities for transmission lines.

The receiver aperture plane is 1.22 meters (4 feet) wide and oriented at 45 degrees from the plane of the heliostat field. The diameter of the receiver cavity is 1.83 meters (6 feet). These dimensions were optimized, as described in Section 2.0 on the basis of maximum collected energy at the receiver aperture plane. The height of the tower and the receiver length were fixed at 61 meters to permit erection of towers and receivers with standard high-lift truck cranes.

Each receiver section receives feedwater and discharges rated steam for transport to the power plant. There are two alternate concepts for the steam generator. One alternative is a once-through-to-superheat concept using a horizontal array of tubes distributed about the inner circumference of the cavity (see Figure 4-1). The other alternative is a natural-convection, gravity-feed concept using two rows of vertical tubes located in the aperture plane (see Figure 4-2).

The feasibility of generating rated steam for operation of an EPGS has been analytically established. The once-through concept has been selected as the baseline concept on the basis of lower capital cost and lower reflection and re-radiation losses. Final selection of a concept will require more detailed evaluation, analytically and experimentally.

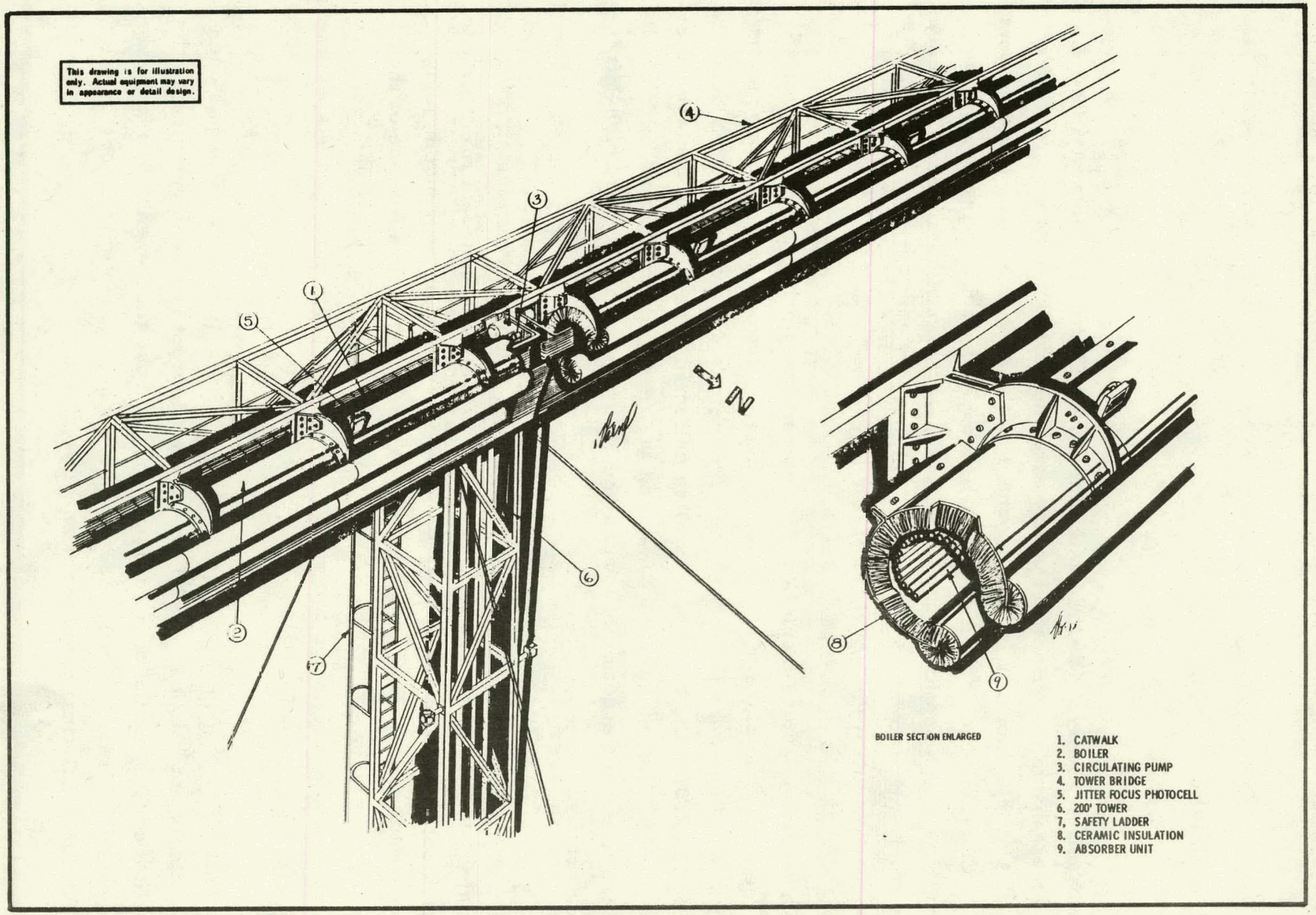

Figure 4-1 ONCE-THROUGH RECEIVER CONCEPT

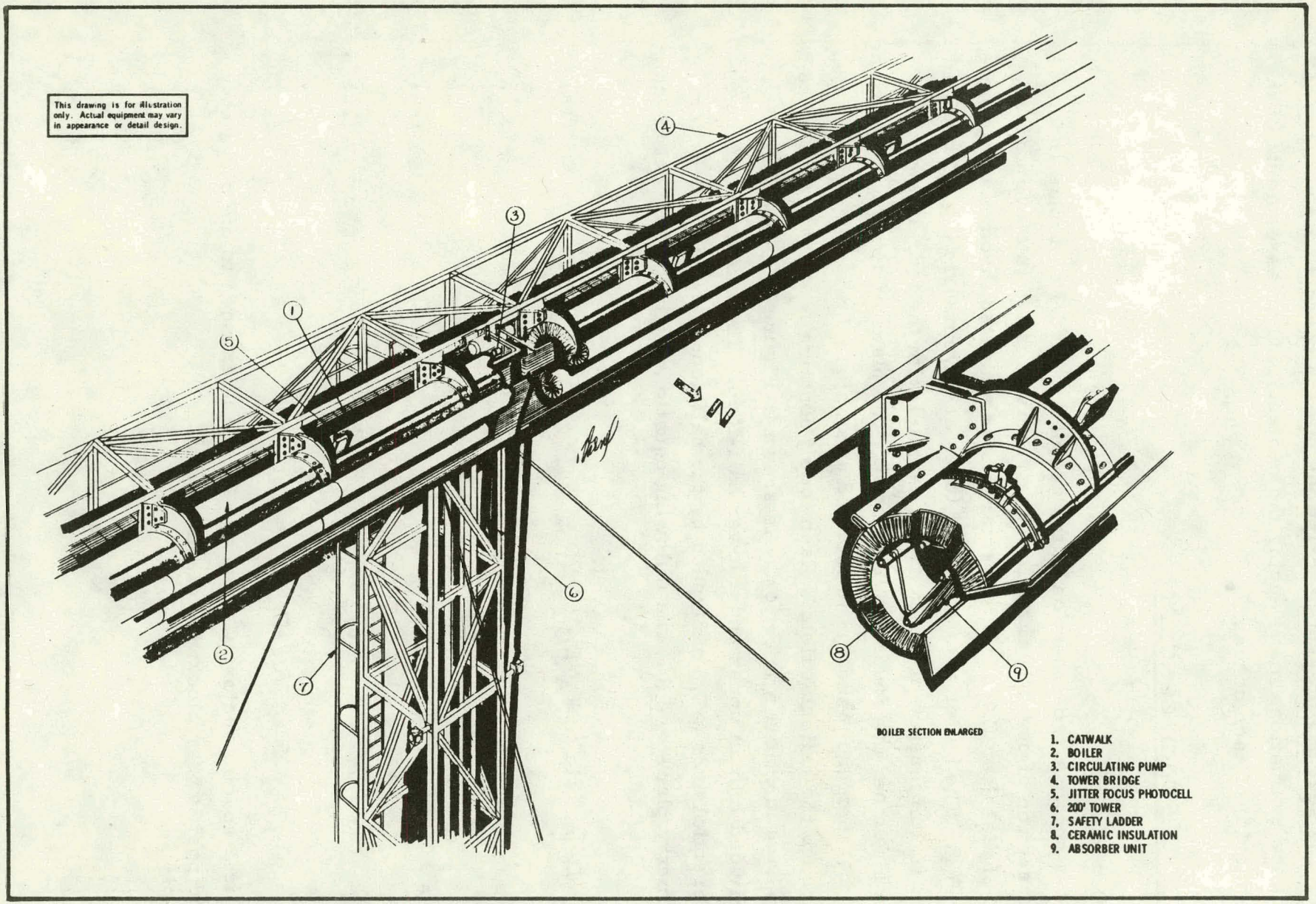

Figure 4-2 NATURAL CONVECTION RECEIVER CONCEPT

The following sections present descriptions of each concept, a summary of performance evaluations made during the project, and an assessment of the relative merits of each concept.

4.1 ONCE-THROUGH CONCEPT

4.1.1 Description

Figure 4-3 shows a cross section of the geometric model of a once-through receiver section of overall length l_R. The receiver cavity is a cylindrical segment of diameter D_C. Incident solar flux is admitted through an aperture of width W_A. The boiler and superheat tubes are symmetrically distributed about the circumference of the cavity in parallel with the long axis of the cavity in L number of groups (called loops). The plane of symmetry is orthogonal to the aperture plane and is inclined at an angle T with the horizontal plane through the heliostat field. Each loop j contains N_j tubes. All tubes in a loop have identical properties. As shown in Figure 4-3, each loop is evenly divided into an upper and a lower half-loop. The midpoints of the circumferential arcs (ΔC_j) subtended by the half-loops are displaced from the symmetry plane by $\pm\theta_j$. The following equations define the layout of loops about the cavity:

$$S = D_C\left[\pi - \sin^{-1}(W_A/D_C)\right] / \sum_{k=1}^{L} D_{ok}\, N_k \qquad (1a)$$

$$\Delta C_j = 0.5 S D_{oj}\, N_j \qquad (1b)$$

$$C_{j2} = \pm 0.5 S \sum_{k=1}^{j} D_{ok}\, N_k \qquad (1c)$$

$$C_{j1} = \pm C_{j2} \mp \Delta C_j \qquad (1d)$$

$$\text{and } \theta_j = (C_{j1} + 0.5\Delta C_j)/0.5 D_C \qquad (1e)$$

where S is a spacing factor, C is an arc length referenced to the symmetry plane and positive for clockwise displacement.

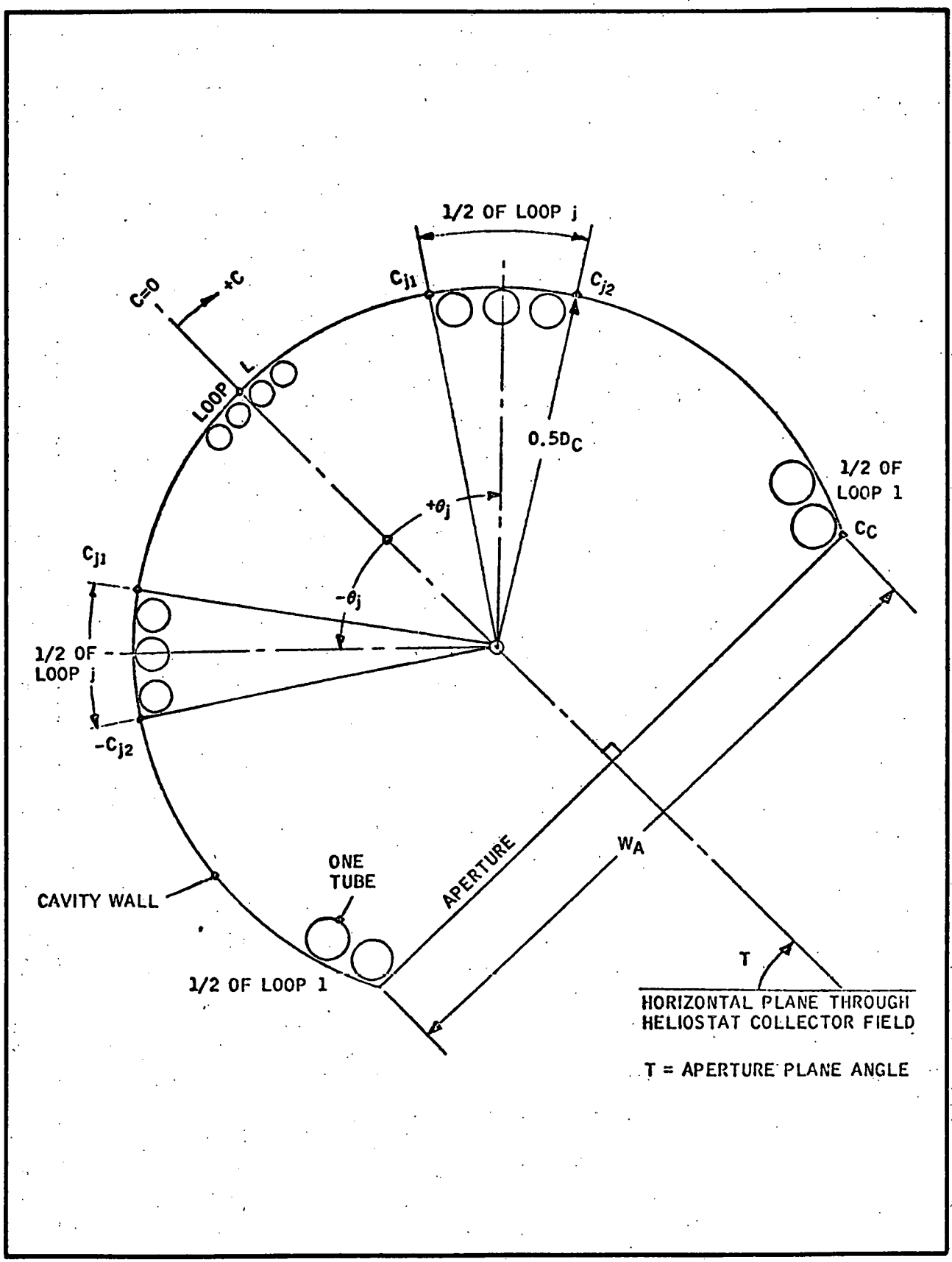

Figure 4-3 GEOMETRY OF TUBE DISTRIBUTION IN RECEIVER CAVITY

The spacing factor defined by Equation 1a yields a circumferential pitch of SD_{oj} in Loop j, and spacing of $0.5S\,(D_{oj} + D_{oj+1})$ between loops, as shown in Figure 4-4. The equivalent linear spacings are nearly equal to the circumferential spacings shown in Figure 4-5, because the cavity diameter is large in comparison with the tube diameters.

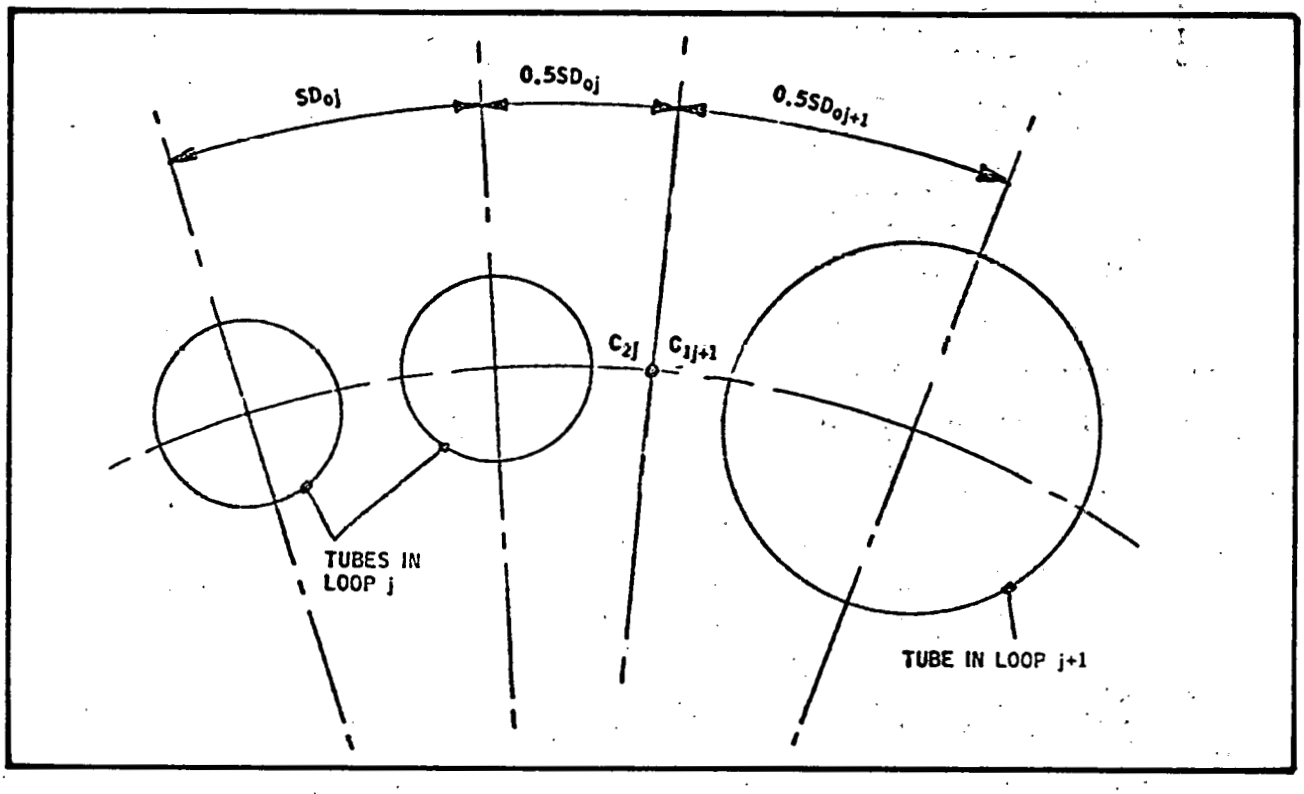

Figure 4-4 SPACING BETWEEN TUBES AND LOOPS

Figure 4-5 shows the path of fluid flow in a receiver section. Feedwater enters each half of Loop 1; superheated steam exits from Loop L. Flow is concurrent in the tubes within a loop and countercurrent in adjacent loops. The flow pattern is arranged so that heating of feedwater to saturation is accomplished in the outer loops by the low-energy portion of the incident solar flux distribution within the cavity. Saturation boiling occurs in the middle loops. The majority of superheating occurs in Loop L, which intercepts the peak flux intensity.

Figure 4-6 shows a plan view of the receiver configuration developed from parametric analysis conducted in the Central Receiver Research Study, using the model in Appendix B. Table 4-1 lists the properties of each loop.

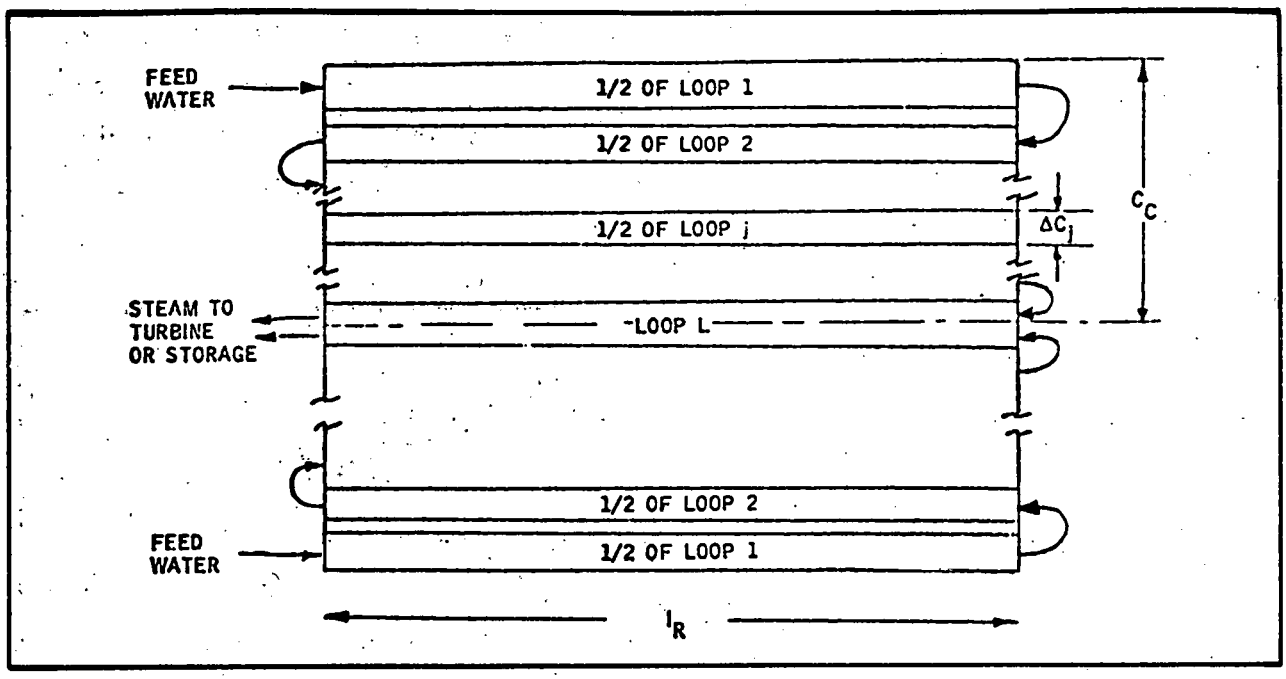

Figure 4-5 FLOW MODEL OF WORKING FLUID WITHIN RECEIVER SECTION

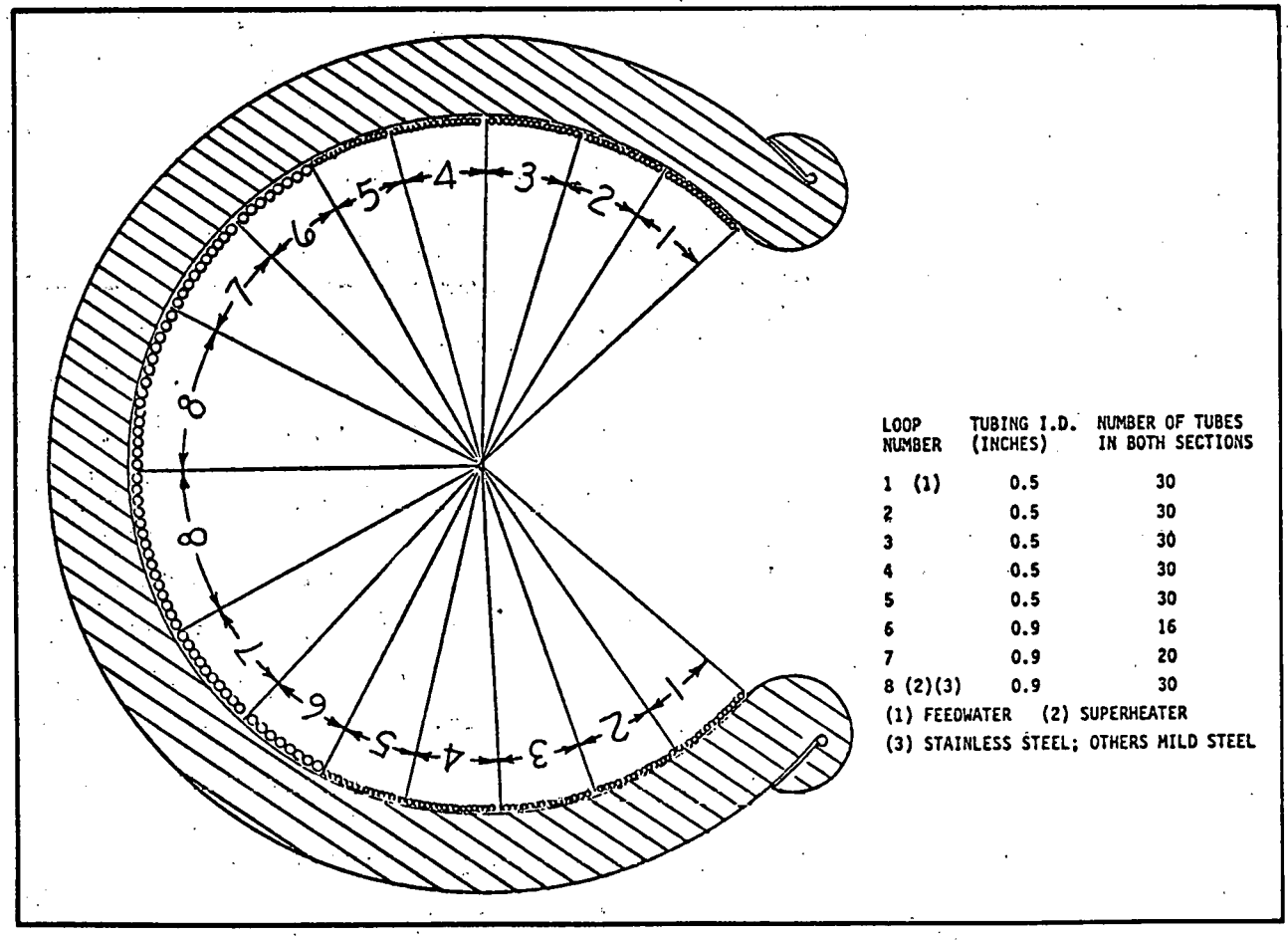

LOOP NUMBER	TUBING I.D. (INCHES)	NUMBER OF TUBES IN BOTH SECTIONS
1 (1)	0.5	30
2	0.5	30
3	0.5	30
4	0.5	30
5	0.5	30
6	0.9	16
7	0.9	20
8 (2)(3)	0.9	30

(1) FEEDWATER (2) SUPERHEATER
(3) STAINLESS STEEL; OTHERS MILD STEEL

Figure 4-6 ONCE-THROUGH CONCEPT, RECEIVER CROSS SECTION

Table 4-1 CHARACTERISTICS OF ONCE-THROUGH RECEIVER TUBE LOOPS

Loop	Tube inside diameter, centimeters (inches)	Number of tubes*	Position (see Figure B-2 in Appendix B)		Material
			C_{j2}, meters (feet)	θ_j, radians (degree)	
1 (Feed)	1.27 (0.5)	30	2.20 (7.22)	2.28 (130.5)	Mild steel
2	1.27 (0.5)	30	1.96 (6.43)	2.01 (115.1)	Mild steel
3	1.27 (0.5)	30	1.71 (5.61)	1.74 (99.7)	Mild steel
4	1.27 (0.5)	30	1.47 (4.82)	1.47 (4.82)	Mild steel
5	1.27 (0.5)	30	1.22 (4.00)	1.20 (69.0)	Mild steel
6	2.29 (0.9)	16	0.98 (3.21)	0.94 (53.9)	Mild steel
7	2.29 (0.9)	20	0.74 (2.43)	0.65 (37.1)	Mild steel
8 (Exit)	2.29 (0.9)	30	0.45 (1.48)	0.24 (13.9)	Stainless steel

* Half in each half of cavity

4.1.2 Performance

The circumferentially distributed once-through concept was subjected to a series of iterative performance analyses using the computer model described in Appendix B. The purpose of the analyses was to establish a feasible configuration of tubes and loops for operation at a 2:00 p.m. winter solstice design point in a 10 MWe plant configuration (see Appendix D). The following parameters were fixed for all analyses:

- 61 meter (200 foot) tube length
- Mild steel tubes for preheat and boiling loops, stainless steel tubes for superheat loop
- Feedwater in at 216 °C (421 °F)
- Steam out at 538 °C (1,000 °F)
- Tube absorptivity = 0.9, emissivity = 0.7
- Incident flux distribution from an optimized flat North collecter field.

A six-loop configuration using 10 each 2.54 centimeter (1-inch) diameter tubes per loop was chosen as a starting point for the iterative analysis. The output of one iteration was used to modify the diameter and number of tubes per loop for the next iteration until a feasible configuration (rated steam at required flow rate) was found.

The analysis was repeated with eight- and ten-loop configurations. The eight-loop configuration described in the preceding section was chosen as the best balance between absorbed energy efficiency and total weight of tubing. Further studies to optimize performance on the basis of system economics and more detailed design studies were outside of the funded scope of the project.

Figures 4-7 through 4-10 show the performance of the eight-loop configuration on three solar days, using the input from a North flat collector field optimized for 2:00 p.m. winter solstice. Receiver efficiencies shown in Figures 4-7 through 4-9 are defined as

$$\frac{\text{Change in available energy of working fluid } (M \Delta A)}{\text{Solar energy at receiver aperture}}$$

where

M = Mass flow rate of working fluid

ΔA = Available energy of outlet steam
- Available energy of inlet feedwater

A = Enthalpy - $T_a S$

T_a = Ambient temperature

S = Entropy

Available energy is used in the efficiency computation to account for pressure losses as well as changes in sensible and latent heat content of the working fluid.

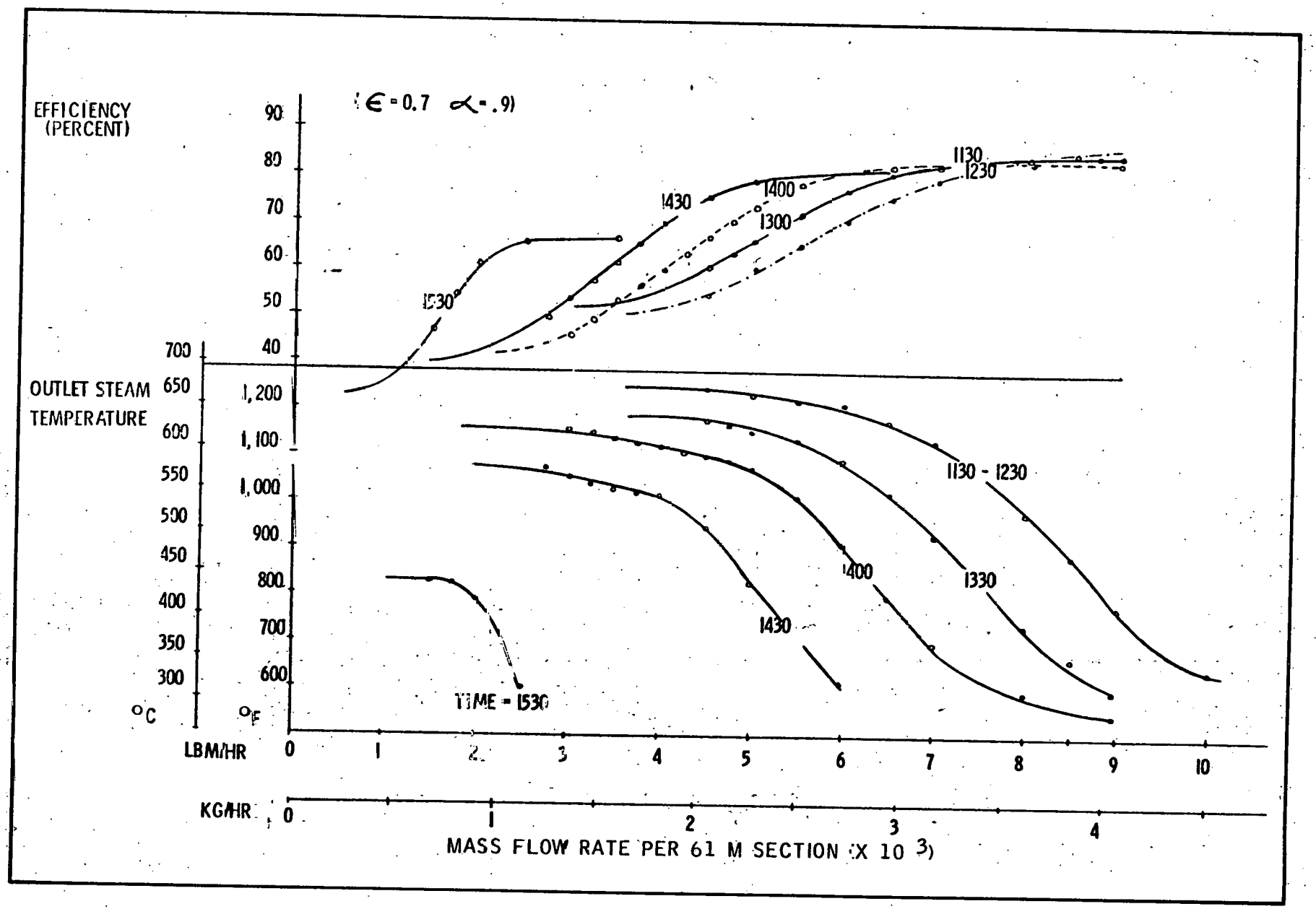

Figure 4-7 PERFORMANCE OF ONCE-THROUGH RECEIVER AT WINTER SOLSTICE

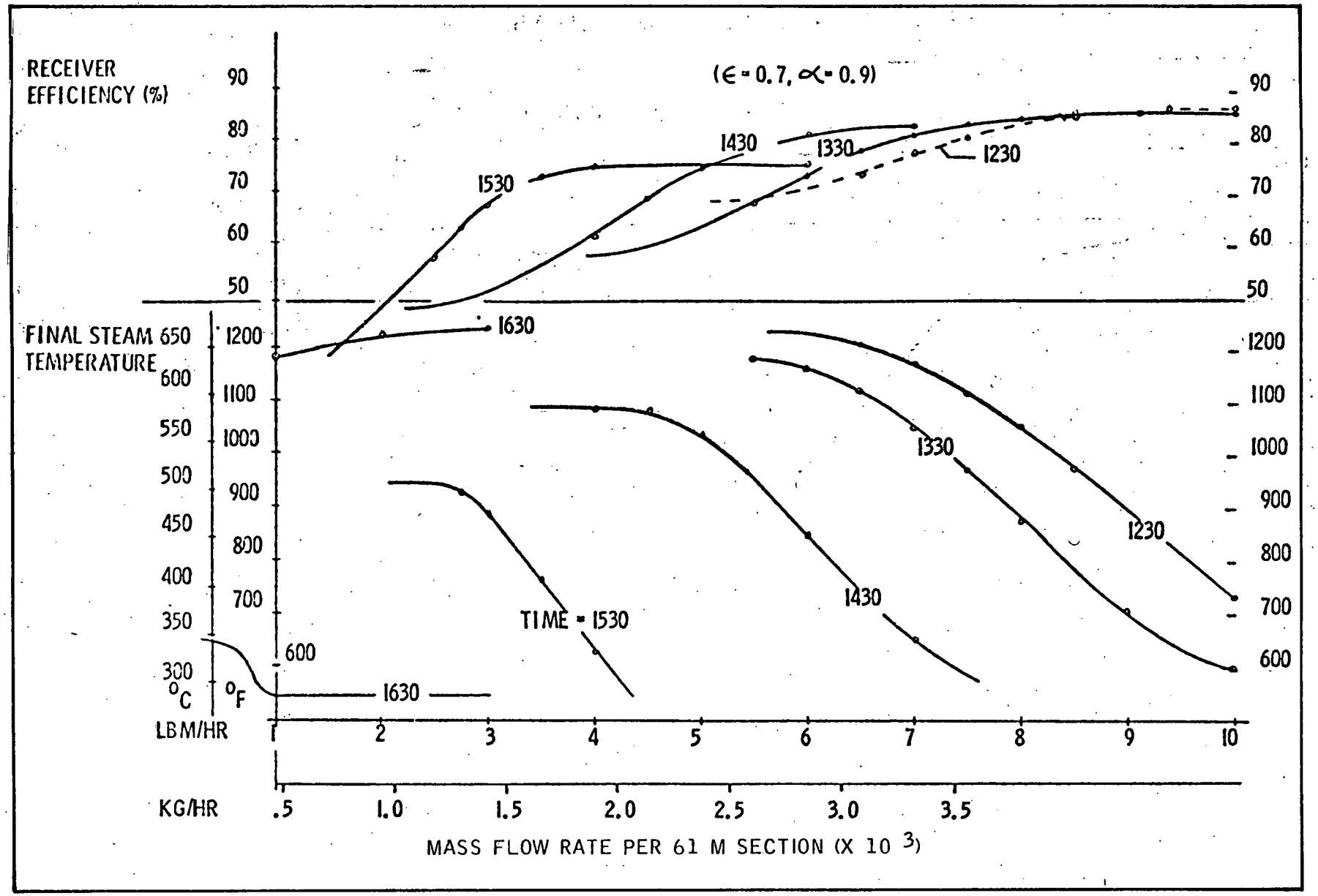

Figure 4-8 PERFORMANCE OF ONCE-THROUGH RECEIVER AT EQUINOX

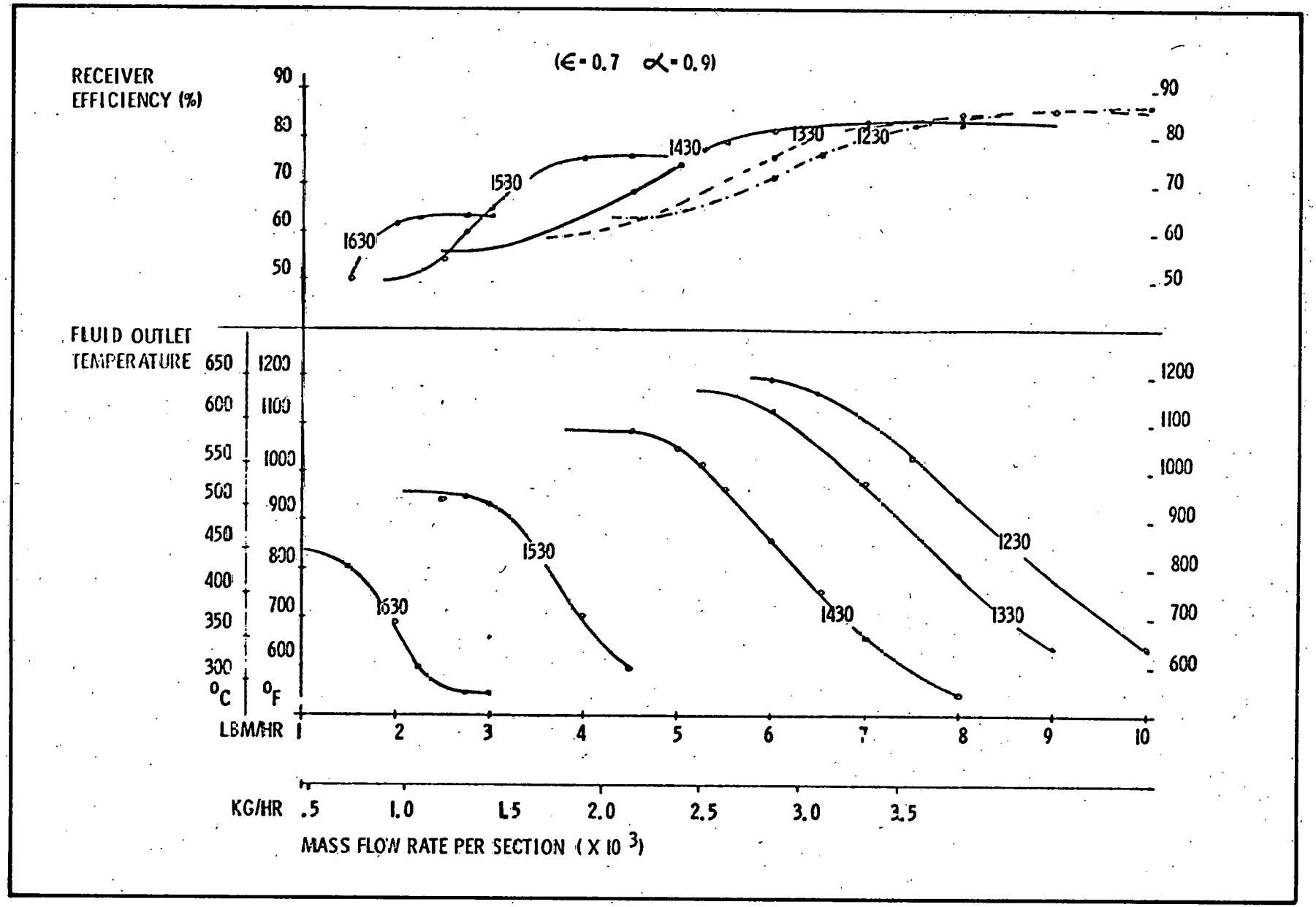

Figure 4-9 PERFORMANCE OF ONCE-THROUGH RECEIVER AT SUMMER SOLSTICE

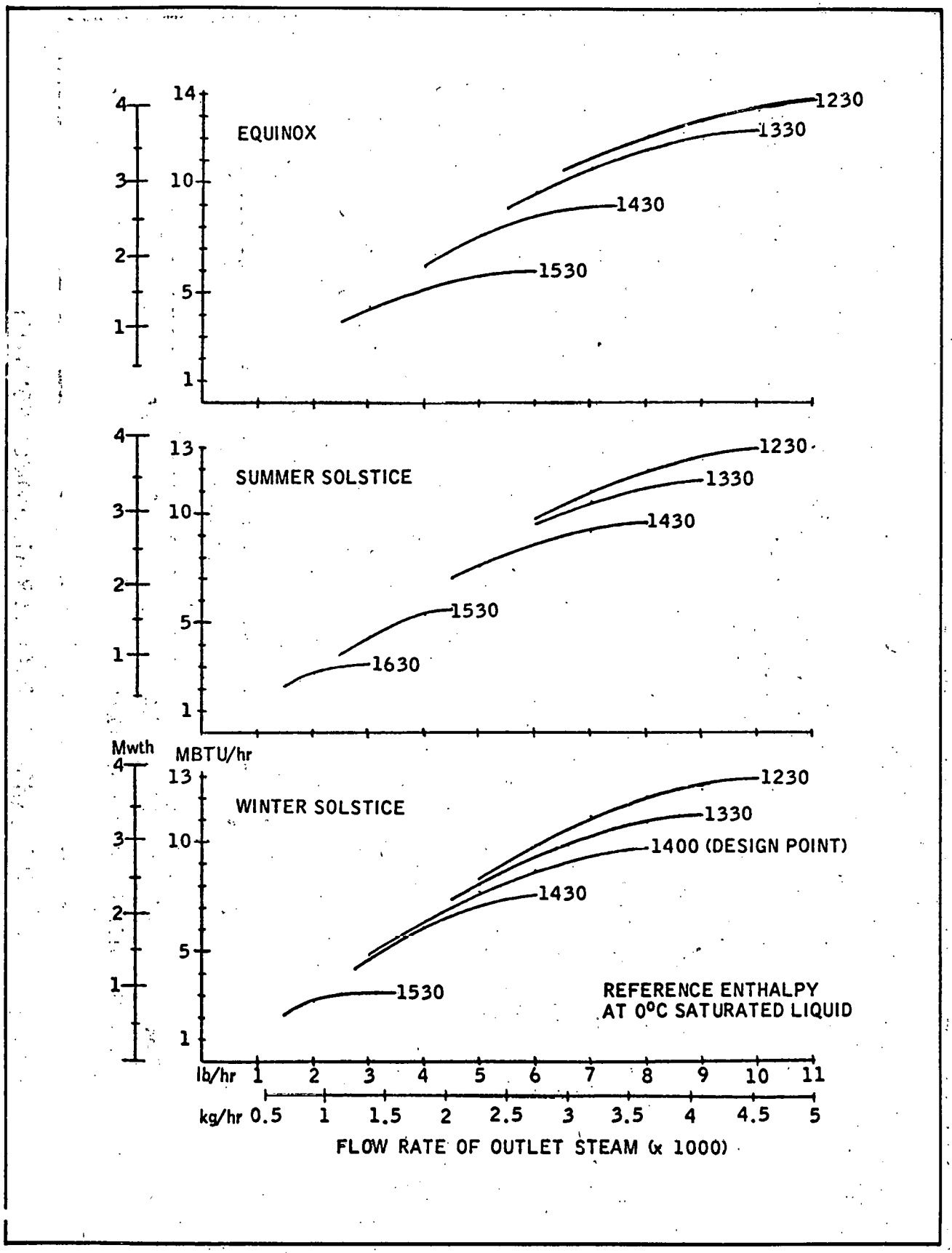

Figure 4-10 HEAT CONTENT OF OUTLET STEAM - ONCE-THROUGH RECEIVER

The performance data summarized in Figures 4-7 through 4-10 were used throughout the project for plant sizing estimates. Check runs of receiver performance input from a collector field optimized for an equinox design point were made to verify the applicability of the receiver configuration to a different design day. Appendix D contains these computations.

4.2 NATURAL CONVECTION CONCEPT

4.2.1 Description

The natural convection boiler consists of a double screen of vertical boiler tubes mounted in the aperture plane of the receiver cavity (see Figure 4-11). A receiver 61 meters (200 feet) long contains approximately 1,600 boiler tubes of 9.5-millimeter (3/8-inch) outside diameter. The outer row of tubes generates and delivers saturated steam to the separation drum which feeds the second row of superheater tubes and returns circulating water to the first row. Superheated steam output is collected in a plenum header which is mounted inside the boiler cavity to minimize heat losses.

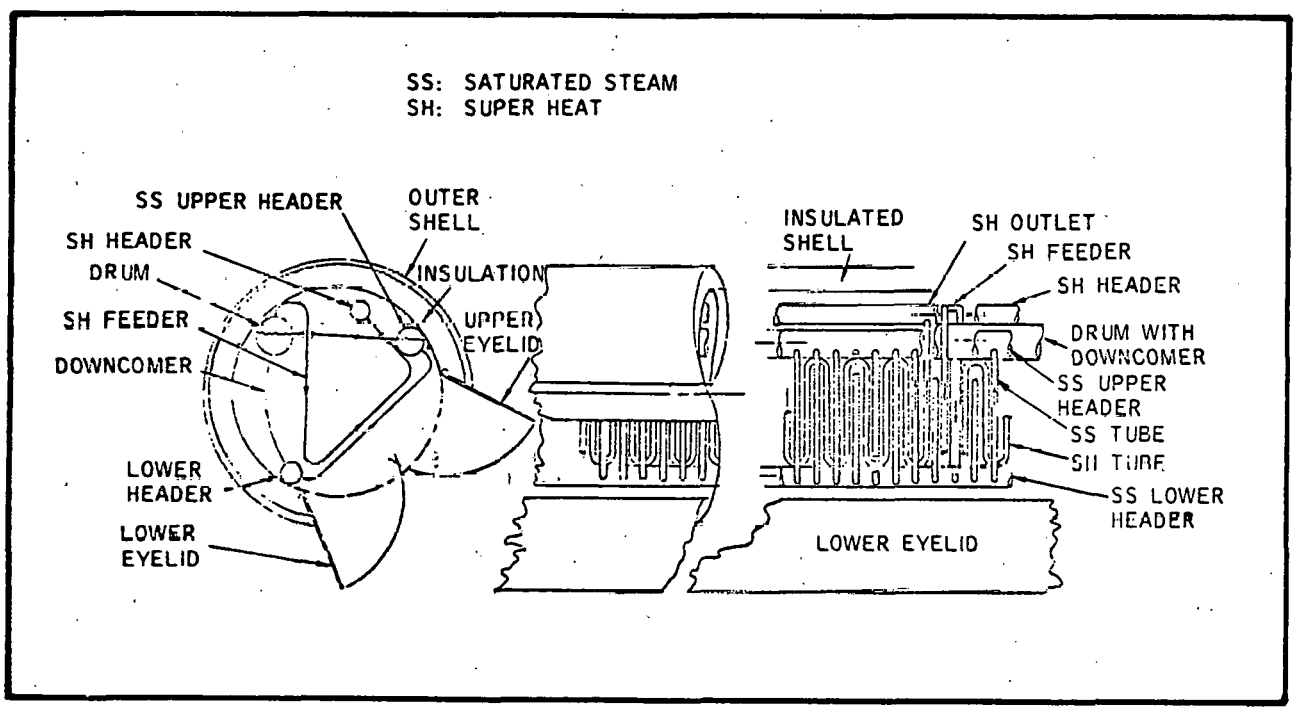

Figure 4-11 NATURAL CONVECTION RECEIVER CONCEPT

The gravity-feed natural convection boiler is equipped with a double ladder, or double screen, of heat-absorbing boiler tubes, and appropriate shell insulation (see Figure 4-12). The receiver absorptivity is enhanced and the radiant losses are minimized by the screening effect of the two rows of closely spaced boiler tubes. The tube bundle also acts as a wall to reduce convective losses from wind blowing into the cavity. The downward tilt of the cavity traps lighter hot air in the upper portion, minimizing natural circulation in the cavity. The cooler boiler tubes are on the outboard side and the warmer superheater tubes are in the inside. Radiant heat losses from the superheater tubes are partially recovered by the outer tube row. The eyelids are used to gather light not focused into the boiler aperture and to close the aperture at night.

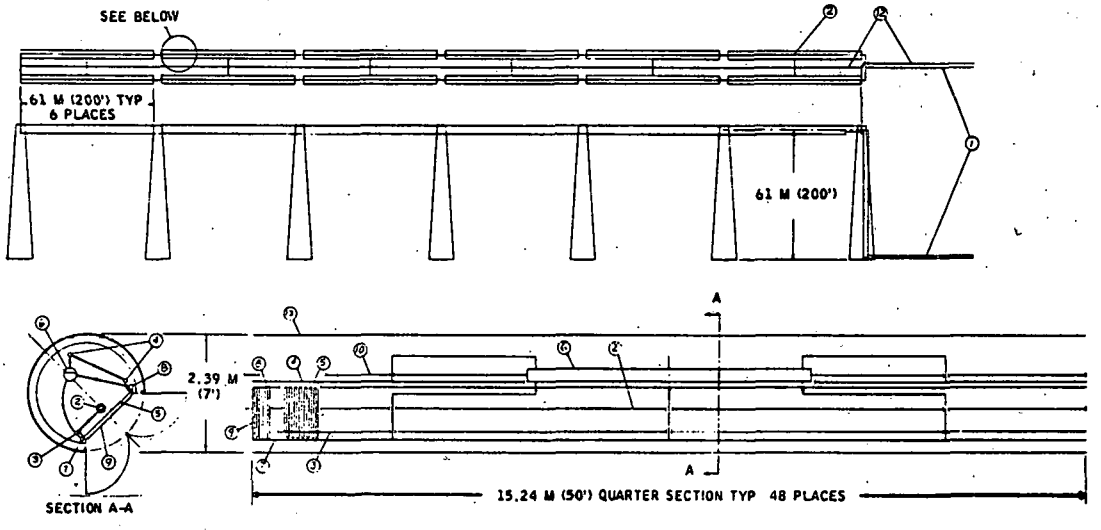

1. STEAM OUTLET LINE
2. SUPERHEAT PLENUM
3. SUPERHEATER OUTLET HEADER
4. SUPERHEATER SUPPLY HEADER
5. SUPERHEATER TUBE BUNDLE
6. SEPARATION DRUM
7. BOILER LOWER HEADER
8. BOILER UPPER HEADER
9. BOILER TUBES
10. EQUALIZER
11. ATTEMPORATOR (NOT SHOWN)
12. BOILER FEED LINE
13. OUTER SHELL

Figure 4-12 PIPING SCHEMATIC FOR NATURAL CONVECTION RECEIVER CONCEPT

A heat balance model of the natural convection boiler was developed with incident flux at the receiver aperture (q_i) as the independent variable. The case of zero steam flow (dry tubes) was first examined to determine the average temperature obtainable at various locations in the receiver cavity. The results are plotted in Figure 4-13 using a wind velocity of 6.7 meters per second (15 miles per hour). The results show that an average temperature of approximately 838°C (1,540°F) is obtained for an incident heat flux of 32.9 kilowatts per square meter (10,000 Btu/hr-ft) on any uncooled cavity surface.

The model was used to determine the cavity equilibrium temperatures when the incident flux passes through a screen of boiler tubes maintained at boiler operating temperatures of 282°C to 510°C (540°F to 950°F).

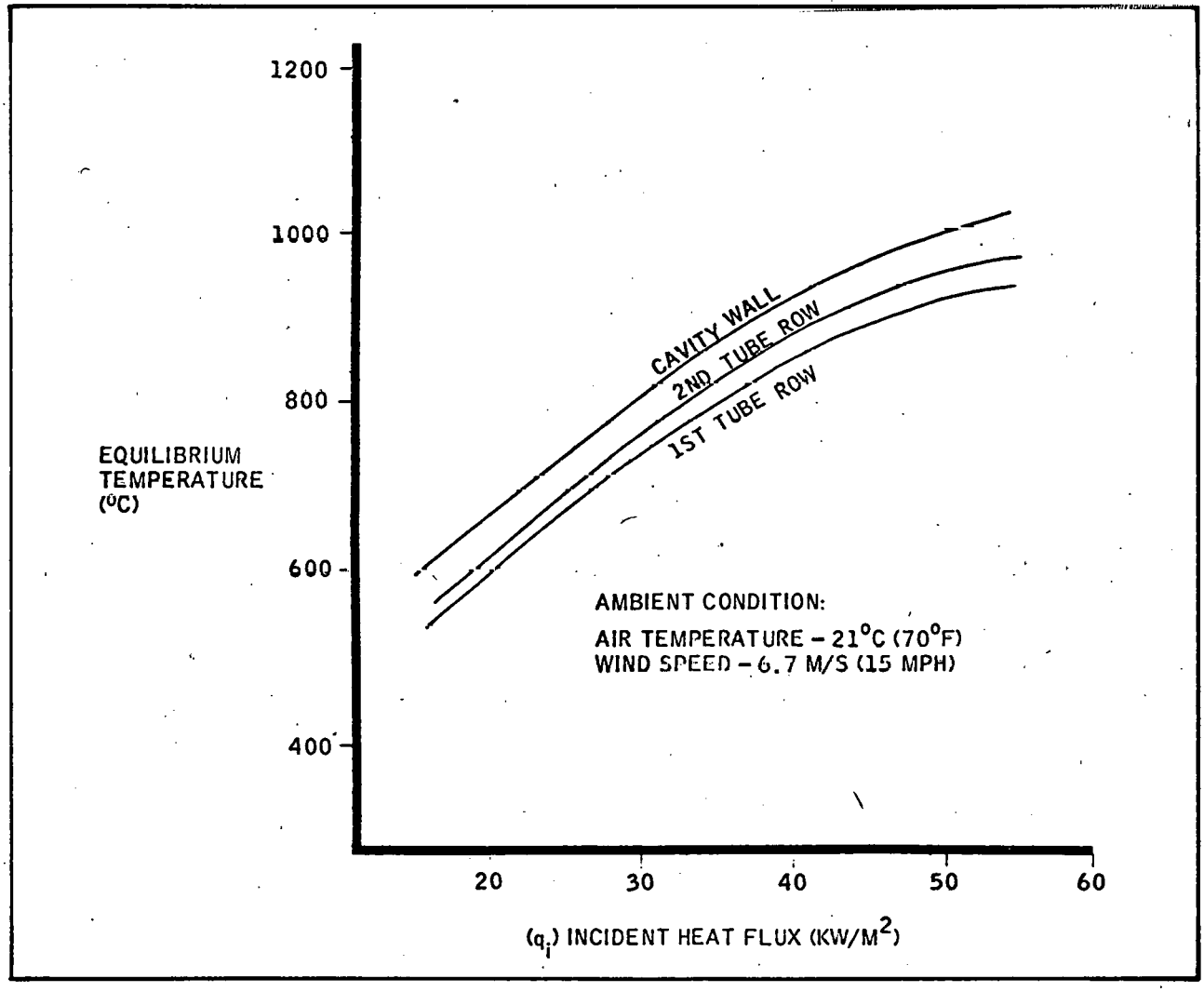

Figure 4-13 RECEIVER CAVITY EQUILIBRIUM TEMPERATURE DISTRIBUTION AS A FUNCTION OF INCIDENT HEAT FLUX

The model was used to examine conditions at zero steam flow and a threshold incident flux of 6.6 kw/m^2 (2,000 Btu/hr. ft.^{2}). The results are therefore at a flux level below operating conditions, but are indicative of the effect of applying a load on the receiver that is just sufficient to begin boiler warmup at the start of a day. The following equilibrium temperatures were estimated:

$t_{\text{1st Row (boiler)}}$ = 283°C (541° F)

$t_{\text{2nd Row (superheater)}}$ = 328°C (622° F)

t_{Cavity} = 360°C (680° F)

Note that the mean temperature of the superheater row is near the threshold required to begin production of steam for thermal storage.

Analysis of wind losses was also performed. Figures 4-14 and 4-15 show the results of the analysis. For example, a convection loss of 4 percent is estimated at an insolation of 32.9 kilowatts per square meter (10,000 Btu/hr-ft^2) and a 4 meter per second (13 ft/sec) wind speed (50-percentile wind; see Section 3.0, reference 1). The loss increases to 14 percent for a 99-percentile wind of 14 meters per second (46 ft/sec).

The model was used to examine the performance of the receiver using a fixed tube pitch of 3:1. Incident flux and wind velocity were parameters. Model outputs are shown in Figures 4-16 and 4-17. At an incident flux of 26.9 kw/m^2, corresponding to 1400 winter solstice, estimated receiver efficiency is 0.72 at zero wind.

The model was used for a more rigorous analysis of wind losses, using better assumptions for estimation of hot-side approach ΔT. The analysis confirmed the estimates for convection losses, which are illustrated in Figure 4-18 for an 8.9 meter per second (20 mile per hour) wind. Useful steam is obtained at a threshold of 7.9 kilowatts per square meter (2,500 Btu/hr-ft^2) flux at the receiver aperture (q_i). At 26.9 kilowatts per square meter (8,500 Btu/hr-ft^2) rated steam at 510° C (950° F) is available for operation of the turbine.

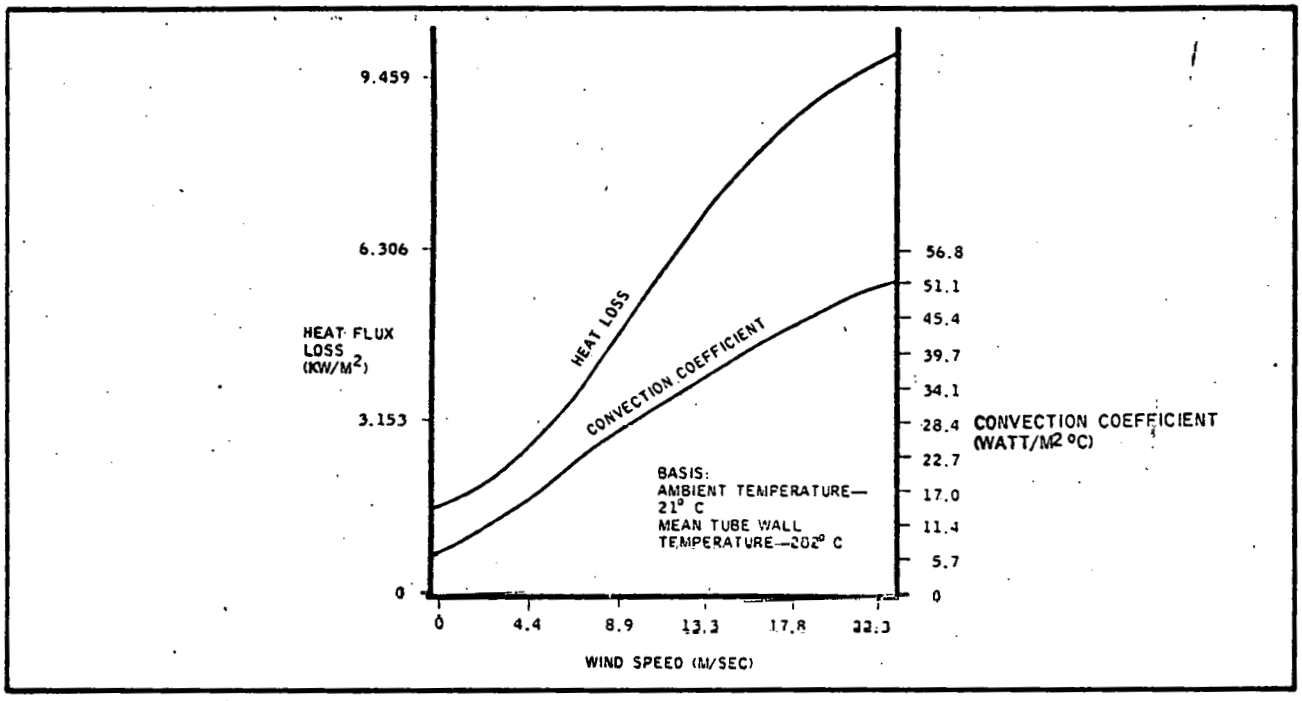

Figure 4-14 WIND LOSSES FROM RECEIVER AND CONVECTION COEFFICIENT VERSUS WIND SPEED

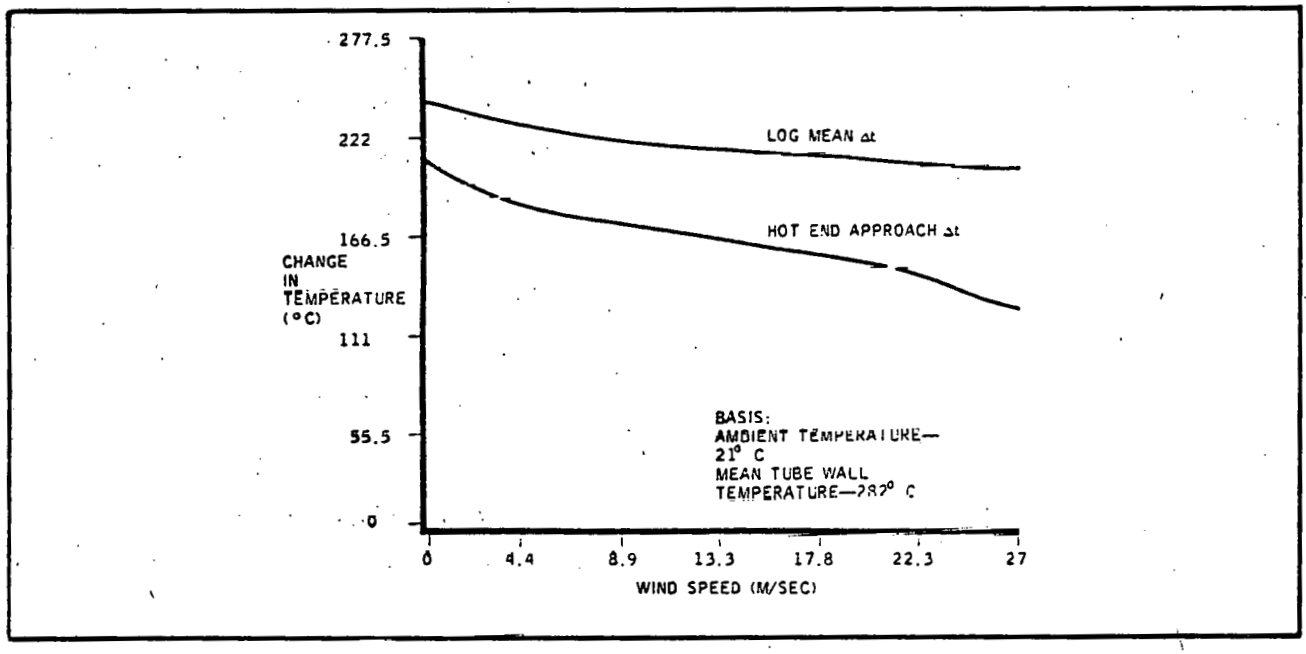

Figure 4-15 TEMPERATURE DIFFERENCES ACROSS BOUNDARY LAYER FILM FOR CALCULATION OF RECEIVER WIND LOSSES

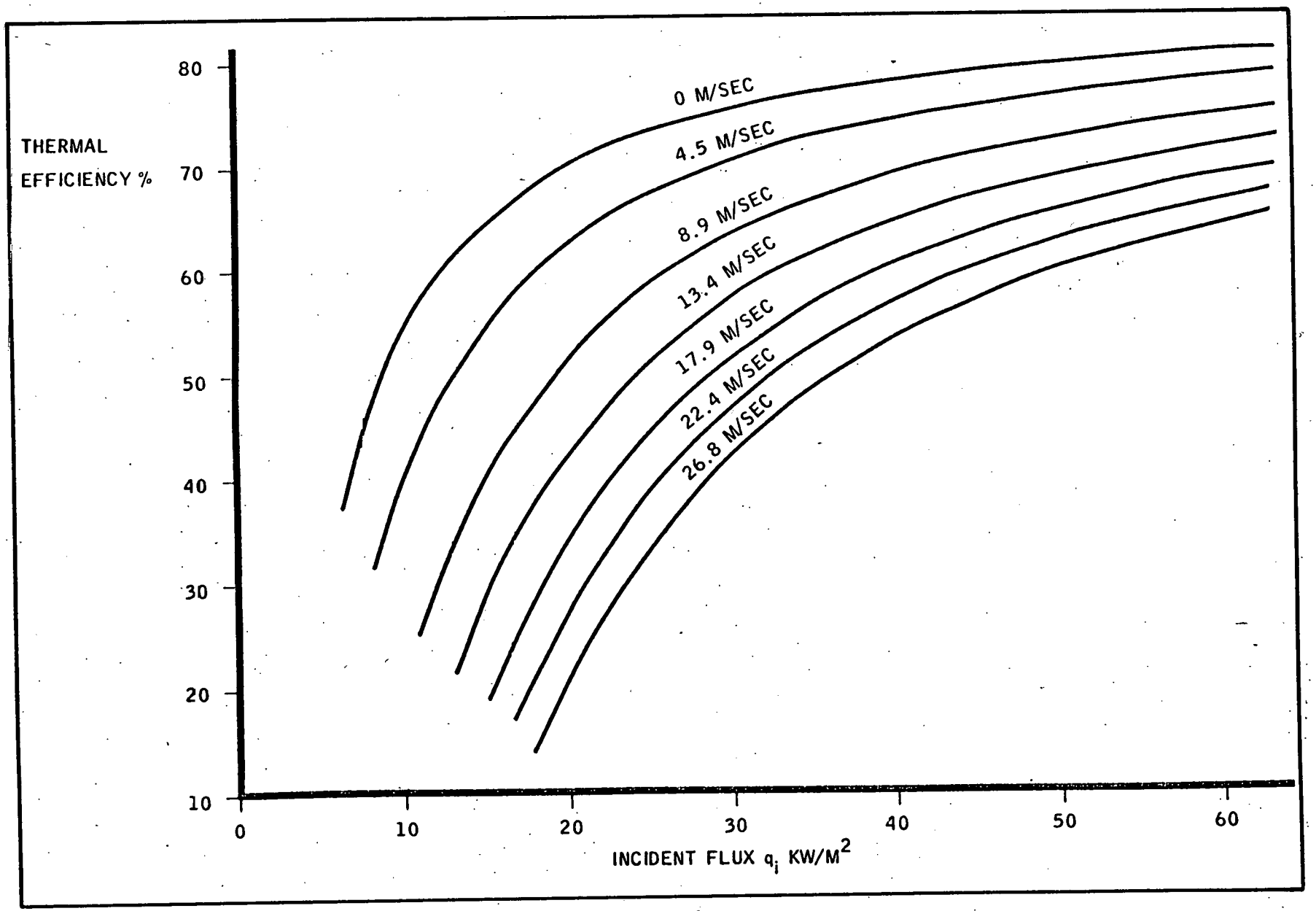

Figure 4-16 EFFECT OF WIND SPEED ON BOILER EFFICIENCY

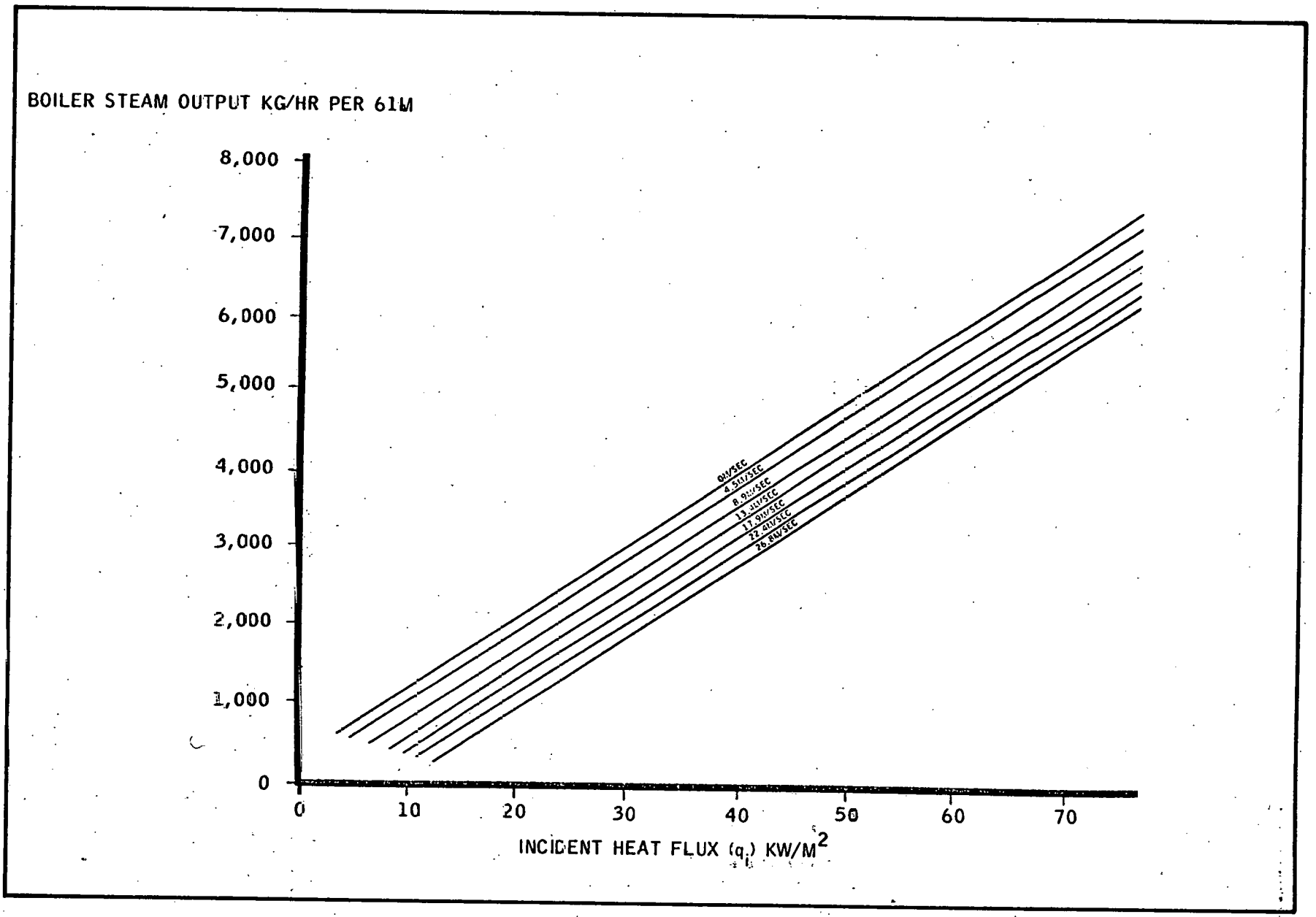

Figure 4-17 EFFECT OF WIND SPEED ON BOILER OUTPUT

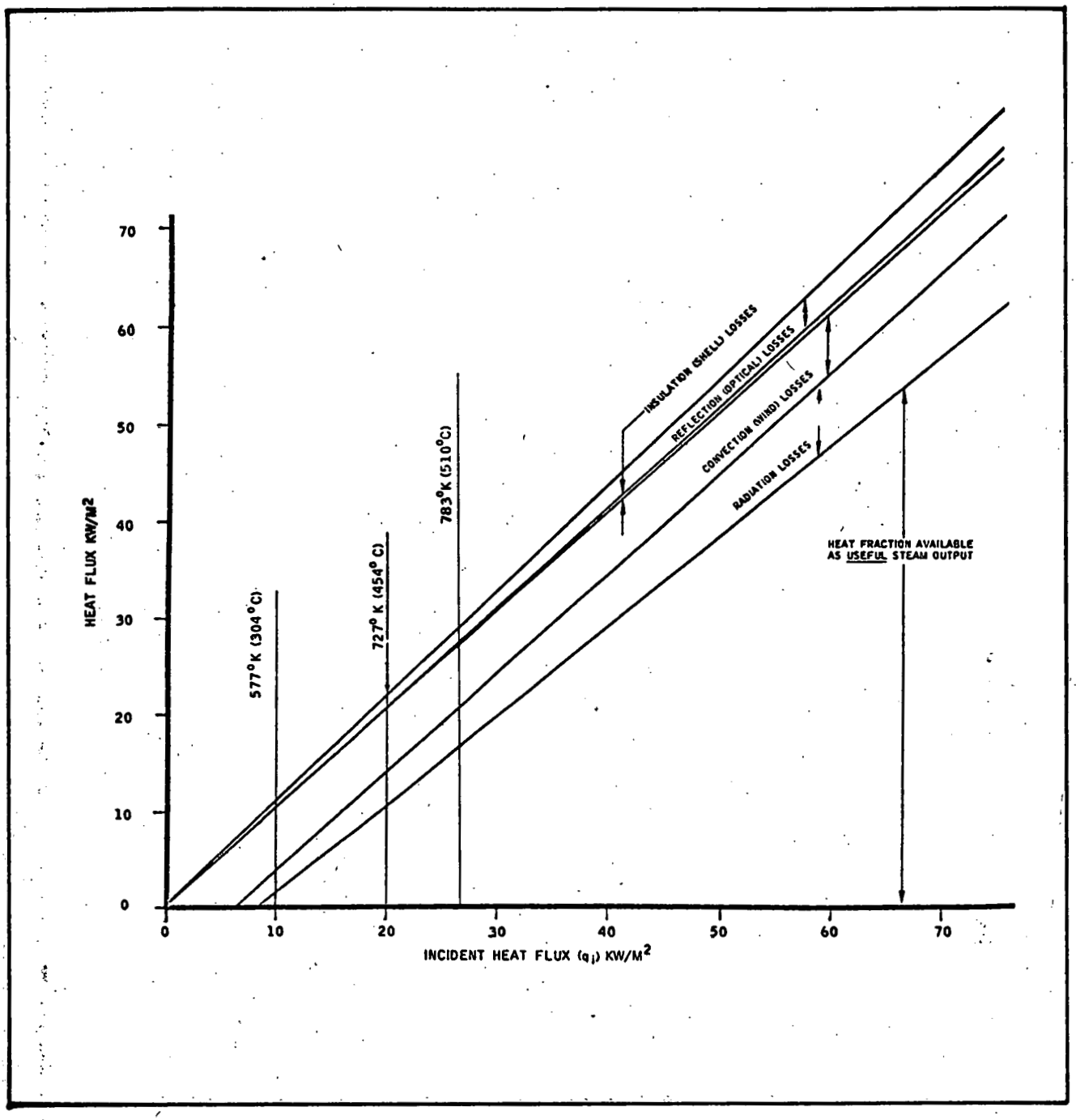

Figure 4-18 THERMAL LOSSES IN NATURAL CONVECTION RECEIVER (20 MPH WIND SPEED)

4.3 COMPARATIVE ASSESSMENT

Both receiver concepts involve benefits and potential limitations which must be explored through further analytical and experimental evaluation before a final choice of concept can be made. The major benefits and limitations are presented in this section.

4.3.1 Performance

Analysis work to date has established that both concepts are feasible for production of rated steam at the conditions required by the baseline EPGS from the energy input by the collector field.

Thermal efficiency of the once-through concept is, on average, 5 percent higher than that of the natural convection concept. This higher efficiency results from lower reflection and re-radiation losses in the once-through concept because the tubes reside around the inner wall of the receiver cavity and therefore have a higher view factor with respect to each other.

Convection loss due to ambient wind is a potential problem for both concepts because the receiver is an open cavity. Figure 4-14 in Section 4.2.2 shows estimated convection loss for the natural convection concept as a function of wind velocity. Applying the wind conditions specified for point focus systems (1) yields an expected loss of 4 percent for a normally incident wind (wind velocity vector normal to aperture plane).

The magnitude of the convection loss is a function of the orientation of the wind vector with respect to the aperture plane. Both concepts are probably most vulnerable to a normally incident wind, but the relative vulnerability has not been explored. Further analysis of the effect of wind is required.

One important point to be noted is that both concepts, being enclosed, will exhibit lower vulnerability than the point focus baseline receiver and distributed line focus systems with transparent cavities, both of which are exposed to all orientations of wind.

4.3.2 Cost

It is estimated that the cost of the once-through concept will be lower than that of the natural convection concept because of simpler design and less material per unit heat transfer area. Cost estimates of both concepts were made for the economic evaluations performed in the Central Receiver Research Study. The total cost per installed length of receiver (less support structure) for the once-through concept is estimated to be 13 percent less than for the natural convection concept. This difference is one of the principal reasons that the once-through concept is the initial selection for the 100 MWe plant.

4.3.3 State of the Art

The natural convection concept is based on standard and well-proven design practice. Similar designs have been in commercial use for more than 30 years, and there is extensive evidence in the literature to verify the thermal performance and stability from all types of process heat input.

The once-through concept is not as well proven in commercial operation, but is state-of-the-art technology. Indeed, the selection of a once-through point focus receiver for the 10-MWe Barstow pilot plant demonstrates this point because one of the requirements of plant design was the use of state-of-the-art technology.

One reason that once-through designs are less favored for steam generation application is the relatively high potential for tube burnout due to flow instability and/or flow reduction from scaling. This has been a problem in commercial systems for tube sizes and flow rates comparable to those of the once-through concept in which incident flux intensities reach 98 to 164 kilowatts per square meter (30,000 to 50,000 Btu/hr-ft^2) (2). Because the maximum incident flux from a noon equinox field is about 43 kilowatts per square meter (13,100 Btu/hr-ft^2), tube burnout should not pose a problem.

THIS PAGE

WAS INTENTIONALLY

LEFT BLANK

5.0 CONTROLS

Because the solar electric plant concept uses sunlight collected by the heliostat fields to supply energy to the receiver boilers, the sun/heliostat/receiver relationship is the key to the control of plant output. Additional environmental factors -- wind, clouds, etc., -- also influence performance. Despite the complex parametric interrelationships, the primary controllable factors of plant output are mirror field elevation angle and focusing.

5.1 PLANT CONTROL CONCEPT

Figure 5-1 illustrates the proposed control system configuration for the solar power generating plant. Table 5-1 illustrates the general operating modes. As can be noted, all the data is channeled to and all commands are generated from the central computer. A steam output requested by the power plant computer is translated to heliostat commands by the central computer. Command actions are verified by monitoring receiver boiler performance and off-axis sensors. Sun angle perturbations and local environmental conditions are monitored to make corrections.

The components of the control system are treated in subsequent paragraphs.

5.1.1 Central Computer

As can be seen from Figure 5-2, the central computer is the key processing element in the entire control system. Responding to steam output requests from the power plant computer, the central computer translates these requests to specific heliostat operation and observes the effect of its control response by monitoring receiver performance and the off-axis sensors. The central computer also stores significant performance data for future retrieval and analysis. It also supports the heliostat operator interface for displaying performance data and providing a means of entry for operator intervention.

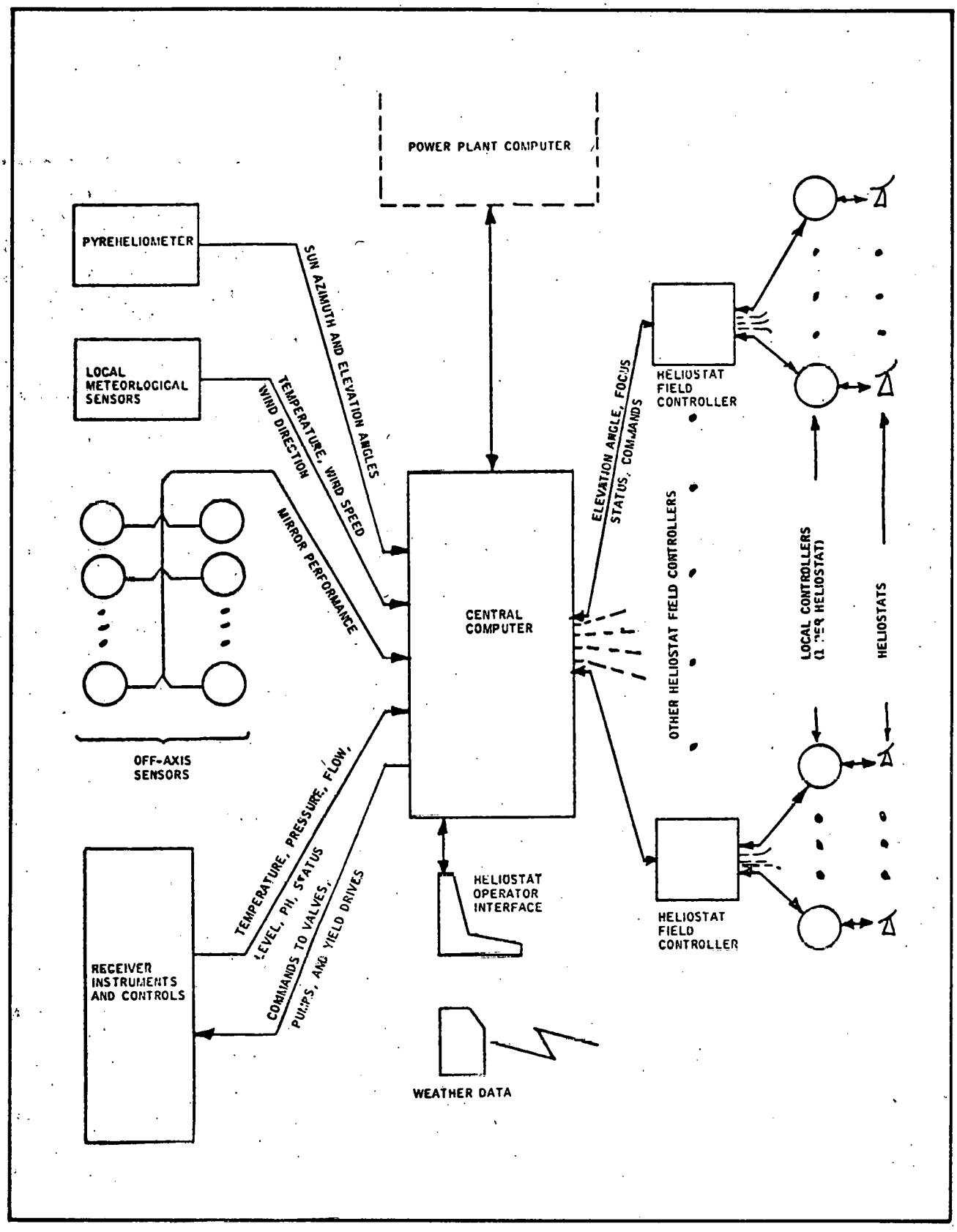

Figure 5-1 FUNCTIONAL BLOCK DIAGRAM — CONTROL SUBSYSTEM

Table 5-1 CENTRAL RECEIVER SOLAR POWER PLANT OPERATING MODES

STARTUP	Before sunrise, the heliostats are destowed (see Table 5-2) and brought into tracking position and focused. The receiver eyelids are then opened, and feedwater levels and rates are brought into compliance.
START-OF-DAY CALIBRATION	As soon as practicable during early light, each heliostat in turn is operated in the nutating mode (see Table 5-2). Through off-axis sensor feedback, corrections to the heliostat elevation and focus tracking systems are made and verified. Before and after calibration, the heliostats are operated in the run mode.
RUN	The central computer sends continuous updating information on elevation angle and focus. This data is based on the day's ephemeris data stored in memory and corrected for solar aberration by pyrheliometer data. During periods of cloud obscuration, the most recently corrected ephemeris data will be used. The power plant computer will request a steam demand which will be translated to heliostat operation by the central computer. Increase or decrease in energy required for all or portions of the boiler will be met by adjusting the focus of appropriate heliostats. For mirror images wandering outside the aperture boundaries, as determined by the off-axis sensors, attempts will be made to bring them into compliance. Failure of these corrective attempts will initiate an emergency defocus and stowing action of the malfunctioning heliostat.
RE-CALIBRATION	If a trend toward a heliostat malfunction is detected by the central computer, a recalibration of any heliostat can be commanded using the same procedure as the start-of-day calibration mode.
EMERGENCY	In the event of sudden storm conditions or plant malfunction, all or any portion of the heliostat fields can be commanded by the central computer to go into a defocus and stow mode. The eyelids on the receiver would also close. The central computer, however, would continue to operate — updating its ephemeris data so that a restart would be possible.
RESTART	In the event that plant operation has been interrupted by an emergency mode command, operation can be restarted by following the same procedure as startup and start-of-day calibration modes.
HELIOSTAT SHUTDOWN	At the end of the operating day, the heliostat fields will be gradually defocused and stowed in a defined program as the collected solar energy loses its efficacy. The eyelids over the unimaged portion of the receiver will be closed to retain residual energy; this also minimizes losses during the night.
MAINTENANCE	After shutdown or during plant operation, routine or emergency maintenance will be performed. Service personnel will have direct manual control over the stow drive of any heliostat at its local controller cabinet. Field controller and central computer commands will be disabled during this mode.

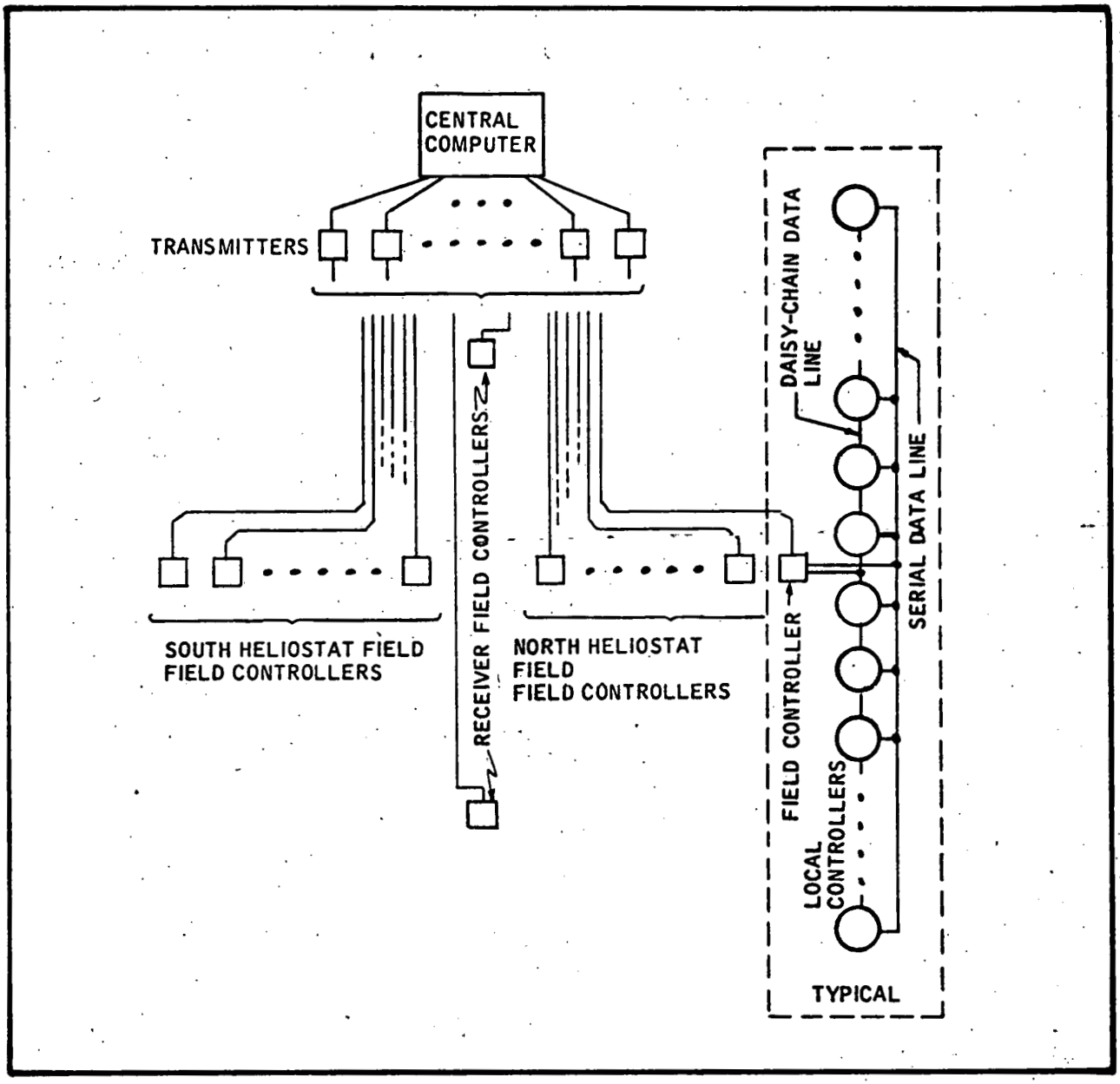

Figure 5-2 DATA MULTIPLEXING CONFIGURATION

The computing task required of the central computer is not very complex. Solar ephemeris data stored in the memory is translated to heliostat elevation angles and focus through simple geometric relationships. The data updating time requirements are not severe. It would also be necessary for the computer to operate in a real-time mode.

The requirements thus outlined can be easily satisfied by a minicomputer such as a Digital Equipment Corporation PDP-11. A typical configuration would include a real-time operating system, dual disk drives, inputs and outputs, and support for video terminals for operator interface.

It would at first appear that the data input/output requirements would be prohibitive considering the large amount of field equipment. However, analysis shows that significant reduction in the amount of data handling can be achieved by treating devices in groups and by transmitting incremental position data.

Field devices can be grouped together according to data handling. For example, considering the geometry of the heliostat field, each east-west heliostat row has the same elevation angle and focus requirement. All that would thus be necessary is to transmit that row's elevation and focus reference data to a receiver and, from there, to each local heliostat controller in a daisy-chain fashion. Control of incident energy at the receivers is accomplished by defocusing groups of mirrors. Receiver monitoring and control can be similarly treated. There are, however, occasions when local conditions will necessitate a correction for an individual field device. Provision will be made for address and control of the individual devices.

Transmitting absolute position data results in a restrictively large data rate -- even with device grouping. However, considering that the only requirement is for the incremental position reference to which a local controller can respond, the data volume (and hence rate) is substantially reduced. Heliostat elevation and focus commands are easily adjustable to incremental position commands.

The data handling methodologies described above suggest a multiplexing configuration, such as that shown in Figure 5-2. Section 6.0 contains a typical configuration for a 100 MWe plant sizing. A more detailed analysis beyond the scope of this project, is required to determine the exact sizing of components.

As illustrated in Figure 5-2, field device commands will be sent from the central computer input/output port to a transmitter and thence to a field controller via a twisted shielded pair. The field controller, in turn, sends the command through a parallel daisy-chain line operating through the local controllers. A serial data line can address local controllers individually for specific corrective data or for monitoring individual performance. This latter mode can present an indication of signal and/or line integrity by checking whether a particular local controller has received the signal. The checked controller can then be varied during subsequent command cycles.

5.1.2 Field Controllers

Interposed between the central computer and the local controllers, the field controller serves as the signal conditioning link. Data from the transmitter (see Figure 5-2) is converted to a parallel data line (the daisy chain) and a serial data line.

The equipment itself would be mounted in the field in an enclosure at a position to minimize line runs. Lines running to and from the controller would use direct burial, twisted shielded pairs. Several commercial systems are available which can be used (such as that made by Larse Corporation), and no severe requirements are anticipated which would preclude their use.

5.1.3 Heliostat Local Controller

The control will take reference and command signals from the heliostat field controllers and translate them into motor commands for the elevation drive and two focus drives. A local subloop control will exist for these drives through the use of encoders feeding back to the local controller. The local controller will then drive the motors to cause a zero difference between the reference and encoder signals. Section 5.2 contains a detailed description of the heliostat control concept.

5.1.4 Sun Angle Tracking

A sun tracker mounted in the field will transmit solar azimuth and elevation angular data to the central computer. These data will be used to correct the ephemeris angular data in the computer memory for local atmospheric

conditions. During periods of cloud obscuration, the most recent corrected ephemeris data will be used until the solar image is again captured by the sun tracker.

5.1.5 Meterological Data

At least two anemometers (ground and tower) and several temperature sensors will transmit local meteorlogical data to the central computer. Wind velocity, direction, and temperature cause deflections in mirror structures. Data on these parameters can be used to correct for these deflections. The heliostat operator will also have access to U.S. Weather Bureau reports of the area so that appropriate action can be taken in advance of an approaching storm.

5.1.6 Off-Axis Sensor

Sensors are required above and below the receiver aperture to detect when the solar image from one or more mirrors is within the opening. A scanning video-type sensor system can be employed to exactly identify the mirror(s) which have an off-axis image. The time of day an image is noted by a sensor can determine the mirror's azimuth with relation to the sensor (through the sun's azimuth at that time). The raster line at occurrence gives a determination of the exact mirror location. By spacing the sensors at regular intervals along the receiver, failure of any one sensor would not allow a malfunctioning mirror to exceed control limits.

The off-axis sensors would operate in one of two modes (see Table 5-2). During the run mode operation, the sensors would operate in the alarm monitoring mode. The calibration mode would be used on start-of-day calibration and recalibration during the day.

Table 5-2 OFF-AXIS SENSOR — OPERATING MODES

ALARM MONITORING	The central computer scans an alarm status output of each off-axis sensor. The sensor's control analyzes intensity/position data to determine the presence of an off-axis image. Upon such determination, it puts a bit on the alarm output. The central computer detects this bit, addresses the sensor, and interrogates the sensor control as to the position of the alarm. With this information, the central computer can determine which mirror has malfunctioned and command appropriate action.
CALIBRATION	The central computer enables the off-axis sensors to view the image of a particular mirror operating in the nutating mode. Intensity and position data is sent from these off-axis sensors to the central computer.

Several concepts for off-axis sensor configurations were evolved. The most promising concept consists of an electro-optic detection device (camera), a hard-wired analog signal conditioner with digital conversion, a data processor for evaluation correlation, and two-way communication with the master control computer. A sensor is mounted on each receiver section to view the portion of the heliostat field illuminating that receiver segment. For an East/West field axis, the camera sweeps at an angle, ψ, relative to the receiver normal, where

$$\psi = \tan^{-1} (\sin(\text{solar azimuth angle})/(\tan(\text{solar elevation angle}))$$

Each sensor sweeps the field under program control. An improperly aimed or focused heliostat is detected at the sensor aperture as a specular flash at its image position. The control system identifies the row position and addresses the errant heliostat on a priority basis to correct the alignment or disable (defocus and stow) the heliostat.

Focal line intensity profiles at representative positions along the heliostat lengths can be obtained by a program which directs each heliostat to sweep across the sensor aperture. The analog signals from the sensors are correlated with the angular mirror tracking information to obtain the central position and width (in angular units) of the focal line. If two dimensional image information is available, intensity profiles can be computed. The control computer can use the data to check for tracking accuracy, linearity, proper focus, and mirror uniformity.

The most promising camera concept is a video type employing a solid state charge coupled diode (ccd) array. The field is scanned at standard video rates and imaged on the ccd array. The silicon diodes have good optical response, overload recovery, and resistance to thermal damage. Self-scanned diode arrays are a positive alternative because less complicated driving circuitry is required, but at the expense of poorer sensitivity and dynamic range.

The optics requirements are not severe. A camera mounted on the receiver is capable of monitoring 73-meter (240 foot) lengths of the heliostat field with 65 degree viewing angle optics for depths of field from 61 to 183 meter (200 to 600 feet).

5.1.7 Receiver Instrumentation and Control

Despite the length and configuration, the receivers can utilize the same control strategy as applied to conventional steam generators. Response time, operating conditions, and control actions are such that individual receiver sections can be controlled on a local controller subloop basis. Only reference signals and subloop status signals need be transmitted between the central computer and the receiver.

The instrumentation and control equipment is commercially available, even with digital input and output capability. Subloops can be controlled either by microprocessors or by standard process control. The optimum configuration would be determined by equipment cost and cost of satisfying computer control requirements.

Basically, levels, flows, pressures, and temperatures are the measured variables for the boiler control. Additionally, the operation of the aperture eyelids must respond to computer command.

5.1.8 Power Distribution

A portion of the power plant output is required to provide power for the mirror drives, receiver equipment, area lighting, etc. Figure 5-3 represents a typical configuration for the auxiliary power distribution. Such a configuration would provide for redundancy, overload protection, and circuit isolation. Power would be distributed at high voltage (4,160 volts) and decreased to 240 or 480 volts for the use points.

As shown in Figure 5-4, the high-voltage lines for the mirror field and lighting would be axially suspended from bracket arms affixed to the sides of the towers. Substations of 100 kva tapping the lines at appropriate points would decrease the voltage to 120 to 240 volts for distribution to the mirror controls. Direct-burial cable would be used for these connections. A similar arrangement would be used for the lighting circuits.

For the receiver, a high-voltage line would be suspended beneath the boiler catwalk. Stepdown transformers would be mounted at appropriate locations to power various boiler apparatus, instrumentation, and eyelid machinery.

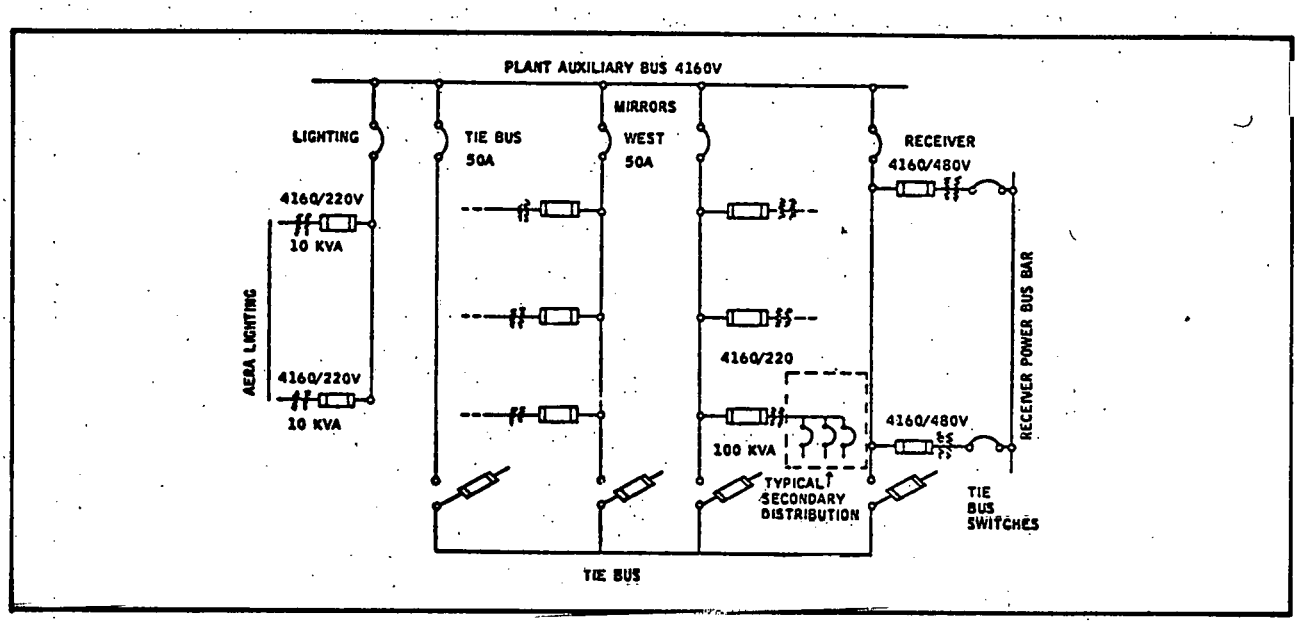

Figure 5-3 ONE-LINE DIAGRAM — PROPOSED FIELD EQUIPMENT POWER DISTRIBUTION

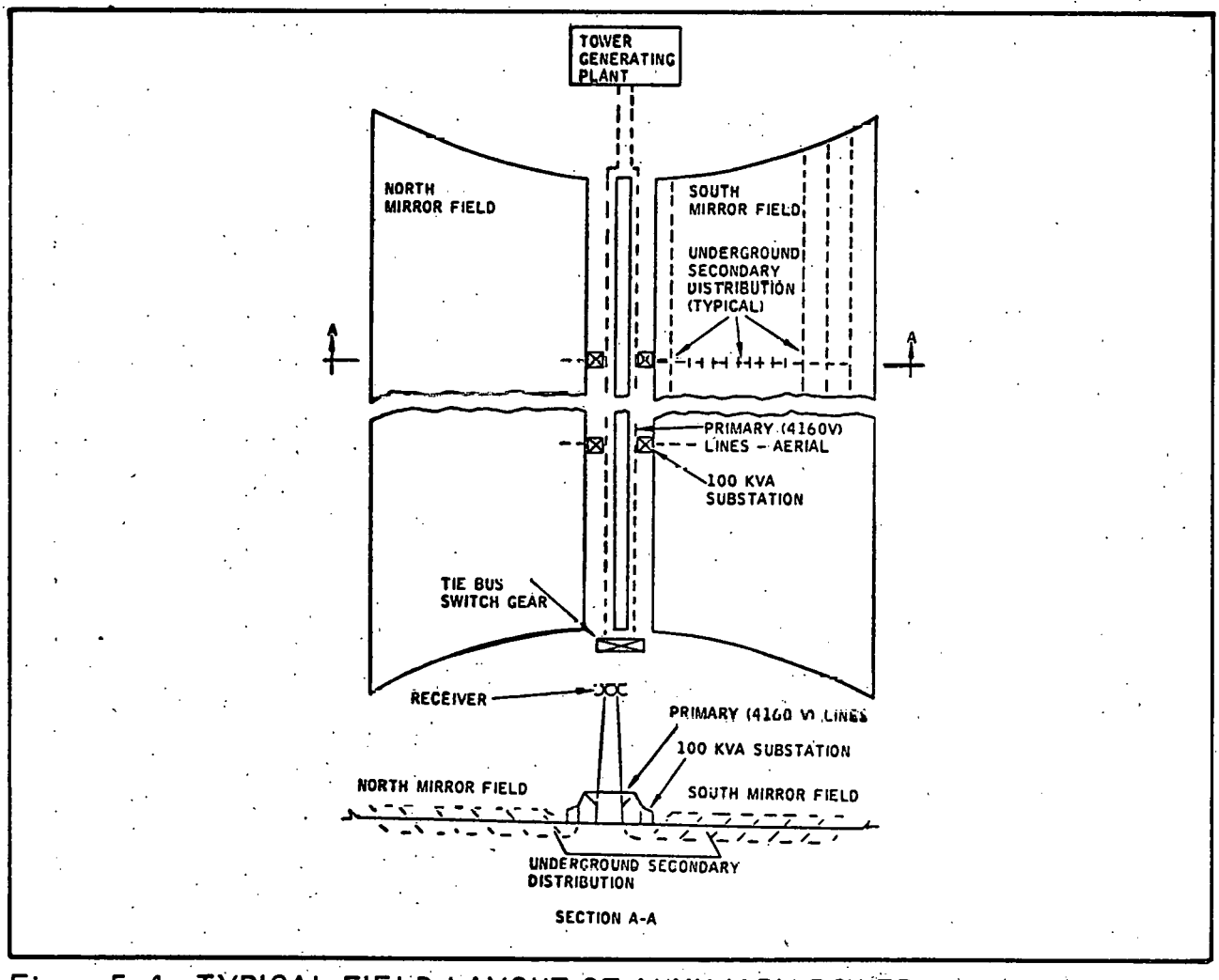

Figure 5-4 TYPICAL FIELD LAYOUT OF AUXILIARY POWER DISTRIBUTION

A tie feeder could probably be routed underground to a tie bus switching cabinet, allowing for at least partial plant operation in the event of a feeder or main breaker malfunction.

5.2 HELIOSTAT CONTROL

5.2.1 Requirements

Elevation and focus control of a heliostat were examined in detail, based on an optimum receiver aperture of 1.22 meters (4 feet) and total control error of 2 milliradian for both elevation control and focus control. These accuracies can be obtained from commercially available control components. Central control requirements are summarized in Tables 5-3 and 5-4.

Table 5-3 HELIOSTAT ELEVATION DRIVE SYSTEM REQUIREMENTS

Item	Requirement
Accuracy	
Main Gear Backlash	1 mrad (3.4 arc min)
Servo System	1 mrad (3.4 arc min)
Total (worst case)	2 mrad (6.8 arc min)
Servo Error	0.1 mrad (21 arc sec)
Speeds	
Tracking (max)	0.048 mrad/s (10 deg/hr)
Slewing (max)	26.2 mrad/s (0.25 rpm)
Travel Limits	
Tracking	1.57 rad (90 deg)
Slewing	3.14 rad (180 deg)
Encoder Resolution	2^{14} = 16,384 bits for 90 deg
Data Update	New elevation information from main computer every 2 sec
Loads	
Inertia	1,000 in-lbs
Roller Friction	24,000 in-lbs
Wind (max)	33,000 in-lbs

Table 5-4 HELIOSTAT FOCUS DRIVE SYSTEM REQUIREMENTS

Item	Requirement
Accuracy	
Drive System	1 mrad (3.4 arc sec)
Mirror irregularities	1 mrad (3.4 arc sec)
Total (worst case)	2 mrad (6.8 arc sec)
Mirror Chord Limits	At 0 m. 14 to 18 mm (0.55 to 0.71 in) At 150 m. 2 mm to 7 mm (0.08 to 0.28 inch)
Mirror Chord Accuracy	0.25 mm (0.01 in)
Servo Error	0.025 mm (0.001 in)
Focus Speed (max)	0.64 mm/hr (0.025 in/hr)
Data Update	New focus information from main computer every 143 sec

The elevation control, shown in Figure 5-5, provides the accuracy requirements and is cost effective. It is a direct gear drive with a 200-step-per-revolution, bidirectional, DC stepping motor used for tracking and jitter and an induction motor for stowing. A clutch would connect the stepper drive to the input shaft of the gearbox. This clutch would be engaged during tracking and jitter, and disengaged during slewing. The torque required for the slew motor armature (de-energized) is insignificant when compared to the load torque so it can be driven during the low-speed modes. During slewing, the stepper drive would have to be disconnected to prevent overspeed damage. By tying both drives at each end of a double-ended gearbox input shaft in this manner, a component saving is realized.

The gearbox for the elevation control is the primary error component due to backlash. The control requirements were examined by engineers at the FMC Drive Division, whose principal product line is gear reducers. From this examination, it was concluded that the 1-milliradian backlash requirement is attainable in practice. A gear ration of 5,000:1 is required for proper tracking speed ratios and torque multiplication*. This requires a stepper drive rate of 8 steps per second during tracking mode, which is well within the speed-torque characteristics of the stepper motor. Also, the required slewing motor speed is 1,250 rpm, near a standard speed for AC induction motors.

* A commercial FMC gear box, modified to 4900:1 ratio was used in the experimental heliostat.

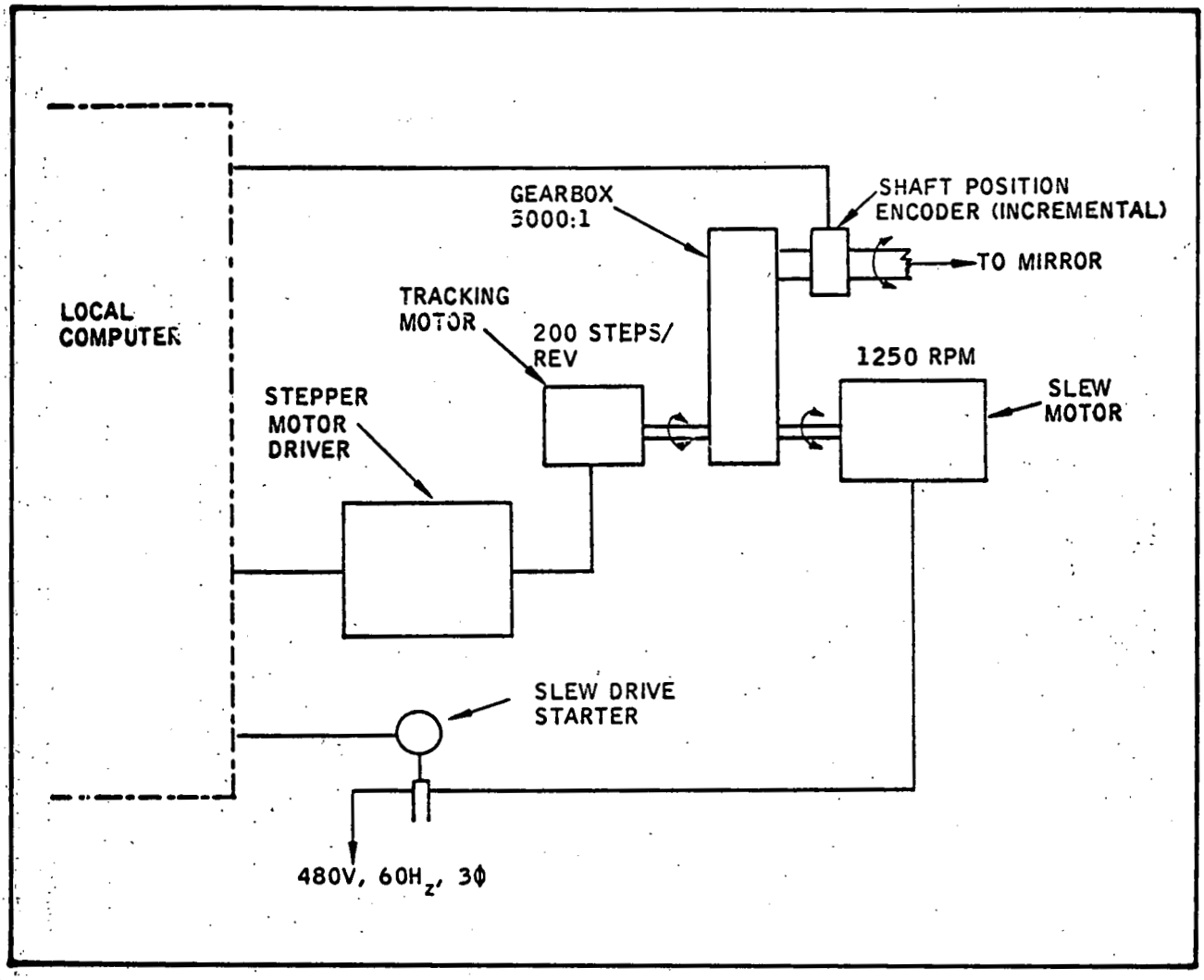

Figure 5-5 HELIOSTAT ELEVATION DRIVE SYSTEM

The encoder is tied directly to the mirror shaft. An incremental encoder was used for cost considerations. Because the full 2^{14} encoder bits are required for a 90-degree rotation, a timing belt drive is needed to provide the proper ratio. This requires memory capability in the microprocessor local controller to determine actual shaft angle, and a reference mark for the controller to establish a "zero degree" point.

It is necessary then, in the startup procedure to acquire this point. The point would be reacquired after any power or memory losses occurred. The configuration of Figure 5-6 was developed for the focus control as the most cost effective configuration to meet the requirements. Again a 200-step-per-revolution, DC stepper motor is used. The motor is connected to the ball

screw through a clutch. The ball screw is directly connected to the mirror focus bar linkage. In the event of a fail-safe signal or a power failure, the stepper motor clutch is disengaged and the ball-screw spring drives the mirrors to a convex position.

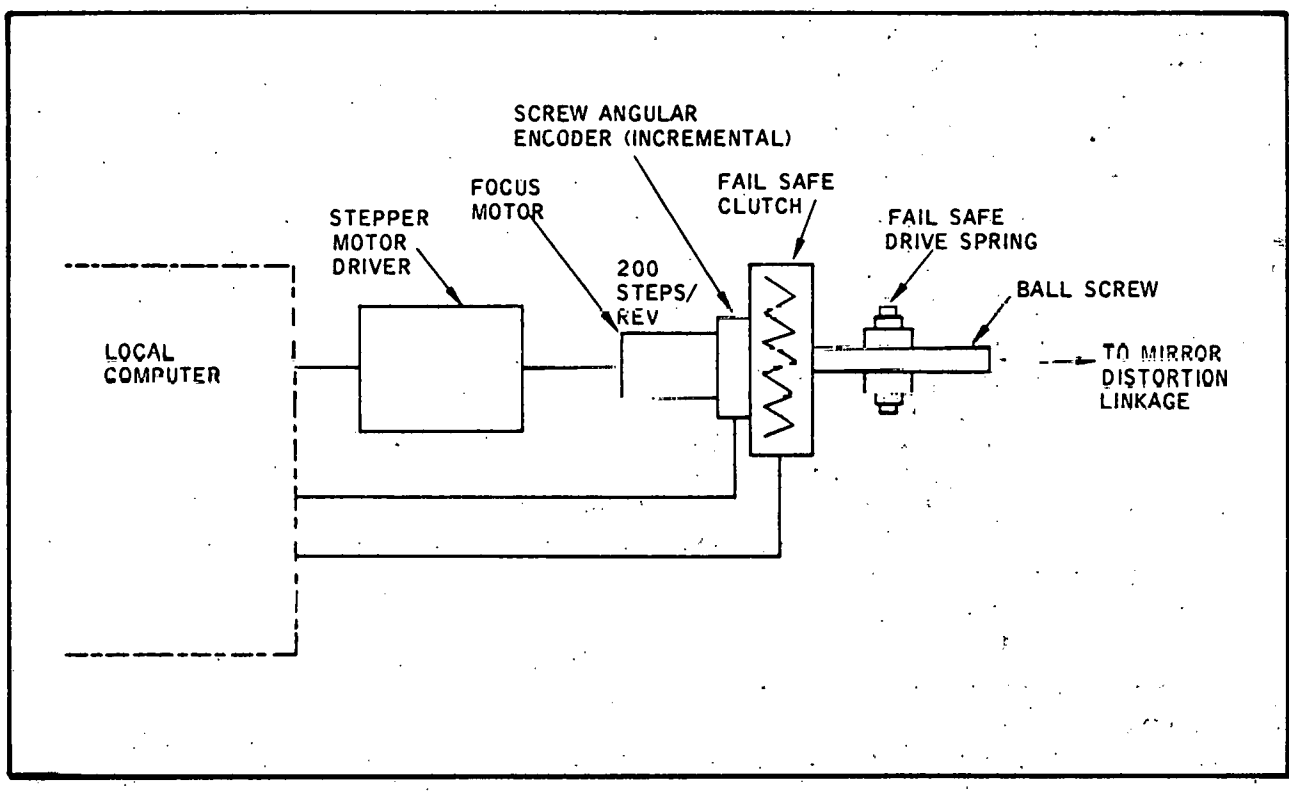

Figure 5-6 HELIOSTAT FOCUS DRIVE SYSTEM

5.2.2 Operating Modes

The operating modes to which the local controller must respond are shown in Tables 5-5 and 5-6 and in Figures 5-1, 5-2, and 5-7 through 5-11.

5.3 LOCAL CONTROLLER CONFIGURATION

At each heliostat, a local control translates commands sent from the central computer into aiming and focusing movements (Figure 5-12).

A microprocessor (4040) acts as a closed-subloop for control of aiming and focusing. The incremental aiming commands are converted to absolute angles and compared against the value generated by the elevation encoder. A finite number of step pulses based on the difference in values is sent to the elevation stepper by its translator. Focusing entails sending the incremental commands to each focus stepper.

Table 5-5 HELIOSTAT OPERATING MODES — ELEVATION

TRACKING	Mirror frame is moved to angular reference position by stepping motor. Reference position is determined by central computer and transmitted to local control (see Figure 5-7).
SLEWING	Mirror frame is moved toward angular reference position by stepping motor operating in high speed mode (10 times normal speed). Slewing will be determined by the local control (see Figure 5-7).
NUTATING	Mirror frame is moved at slewing speed about the angular reference position by the stepping motor. The excursion limits of the mirror in this mode is ±2 mrad about the angular reference position. Nutating will be requested by the central computer and interpreted by the local control (see Figure 5-8).
STOWING	Mirror frame is moved at 0.25 rpm by the stowing motor (stepping motor is declutched). The rotational direction chosen will always be with the direction of the wind. Stowing can be requested by the central computer or through an emergency defocusing action. Stowing limits will be set by limit switches. When in the stowed position, a pin will lock the frame in the position (see Figure 5-10).
MANUAL	Mirror frame is moved at 0.25 rpm by the stowing motor responding directly to a selector switch at the mirror site.
DESTOWING	Mirror frame is moved at stowing speed by stowing motor toward reference position until limit is passed. At this point, regular tracking/slewing mode is engaged (see Figure 5-11). In the event that the mirror does not destow in three attempts, an alarm will be sent to the central computer.

Table 5-6 HELIOSTAT OPERATING MODES — FOCUS

TRACKING	Mirror deforming apparatus is moved to reference position by stepping motor. Reference position is determined by central computer and transmitted to local control (see Figure 5-7).
SLEWING	Mirror deforming apparatus is moved toward reference position by stepping motor operating in high speed mode (10 times normal speed). Slewing will be determined by local control (see Figure 5-7).
DEFOCUSING	Mirror deforming apparatus is moved to convex position by spring. Clutch to stepping motor is disconnected. Defocusing will be requested by the central computer. Defocusing will automatically occur in the event of loss of power or loss of data from the local control (see Figure 5-9).

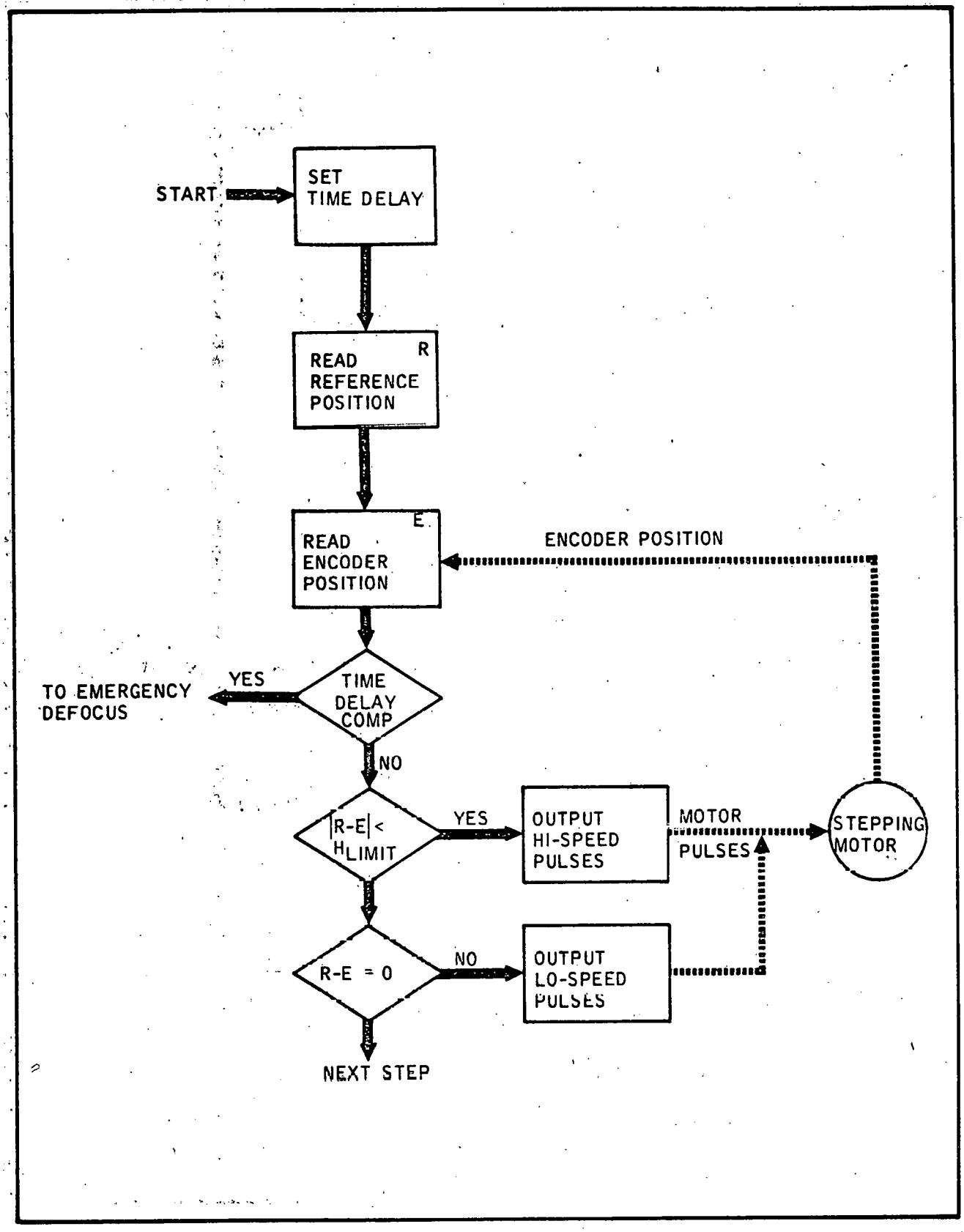

Figure 5-7 OPERATION SEQUENCE FOR TRACKING/SLEWING MODE (ELEVATION OR FOCUSING)

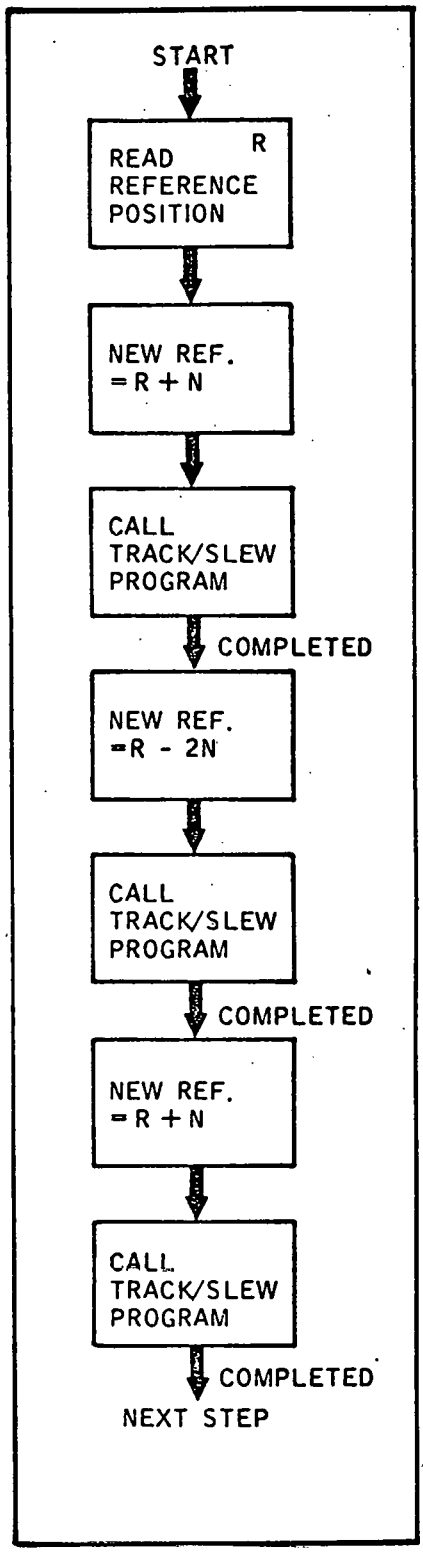

Figure 5-8 OPERATION SEQUENCE FOR ELEVATION NUTATING MODE

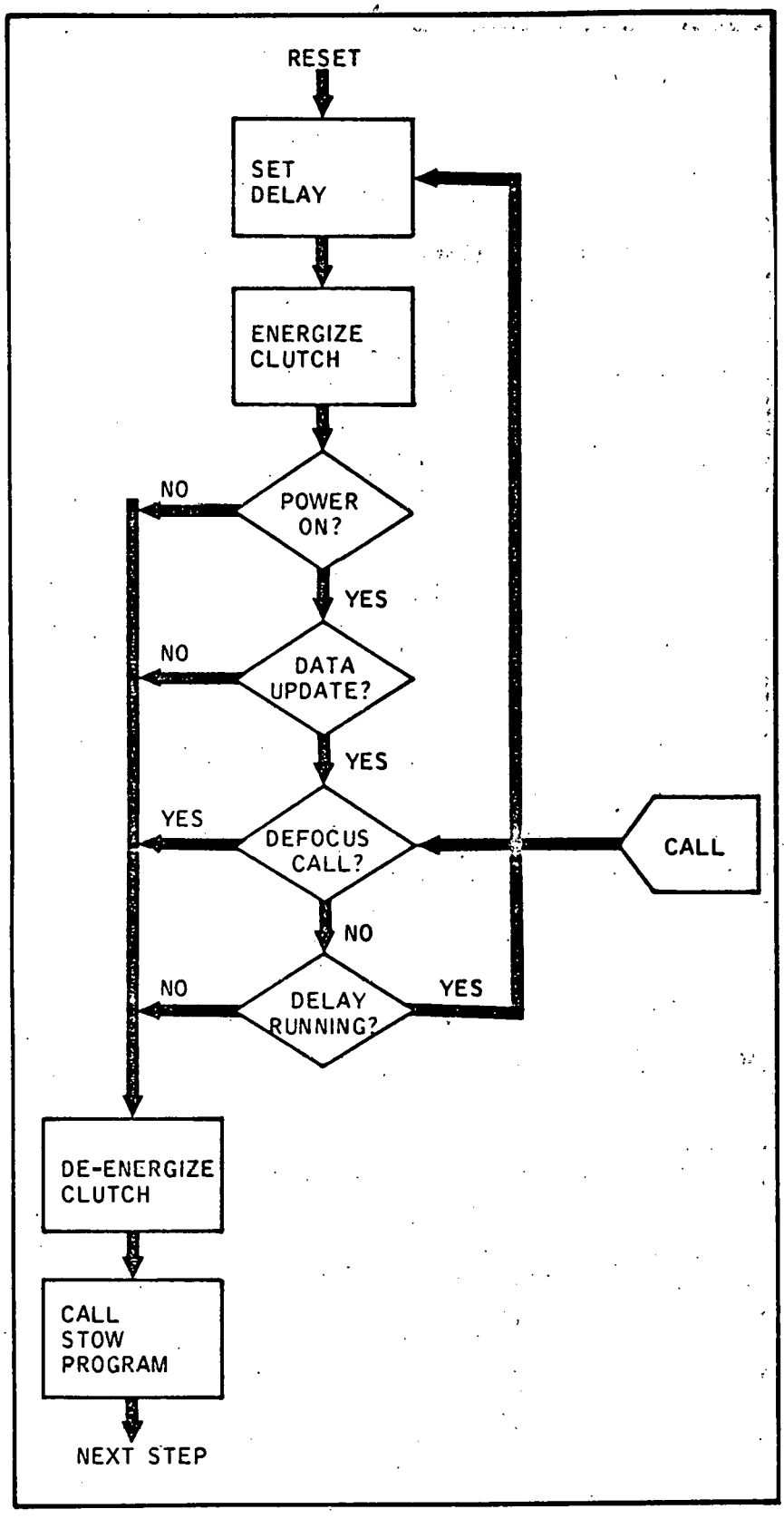

Figure 5-9 OPERATION SEQUENCE FOR FAIL-SAFE DEFOCUS

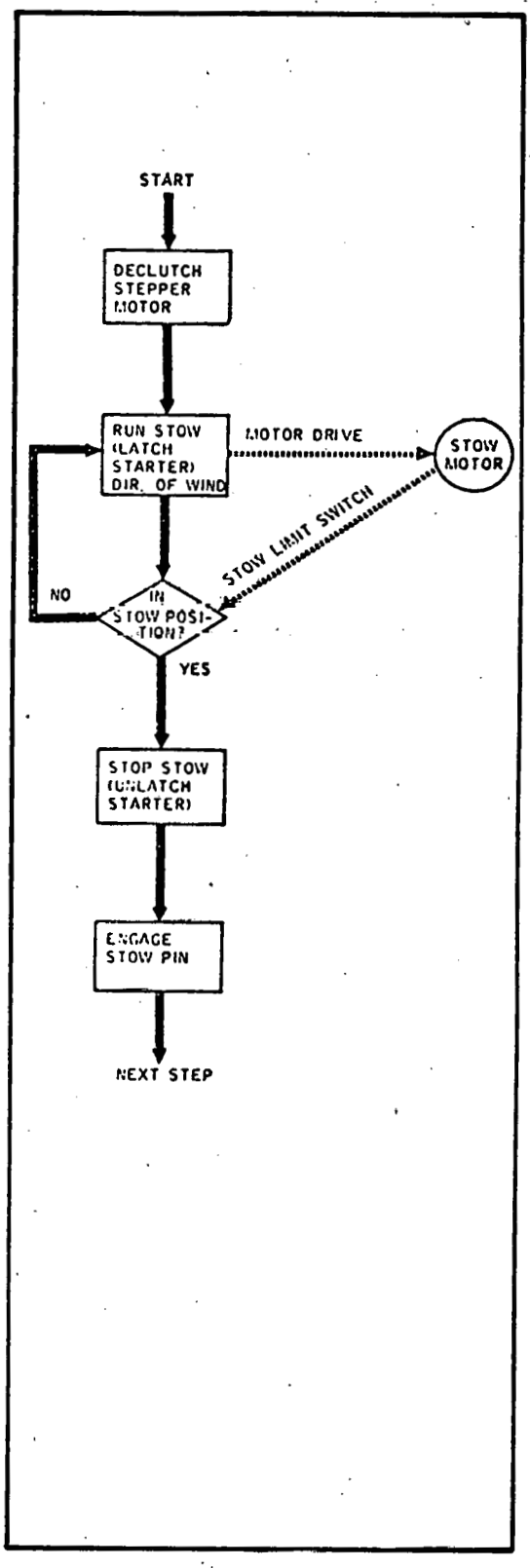

Figure 5-10 OPERATION SEQUENCE FOR ELEVATION STOWING MODE

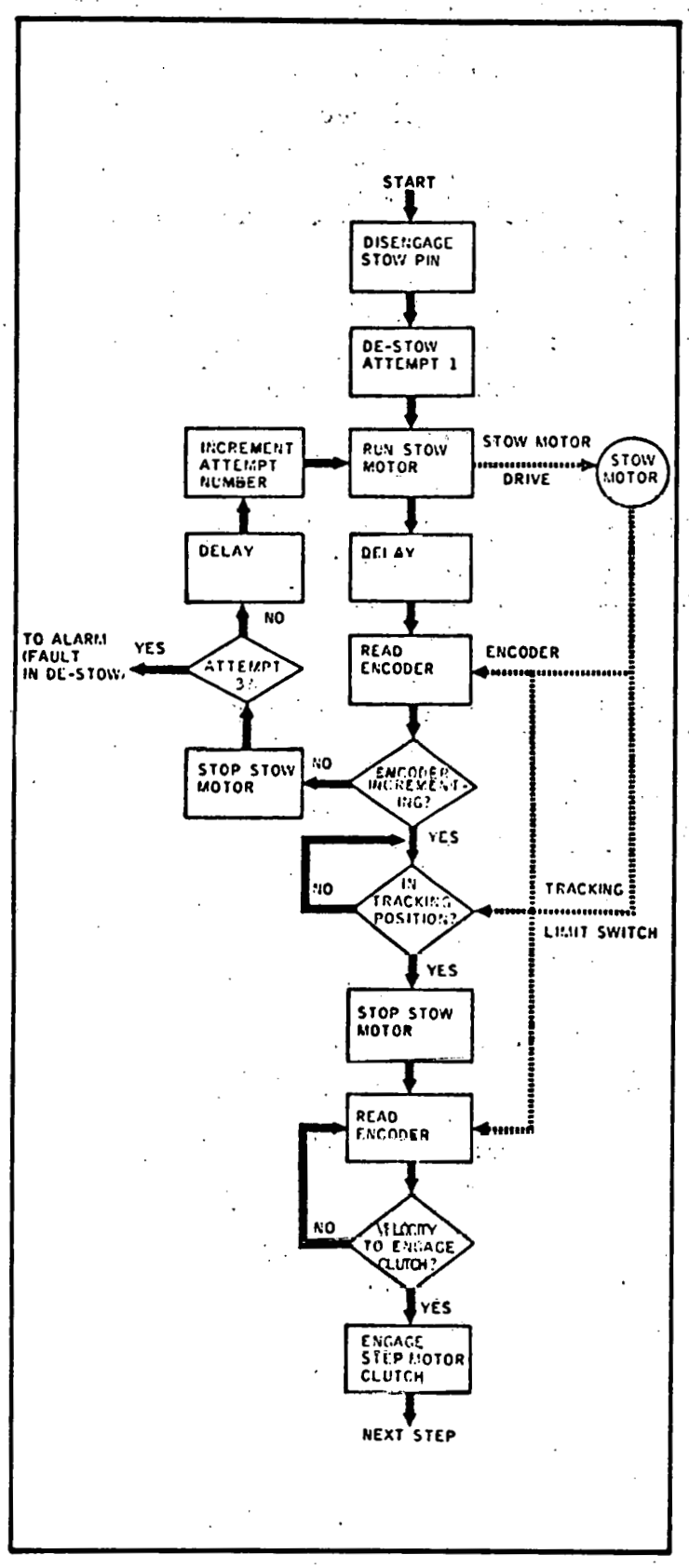

Figure 5-11 OPERATION SEQUENCE FOR ELEVATION DESTOW MODE

A watchdog timer is incorporated apart from the microprocessor so that in the event commands are not updated within a preset time, the heliostat is defocussed and stowed.

5.4 PROJECT DEVELOPMENT WORK

Development work during the project included fabrication of a heliostat local controller, development of computer programs to simulate operation of the central computer, and programming of the local controller for use in the planned heliostat field experiment. A DEC 11/03 computer was purchased to serve as the simulated central computer. Tables 5-7 through 5-11 summarize the program logic developed for the test computer and local controller.

Table 5-7 TEST COMPUTER/LOCAL CONTROLLER OPERATION

Step	Description	
1	Get sun angles and run in off-line program	
2	Create object tape from off-line program	
3	Load object tape into test computer	
4	Run (Set clock for correct time and date)	
	a. Start up mode	(0) Set starting time. (1) Command out of stow position every second. Maximum speed 100 steps per second. (2) Test every ten seconds for position. (3) Change from fast movement to stopping when within stepping motor takeover limits. (4) Step to starting position. (5) Omit zero steps until ready to start tracking. Print starting time.
	b. Tracking mode	(1) When starting time is reached, the system automatically starts tracking using table. Prints first line. (2) Automatic printout of mirror angle and focus (in number of steps) every six minutes.
	c. Slew test mode	(1) Print out starting position. (2) Increase angle by 2 mrad and print out position. (3) Decrease angle by 4 mrad of start and print out position. (4) Increase angle to angle of tracking and print out position. (5) Return to auto tracking mode.
	d. Inquire mode	(1) Test computer transmits inquiry code. (2) Local controller transmits angle position in absolute steps using 4 hexidecimal numbers (16 bits). (a) upper 4 bits (+30 hexidecimal) (b) next 4 bits (+30 hexidecimal) (c) next 4 bits (+30 hexidecimal) (d) lowest 4 bits (+30 hexidecimal) (3) Local controller transmits focus in absolute steps using 4 hexidecimal numbers.

Table 5-8 LOCAL CONTROLLER OPERATION

Step	Description
1	Must be able to receive and transmit at same time (Use a URART). Must be able to receive new data at least every second.
2	Must act on following commands:
	a. Inquiry (I) - Transmit absolute angle and action received commands focus. b. Address (A) - Receive commands and act on them. c. Stow (S) - Turn on or continue on stow motor all others off. d. Destow (D) - Turn on or continue destow motor all others off. e. Stepper commands (X) or (Y) - Step motor X or Y positions forward or reverse - all other motors off.
3	Each received transmission has 3 characters ASCII
	a. First character is either A or I and addresses local controller and enable command to be received. If I, local controller will store present absolute angle and focus and begin transmitting values in hexidecimals. The angle is transmitted first starting with the most significant digit (MSD), then focus starting with MSD. Angle takes four digits and focus takes four.
	b. Second character controls the angle as follows: (1) D for angle stow motor in destow. (2) S for angle stow motor in stow. (3) N for number of steps to stepping motor. (4) If the ASCII value of the angle is between 20 hexidecimal and 30 hexidecimal, then the number is negative. Negative number steps elevation drive or focus drive motor in reverse. (5) If the ASCII value of the angle is between 30 hexidecimal and 40 hexidecimal, then the number is positive. Positive number steps elevation drive or focus drive, motor forward.
	c. Third character controls focus and controls focus motors as in b.
4	Local controller data received and transmitted. Receives 3 characters Omits 8 characters 11 characters

Notes: If bit 17 set (i.e. 2^{16}), then transmit value 30 to 40 hexidecimals. If bit 17 clear (i.e. 2^{16}), then transmit value 20 to 30 hexidecimals. 2^{16} is set for angle E = 24 degrees.

Table 5-9 EXAMPLES OF TRANSMISSION RECEIVED BY LOCAL CONTROLLER

Code	Meaning
ADD A	Address local controller, turn on (or leave on) Angle Destow motor, turn on (or leave on) Focus Destow motor.
IDD	Command local controller to return absolute Angle and Focus, turn on (or leave on) Angle Destow motor, turn on (or leave on) Focus Destow motor.
AXY	Address local controller, step Angle X steps, step Focus Y steps.
IXY	Command local controller to return absolute Angle and Focus. Step Angle X steps, step Focus Y steps. NOTE: LSD of X or Y is the number of steps. If MSD of X or Y = 3, then number is positive. If MSD of X or Y = 4, then number is negative.
A37	Address local controller, step Angle 3 steps forward, step Focus 7 steps forward.

	Hex	Meaning
A	41	Address local controller
I	49	Command local controller to return Angle and Focus.
D	44	Turn on (or leave on) Destow Motor.
S	53	Turn on (or leave on) Stow Motor.
X	See below. If X positive then X is between 30 Hex and 40 Hex. If X negative then X is between 20 Hex and 30 Hex.	

Number	X-Positive		X- Negative		Number
	Hex	Print	Hex	Print	
0	30	0			0
1	31	1	21	!	1
2	32	2	22	"	2
3	33	3	23	#	3
4	34	4	24	$	4
5	35	5	25	%	5
6	36	6	26	&	6
7	37	7	27	'	7
8	38	8	28	(	8
9	39	9	29	)	9
10	3A	:	2A	*	10
11	3B	;	2B	+	11
12	3C	<	2C	,	12
13	3D	=	2D	-	13
14	3E	>	2E	.	14
15	3F	?	2F	/	15

Table 5-10 TEST COMPUTER OPERATION

Mode	Tasks
Normal Operation (for angle and focus)	1. Take difference from the object. (This is steps per seconds).
	2. Store remainder. For each transmission, decrement remainder and test. If remainder is 0 then increment step and transmit. Repeat procedure. Transmit step and go on to step 3 if six minutes has elapsed.
	3. Every 6 minutes: • Send inquiry and compare with table. • Send correction. • Print with time and absolute. • Go to step 1.
	4. Type S for Slew Test.
	5. Type C for command mode while running to reset clock, etc.
Slew Test Mode	1. Inquire about present position. Print out time and value.
	2. Move 2 mrad from elevation. Print out.
	3. Move to -2 mrad from elevation. Print out.
	4. Return to tracking elevation.
	5. Return to normal operation.

Table 5-11 EXAMPLE OF TYPICAL TRANSMISSION

	Time Seconds	Description	
Print S Angle	0	ISY	Inquiry, Angle Stow On, Step Focus Y
	1	ASZ	Angle Stow on, Step Focus Z
Print + Angle	2	IDX	Inquiry, Angle Destow On, Step Focus X
	3	ADY	Angle Destow, Step Focus Y
	4	ADW	Angle Destow, Step Focus W
	5	ADU	Angle Destow, Step Focus U
Print - Angle	6	ISW	Inquiry, Angle Stow On, Step Focus W
	7	ASV	Angle Stow On, Step Focus V
	8	IOT	Inquiry, Step Angle O, Step Focus
	9		(Add correction if needed)
	10		

NOTE: Slew routine takes about 20 seconds, and is set not to start during 20 seconds before next automatic inquiry and print out which occurs every six minutes.

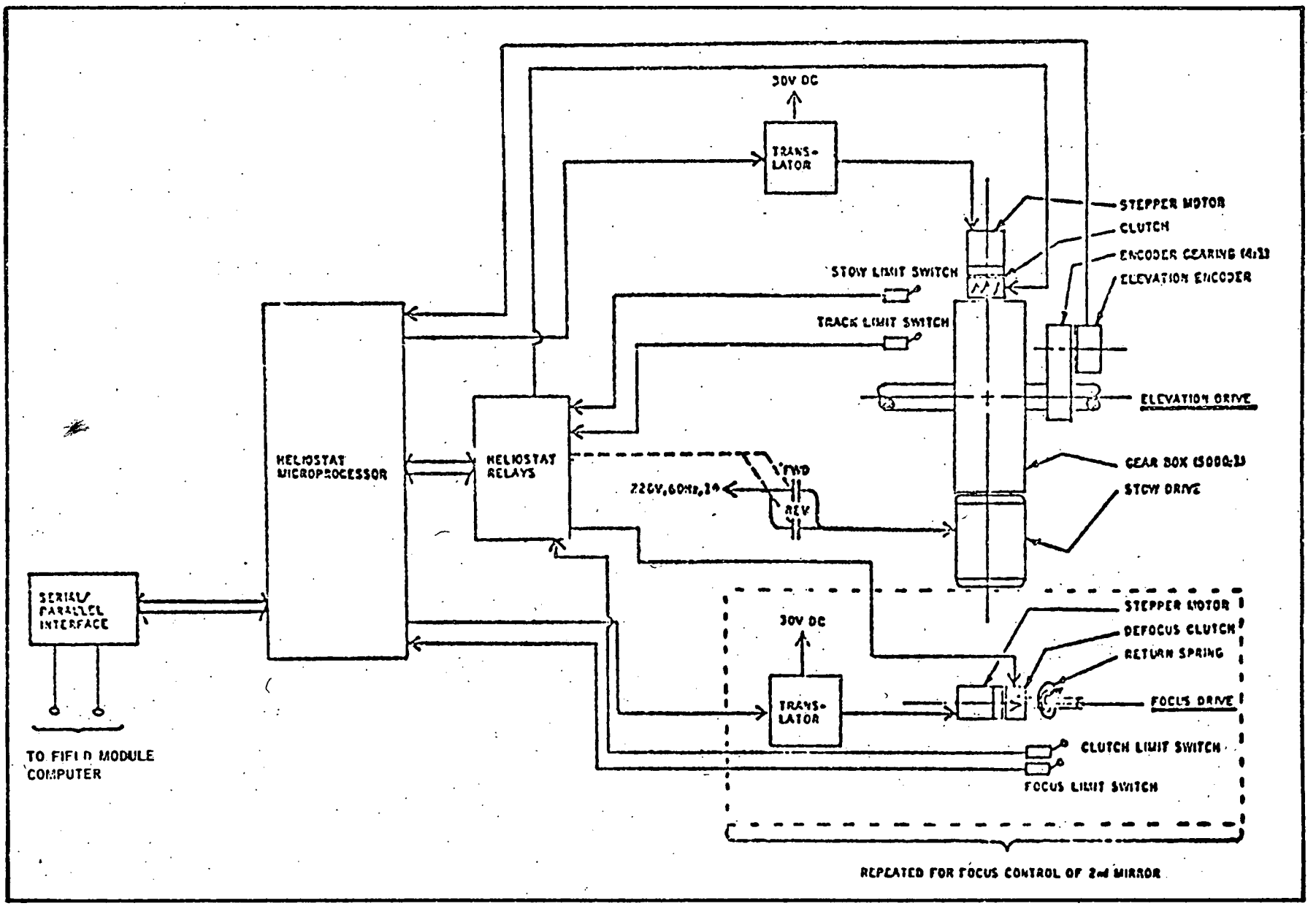

Figure 5-12 HELIOSTAT LOCAL CONTROLLER

THIS PAGE

WAS INTENTIONALLY

LEFT BLANK

6.0 100 MWe POWER PLANT CONCEPT

The baseline 100 MWe plant layout has been developed using a combination of computer analysis and FMC's accumulated component design data. Collector field heliostat spacing, end configuration, and receiver/field attitude have been optimized, within the boundary constraints of the field, tower, and heliostat dimensions, and the field design points. The 100 MWe configuration is essentially a scaling up of the 10 MWe concept (Appendix D) constrained by realistic piping requirements, and sized for a different design point day.

The following prefatory comments apply to the baseline concept.

The collector field/receiver configuration is not necessarily optimal from an overall systems viewpoint. Field and tower dimensions, heliostat size, and other boundary conditions have not been rigorously optimized because the purpose of this study was to establish basic feasibility. However, these boundary conditions provide a reasonable starting point for a systematic parametric system optimization.

The baseline configuration contains only north heliostat fields, a result of our previous study and evaluation by the Aerospace Corporation. The original FMC concept contained north and south fields with receivers mounted on both sides of the towers. The south field was eliminated because at winter solstice design point fewer heliostats are required using north fields. Reassessment of the original concept in light of an equinox design point indicates that reinstatement of the south fields may result in a lower overall system cost by reducing requirements for the number of towers, receiver support structure, and pipe runs between receivers and turbine. Verification of this assessment should be an important element of future studies.

A design point of 3:00 p.m. on the equinox was used for the baseline configuration for comparison with a point focus plant designed for the day of maximum collected energy at the receiver. This day is summer solstice for the FMC concept. However, in the field sizing analysis (Appendix D), we found that the number of heliostats in the summer solstice field was larger than the number in the equinox field, but the additional energy colllected by the summer solstice field was not proportionately more than that collected by the equinox field. Thus, we believe that an equinox field sizing is more nearly optimum than a summer solstice sizing on the basis of minimizing annual busbar cost.

The characteristics of the baseline energy storage subsystem (ESS) and electric power generating subsystem (EPGS) are those developed by McDonnell Douglas (MDAC) for a 100 MWe configuration. These characteristics were selected for three reasons:

- The ultimate economic attractiveness of one solar thermal power concept over others will be dictated by the fraction of total life cycle cost (capital plus operating) contributed by the solar-to-thermal energy conversion subsystems (i.e., concentrator, receiver, and thermal transport subsystems).
- A wealth of developmental and experimental data are available for ESS and EPGS concepts from the point focus projects.
- The MDAC ESS and EPGS are most compatible with the FMC line focus concept, based on our previous studies.

6.1 DESCRIPTION

6.1.1 Plant Layout

The plan view of the baseline concept, configured for a 3:00 p.m. equinox design point, is shown in Figure 6-1. The collector field consists of 170 receiver sections or modules, 8,782 heliostat units (36-meter by 3.05-meter glass area), and 49 half units (18-meter by 3.05-meter glass area). The total glass area is 0.967 square kilometer (1.05×10^6 ft^2).

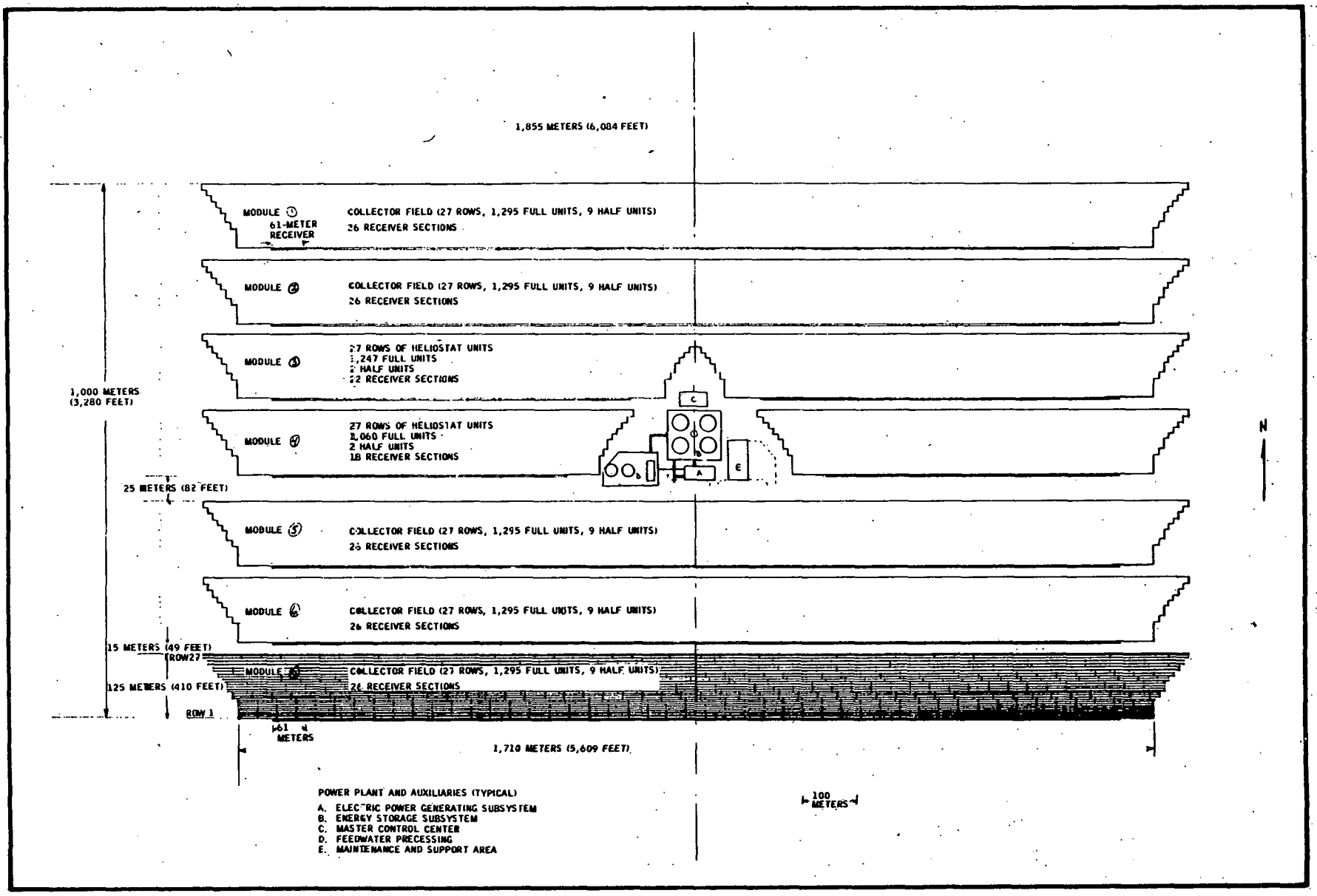

Figure 6-1 PLAN VIEW, BASELINE PLANT CONFIGURATION

The collector/receiver subsystems are arrayed in seven field modules. Each module contains 27 rows of south-facing heliostats. Table 6-1 summarizes the field configuration, and Figure 6-2 shows the spacing of heliostat rows in a module.

Table 6-1 NUMBER OF HELIOSTATS AND RECEIVERS IN BASELINE CONCEPT

Field Module	Number of heliostats*		Receivers
	Full units	Half units	
1	1,295	9	26 (North end of field)
2	1,295	9	26
3	1,247	2	22
4	1,060	2	18
5	1,295	9	26
6	1,295	9	26
7	1,295	9	26 (South end of field)
Total	8,782	49	170

* 8,831 drive/control units

This particular layout is typical of a number of alternate layouts and is not necessarily optimum.

Each receiver section is 61 meters long and 61 meters high. The baseline receiver concept is a once-through-to-superheat concept (Section 4.1) which was chosen as the baseline primarily because of lower capital cost than the alternate natural convection concept. One receiver section, using either concept, has been configured to receive feedwater at 216°C (420° F) and discharge steam at 510°C (950°F) and 10.2 MPa (1,500 psia).

The baseline receiver contains 16 groups of tubes, arrayed circumferentially on the inner wall of the receiver cavity and symmetrically with the normal to the receiver aperture plane. Feedwater enters the two outermost

	MINIMUM (ROWS 1-2)	MAXIMUM (ROWS 26-27)
CENTER-TO-CENTER	3.71 M (12.2 FEET)	6.56 M (21.5 FEET)
CLEARANCE, HORIZONTAL STOW	0.66 M (2.2 FEET)	3.51 M (11.5 FEET)
CLEARANCE, VERTICAL STOW	2.50 M (8.2 FEET)	5.35 M (17.6 FEET)

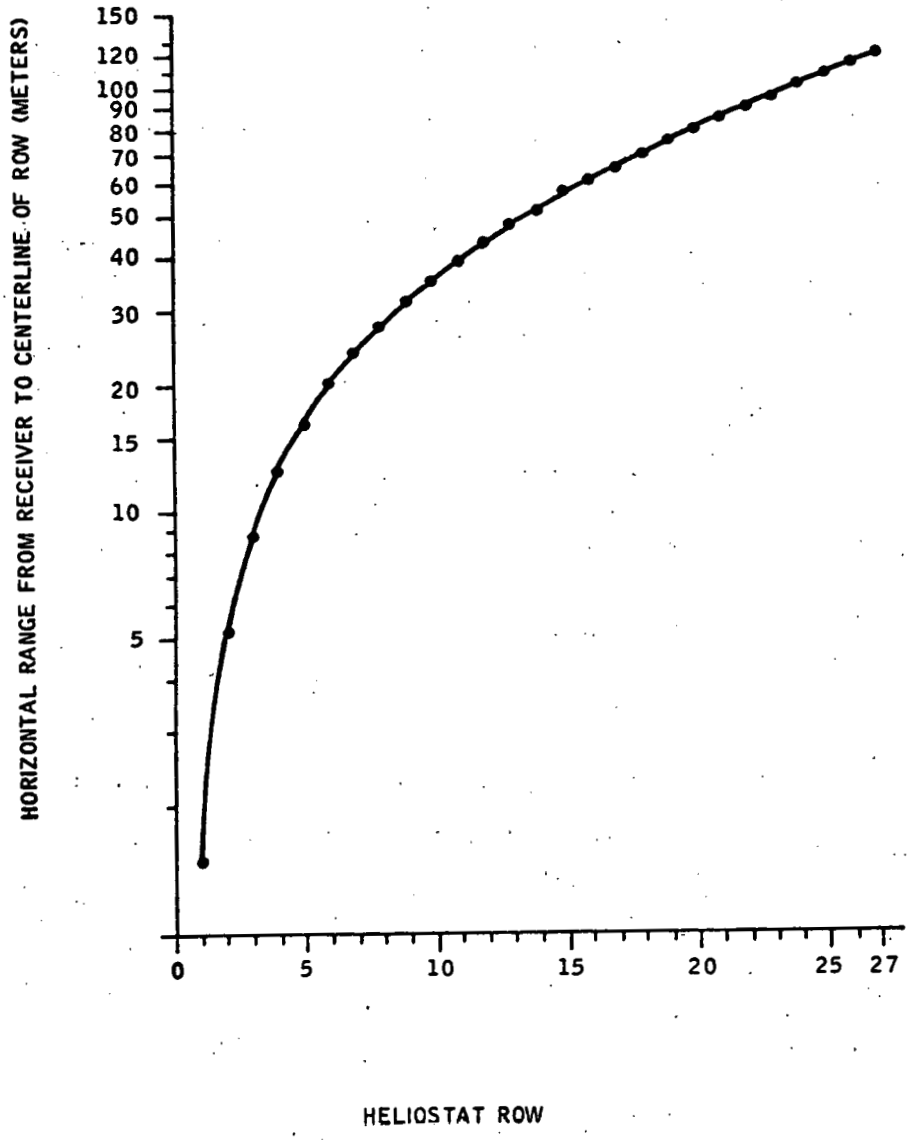

Figure 6-2 SPACING OF HELIOSTAT ROWS IN A MODULE

groups (nearest the aperture) and passes to inner groups in a counter-current flow pattern (flow is countercurrent in adjacent groups). Preheat and boiling occur in the outer and middle groups. Superheating occurs in the innermost group (symmetrically about the cavity centerline).

The feedwater and superheat groups in the receivers in one field module are manifolded to common headers and downcomers to minimize pipe runs.

Each field module is controlled by a minicomputer located in its center. Each minicomputer communicates with the master control computer. An open-loop control strategy will be used. Each minicomputer will receive positional signals from heliostats in the field module, compare actual positions with positions predicted by the master computer, communicate abnormal events to the master computer, and transmit repositioning signals to the heliostats. The master computer will predict sun positions with an algorithm and data from a tracking pyroheliometer.

6.1.2 Thermal Transport Subsystem

6.1.2.1 Description

Conceptual layout of the heat transport subsystem for the baseline plant is shown in Figure 6-3. This arrangement will permit isolation of or valving from a receiver section, groups of receiver sections, or up to one-half of the receiver sections in a field module for maximum repair, maintenance, and operating feasibility. The layout is symmetrical about the north-south centerline of the baseline plant, which contains seven field modules. In each half of the plant, a receiver manifold parallels each row of receiver sections and connects to each adjacent row and to an intermediate north-south manifold located between

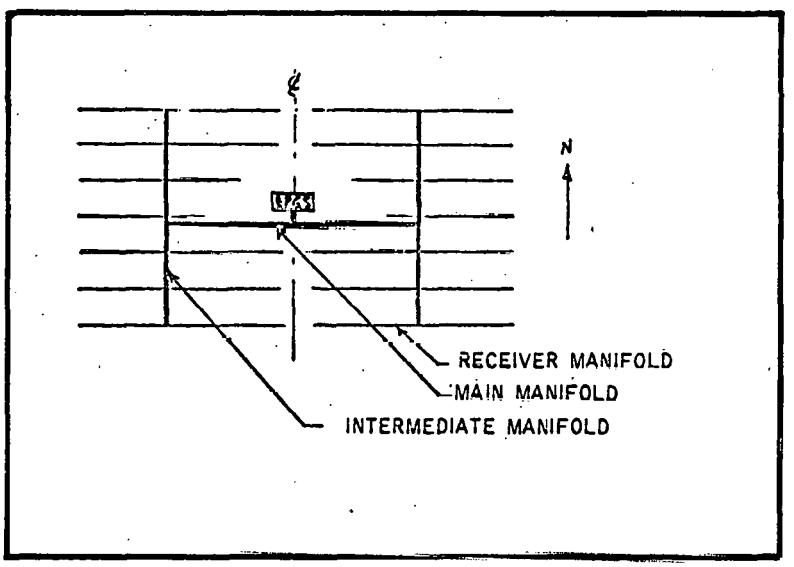

Figure 6-3 PIPING SCHEMATIC

Receiver Sections 7 and 8. This intermediate manifold is connected to a main manifold (near Field Module 4) which connects the intermediate manifolds with the EPGS. All lines are sized for maximum feedwater velocities between 2.1 and 3.0 meters per second (7 to 10 feet per second) and high-pressure steam velocity of 46 meters per second (150 feet per second) at maximum insolation.

6.1.2.2 Steam Transport

Steam manifold lines will be located within the receiver cavity adjacent to the superheat tubes. Receiver feedwater manifold lines will also be within the cavity adjacent to the first pass tubes. The manifolds will incorporate insulated thermal expansion loops between the receiver sections but will not be insulated to within the receivers to permit absorption of solar insolation.

Insulated vertical riser lines will connect the receiver manifolds to the intermediate manifold, which will be elevated about 6 meters (20 feet). This elevation is sufficient to clear the mirror cleaning vehicle. An alternate design would place the intermediate manifold lines below ground level in open trenches for clearance with cleaning equipment, but this design poses a serious problem in dealing with flash-flood runoff.

Thermal expansion loops at intervals on the insulated intermediate manifolds will minimize thermal stresses and the manifolds will be connected to an insulated main manifold near Field Module 4. The main manifold will also be elevated about 6 meters to a location adjacent to the EPGS building where a single main line connects to ESS and EPGS piping. This manifold will incorporate expansion loops to minimize thermal expansion stresses.

Piping insulation will be calcium silicate, Johns-Manville Thermo-12 or equal, of thickness recommended for steam generation service of 482 to 537°C (900 to 999°F) for steam lines and 204 to 259°C (400 to 499°F) for feedwater lines. The insulation will be jacketed with aluminum sleeving for weather protection.

This layout will provide receiver manifold lines small enough for location in the receiver cavity where further heating of the steam will occur and piping insulation will not be required.

6.1.2.3 Feedwater Transport

The feedwater system will be routed parallel with the steam system and will be similarly equipped with valves, etc. The receiver manifold will be located adjacent to the first pass of tubes in the receiver.

Table 6-2 contains a summary of the line sizes required for the baseline heat transport subsystem. These sizings were used to estimate subsystem costs (Appendix E).

Table 6-2 PIPE SIZES FOR BASELINE THERMAL TRANSPORT SUBSYSTEM

Number of Receiver Sections	Feedwater Transport System			Steam Transport System	
	Flow Area (in^2)		Nominal* Pipe Size (in)	Minimum Flow Area (in^2)	Nominal** Pipe Size (in)
	Maximum	Minimum			
1	1.675	1.173	1.25	1.481	1.50
2	3.35	2.346	2.00	2.962	2.50
3	5.025	3.519	2.50	4.443	3.00
4	6.70	4.692	3.00	5.924	3.50
5	8.375	5.865	3.00	7.405	4.00
6	10.05	7.038	3.50	8.886	4.00
7	11.725	8.211	3.50	10.367	4.00
13	21.775	15.249	5.00	19.253	6.00
26	43.55	30.498	6.00	38.506	8.00
39	65.325	45.747	8.00	57.759	10.00
46	77.05	53.958	10.00	68.126	12.00
85	142.375	99.705	12.00	125.885	16.00

* All sizes are Schedule 80.
** 1.5 to 4.0 inch are Schedule 160, 4 to 16 inches are Schedule 120.
See Appendix E for sizing of lines.

6.1.3 Energy Storage Subsystem

Of the thermal storage technologies now available, the McDonnell Douglas Astronautics Company dual-medium sensible-heat thermocline storage concept (1) is judged the system most compatible with the FMC line focus concept. The MDAC concept uses a low-cost stationary solid bed to store most of the energy, with a suitable liquid to transfer energy into and out of the bed (and to store part of the energy directly). This dual-medium type of system combines advantages of a low-cost solid with the flexibility, low pumping power, and moderate heat-exchanger requirements of a liquid energy storage system.

Conceptually, it its simplest form, the system uses a bed (shown in the center of Figure 6-4) of an inexpensive solid (e.g., rock, ore, metal scraps). An appropriate high-temperature liquid fills the voids in the bed and circulates through the bed to deposit or withdraw energy.

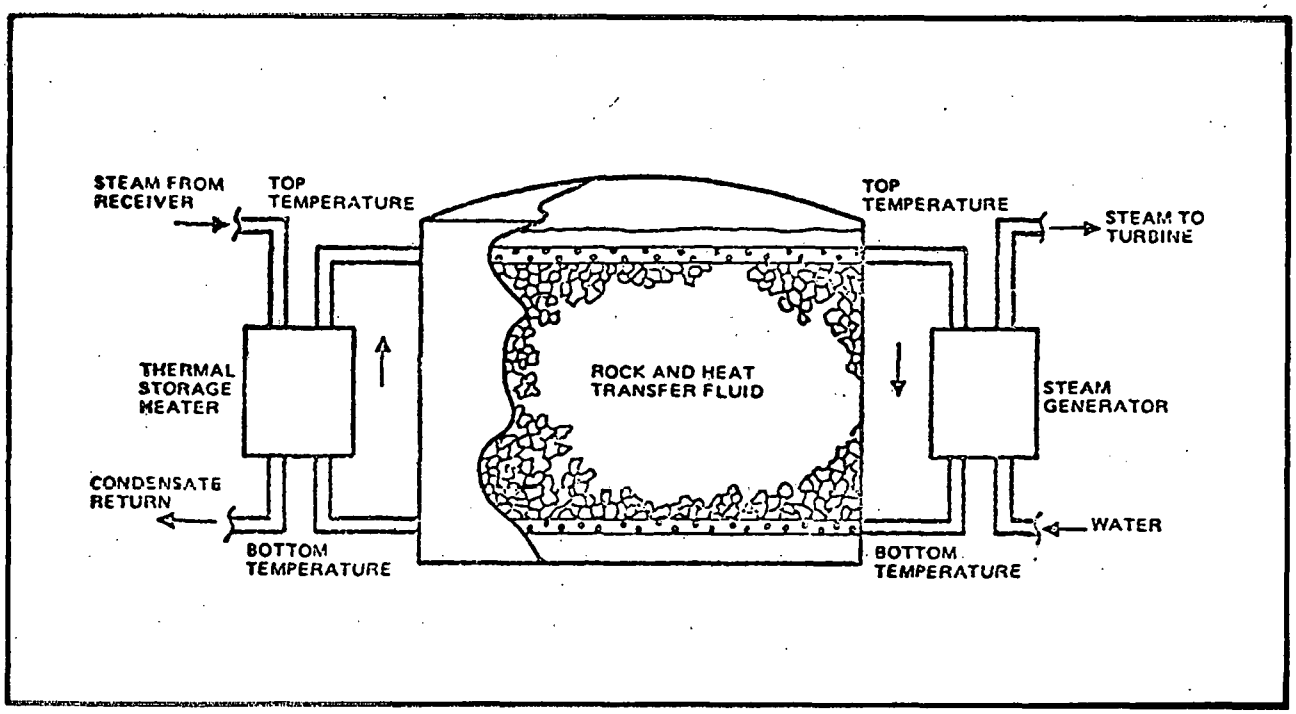

Figure 6-4 DUAL MEDIUM THERMAL STORAGE CONCEPT

In the cyclical operation, heating of the bed (charging) is achieved by removing lower-temperature fluid from the bottom of the bed, heating it in a heat exchanger with steam from the receiver, and returning the fluid to the

top of the tank. A fairly sharp temperature transition (a thermocline) is maintained naturally between hot and cold fluid because of the lower density of hot fluid. This thermocline moves downward through the bed during charging and upward during extraction. When the storage unit is completely charged, all of the bed and the fluid are at the maximum temperature and the thermocline does not exist. The extraction loop uses fluid to remove energy from the storage unit and produces steam for power plant operation or other plant functions such as equipment heating.

The large cost saving for this type of thermal energy storage results principally from two factors: (1) replacement of about 75 percent of the expensive storage liquid with inexpensive rock, and (2) use of the thermocline principle to reduce the tankage volume substantially, compared with a system with separate tanks for hot and cold storage.

6.1.4 Electric Power Generation Subsystem

The analyses performed to date on the FMC line focus concept have been based on the EPGS selected for use by McDonnell Douglas. This alternative is proposed for the FMC baseline configuration.

Briefly, the EPGS consists of a 100 MWe (112-MWe rating) industrial turbine manufactured by the General Electric Company. The inlet steam temperature may be specified at any range of 482 to 538° C (900 to 1,000° F) and 8.7 to 10.1 MPa (1,265 to 1,465 psia). FMC's previous work on receiver concepts centered on producing steam at 538° C (1,000° F) and 6.9 MPa (1,000 psia). Additional analysis (Appendix D) was performed to verify that the baseline receiver concept can operate at the higher pressures required for turbine operation. The thermal transport subsystem for the baseline has been sized for the inlet and outlet conditions of the MDAC EPGS (2).

There appear to be no unique problems in adapting the MDAC concept of interstage steam extraction for feedwater preheating to the FMC baseline. Manifolding and control of preheated feedwater for distribution to receiver sections can be performed downstream of preheating.

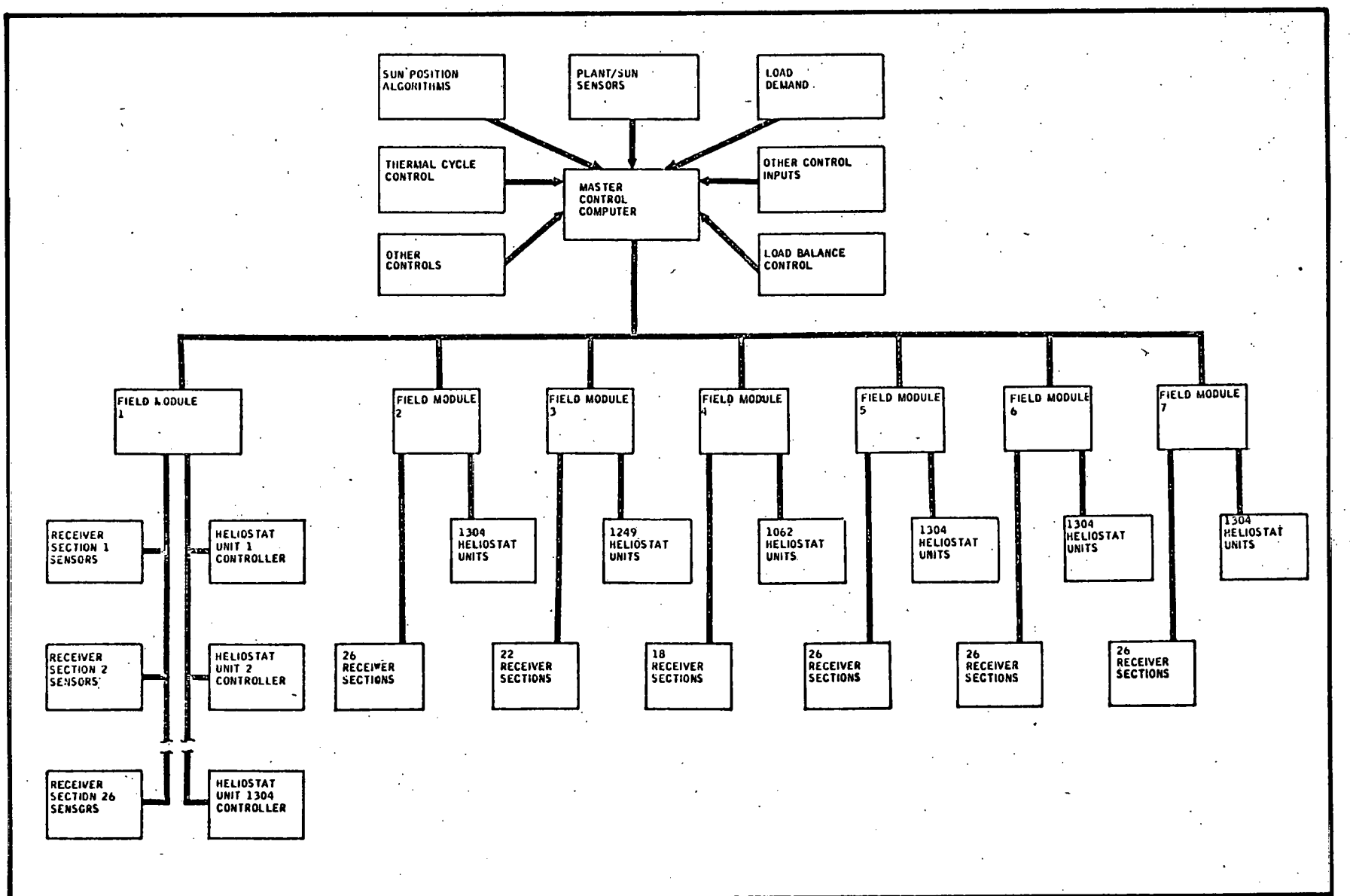

Figure 6-5 MASTER CONTROL SUBSYSTEM CONCEPT

6.1.5 Master Control Subsystem

The baseline plant is controlled through a central computer, which monitors the receivers, heliostat field modules, and auxiliary sensors. The central computer responds to power plant steam demand by issuing commands to control the heliostats and the receivers in the field modules. A display is available to the operator who can modify the commands as appropriate or can perform the required test and maintenance functions. The central computer communicates with smaller minicomputers in each field module. Each field computer controls all of the heliostat units in that field module. Figure 6-5 shows the baseline configuration. Section 5 contains a description of control logic.

6.2 ESTIMATES OF PERFORMANCE

The computer model described in Appendix A was used to size the heliostat field and make estimates of hourly performance at three solar days. The energy outputs of the collector field were used with the receiver performance data in Section 4.0 to estimate plant electrical output. Computational details are contained in Appendix D.

6.2.1 Field Sizing and Energy Output

The optimum spacing of heliostat rows gives maximum ground coverage without blocking and screening. Providing access clearance between rows imposes an additional constraint. Because of the apparent solar motion, the optimum spacing is only valid for a specific time or design point. Row density increases as the design point progresses from winter to summer solstices. For the baseline system, the equinox at 3:00 p.m. was selected as the design point for field row spacing and butterfly area sizing. A quadratic row spacing was found to give optimum ground cover. For plant sizing, summer solstice at 3:00 p.m. was the design point. Field performance was calculated for the solstices and autumnal equinox using the parameters listed in Table 6-3.

Table 6-4 summarizes data shown in Figures 6-6, 6-7, and 6-8. Hourly intensity profiles for a north field at summer solstice are shown in Figure 6-7. The net thermal power admitted through the receiver aperture for the 170-module baseline system as a function of hour of day is given in Figure

6-7 for the three representative days. Projected total thermal energy entering the receiver is plotted over one-half year in Figure 6-8. It is interesting to note that although the highest peak power is obtained on the equinox, the highest total energy is collected on summer solstice.

Table 6-3 PARAMETERS FOR CALCULATION OF COLLECTOR FIELD PERFORMANCE

Parameters	Dimensions
Field width	122 meters
Receiver height	61 meters
Aperture plane angle	45 degrees
Tracking error	2 milliradians
Aiming error	2 milliradians
Surface error	2 milliradians
Heliostat size	36 meters x 3 meters
Minimum row spacing	3.7 meters
Maximum row spacing	6.9 meters
Quadratic spacing	
Number of rows	27
Mirror reflectance	0.9
Receiver segment	61 meters
Latitude	35 degrees
Field sizing design point	Day 81, 3:00 p.m.
Plant sizing design point	Day 172, 3:00 p.m.

Table 6-4 TOTAL ENERGY INTO RECEIVER FOR 100 MWe BASELINE PLANT (170 MODULES)

Time of year	KJ	MWthH
Summer solstice	16.3×10^9	4.54×10^3
Equinox	14.9×10^9	4.14×10^3
Winter solstice	10.2×10^9	2.85×10^3
Year total	5.13×10^{12}	1.43×10^6

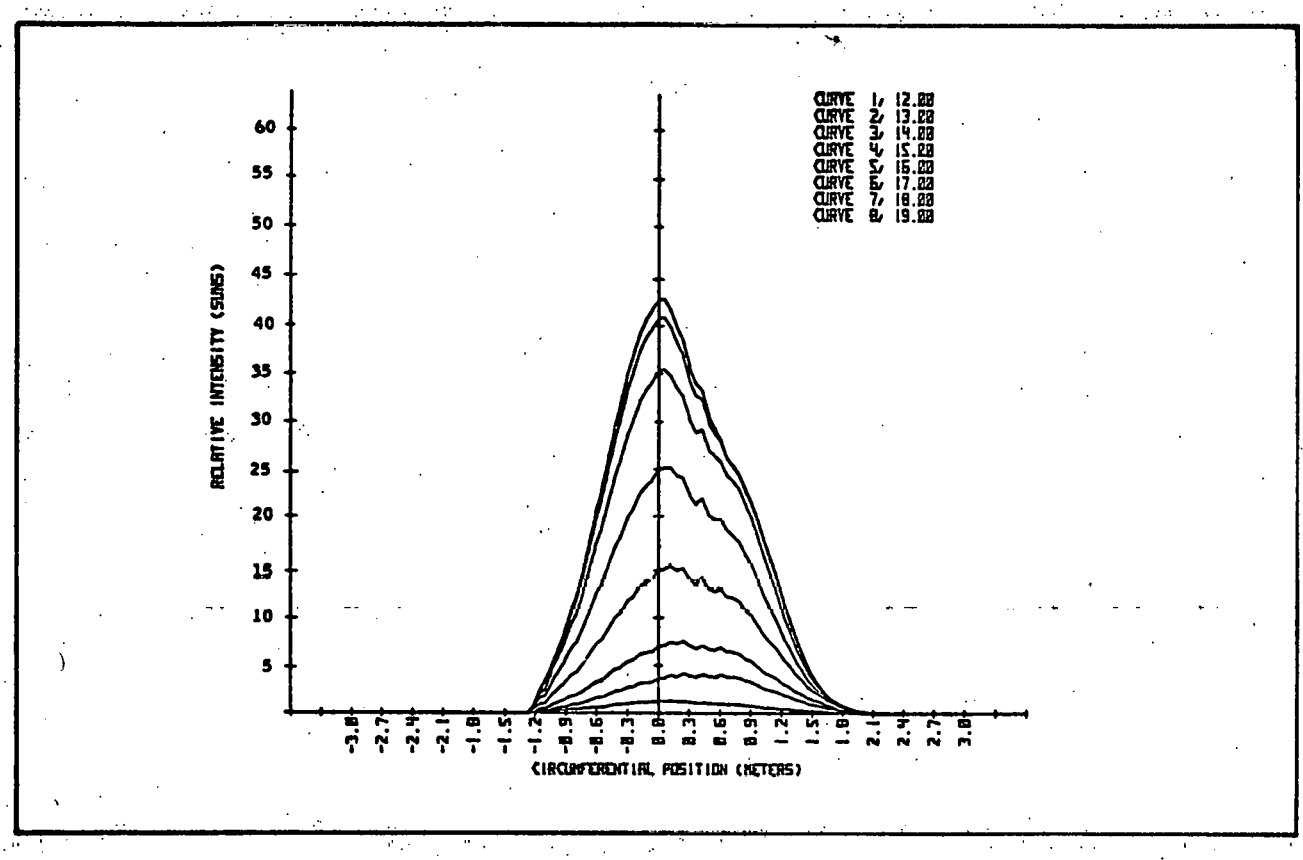

Figure 6-6 FLUX DISTRIBUTION OF INTERNAL RECEIVER CIRCUMFERENCE FOR NORTH FIELD ON SUMMER SOLSTICE

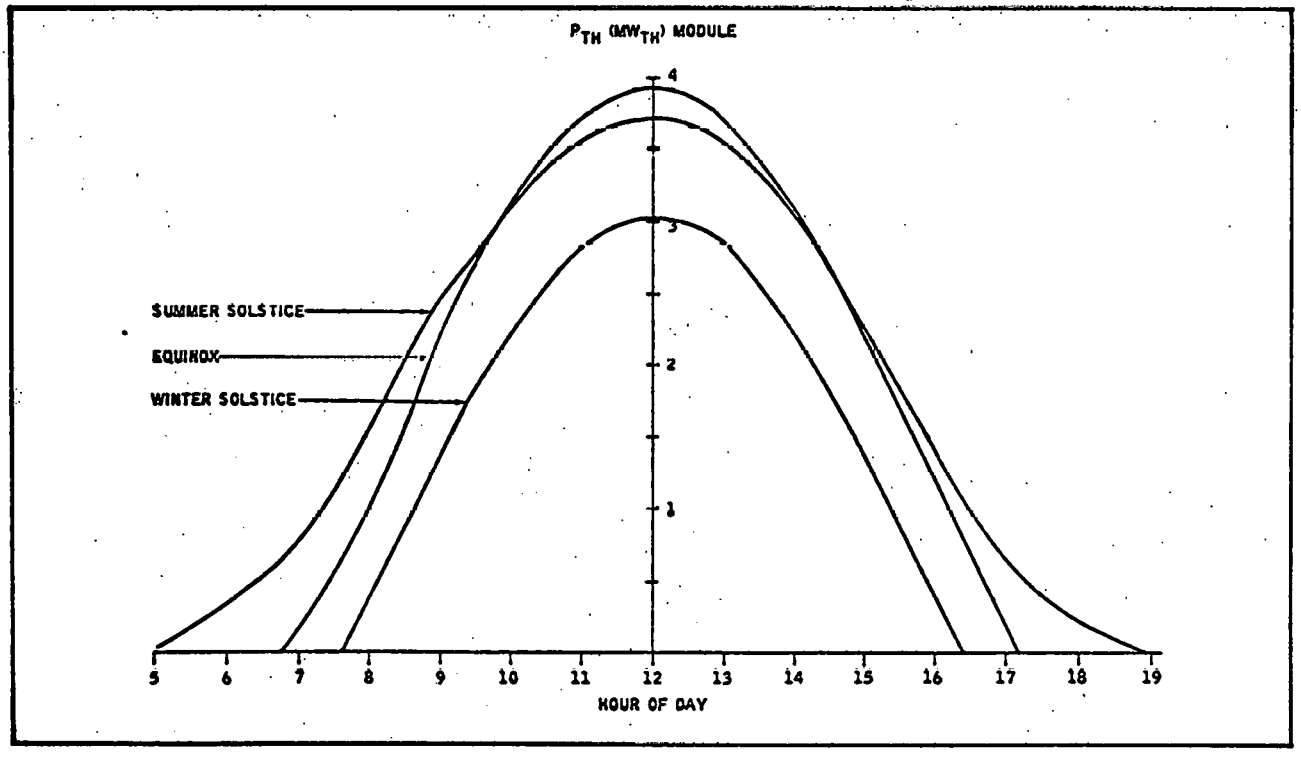

Figure 6-7 HOURLY POWER INTO RECEIVER FOR NORTH FIELD, SIZED FOR 3:00 P.M. ON EQUINOX

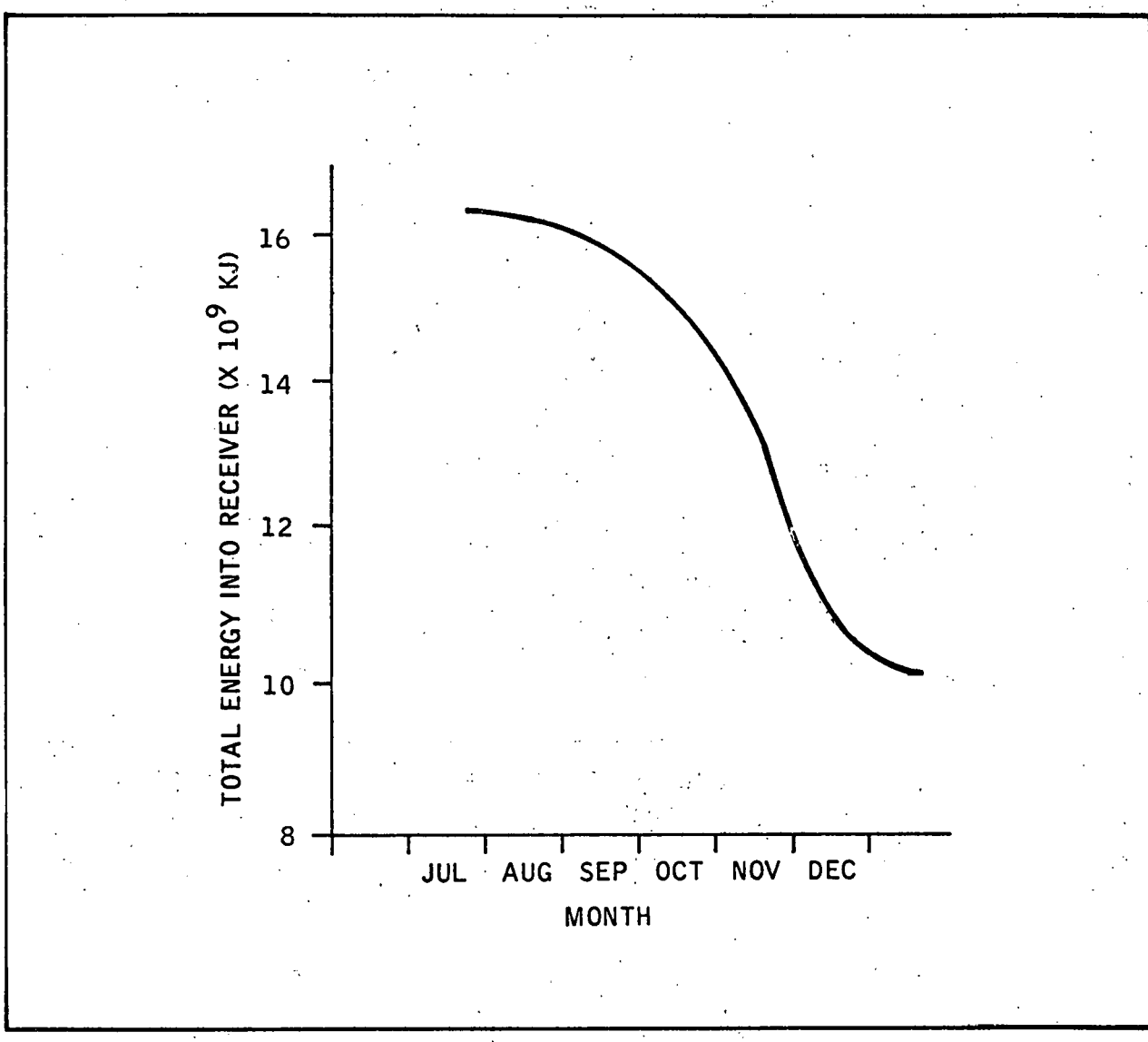

Figure 6-8 PERFORMANCE OF NORTH FIELD, SIZED FOR 170 MODULES

6.2.2 Annual Electric Output

Tables 6-5 and 6-6 show the estimated performance of the plant concept for the field design day (equinox), plant design day (summer solstice) and winter solstice. Appendix D contains the computations. Figure 6-9 shows the estimated electrical output over a six-month period. The estimate of total annual busbar power, assuming symmetry about summer solstice, is shown in Table 6-7.

Table 6-5 PERFORMANCE OF BASELINE CONFIGURATION (EQUINOX DESIGN DAY)

Hour	Energy input (MWh-th)		Busbar power direct operation (MWe)	Mass flow rate (kg/sec)		
	At receiver apertures	To thermal storage		One receiver	Storage	Turbine
0700-0800	166.6	91.7	0	0.28	48.4	0
0800-0900	370.4	293.9	0	0.91	154.9	0
0900-1000	531.3	151.1	0	1.09	185.6	0
1000-1100	635.6	255.3	100	1.36	110.1	120.8
1100-1200	671.2	290.4	100	1.44	124.8	120.8
1200-1300	630.4	249.8	100	1.34	107.3	120.8
1300-1400	530.2	148.9	100	1.09	63.8	120.8
1400-1500	370.4	126.6	50	0.68	54.4	60.4
1500-1600	173.9	119.2	0	0.37	62.8	0
Totals	4,080.0	1,726.9	550			

Total electric energy = 550 (direct) + 426 (storage) = 976 mweh

Table 6-6 SUMMARY OF BASELINE CONCEPT PERFORMANCE

Day	Total energy to receivers (mwh-th)	Busbar energy (MWeh)		Hours of operation	
		Direct	From storage	100MWe	70MWe
Equinox (design day)	4,080	550	426	5.5	6.1
Summer solstice	4,439	600	454	6.0	6.5
Winter solstice	2,846	500	218	5.0	3.1

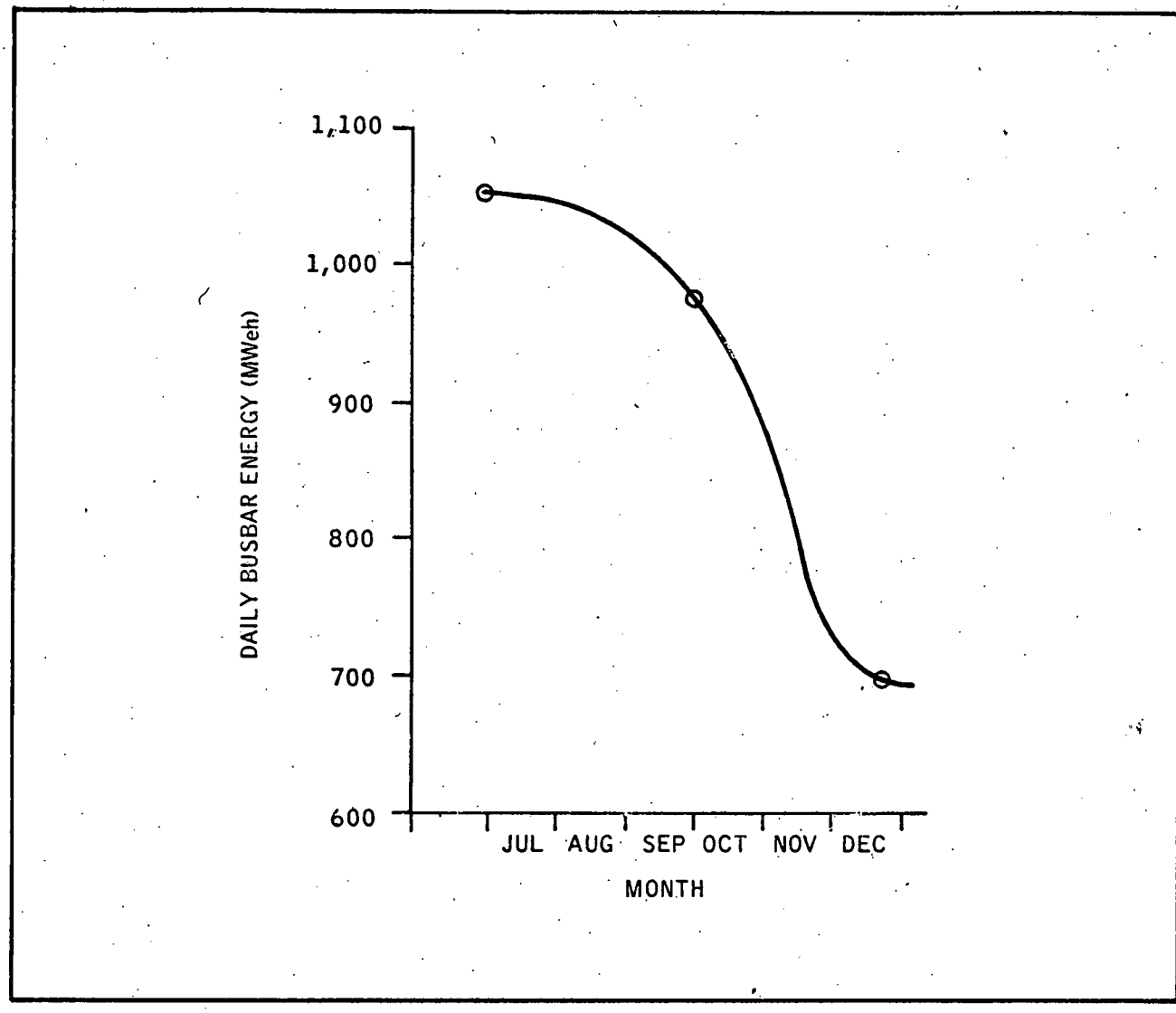

Figure 6-9 ANNUAL BUSBAR POWER OF BASELINE CONFIGURATION

Table 6-7 ESTIMATE OF TOTAL ANNUAL BUSBAR ENERGY

Month(s)	Number of days	Average daily output (MWeh)	Total output (MWeh)
December, January	62	700	43,400
November, February	58	800	46,400
October, March	62	930	57,660
September, April	60	1,020	61,200
August, May	62	1,040	64,480
July, June	61	1,050	64,050
Annual	365	924	337,190

The plant operates at an average of 5.5 hours per day at 100 MWe (200,750 MWeh annual) and an average of 5.3 hours per day at 70 MWe from thermal storage (136,440 MWeh). Table 6-8 shows hours of operation on three calendar days.

Table 6-8 HOURS OF OPERATION

Day	Estimated hours of operation		Load factor*
	From receivers at 100 MWe	From thermal storage at 70 MWe	
Equinox (field design day)	5.5	6.1	0.41
Summer solstice (plant design day)	6.0	6.5	0.44
Winter solstice	5.0	3.1	0.30
Annual	5.5	5.3	0.38

* Capacity = 100 MWe by 24 hours per day = 2,400 MWeh

6.2.3 Plant Efficiencies and Power Flow

Overall plant efficiencies and power flow at noon equinox were computed for an incident solar flux of 950 W/m^2, and assuming that 96.5 percent of the collectors are operational. Under these conditions, the operational power level is as follows:

- Total collector area = (8,806.5 heliostats) (110 m^2/heliostat) = 968,715m^2
- Operational power level = (0.965) (968,715) (950 x 10^{-6}) = 888 MW

Table 6-9 and Figures 6-10 and 6-11 show the power flows and subsystem efficiencies at noon equinox. The subsystem efficiencies (η_j) were derived as follows (see Figure 6-10 for j indexes):

- Collector Field

  η_1, η_3, η_5, η_6, computed by collector field program.

  η_2 is an assumed value

  η_4 (end losses) is computed as follows:

  The butterfly mirror area is incorporated on each end of the field to provide full illumination for the length of the receiver during a specified operating time range. Within this operating duration, an area of mirror

surface equal to the butterfly area is not illuminating the receiver. The concentrator end loss effect is the fraction of mirror area illuminating the receiver. As shown in Figure 6-1, 18 butterfly areas are used in the field configuration. The total area of one butterfly (Appendix A) is $7105 m^2$. Since the total collector area is $968,715 m^2$.

$$\eta_4 = [968,715-(18)(7,105)]/968,715 = 0.868$$

Table 6-9 SUBSYSTEM AND SYSTEM EFFICIENCY AT NOON EQUINOX

Efficiency	Direct from receivers	Direct from storage
Collector	0.712	0.712
Receiver	0.860	0.860
Piping	0.970	0.970
Storage	–	0.940
Turbine	0.377	0.268
Parasitic	0.89	0.92
System	0.20	0.14

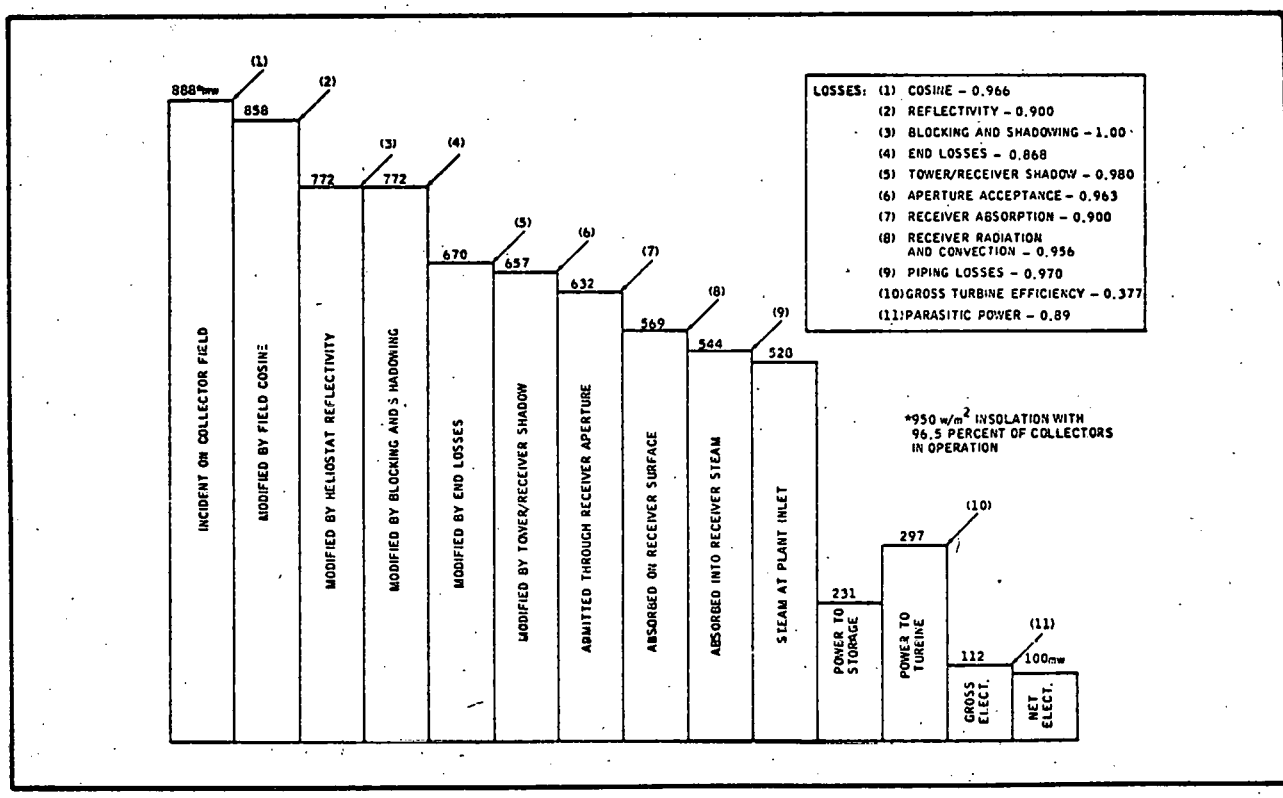

Figure 6-10 POWER FLOW FOR 100-MWe CONCEPT (EQUINOX NOON)

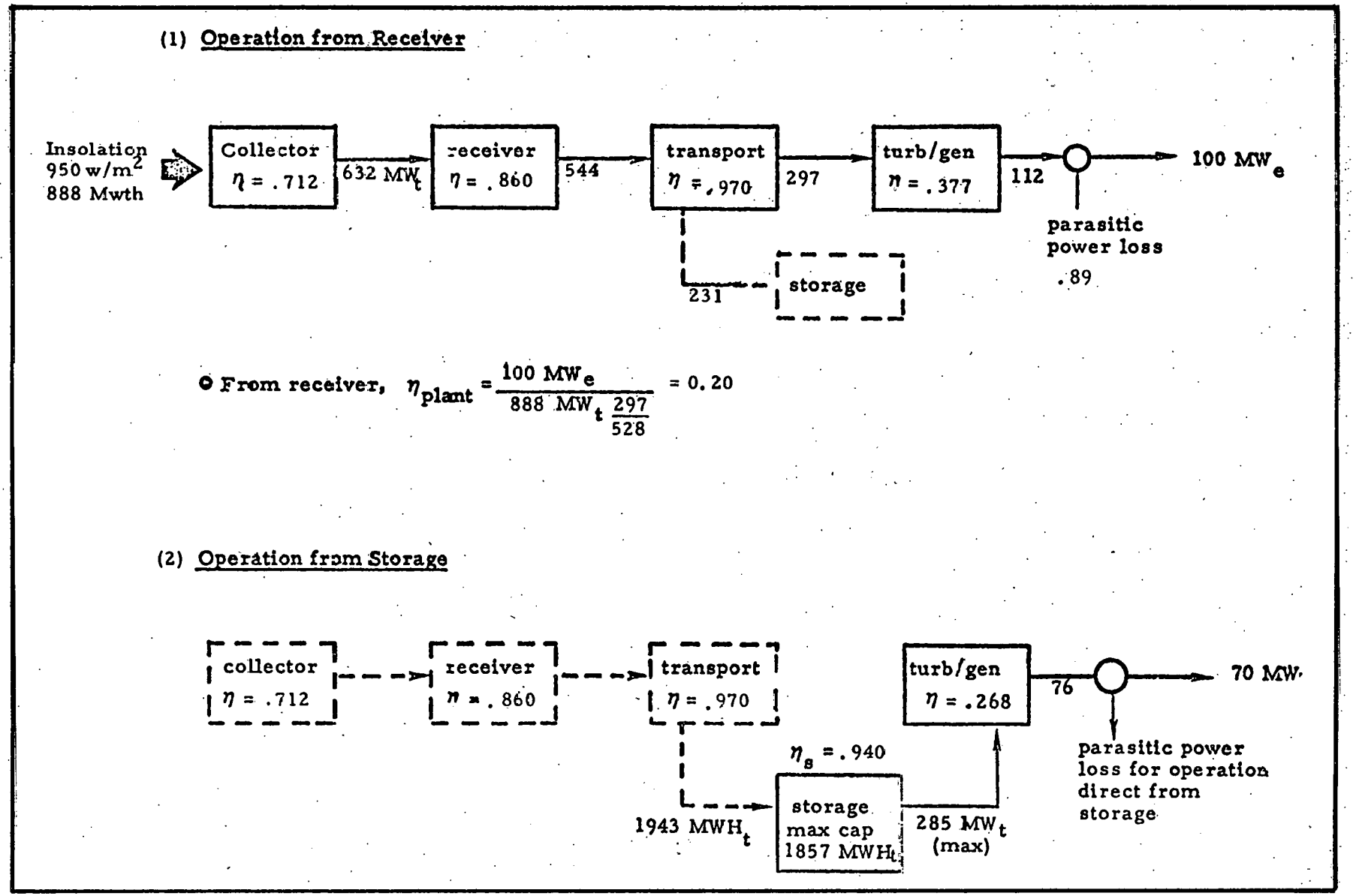

Figure 6-11 PLANT PERFORMANCE EFFICIENCIES, 100 MWe CONCEPT

- Receivers

  The receiver performance was calculated using the methodology and program described in Appendix B. This calculation rigorously treats the thermodynamic heat transfer and loss mechanisms. The output gives steam temperatures, flow rates, and overall receiver efficiencies, but not individual loss path fractions. A minor program modification would be required to provide this information directly. Since receiver absorptivity is an input parameter, we calculated the radiation and convection loss factor, η_8 from the total receiver efficiency, assuming that other loss paths are negligible.

  Assume η_7 = absorptivity of receiver tubes = 0.9

  From Table D-13, Appendix D, overall receiver efficiency = $\eta_7 \eta_8 = 0.860$

  Then, $\eta_8 = 0.860/0.9 = 0.956$

Since the cavity design results in collection of much of the reflected incident light, the effective receiver absorptivity is significantly higher than 0.9 and therefore the true value of η_8 is probably somewhat lower. The product, however, is the calculated receiver efficiency, which is 0.860 in any case.

The cavity receiver design is inherently a lower radiation and convection loss configuration than an exposed cylinder, such as the receiver configuration of the MDAC concept. So, one would expect a lower value of η_8 for the MDAC concept.

For noon equinox, MDAC quotes a value of 0.952 for η_8 and a overall receiver efficiency of 0.904 (5). Comparison with the values computed above suggests that the line focus receiver efficiency is realistic and perhaps conservative.

- Piping Losses

  η_9 is based on the discussion in Section D.1 of Appendix D. We believe the value of 0.97 to be realistic, since a more complex piping network than the point focus concept is required. For comparison, MDAC quotes a value of 0.994 for their commercial concept (5).

- Electric Generation Losses

  η 10, η11, and efficiency of thermal storage are taken from the performances of the MDAC commercial concept (5).

6.3 PLANT ECONOMICS

Estimates of plant investment and operational costs were based on costs developed early in the project for a 10 MWe plant configuration (Appendix E). The JPL/EPRI methodology (3) was used to estimate busbar power costs. Costing factors were taken from guidelines recommended by DOE for comparison of point focus and line focus power systems (4).

6.3.1 Capital Costs

Table 6-10 shows the capital costs estimated for the first plant and the 80th plant.

Table 6-10 ESTIMATES OF CAPITAL COSTS FOR 100 MWe PLANT

Item	Note	Capital Costs,[1] $/kWe	
		1st Plant	80th Plant
Land, yardwork	2	3	3
Structures and improvements	3, 4	51	39
Turbine plant	3, 4	242	187
Electric plant	3, 4	88	68
Collectors	5	634	325
Receiver	5	209	107
Towers	5	60	31
Thermal storage	3	215	155
Distributables	4, 6, 9	86	36
BOP	3, 4	53	38
Direct Cost		1,640	989
Indirect Cost	7, 8	328	198
Total		1,968	1,187

1. Costs are in 1978 dollars and include burden, contingency, and fee.
2. Based on 500 acres at $500 per acre.
3. 0.95 Learning curve.
4. From Reference 4.
5. 0.90 Learning curve.
6. 69 Percent reduction from 1 unit due to larger cost base for 80 units.
7. 20 Percent of Direct Costs.
8. Indirect Costs include A&E services, construction management, solar integrator, and plant startup.
9. Distributables include contractor field office, insurance (project and equipment), construction equipment, spares, and taxes.

The pie diagram in Figure 6-12 shows the percentage costs for both the total plant and the collector subsystem for the first plant. Appendix E contains the detail cost computations for the collector, receiver, thermal transport, and master control subsystems. Costs for the other components are taken from those for the MDAC commercial concept (4).

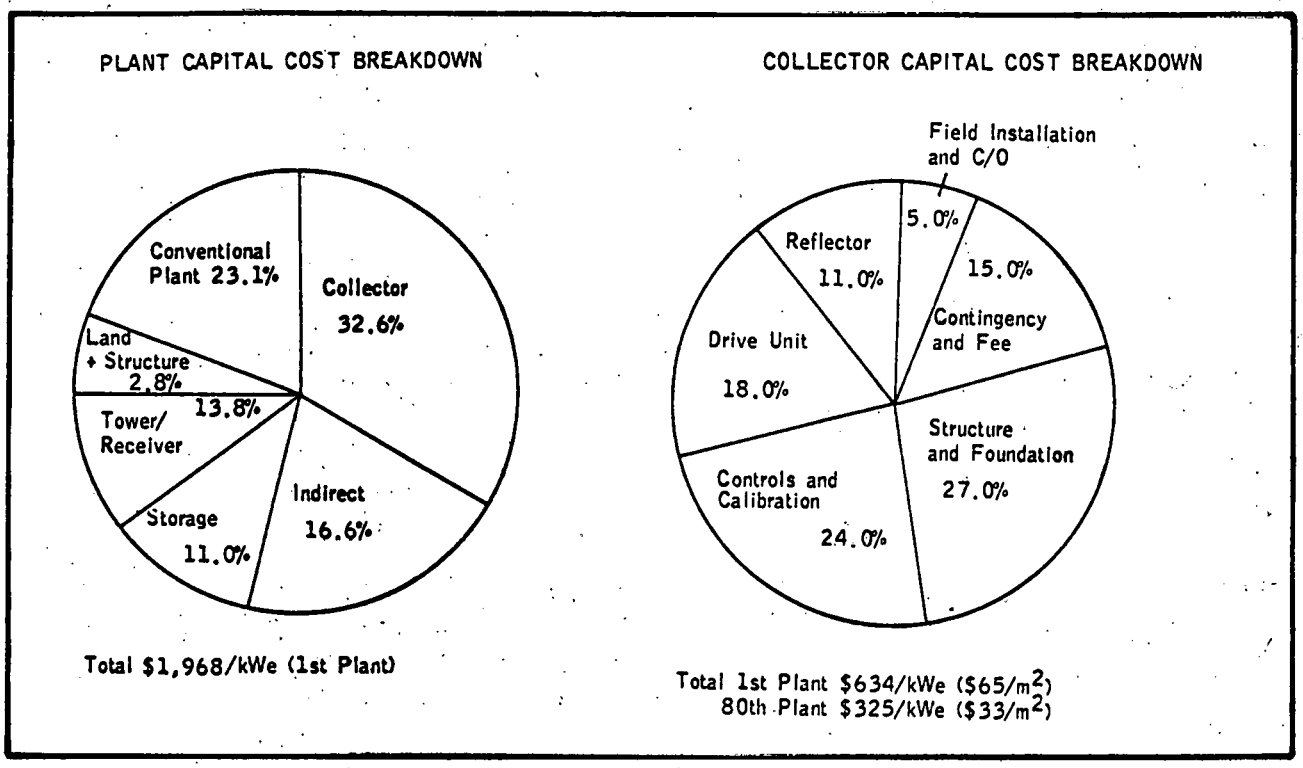

Figure 6-12 SYSTEM AND HELIOSTAT COST DISTRIBUTION SUMMARY

6.3.2 Cost of Service Calculation

The following are data input for the cost of service calculation (3, 4):

	Symbol (4)	Value
• Plant		80th unit
• System lifetime	N	30 years
• First year of operations	y_{co}	1990
• Site		Inyokern
• Type of ownership		Investor owned
• Total capital for 80th plant	CI_t	$1,187
• Operations and maintenance	X_o	1 percent
• Annual "other taxes"	β_1	0.02
• Annual insurance premiums	β_2	0.0025

	Symbol (4)	Value
• Income tax rate	r_1	0.50
• Ratio of debt to total capitalization	D/V	0.0025
• Ration of common stock to total capitalization	C/V	0.27
• Ratio of preferred stock to total capitalization	P/V	0.18
• Debt interest rate	k_d	0.09
• Annual rate of return on common stock	k_c	0.15
• Investment tax credit	α	0.10
• Depreciation (straight line)	$DPF_{m,k,\eta}$	
• Rate of general inflation	k_e	0.05
• Escalation plus inflation rate for capital costs	g_c	0.065
• Escalation plus inflation rate for operating costs	g_o	0.065
• Escalation plus inflation rate for maintenance cost	gm	0.065
• Base year for constant dollars	y_b	1978
• Cost of capital	k	0.085
• Capital recovery factor	$CRF_{k,\eta}$	0.0931
• Annualized fixed charge rate	$\overline{FCR}$	0.157
• Present value of capital investment	CI_{pv}	$2,575
• Present value of recurrent costs	X_{pv}	$575
• Annualized system resultant cost	$\overline{AC}$	$254
• Levelized bus bar energy cost	$\overline{BBEC}$	71 $\frac{\text{mills}}{\text{kWeh}}$

6.4 COMPARISON WITH POINT FOCUS SYSTEM

This section contains a comparison of the FMC baseline configuration with a typical concept for a point focus system. General comparisons of the two concepts are offered to introduce the underlying basis for FMC's longstanding support of the line focus approach to commercially feasible solar power generation. Specific comparisons are then presented, using the concept evolved by McDonnell Douglas Astronautics Company as a basis for comparison. The abbreviation "MDAC PFS" is used when this concept is referenced.

6.4.1 General Comparisons

6.4.1.1 Collector Field Linearity

Use of parallel lines of essentially flat, rectangular heliostats offers cost benefits from initial production through maintenance and operation. Fabrication and assembly of the heliostat support structure can be highly automated with fewer assembly steps than required for a point focus heliostat. The size (18.3 meters by 3.05 meters) of a heliostat section permits complete assembly of the section at the factory and shipment of the complete assembly on a railcar or flatbed trailer. Labor-intensive field assembly will thus be minimized.

Elimination of azimuthal tracking, combined with use of computer-controlled mirror focusing and two-point support (each end of a heliostat section), will (1) relax manufacturing tolerances for mirror alignment, (2) simplify the design of the drive mechanism, (3) reduce the effect of wind and vibration on tracking performance, and (4) allow control of a larger mirror area (e.g.: 110 square meters versus 38 square meters for the MDAC PFS by a single control unit (6).

Field linearity is better suited to automated cleaning of reflecting surface. Dirt accumulation on reflecting surfaces is a major vulnerability of all solar thermal systems, as evidenced by the experiences of the Phase I point focus contractors during field tests (7a) and the initiation of dust buildup studies (8). This evidence clearly shows that frequent cleaning of reflecting surfaces will be required to maintain design performance of a commercial solar thermal plant. If a monthly cleaning cycle is assumed (360 evening hours per month), then a 100-MWe plant, with about 1 million square meters (247 acres) of reflecting surface will require a cleaning rate of about 2,800 square meters per hour. This is equivalent to cleaning one FMC heliostat unit every 2 minutes, or one MDAC PFS heliostat every minute. In either case, a mechanized cleaning vehicle is required.

Consider, however, that the reflecting surface in the FMC configuration is laid out in straight lines of almost continuous surface, whereas the field in the MDAC PFS consists of a collection of discrete areas of surface, separated by

open areas, and distributed in a complex circular arrangement. Indeed, the total land area required for the FMC baseline configuration is one-third less than that required by the MDAC PFS.

It is concluded from this comparison that (1) the cleaning cycle time for the baseline configuration will be one-third to one-fourth the cycle time for the MDAC PFS because both contain about the same area of reflecting surface, and (2) the linear field arrangement will be better suited for development of a mechanized cleaning vehicle.

An illustration of a cleaning vehicle, conceived by the FMC Sweeper Division (designers and manufacturers of industrial sweepers and scrubbers), is shown in Figure 6-13. The vehicle can be adapted for either wet or dry cleaning. In a wet-cleaning configuration, wash fluid would be applied at the front end and recovered at the rear end to comply with environmental requirements.

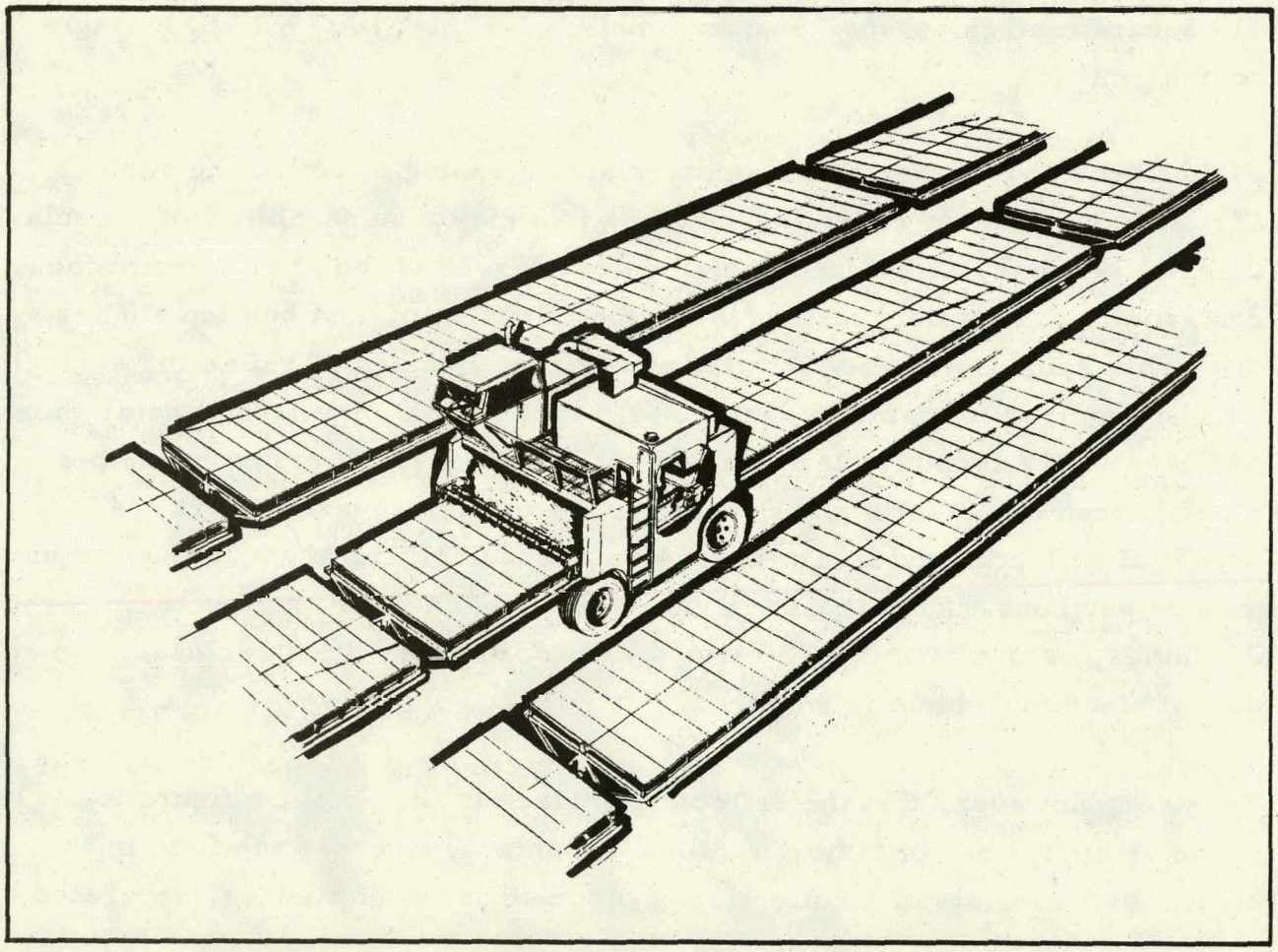

Figure 6-13 LINE FOCUS HELIOSTAT CLEANING VEHICLE

6.4.1.2 Power Unit Modularity

The baseline configuration comprises 170 power units, in which a power unit is defined as one receiver section with associated heliostat field. Each power unit delivers rated steam equivalent to about 1 MWe peak generating capacity. The power units have been grouped into seven modules in an aspect ratio of about 1.8:1 to illustrate one of many possible configurations. Other configurations are equally feasible, with the primary constraint being minimization of cost and thermal losses of the fluid transport network.

Several benefits, including the following, are associated with the FMC line focus unit concept over point focus systems:

- Choice of configuration for a given capacity plant to take advantage of available land areas, or to minimize environmental impacts. Point focus systems are fixed in configuration for a given capacity.
- Increasing existing plant capacity by adding more power units. This procedure provides a long-term economic benefit because the installation of a large plant can be planned incrementally to match the increase in load demand up to maximum capacity. This incremental installation is achieved by adding line focus power units to existing field modules.
- The fabrication of power units for a wide range of plant capacitits from one set of production processes and facilities. A plant size of 10 MWe will differ from a 1,000 MWe size only in the number of power units required because the same heliostats, receivers, and towers are used. Point focus systems require different sizes of receiver and tower for different plant capacities, and a new field construction for each plant.
- Maximum learning curve cost reductions for heliostat, receiver, and tower fabrication and installation are achieved with the first plant.

6.4.1.3 Receiver Vulnerability

The line focus receiver area is spread over several low towers; a point focus receiver must be concentrated in a small area on one high tower. Thus, decentralized line receivers are less vulnerable to earthquake, lightning strike, component failure, or sabotage with respect to fraction of collected energy lost given an incident. Sabotage is included because utility company facilities are a frequent target for violence-prone militants.

6.4.1.4 Heliostat Control

The FMC heliostat is controlled in elevation and focus. Because of the nature of the system, there is no requirement to control in azimuth once the heliostat is installed in the field. Elevation control is of relatively low response compared with azimuth control because the sun elevation exhibits a small day-to-day change. Moreover, point focus heliostats are more sensitive to azimuth errors, and are especially sensitive to backlash as the age of the heliostats increases (7b), and to misalignment of the azimuth drive (7c). Reduction of these errors would increase the production costs currently projected for point focus heliostats (7d).

6.4.2 Comparison of System Physical Characteristics

Table 6-11 contains a comparison of physical characteristics of the MDAC and FMC 100-MWe concepts. Note that the FMC concept contains more collector mirror area, but less land area, which reflects the higher land utilization of the line focus collector field. Note also that a single local control unit controls almost three times the mirror area than in the MDAC PFS.

Table 6-11 100 MWe PLANT CHARACTERISTICS

	MDAC PFS	FMC Line Focus System
Reflector (heliostat) area	38 m^2 (409 ft^2)	110 m^2 (1,181 ft^2)
Heliostat weight without drive assembly per unit area	35 Kg/m^2 (71 lbs/ft^2)	3.6 Kg/m^2 (7.3 lbs/ft^2)
Number of heliostats	22,914	8,806.5*
Mirror area	0.87 x 10^6 m^2 (9.4 x 10^6 ft^2)	0.97 x 10^6 m^2 (10.4 x 10^6 ft^2)
Collector land area	3.66 x 10^6 m^2 (39.4 x 10^6 ft^2)	2.09 x 10^6 m^2 (22.5 x 10^6 ft^2)
Tower height	242 m (794 ft)	61 m (200 ft)
Height to receiver midpoint	268 m (879 ft)	61 m (200 ft)
Receiver diameter	17 m (56 ft)	1.8 m (6 ft)
Receiver length	25.5 m (84 ft)	10,363 m (34,000 ft) 170 sections, each 61 m (200 ft)

* 8,782 full units plus 49 half units (8,831 controllers).

6.5 PLANT PERFORMANCE WITH NORTH AND SOUTH HELIOSTAT FIELDS

In the initial analysis of the FMC line focus system, the field was sized for operation on winter solstice. In this sizing, the South heliostat field required

half again as many rows as the North field for equivalent energy delivered through the receiver aperture. Economic analysis indicated that the South field was not cost effective (Appendix D).

However, the commercial plant requirements call for plant sizing on the day of maximum energy collection, which is summer solstice. Calculations were made for the output of a South field of the same sizing as for the North field. Comparison of North and South field performance is given in Table 6-12.

Table 6-12 PERFORMANCE COMPARISON OF EQUALLY SIZED NORTH AND SOUTH FIELDS

	Summer solstice concentration (meter-suns)		Equinox concentration (meter-suns)		Winter solstice concentration (meter-suns)	
Hour	North	South	North	South	North	South
5	2.02	2.02	–	–	–	–
6	9.24	10.61	–	–	–	–
7	16.30	17.83	4.92	4.34	–	–
8	29.48	29.54	20.74	17.82	11.15	10.91
9	43.45	43.72	39.79	33.74	27.01	23.96
10	54.59	53.91	54.22	45.69	39.80	34.12
11	62.65	60.40	63.30	53.15	48.72	40.59
12	64.97	82.71	66.43	55.77	50.92	42.85
	9.62×10^7 KJ/module	9.54×10^7 KJ/module	8.70×10^7 KJ/module	7.41×10^7 KJ/module	6.02×10^7 KJ/module	5.28×10^7 KJ/module

The comparison is shown graphically in Figures 6-14 and 6-15. These data indicate that North and South fields perform equally well on the summer solstice, but the South field absorption falls to about 85 percent of that of the North field at the equinox and winter solstice. Figure 6-15 shows that the net electrical output from a South field falls to 72 percent of the North field output at winter solstice. This further reduction is due to decreased receiver efficiency at lower input levels. The average electrical output of a South field is 85 percent of that of the north field.

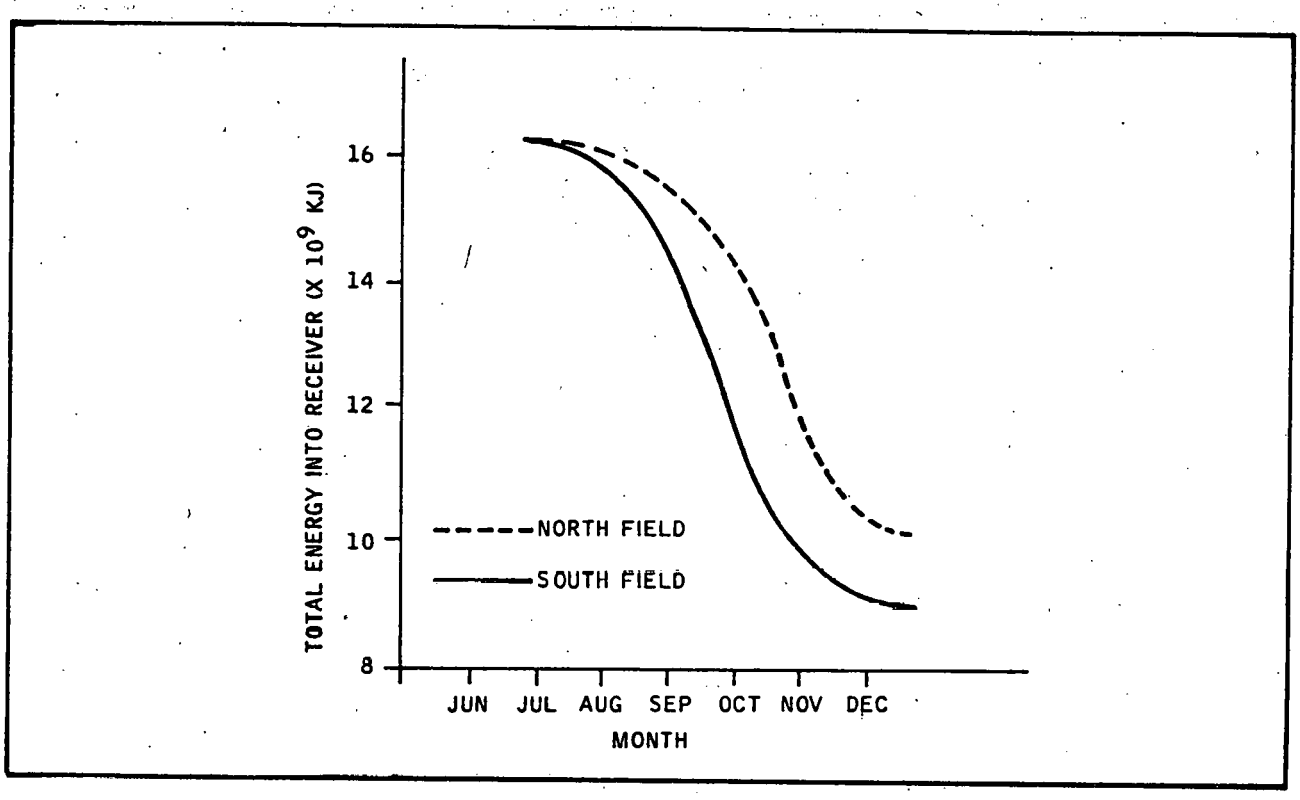

Figure 6-14 PERFORMANCE OF NORTH AND SOUTH FIELDS, SIZED FOR 170 MODULES

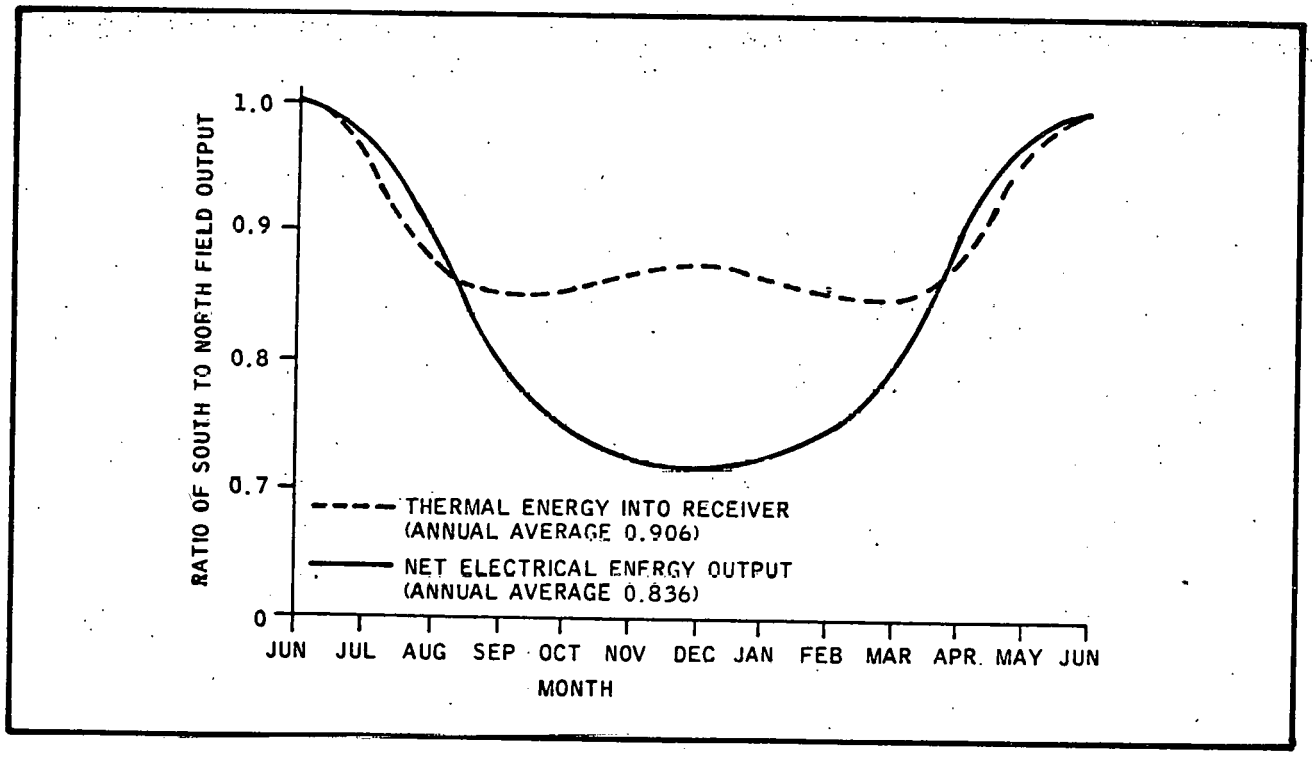

Figure 6-15 COMPARISON OF OUTPUT OF SOUTH TO NORTH FIELD SYSTEMS OF EQUAL SIZING

A plant comprising siamesed receivers fed by North and South fields, respectively, can be expected to provide savings in piping and towers. Countering this, for the same output, more modules would be required. The overall system tradeoff may well indicate that a north/south configured plant is economically superior.

THIS PAGE

WAS INTENTIONALLY

LEFT BLANK

Appendix A

CONCENTRATOR FIELD ANALYSIS MODEL

THIS PAGE

WAS INTENTIONALLY

LEFT BLANK

Appendix A

CONCENTRATOR FIELD ANALYSIS MODEL

This appendix contains the model used to configure the FMC baseline concentrator field, and to examine alternate field configurations.

A.1 DISCUSSION

The performance characteristics of the collector field are pivotal to the operation and design of the other subsystems. The intensity of the reflected flux at the receiver aperture, together with its spatial and temporal distributions, impose strong constraints on the receiver design and the amount of energy storage needed. Similarly, the operational requirements of the collector field largely dictate the type of control subsystem employed. A good prediction of the performance capabilities of candidate collector field configuration is prerequisite to concept selection and design of the rest of the system.

The following collector field parameters are treated as variables. Each can be systematically varied in any order, the others being held constant to assigned values.

- Field width
- Heliostat row spacing, constant or variable
- Heliostat row elevation, constant or variable
- Receiver height
- Surface reflectance
- Tracking error
- Surface roughness
- Axial orientation (North/South, East/West)
- Season of year
- Field type (North, South, East, or West)
- Aperture plane angle.

The program calculates hourly flux intensity profiles on the aperture plane or the inside receiver circumference on any solar day. Also calculated are hourly variations in mirror shaping and screening, and end compensation areas.

Given field size and spacing parameters, the number and positions of heliostat rows is calculated. Individual heliostats are small aperture imaging devices. An ideal heliostat perfectly focused and aimed produces a sharp line image at the aperture, the width of which is determined by the optical path length. The intensity across the width is directly proportional to the divergence angle distribution. The relative intensities at different width distances from the line center are given in Table A-1.

Table A-1 RELATIVE INTENSITY ACROSS THE SOLAR DISK [1,2]

w	I
0.00	1.000
0.50	0.934
0.75	0.788
0.98	0.490
1.00	0.390

An empirical equation, the solar limb darkening equation,[3] fits the distribution to a fair degree.

$$I = I_o(1 - 0.61(1 - \sqrt{1 - w^2})) \quad (1)$$

The divergence angle distribution, and hence the focal line width, is further broadened by tracking and focusing errors, surface irregularities, etc., which can be expressed in angular terms. If these error sources are normally distributed independent quantities, their errors propagate as the square root of the sum of the squares.[4] To give the total perturbation error, the perturbed divergence distribution is obtained by convoluting the initial distribution represented by Equation 1 with a normal distribution function described by the total perturbation error. If the maximum solar divergence angle is $\pm\alpha$, the total perturbation error is σ, and the actual angle is δ, the distribution of δ can be expressed:

$$N_\delta = \frac{N_o}{\alpha\sqrt{2\pi}} \sum_{x=-\alpha} \left(1 - .61\left(1 - \sqrt{1 - \frac{x^2}{\delta^2}}\right)\right) \mathrm{Exp}\left(-\left(\frac{\delta - x}{\sigma}\right)^2 / 2\right) \quad (2)$$

Normalized angular distributions for tracking and surface errors of 2 mrad apiece and 1 mrad apiece, are given in Figure A-1. These distributions determine the shape of all image lines. The width and intensity vary with focal length.

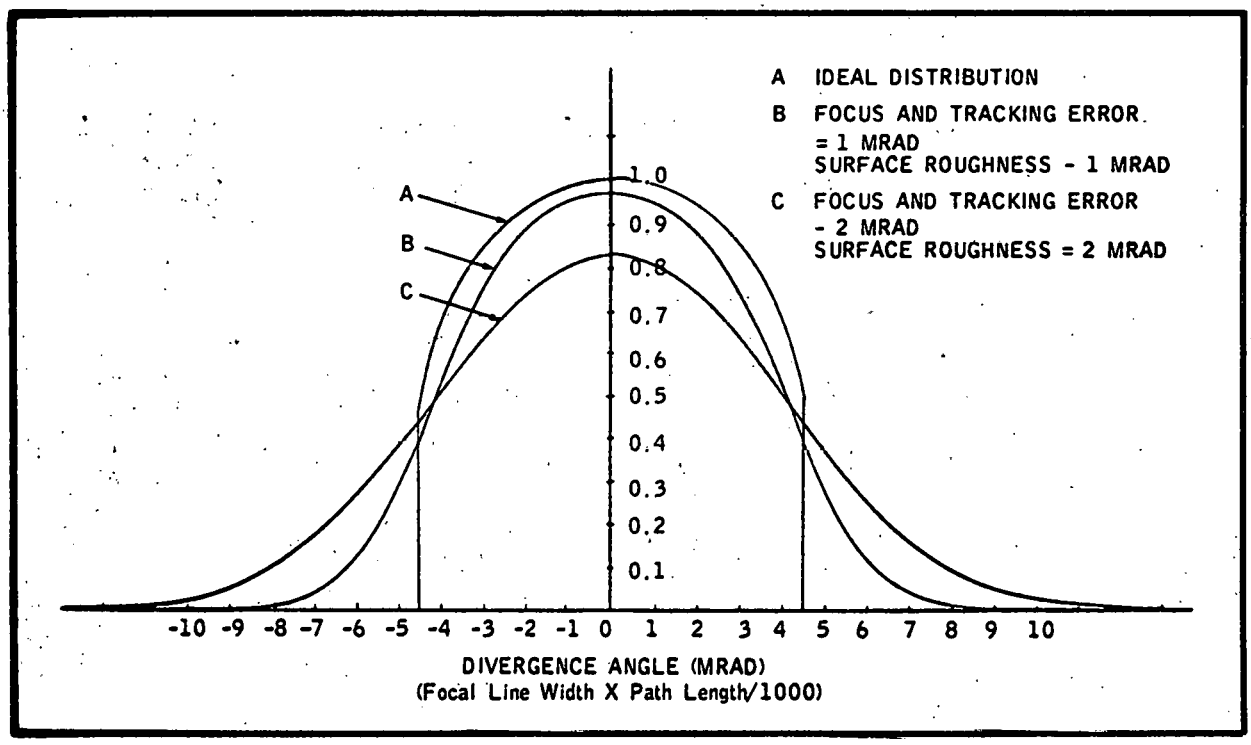

Figure A-1 IDEAL AND PERTURBED SOLAR DIVERGENCE ANGLE DISTRIBUTION

Shadowing factors for each mirror row are calculated. Screening factors are calculated, bearing in mind that partially shadowed surfaces are operationally unscreened. The location of the receiver shadow is determined and its effect is included. Reflectance as a function of incident angle is calculated. All loss factors are collected into an overall value, and the intensity profile of each heliostat row as projected onto the receiver plane is calculated and summed to obtain the overall flux. The procedure is repeated for each hour of the day to obtain an hourly sequence of receiver aperture flux spectra.

A.2 DIVERGENCE ANGLE DISTRIBUTION

The method and equation for determining the normalized divergence angle distribution has been given. The initial unperturbed intensity factor, N_o, is:

$$N_o = \frac{w}{2(1-\mu(1-\pi/4))ad} \tag{1}$$

where

w = mirror width (10 feet)
a = the solar divergence half angle (4.6 mrad)
μ = Solar limb darkening factor (0.61)
d = the optical path length.

This factor was obtained by integrating the unperturbed solar divergence distribution and equating the integral to a unit solar intensity over the mirror width, w.

A.3 TRACKING AND DISPLACEMENT RELATIONSHIPS

A cylindrical mirror behaves like a plane mirror in the axial plane, and like a parabolic mirror in the normal plane. Solar rays with azimuth angle β and elevation angle θ incident upon a north/south or east/west axis cylindrical mirror can be analyzed by reduction to the projected angles ϕ in the north/south axis and ψ in the east/west plane (Figure A-2.) It can be shown that:

$$\tan\phi = \cos\beta/\tan\theta \tag{2}$$

$$\tan\psi = \sin\beta/\tan\theta. \tag{3}$$

An array of cylindrical mirror focusing on a central line receiver tracks the sun by rotating about the planar axis with the relationship:

$$\alpha=(\gamma - \psi \text{ (or } \phi))/2 \tag{4}$$

where

α = mirror normal displacement, relative to earth normal

γ = $\tan^{-1} y_i/h$

y_i = mirror distance from receiver axis

h = receiver height.

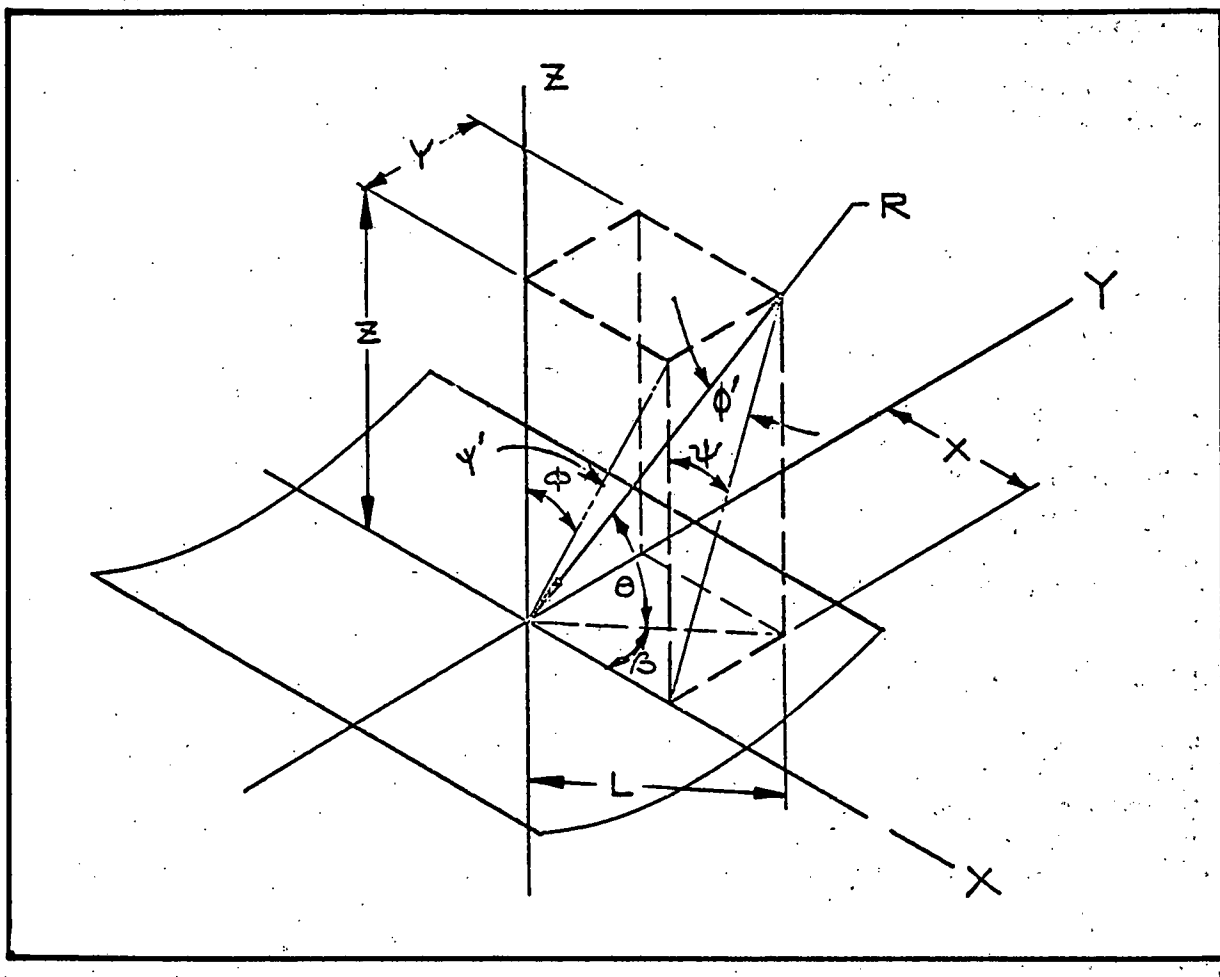

Figure A-2 ANGULAR ANALYSIS DIAGRAM

The sign convention is that angles are positive when pointing toward the receiver. Upon rotation about the mirror axis, the reflected ray describes a cone with a constant angle relative to the normal plane

$$\tan\phi' = \cos\beta \Big/ \sqrt{\sin^2\beta + \tan^2\theta} \qquad (5)$$

$$\tan\psi' = \sin\beta \Big/ \sqrt{\cos^2\beta + \tan^2\theta} \qquad (6)$$

The path length of the ray upon intercepting the receiver is:

$$d = \left(\sqrt{y_i^2 + h^2}\right) \Big/ \cos\left(\phi'(\text{or}\,\psi')\right) \tag{7}$$

and the linear displacement of the interception point along the receiver axis is:

$$x = \left(\sqrt{y_i^2 + h^2}\right) \tan\left(\phi'(\text{or}\,\psi')\right) \tag{8}$$

In addition, if the mirror rotates in one axis only, and is horizontal in the other, the angle, B , between the incident ray and the mirror normal is:

$$\cos B = \sin\theta\,(\cos\alpha + \sin\alpha \tan(\psi \text{ or } \phi)) \tag{9}$$

If the mirror field is not flat, the height term, h, is the height difference between receiver and mirror.

A. 4 SHADOWING AND SCREENING FACTORS

The performance of an isolated heliostat would be essentially governed by the factors described above. However, when placed in an array, neighboring heliostats shadow each other in two ways:

- A mirror can be shaded from incident solar rays.
- A mirror's view of the receiver can be obscured.

The former is called shading; the latter is screening. Shading and screening for the pertinent cases is illustrated in Figure A-3. If S_N is the center-center heliostat spacing, it can be shown that the length of mirror N, ℓ_N , screened by mirror N-1 is:

$$\ell_N = \frac{[.5w(\cos\alpha_{N-1} + \cos\alpha_N + (\sin\alpha_{N-1} + \sin\alpha_N)\tan(\gamma_N - b_N) - S_{N-1}]\cos(\gamma_N - b_N) -}{\cos(\gamma_N - \alpha_N - b_N)}$$

$$\frac{(Z_N - Z_{N-1})\sin(\gamma_N - b_N)}{\cos(\gamma_N - \alpha_N - b_N)} \tag{10}$$

where

Z_N is the heliostat elevation and ℓ_N is the focusing convergence angle:

$$b_N = \tan^{-1}\left(\frac{.5w - d\tan\alpha}{d}\right). \tag{11}$$

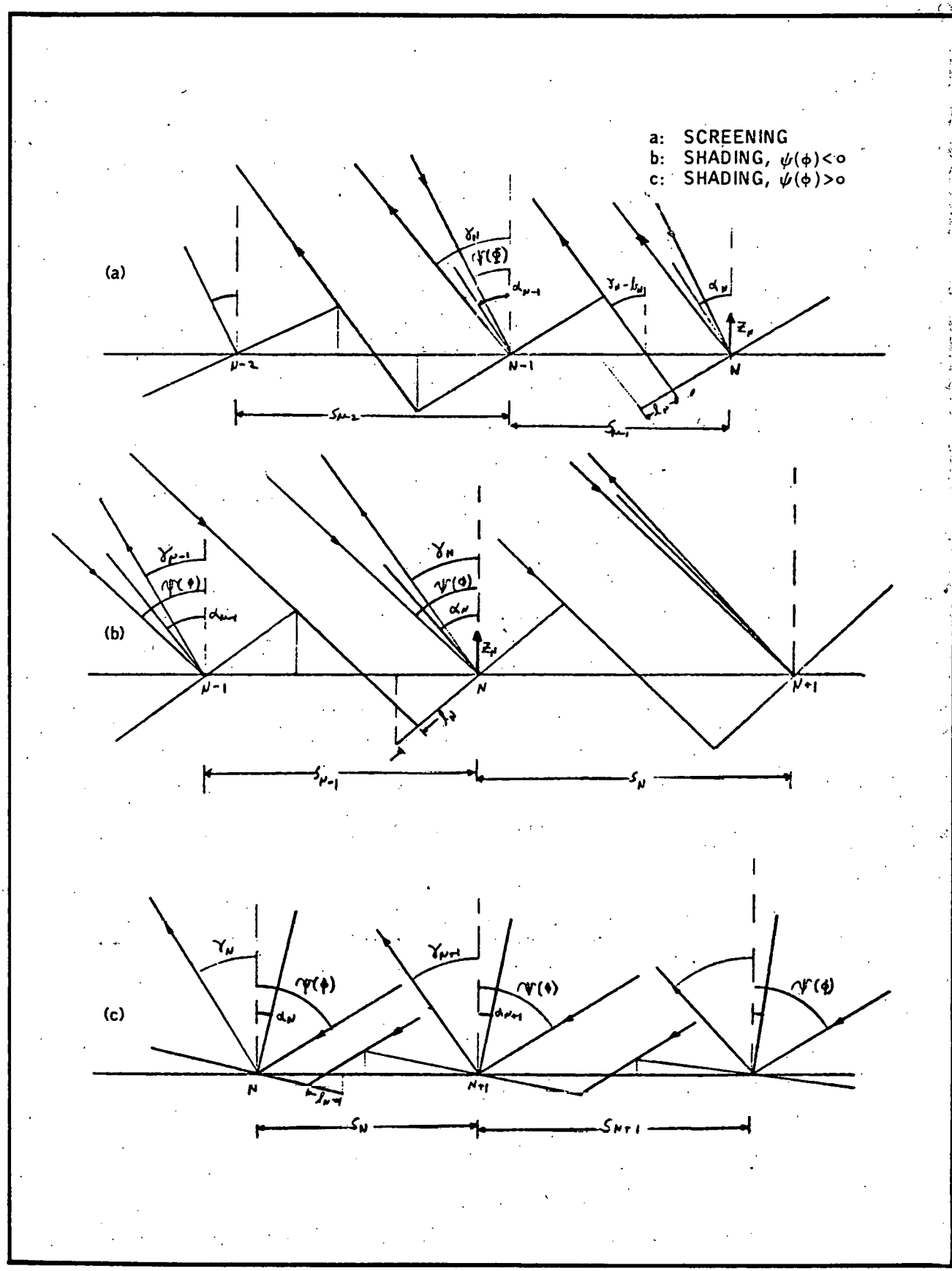

Figure A-3 SHADING AND SCREENING GEOMETRIC RELATIONSHIPS

The screening factor, F_{scr}, is

$$F_{scr} = (w - \ell_N)/w. \tag{12}$$

There are two cases of shading, corresponding to the cases of positive and negative projected incoming solar angle.

- Case 1 -- $\psi(\phi)<0$ (Figure 6b)

  The receiver lies between the sun and the heliostat. Mirror N shadows mirror N+1. Then, the shaded mirror length, ℓ_N, is:

$$\ell_N = \frac{[0.5w(\cos\alpha_{N-1} + \cos\alpha_N) - (\sin\alpha_{N-1} + \sin\alpha_N)\tan(\psi(\phi)) - S_{N-1}]\cos(\psi(\phi))+}{\cos(\psi(\phi) + \alpha_N)} \tag{13}$$

$$\frac{(Z_N - Z_{N-1})\sin(\psi(\phi))}{\cos(\psi(\phi) + \alpha_N)}$$

- Case 2 - $\psi(\phi)>0$ (Figure 6c)

  The heliostat lies between the sun and the receiver. Mirror N+1 shadows mirror N.

$$\ell_N = \frac{[0.5w(\cos\alpha_N + \cos\alpha_{N+1}) - (\sin\alpha_N + \sin\alpha_{N+1})\tan(\psi(\phi) - S_N]\cos(\psi(\phi))+}{\cos(\psi(\phi) + \alpha_N)} \tag{14}$$

$$\frac{(Z_{N+1} - Z_N)\sin(\psi(\phi))}{\cos(\psi(\phi) + \alpha_N)}$$

In both cases, the shading factor, F_{sh}, is

$$F_{sh} = (w - \ell_N)/w. \tag{15}$$

Inspection of Figure A-3 reveals that shading and screening are normally exclusive terms. When both occur simultaneously, it is always on the same end of the mirror. In this case, the smaller factor dominates. In practice, one of the factors is always unity for a given heliostat. In the limit, for closely spaced fields where shading or screening factors are less than unity, the sum over the collector field of the product of the shading or screening factors and the individual cos B values (Equation 9) converges to the cosine of the solar elevation angle.

A.5 RECEIVER/TOWER SHADOWING

When the incident direction is negative, the receiver and towers cast shadows on the mirror field. To correct for the receiver shadow, the position of the shadow is calculated by the appropriate equation (Equation 16 or 17).

For a flat or linearly terraced field,

$$y_s = \frac{h \tan(\psi(\phi))}{1 - k \tan(\psi(\phi))} \tag{16}$$

where k = slope of terracing.

For a parabolic terraced field,

$$y_s = \frac{\sqrt{1 + 4hk \tan^2(\psi(\phi)) - 1}}{2k \tan(\psi(\phi))} \tag{17}$$

where k = slope of terracing.

For a linear terraced field, the width, w_s, of the shadow is:

$$w_s = (w_r + d_s a)/\cos(\psi(\phi) + \tan^{-1} k) \tag{18}$$

and for a parabolic terraced field, the width, w_s, of the shadow is:

$$w_s = (w_r + d_s a)/\cos(\psi(\phi) + \tan^{-1}(2k x_s)) \tag{19}$$

where

w_s = cross sectional width of the receiver

d_s = path length (Equations 7 and 8)

x_s = linear displacement (Equations 7 and 8).

Because the shadow displacement is in the opposite direction as the reflection displacement, the receiver shadow only partially overlaps the working reflecting field. The effective receiver shadowing is reduced by the factor:

$$F_{rs} = (L - 2x_s)/L \tag{20}$$

where L is the receiver length.

The heliostats lying at $y_s \pm .5w_s$ are reduced by a factor weighted by the amount of mirror and field overlap. Tower shadows are calculated in a similar manner, assuming rectangular pyramid-shaped towers with a fractional opacity value.

A.6 APERTURE INTENSITY PROFILES

The aperture is tilted at an angle, T, with respect to the horizontal. The projected beam width, w_p , from each heliostat is:

$$w_p = w_{\delta N} / \cos (\gamma_N - T) \tag{21}$$

where $w_{\delta N}$ is the normal beam width for an angular divergence δ from a mirror at Row N and is equal to $\delta_i d_N$. The aperture plane is divided into finite intervals, the equivalent divergence angle for each increment is calculated, the intensity factor for that angle is interpolated from the divergence angle distribution curve, and the appropriate intensity contribution, corrected for all losses, is added to the intensity at the interval.

A.7 DIRECT INTENSITY DISTRIBUTION ON INNER RECEIVER CAVITY WALLS

The direct intensity distribution of inner surfaces is useful for the design and evaluation of alternate forced-flow boiler and superheater configurations. The intensity distribution calculation portion of the field performance program was modified to obtain the distribution around the inside receiver circumference.

The calculation was performed using the following procedure. The principle ray of the beam from a heliostat passes through the center of the aperture with an angle, Y, relative to the vertical (Figure A-4.)

The aperture makes an angle, T, with respect to the horizontal. The normal width of the beam entering the aperture is 4/cos (T - Y) or the calculated divergent width, whichever is smaller. The position along the circumference, C_o , intersected on this principal ray is calculated by the relationship

$$C_o = 3\phi_o$$

where

$$\phi_o = \pi/2 + T - Y - \theta_o$$

$$\theta_o = \cos^{-1} \frac{2.24 \sin (T-Y)}{3}$$

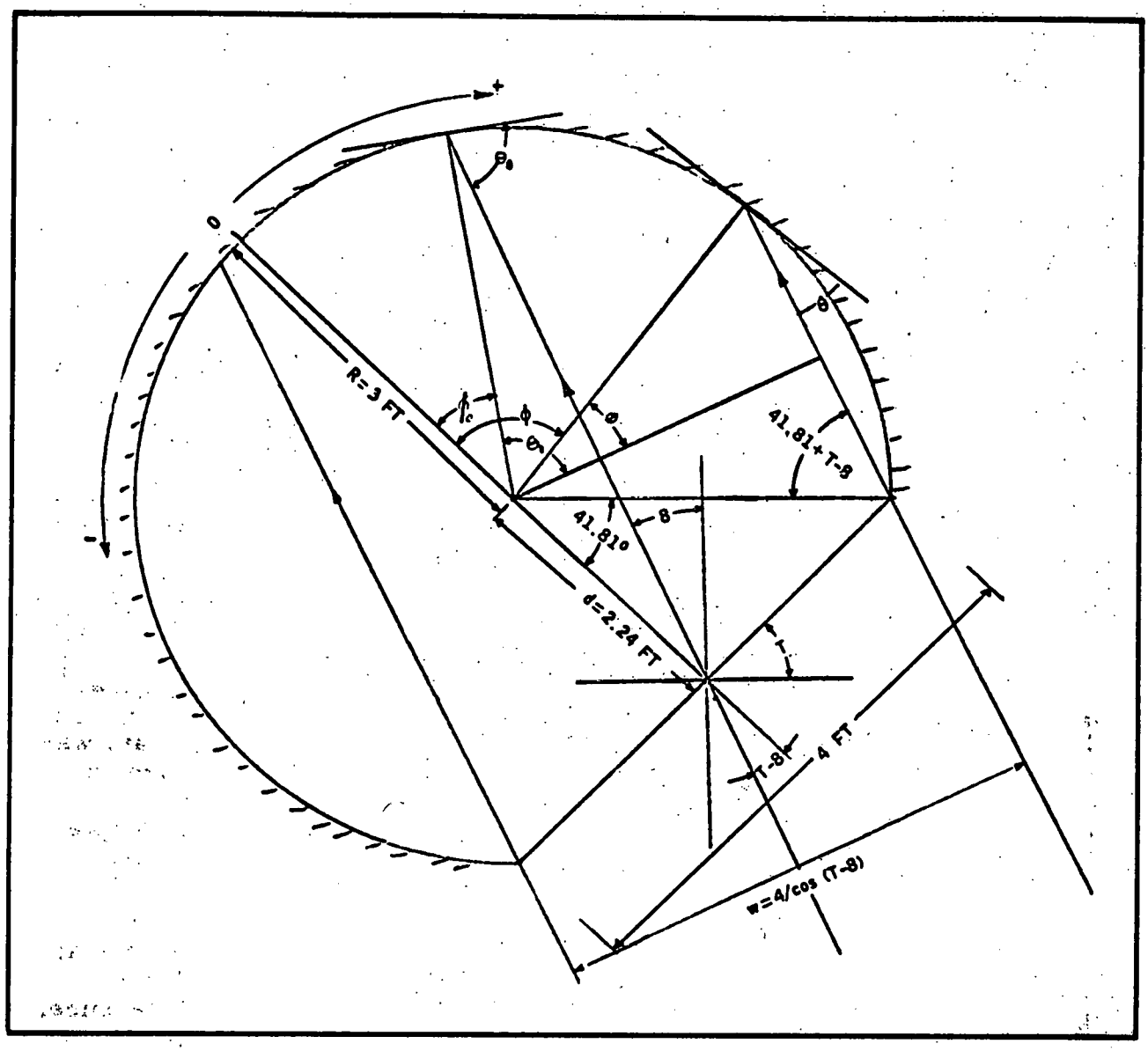

Figure A-4 GEOMETRY FOR DETERMINING INNER WALL INTENSITY DISTRIBUTIONS

The circumference is divided into finite-size elements of length ΔC. The corresponding normal-width element, ΔW, is

$$\Delta W = \Delta C \sin \theta$$

To good approximation, the pathlength, D_o, traveled by the beam element, ΔW_o, is

$$D_o = D_1 + 2.24 \cos (T-\gamma)$$

where D_1 is the calculated pathlength from heliostat to aperture plane.

Given the total pathlength and the normal beam width increment, the angle corresponding to the angular divergence intensity distribution function, and the product of this intensity term and sin is added into the ΔC_o interval.

Since $\Delta C = 3\Delta\phi$, finite intervals can be successively calculated around the circumference with

$$\phi_i = \phi_o \pm i\ \Delta C/3$$

$$\theta_i = \theta_o \pm i\ \Delta C/3$$

and

$$W_i = W_i \pm \Delta C \sin(\phi_o - \Delta C/3)$$

with

$$W_o = -0.5\ \Delta C \sin\phi_o \text{ for } \Delta C < 0$$

$$W_o = 0.5\ \Delta C \sin\phi_o \text{ for } \Delta C > 0$$

and

$$D_i = D_o + 3 \sin(\phi_{i-1} + \Delta C/3).$$

The intensity incremental summation described is performed for each interval until $W\Delta$ exceeds the normal beam half-width.

Hourly intensity distributions at winter solstice for a north field sized for solar noon at winter solstice are presented in Figure A-5. The irregularities in the curves are due to a combination of the finite intervals chosen and the fact that the receiver "sees" gaps in the near portion of the mirror field. The integrated area under the curve agrees with the product of the average aperture intensity and the aperture area to within 0.2 percent.

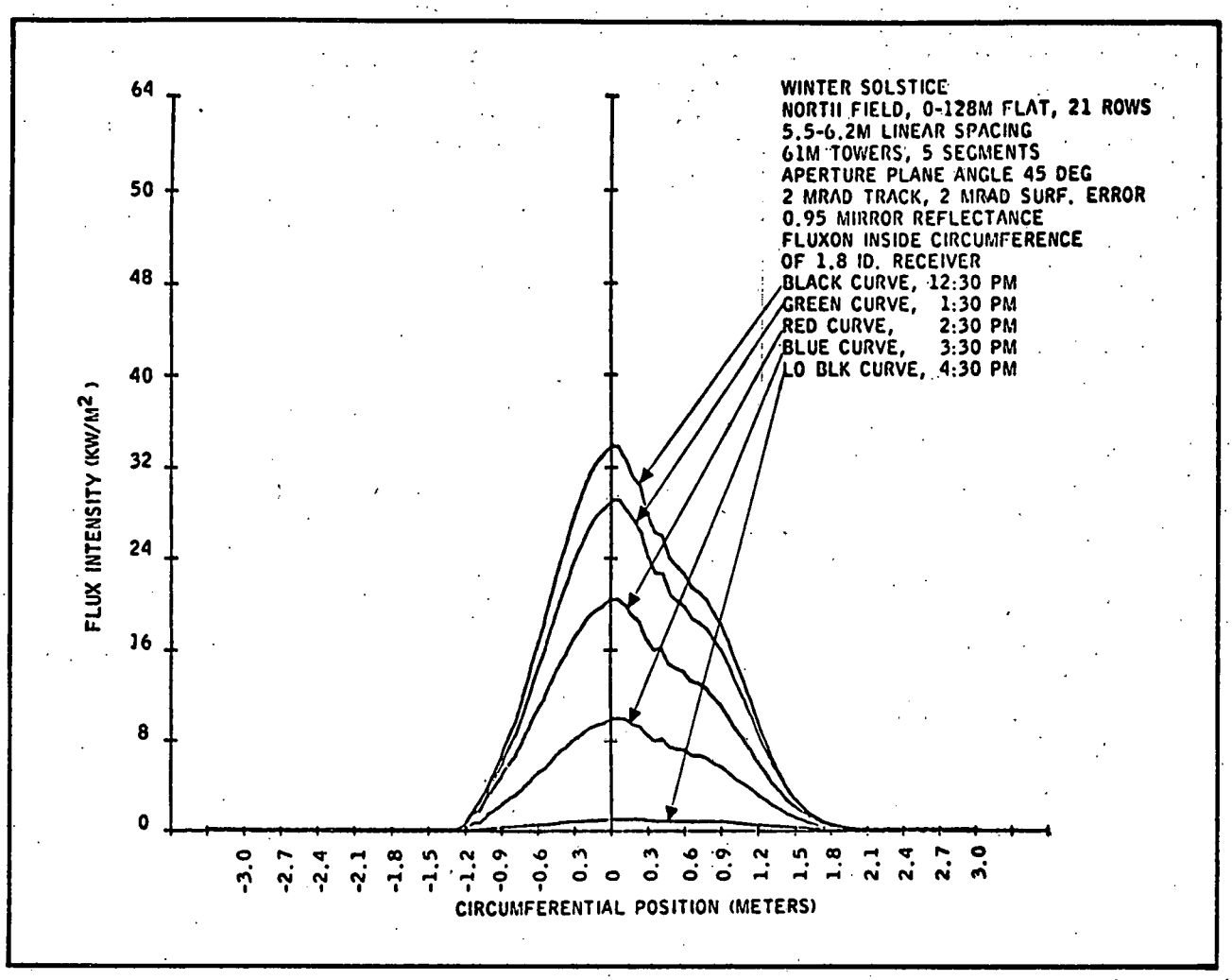

Figure A-5 DIRECT FLUX INTENSITY PROFILE ON INSIDE RECEIVER CIRCUMFERENCE

A.8 TYPICAL OUTPUTS OF MODEL

```
TRACKING ERROR STANDARD DEVIATION, IN MRAD>2
SURFACE ROUGHNESS STANDARD DEVIATION, IN MRAD>2
SOLAR LIMB DARKENING FACTOR>.61
   1      1046.346       0.00
   2      1041.563        .40
   3      1027.297        .80
   4      1003.818       1.20
   5       971.571       1.60
   6       931.191       2.00
   7       883.497       2.40
   8       829.485       2.80
   9       770.318       3.20
  10       707.289       3.60
  11       641.788       4.00
  12       575.242       4.40
  13       509.066       4.80
  14       444.595       5.20
  15       383.029       5.60
  16       325.380       6.00
  17       272.439       6.40
  18       224.751       6.80
  19       182.613       7.20
  20       146.088       7.60
  21       115.032       8.00
  22        89.129       8.40
  23        67.935       8.80
  24        50.926       9.20
  25        37.537       9.60
  26        27.200      10.00
  27        19.372      10.40
  28        13.558      10.80
  29         9.323      11.20
FIELD WIDTH IN METERS>121.93
FIELD EDGE INNER DISTANCE IN METERS>0
APERTURE ANGLE WITH HORIZONTAL (DEG)>45
MINIMUM MIRROR SPACING IN METERS>3.7
MAXIMUM MIRROR SPACING IN METERS>6.9
IF LINEAR SPACING ENTER 1>0
NUMBER OF MIRROR ROWS= 27
MAXIMUM FIELD EDGE ELEVATION IN METERS>0
IF LINEAR SPACING ENTER 1>1
TOWER HEIGHT IN METERS>60.96
MIRROR REFLECTANCE>.9
NUMBER OF 61 METER SEGMENTS>17
RECEIVER LENGTH= 1036.32 METERS
TOWER OPACITY FACTOR>.25
FIELD TYPE (1=N,2=S,3=W,4=E)>1
LATITUDE (DEG)>35
FIELD SIZING DESIGN POINT. DAY OF YEAR>81
 HOUR OF DAY>15
```

DAY OF YEAR= 81, HOUR OF DAY=15.0
NORTH FIELD
EL. ANGLE= 35.48, AZ. ANGLE= -60.27, PSI= -50.62, PHI=-34.83

ROW	XDIS	PDIST	FSHD	FSCR	FCOS	XSAREA	ALFA	MSTR
1	1.52	86.24	1.000	1.000	.677	-185.85	18.13	1.000
2	5.23	86.53	1.000	1.000	.683	-186.48	19.86	1.499
3	8.94	87.13	1.000	1.000	.688	-187.78	21.58	1.510
4	12.66	88.05	1.000	1.000	.693	-189.76	23.28	1.514
5	16.40	89.28	1.000	1.000	.697	-192.41	24.94	1.511
6	20.17	90.81	1.000	1.000	.700	-195.70	26.57	1.503
7	23.97	92.64	1.000	1.000	.702	-199.65	28.15	1.488
8	27.81	94.76	1.000	1.000	.704	-204.22	29.68	1.468
9	31.70	97.17	1.000	1.000	.706	-209.41	31.15	1.446
10	35.64	99.86	1.000	1.000	.707	-215.21	32.57	1.418
RECIEVER SHADOW HERE, ROW 11, F= .876984								
11	39.63	102.83	1.000	1.000	.707	-221.61	33.93	1.216
RECIEVER SHADOW HERE, ROW 12, F= .590727								
12	43.70	106.07	1.000	1.000	.707	-228.60	35.23	.799
13	47.84	109.58	1.000	1.000	.707	-236.18	36.47	1.306
14	52.06	113.37	1.000	1.000	.706	-244.33	37.66	1.262
15	56.38	117.43	1.000	1.000	.705	-253.08	38.80	1.217
16	60.80	121.76	1.000	1.000	.704	-262.42	39.88	1.172
17	65.34	126.37	1.000	1.000	.703	-272.36	40.91	1.127
18	70.00	131.27	1.000	1.000	.702	-282.91	41.89	1.083
19	74.80	136.46	1.000	1.000	.700	-294.10	42.82	1.039
20	79.75	141.96	1.000	1.000	.699	-305.96	43.72	.997
21	84.88	147.78	1.000	1.000	.697	-318.50	44.57	.955
22	90.18	153.94	1.000	1.000	.695	-331.77	45.38	.915
23	95.69	160.46	1.000	1.000	.693	-345.81	46.16	.875
24	101.43	167.35	1.000	1.000	.691	-360.68	46.91	.837
25	107.41	174.66	1.000	1.000	.690	-376.42	47.62	.800
26	113.66	182.40	1.000	1.000	.688	-393.11	48.31	.764
27	120.22	190.62	1.000	1.000	.686	-410.83	48.97	.729

BUTTERFLY AREA= -7105
END LOSSES= 0.00 %

CIRC. POS	INTENSITY	% ENERGY	AV. INT
-1.22	.40	.03	.40
-1.16	1.34	.20	.87
-1.10	2.01	.46	1.21
-1.04	2.77	.84	1.56
-.98	4.16	1.42	2.06
-.91	5.18	2.15	2.56
-.85	5.77	3.01	3.03
-.79	7.55	4.10	3.57
-.73	8.90	5.39	4.14
-.67	10.33	6.89	4.74
-.61	11.29	8.59	5.34
-.55	12.87	10.52	5.97
-.49	14.50	12.70	6.64
-.43	16.17	15.13	7.32
-.37	17.22	17.72	7.99
-.30	18.55	20.53	8.65
-.24	19.97	23.55	9.32
-.18	21.39	26.79	10.00
-.12	22.10	30.15	10.65
-.06	23.28	33.69	11.29
0.00	24.26	37.34	11.90
.06	24.52	41.09	12.49
.12	24.58	44.90	13.04
.18	24.53	48.61	13.51

.24	23.13	52.20	13.92
.30	22.99	55.78	14.29
.37	21.47	59.12	14.58
.43	22.00	62.50	14.85
.49	21.04	65.73	15.07
.55	20.27	68.89	15.26
.61	20.10	71.97	15.42
.67	19.70	75.00	15.56
.73	19.22	77.91	15.66
.79	18.09	80.71	15.74
.85	16.83	83.31	15.78
.91	15.45	85.75	15.78
.98	14.37	87.99	15.75
1.04	12.94	90.02	15.68
1.10	11.36	91.80	15.58
1.16	9.78	93.38	15.44
1.22	8.58	94.73	15.28
1.28	7.14	95.87	15.09
1.34	6.08	96.84	14.89
1.40	4.88	97.62	14.66
1.46	3.83	98.24	14.42
1.52	2.91	98.72	14.18
1.58	2.36	99.11	13.92
1.65	1.69	99.40	13.67
1.71	1.33	99.61	13.42
1.77	.87	99.77	13.17
1.83	.66	99.88	12.92
1.89	.36	99.94	12.68
1.95	.25	99.98	12.44
2.01	.08	100.00	12.21

INTEGRATED INTENSITY= 39.83 METER SUNS
AVERAGE SHADING FACTOR=1.00, AVERAGE SCREENING FACTOR=1.00
MAXIMUM APERTURE FLUX TO NUMBER OF ROWS RATIO= .935
MIRROR AREA EFFICIENCY= 59.46 %
TOTAL FIELD EFFICIENCY= 48.24 %
WORKING MIRROR EFFICIENCY= 69.37 %
WORKING FIELD EFFICIENCY= 56.27 %
PLOT ARRAY IN DATA LINES 6001 TO 6005

A.9 SOURCE LISTING OF MODEL

```
 SAVED 07/27  22:02 VERSION 2.4
10 DIM X(200),Y(200),Z(200),W(42),Q(36),R(30),S(42),D(50),E(50),F(50)
20 DIM G(50),B(35)
30 INPUT IN IMAGE"TRACKING ERROR STANDARD DEVIATION, IN MRAD#":E1
60 INPUT IN IMAGE"SURFACE ROUGHNESS STANDARD DEVIATION, IN MRAD#":E2
90 INPUT IN IMAGE"SOLAR LIMB DARKENING FACTOR#":E3
100 J2=5991
102 J3=' DATA
104 J4=','
106 OPEN /PLOTDATA/,SYMBOLIC FIXED(70) OUTPUT, 10
120 E4=5*SQR(E1**2+E2**2)
130 E5=5/((1-0.2416*E3)*0.0046*E4*SQR(2*PI))
140 E6=1/(E4*SQR(2))
150 FOR I=1 TO 50
160 F(I)=0
170 NEXT I
180 FOR I=1 TO 50
190 E7=2*(I-1)
200 FOR J=-23 TO 23
210 E8=((E7-J)*E6)**2
220 IF E8>227.96 THEN 240
230 F(I)=F(I)+(1-E3*(1-SQR(1-(J/23)**2)))*EXP(-E8)
240 NEXT J
250 F(I)=E5*F(I)
260 PRINT IN FORM"4% 5B 4%.3% 5B %%.%%/":I,F(I),.4*(I-1)
270 IF F(I)/F(1)<0.01 THEN 290
280 NEXT I
290 E0=(I-1)*0.4
300 INPUT IN IMAGE"FIELD WIDTH IN METERS#":S3
330 INPUT IN IMAGE"FIELD EDGE INNER DISTANCE IN METERS#":D6
360 S3=S3*3.2808
370 INPUT IN IMAGE"APERTURE ANGLE WITH HORIZONTAL (DEG)#":T0
400 T0=T0*PI/180
410 INPUT IN IMAGE"MINIMUM MIRROR SPACING IN METERS#":S4
440 INPUT IN IMAGE"MAXIMUM MIRROR SPACING IN METERS#":S5
470 S1=0
480 INPUT IN IMAGE"IF LINEAR SPACING ENTER 1#":S1
510 D6=D6*3.2808
520 S4=S4*3.2808
530 S5=S5*3.2808
540 IF S1=0 THEN 570
550 K1=(S5-S4)/S3
560 GOTO 580
570 K1=(S5-S4)/S3**2
580 D(1)=5+D6
590 FOR I=2 TO 100
600 IF S1=1 THEN 630
610 D(I)=K1*(D(I-1)+5)**2+D(I-1)+S4
620 GOTO 640
630 D(I)=K1*(D(I-1)+5)+D(I-1)+S4
640 IF D(I)+5>S3+D6 THEN 660
650 NEXT I
660 N=I-1
670 PRINT "NUMBER OF MIRROR ROWS=":N
680 INPUT IN IMAGE"MAXIMUM FIELD EDGE ELEVATION IN METERS#":S6
710 S6=S6*3.2808
720 S2=0
730 INPUT IN IMAGE"IF LINEAR SPACING ENTER 1#":P2
760 IF P2=0 THEN 790
770 K2=S6/S3
```

```
780 GOTO 800
790 K2=S6/S3**2
800 INPUT IN IMAGE"TOWER HEIGHT IN METERS#":H1
830 H1=H1*3.2808
840 INPUT IN IMAGE"MIRROR REFLECTANCE#":F9
880 FOR I=1 TO N
890 IF P2=1 THEN 920
900 E(I)=K2*(D(I)-D(1))**2
910 GOTO 930
920 E(I)=K2*(D(I)-D(1))
930 G(I)=ATN((H1-E(I))/D(I))
940 NEXT I
950 INPUT IN IMAGE"NUMBER OF 61 METER SEGMENTS#":K1
970 L1=200*K1
980 PRINT IN IMAGE"RECEIVER LENGTH=%%%%%.%% METERS":L1*.3048
990 INPUT IN IMAGE"TOWER OPACITY FACTOR#":D5
1010 INPUT IN IMAGE"FIELD TYPE (1=N,2=S,3=W,4=E)#":F1
1030 INPUT IN IMAGE "LATITUDE (DEG)#":L6
1080 W0=-1
1090 IF F1=3 THEN 1110
1100 GOTO 1120
1110 W0=1
1120 W1=W0
1130 F2=1
1140 IF F1=1 THEN 1160
1150 GOTO 1170
1160 F2=-1
1170 INPUT IN IMAGE"FIELD SIZING DESIGN POINT. DAY OF YEAR# HOUR OF DAY#&
":D,H
1200 Q9=0
1210 J=H-12
1220 GOTO 1290
1230 Q9=1
1240 INPUT IN IMAGE"1ST DAY# LAST DAY# STARTING TIME# INTERVAL#":D,D9,H9,&
,H
1260 FOR I=D TO D9
1270 PRINT "DAY":D;" TO DAY":D9;"--START AT":H9;", ":H;"HOUR INTERVALS"
1280 FOR J=H9-12 TO 9 STEP H
1290 H8=PI/180
1300 P=0.985626283*(D-172)*H8
1310 A=ASIN(0.398749069*COS(P))
1330 Q1=SIN(L6*H8)
1340 Q2=COS(L6*H8)
1350 A1=SIN(A)
1360 A2=COS(A)
1370 W1=-W0
1380 T1=SIN(15*J*H8)
1390 T2=COS(15*J*H8)
1400 Q=Q2*A2*T2+A1*Q1
1410 IF Q<=0 OR Q>1 THEN 1400
1440 B=PI/2-ACOS(Q)
1460 X=A2-Q*Q2*T2
1470 Y=A1-Q*Q1
1480 Z=-Q*Q2*T1
1490 R=INT((X*Q1*T2-Y*Q2+Z*Q1*T1)/SQR(X**2+Y**2+Z**2)*10**10)/10**10
1530 T=-ACOS(R)
1540 IF T <= 0 THEN 1560
1550 T=T-PI
1560 IF J >= 0 THEN 1630
1570 T=-T
```

```
1630 P=1
1635 T=W1*T
1640 X4=SIN(T)/TAN(B)
1650 X5=COS(T)/TAN(B)*F2
1660 X8=COS(T)/SQR(SIN(T)**2+TAN(B)**2)*F2
1670 X9=SIN(T)/SQR(COS(T)**2+TAN(B)**2)
1680 GOTO 3770
1690 PRINT "ROW    XDIS      PDIST    FSHD    FSCR    FCOS     XSAREA     ALFA &
  MSTR"
1710 FOR K=1 TO 200
1720 X(K),Y(K),Z(K)=0
1730 NEXT K
1750 X1,X2,X3,G8,G4=0
1760 T4=T
1770 IF F1>2.5 THEN 1800
1780 S8=ATN(X5)
1790 GOTO 1810
1800 S8=ATN(X4)
1810 A1=(PI/2-G(1)-S8)/2
1820 A3=(PI/2-G(N)-S8)/2
1830 A4=K2*TAN(S8)
1840 A5=D(N)-5*(COS(A3)-(SIN(A3))*TAN(S8))
1850 IF A4=0 THEN 1870
1860 IF P2=0 THEN 1910
1870 A7=(A4*D(N)-D(N)+5*COS(A3)-5*SIN(A3)*TAN(S8))/(A4-1)
1880 T1=H1*TAN(S8)/(1-A4)
1890 T2=1/COS(S8+ATN(K2))
1900 GOTO 1950
1910 IF S8<0 THEN 1930
1920 A7=(1-SQR(1-4*A4*(D(N)-5*COS(A3)+5*SIN(A3)*TAN(S8)-A4*D(N)**2)))/(2&
*A4)
1930 T1=(SQR(1+4*H1*A4*TAN(S8))-1)/(2*A4)
1940 T2=1/COS(S8+ATN(2*K2*T1))
1950 S9,F4,F6,S7,S1,D1,D2=0
1960 FOR K=1 TO N
1970 D0=SQR(D(K)**2+(H1-E(K))**2)
1980 IF F1>2.5 THEN 2020
1990 X1=D0*X9
2000 D1=D0/COS(ATN(X9))
2010 GOTO 2040
2020 X1=X8*D0
2030 D1=D0/COS(ATN(X8))
2040 G6=1
2050 IF Q9>0.5 THEN 2080
2060 B(K)=X1
2070 GOTO 2120
2080 IF ABS(X1)<ABS(B(K)) THEN 2120
2090 G6=1-(ABS(X1)-ABS(B(K)))/L1
2100 IF G6>0 THEN 2120
2105 IF K=1 THEN 4400
2110 G6=0
2120 G8=G8+G6
2130 X2=X2+X1
2140 IF Q9>0.5 THEN 2160
2150 B(35)=ABS(X2)
2160 IF K=N THEN 2180
2170 A2=(PI/2-G(1+K)-S8)/2
2180 IF S8<0 THEN 2280
2190 IF K=N THEN 2420
2200 A9=D(K+1)-5*(COS(A2)-SIN(A2)*TAN(S8))-(E(K+1)-E(K))*TAN(S8)
```

```
2210 IF D(K+1)<A7 THEN 2240
2220 A8=A5-(E(N)-E(K))*TAN(S8)
2230 IF A8<A9 THEN 2260
2240 S7=5*(COS(A1)-SIN(A1)*TAN(S8))+D(K+1)-A9
2250 GOTO 2270
2260 S7=5*(COS(A1)-SIN(A1)*TAN(S8))+D(N)-A8
2270 S9=((S7+D(K)-D(K+1))*COS(S8))/COS(S8+A2)
2280 IF S9>0 THEN 2300
2290 S9=0
2300 F3=(10-S9)/10
2310 IF S8>0 THEN 2350
2320 IF K=N THEN 2350
2330 S7=5*(COS(A1)+COS(A2)-(SIN(A1)+SIN(A2))*TAN(S8))+(E(K+1)-E(K))*TAN(&
S8)
2340 S9=((S7+D(K)-D(K+1))*COS(S8))/COS(S8+A2)
2350 IF F3<0 THEN 3510
2360 IF (A2+S8)*SGN(A2)>0 THEN 2390
2380 GOTO 2550
2390 IF K=1 THEN 2550
2400 GOTO 2430
2420 F3=1
2430 F5=ATN((5-D1*0.000152)/D1)
2440 G7=5*(COS(A0)+COS(A1)+(SIN(A0)+SIN(A1))/TAN(G(K)+F5))
2445 G7=G7-(E(K)-E(K-1))/TAN(G(K)+5)
2450 G9=(G7+D(K-1)-D(K))*(SIN(G(K)+F5))/SIN(G(K)+F5+A1)
2460 IF G9>0 THEN 2480
2470 G9=0
2480 G5=(10-G9)/10
2490 IF G5<F3 THEN 2510
2500 GOTO 2550
2510 F3=1
2530 IF G5<0 THEN 3550
2540 GOTO 2570
2550 G5=1
2570 P1=1
2580 IF T1>0 THEN 2950
2590 L2=30*(1+D(K)/(H1*TAN(S8))-E(K)/H1)+0.0093*D1
2600 E4=D5*(L2-0.0093*D1)/L2
2610 IF F1>2.5 THEN 2650
2620 E5=D(K)*TAN(T4)
2630 L2=L2/ABS(COS(T4))
2640 GOTO 2670
2650 E5=D(K)/TAN(T4)
2660 L2=L2/SIN(T4)
2670 IF (L2-0.0093*D1)<0 THEN 2810
2680 E6=200-ABS(X1)-ABS(E5)
2690 IF E6>0 THEN 2780
2700 E7=(L2-E6)/L2
2710 IF E7>1 THEN 2740
2720 E7=E7-INT(E7)
2730 GOTO 2750
2740 E7=1
2750 E7=(INT(-E6/200)+E7)/K1
2760 IF E7>1 THEN 2810
2770 GOTO 2790
2780 E7=0
2790 P1=1-E4*(1-E7)*L2/200
2800 GOTO 2820
2810 P1=1
2820 E4=T2*(7+0.0093*D1)
```

```
2830 E7=1-(ABS(X1)+ABS(E5))/L1
2840 IF E7<0 THEN 2860
2850 GOTO 2870
2860 E7=0
2870 T3=(0.5*(E4+10)-ABS(D(K)+T1))/10
2880 IF T3<0 OR T3=0 THEN 2950
2890 IF T3>1 THEN 2920
2900 F7=1-T3*E7*7/(7+0.0093*D1)
2910 GOTO 2930
2920 F7=1-E7*7/(7+0.0093*D1)
2930 PRINT "RECIEVER SHADOW HERE, ROW";K;", F=";F7
2940 GOTO 2960
2950 F7=1
2960 F8=(SIN(B))*(COS(A1)-SIN(A1)*TAN(S8))
2965 G4=G4+F8
2970 IF F3<1 THEN 3000
2980 G3=G5
2990 GOTO 3010
3000 G3=F3
3010 IF D(K)<15 THEN 3030
3020 GOTO 3090
3030 G3=0.9*G3
3040 B3=INT(ABS(X1)/200)
3050 IF B3>K1 THEN 3070
3060 GOTO 3080
3070 B3=K1
3080 P1=P1*((B3+1-ABS(X1)/200)*(1-D5)**B3+(-B3+ABS(X1)/200)*(1-D5)**(B3+&
1))
3090 F0=G3*F7*F8*F9*P*G6*P1
3100 IF K>1 THEN 3120
3110 B1=G3*F7*F8*F9*P1*G6/D1
3120 B2=G3*F7*F8*F9*P1*G6/D1
3130 B2=B2/B1
3140 D2=T0+G(K)
3150 E4=2*SIN(D2)/D1
3160 P3=T0-PI/2+G(K)
3170 P4=0.74536*SIN(P3)
3180 IF P4=0 THEN 3210
3190 P4=ATN(SQR(1-P4**2)/P4)
3200 GOTO 3220
3210 P4=PI
3220 IF P4=0 OR P4>0 THEN 3240
3230 P4=PI+P4
3240 P5=PI/2-P4+P3
3250 P6=2*(P3+E4)+ASIN(.66666667)
3260 P7=2*(P3-E4)-ASIN(0.6666667)
3270 E8=D1+2.236068*COS(P3)
3280 P8=E8+3*SIN(P4)
3290 L0=1/30
3300 E6=P6-P5
3310 E5=100+INT(30*P5+0.5)
3320 IF L0<0 THEN 3340
3330 X(E5)=X(E5)+F(1)*F0*SIN(P4)/P8
3340 P9=0.5*SIN(P4)
3350 FOR L=L0 TO E6 STEP L0
3360 D4=SIN(P4-L)
3370 P9=P9+0.5*D4
3380 E7=E8+3*D4
3390 D3=100*P9/E7
3400 P9=P9+0.5*D4
```

```
3410 IF D3>E0 THEN 3460
3420 D3=2.5*D3+1
3430 E5=E5+SGN(L0)
3435 Z9=INT(D3)
3440 X(E5)=X(E5)+(F(Z9)+(F(Z9+1)-F(Z9))*(D3-Z9))*F0*D4/E7
3450 NEXT L
3460 L0=-L0
3470 IF L0>0 THEN 3500
3480 E6=F7-F5
3490 GOTO 3310
3500 GOTO 3560
3510 F3=0
3520 G5=1
3540 GOTO 3560
3550 G5=0
3560 Z9="4% 4%.%% 6%.%% 3(3%.3%) 7%.%% 5%.%% 3%.3%/"
3565 PRINT IN FORM Z9:K,D(K)*.3048,D1*.3048,F3,G5,F8,.929*X1,A1/H8,B2
3567 F4=F4+F3
3568 F6=F6+G5
3570 A0=A1
3580 A1=A2
3590 NEXT K
3600 L=1
3610 FOR K=1 TO 200
3620 IF X(K)=0 THEN 3660
3630 S1=S1+X(K)
3640 Y(K)=S1/L
3650 L=L+1
3660 NEXT K
3670 L=1
3680 FOR K=1 TO 200
3690 IF X(K)=0 THEN 3720
3700 Z(K)=Y(K)*L*100/S1
3710 L=L+1
3720 NEXT K
3730 L=L-1
3760 GOTO 3940
3770 PRINT
3780 PRINT
3790 PRINT
3810 PRINT IN IMAGE"DAY OF YEAR=%%%%,     HOUR OF DAY=%%.%":D,12+J
3820 IF F1=1 THEN 3890
3830 IF F1=2 THEN 3910
3840 IF F1=3 THEN 3870
3850 PRINT "EAST FIELD"
3860 GOTO 3920
3870 PRINT "WEST FIELD"
3880 GOTO 3920
3890 PRINT "NORTH FIELD"
3900 GOTO 3920
3910 PRINT "SOUTH FIELD"
3920 Z7="EL. ANGLE=%%%.%%, AZ. ANGLE=%%%%.%%, PSI=%%%%.%%, PHI=%%%.%%"
3925 PRINT IN IMAGE Z7:B/H8,T/H8,ATN(X4)/H8,ATN(X5)/H8
3930 GOTO 1690
3940 PRINT IN IMAGE"BUTTERFLY AREA=%%%%%%":.929*X2
3945 Z8="%"
3950 PRINT IN IMAGE"END LOSSES=%%%.%% %":(1-G8/N)*100,Z8
3970 PRINT " CIRC. POS        INTENSITY        % ENERGY          AV. INT"
3975 Z7="%%%.%% 9B 7%.%% 7B 5%.%% 9B 7%.%%/"
3976 L0=0
```

```
3980 FOR K=1 TO 200
3990 IF X(K)=0 THEN 4040
4000 IF INT(K/2)<K/2 THEN 4020
4010 PRINT IN FORM Z7:(K-100)*0.03048,X(K),Z(K),Y(K)
4020 IF X(K)<L0 THEN 4040
4030 L0=X(K)
4040 NEXT K
4060 PRINT IN IMAGE "INTEGRATED INTENSITY=%%%.%% METER SUNS":.03048*S1
4080 Z7="AVERAGE SHADING FACTOR=%.%%, AVERAGE SCREENING FACTOR=%.%%"
4090 PRINT IN IMAGE Z7:F4/N,F6/N
4100 PRINT IN IMAGE "MAXIMUM APERTURE FLUX TO NUMBER OF ROWS RATIO=%.%%%&
":L0/N
4110 PRINT IN IMAGE"MIRROR AREA EFFICIENCY=%%%.%% %":S1*N/(N+2*B(35)/L1)&
/G4,Z8
4115 Z7="TOTAL FIELD EFFICIENCY=%%%.%% %"
4120 PRINT IN IMAGE Z7:10*S1*L1/((L1*S3+20*(B(35)*S3/(N*10)))*SIN(B)),Z8
4130 PRINT IN IMAGE "WORKING MIRROR EFFICIENCY=%%%.%% %":S1/G4,Z8
4140 PRINT IN IMAGE "WORKING FIELD  EFFICIENCY=%%%.%% %":10*S1/(S3*SIN(B&
)),Z8
4390 GOSUB 6000
4400 IF Q9<0.5 THEN 1230
4420 NEXT J
4430 NEXT I
4433 INPUT IN IMAGE"TO RUN AGAIN ENTER 1, TO STOP ENTER 0$": P1
4436 IF P1=1 THEN 1230
4440 END
6000 J2=J2+10
6010 PRINT IN IMAGE "PLOT ARRAY IN DATA LINES %%%% TO %%%%":J2,J2+4
6020 FOR K=1 TO 5
6030 K1=44+20*K
6040 K0=K1+18
6050 WRITE ON 10 IN FORM "4% 6%":J2+K-1,J3
6060 WRITE ON 10 IN FORM "9(5% %)":X(L),J4 FOR L=K1 TO K0 BY 2
6070 NEXT K
6090 RETURN
```

THIS PAGE

WAS INTENTIONALLY

LEFT BLANK

Appendix B

ONCE-THROUGH RECEIVER CONCEPT ANALYSIS MODEL

THIS PAGE

WAS INTENTIONALLY

LEFT BLANK

Appendix B

ONCE-THROUGH RECEIVER CONCEPT ANALYSIS MODEL

This appendix contains the model used to simulate the performance of the FMC baseline receiver subsystem.

B.1 RECEIVER GEOMETRY AND PARTITION MODELS

Figure B-1 shows a cross section of the geometric model of a once-through receiver section of overall length l_R. The receiver cavity is a cylindrical segment of diameter D_C. Incident solar flux is admitted through an aperture of width W_A. The boiler and superheat tubes are symmetrically distributed about the circumference of the cavity in parallel with the long axis of the cavity in L number of groups (called loops). The axis of symmetry is a plane orthogonal to the aperture plane and elevated at an angle T above the horizontal plane through the heliostat field. Each loop j contains N_j tubes. All tubes in a loop have identical properties. As shown in Figure B-1 each loop is evenly divided into an upper and a lower half-loop. The midpoints of the circumferential arcs (ΔC_j) subtended by the half-loops are displaced from the symmetry plane by $\pm\theta_j$. The following equations define the layout of loops about the cavity:

$$S = D_C \left[\pi - \sin^{-1}(W_A/D_C)\right] / \sum_{k=1}^{L} D_{ok}\, N_k \qquad (1a)$$

$$\Delta C_j = 0.5 S D_{oj}\, N_j \qquad (1b)$$

$$C_{j2} = \pm 0.5 S \sum_{k=1}^{j} D_{ok}\, N_k \qquad (1c)$$

$$C_{j1} = \pm C_{j2} \mp \Delta C_j \qquad (1d)$$

$$\text{and } \theta_j = (C_{j1} + 0.5\Delta C_j)/0.5 D_C \qquad (1e)$$

where S is a spacing factor, C is an arc length referenced to the symmetry plane and positive for clockwise displacement.

The spacing factor defined by Equation (1a) yields a circumferential pitch of SD_{oj} in Loop j, and spacing of $0.5S\,(D_{oj} + D_{oj+1})$ between loops, as shown in Figure B-2. The equivalent linear spacings are nearly equal to the circumferential spacings shown in Figure B-2, since the cavity diameter is large in comparison with the tube diameters.

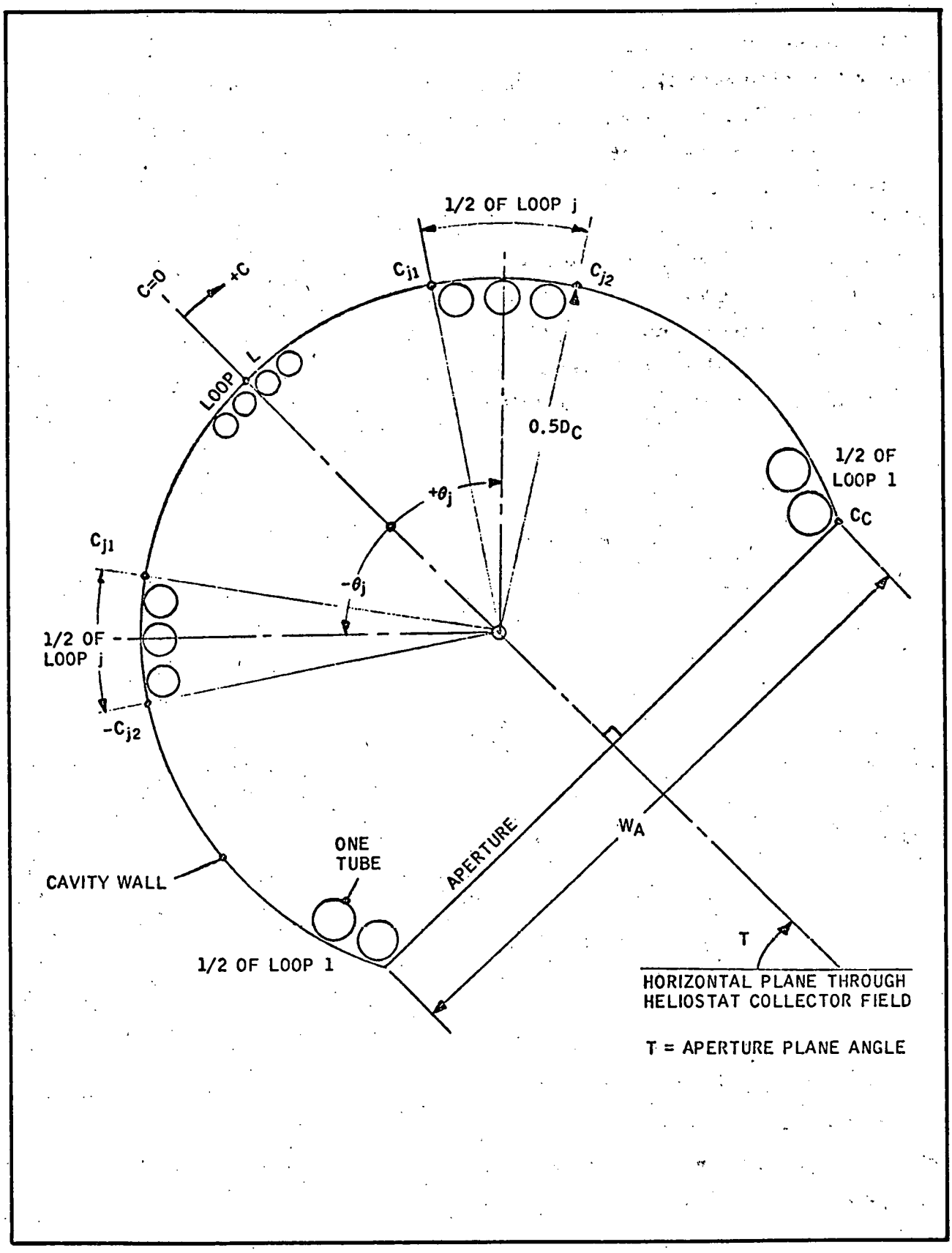

Figure B-1 GEOMETRY OF TUBE DISTRIBUTION IN RECEIVER CAVITY

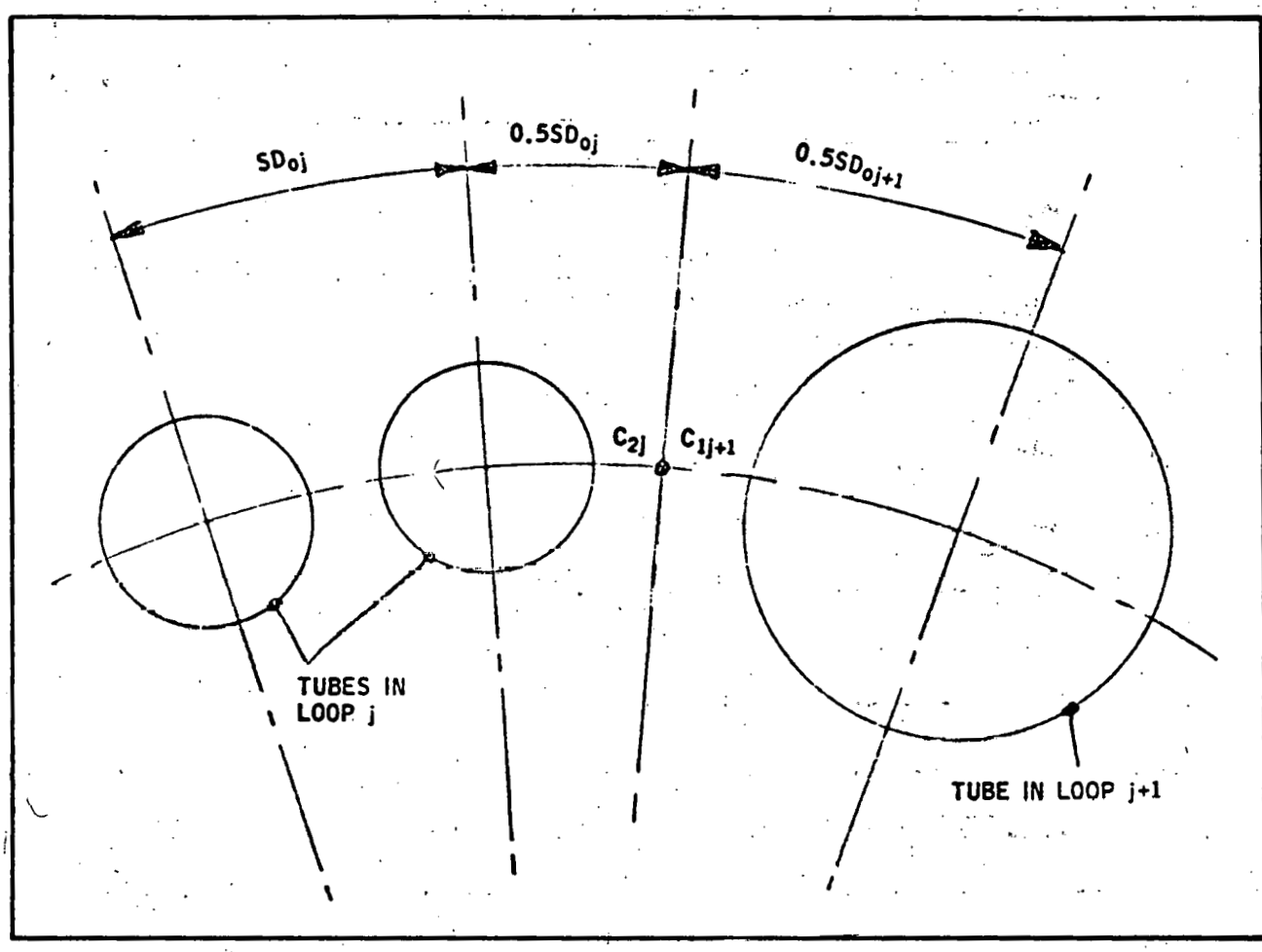

Figure B-2 SPACING BETWEEN TUBES AND LOOPS

Figure B-3 shows the path of fluid flow in a receiver section. Feedwater enters each half of Loop 1; superheated steam exits from Loop L. Flow is co-current in the tubes within a loop and countercurrent in adjacent loops. The flow pattern is arranged so that heating of feedwater to saturation is accomplished in the outer loops by the low-energy portion of the reflected solar flux intensity distribution within the cavity. Saturation boiling occurs in the middle loops. The majority of superheating occurs in Loop L, which intercepts the peak flux intensity.

Development of the receiver energy balance model is based upon a partition of the receiver into M equilength segments, as illustrated in Figure B-4. Spatial segment s is a vertical partition containing L loop segments.

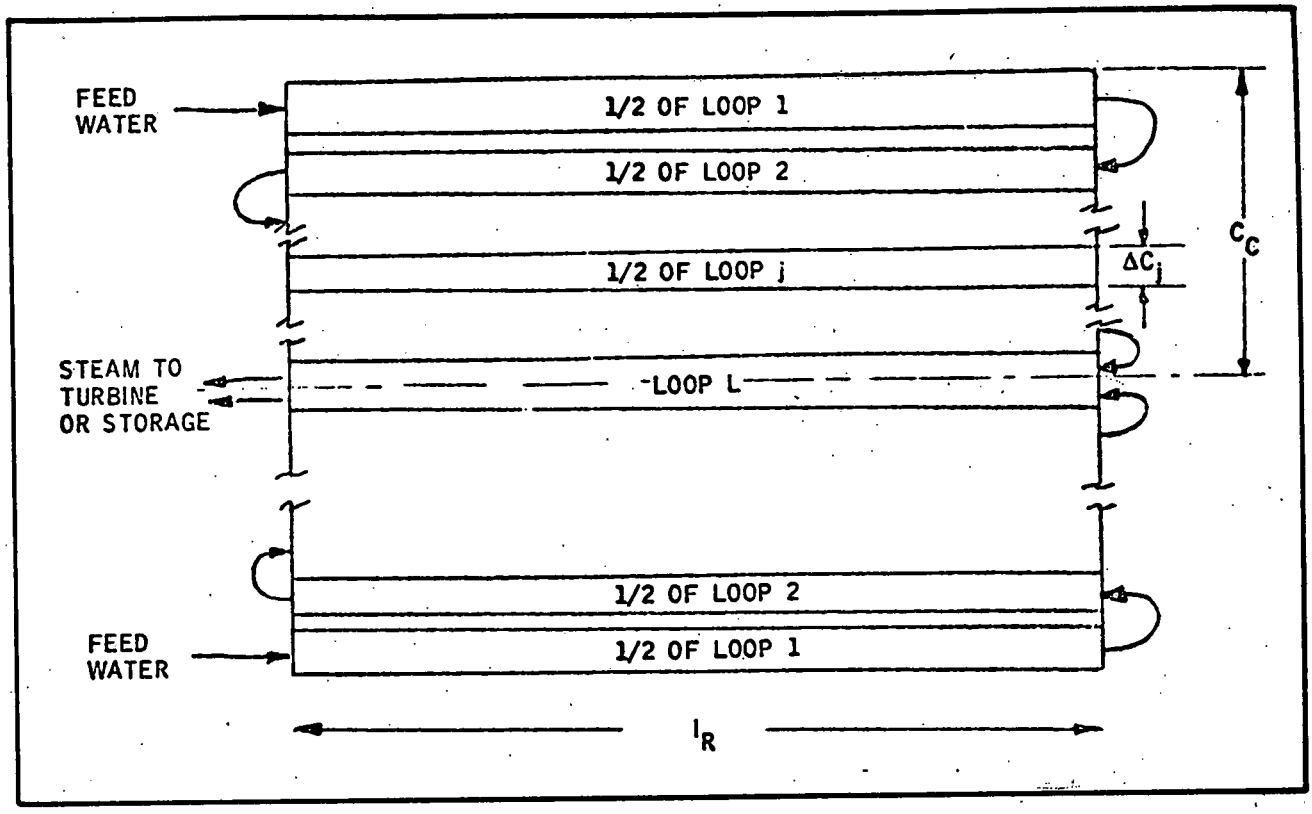

Figure B-3 FLOW MODEL OF WORKING FLUID WITHIN RECEIVER SECTION

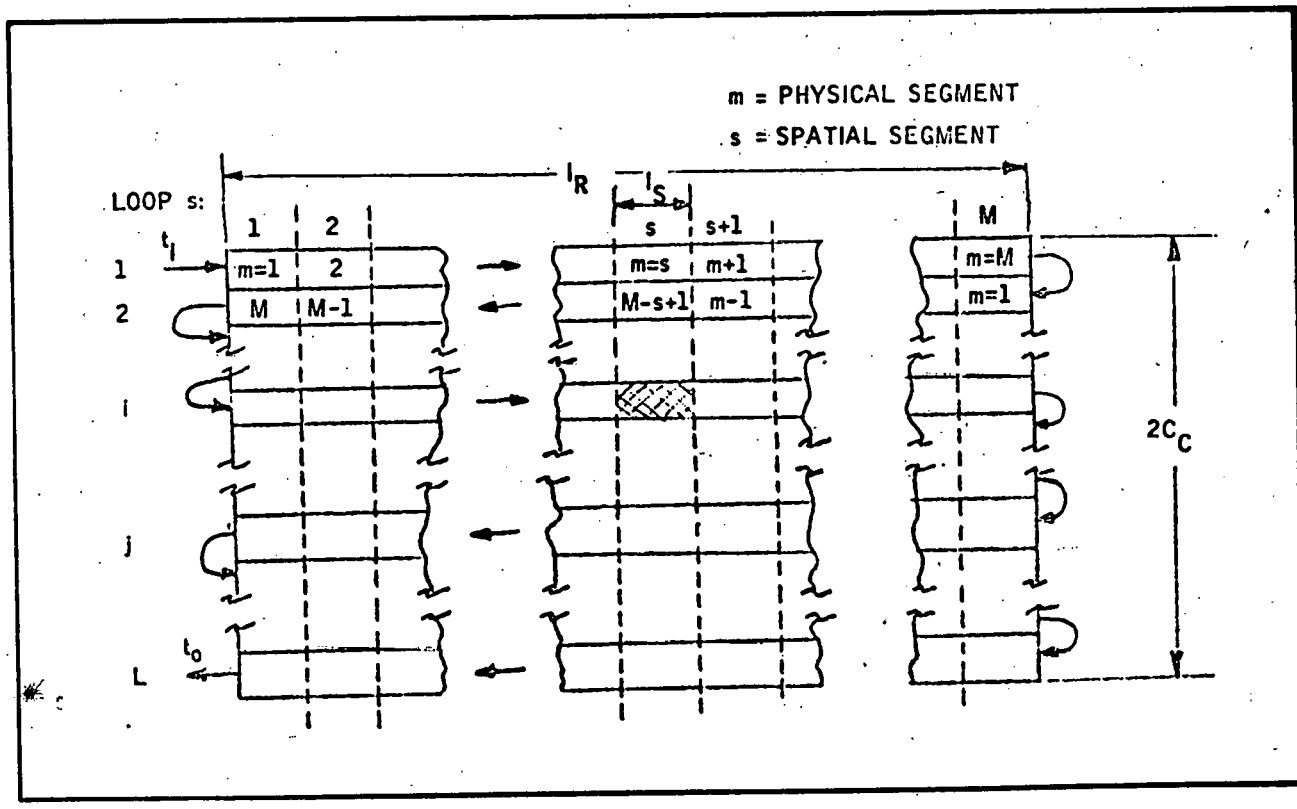

Figure B-4 PARTITION MODEL OF RECEIVER SECTION

Physical segment indexes m are assigned in accordance with the flow direction in a particular loop such that

$$t_{i(m+1)} \geq t_{im} \tag{2a}$$

where

t_{im} = the average temperature of the fluid in loop i, physical segment m.

Separate indexing for spatial and physical segments was used to facilitate development of the energy balance model. The general relationship between segment indexing is

odd numbered loops: $m = s$ (2b)

even numbered loops: $m = M - s + 1$ (2c)

B.2 ENERGY BALANCE MODEL

The following assumptions were used to develop the energy balance used in the calculations:

- Assumption 1: Each spatial section sees the same distribution of solar flux intensity
- Assumption 2: The net incident flux intensity seen by Loop i is the mean value of the intensities seen by the upper and lower halves
- Assumption 3: Convection losses due to ambient wind are negligible
- Assumption 4: Conduction through the cavity wall is negligible.

These assumptions are reasonable for the purposes of concept analysis. Assumption 1 is consistent with the results of the collector field analysis and the projected performance of the control system. Assumption 2 was made to reduce the computational requirements, and is reasonable since the magnitude of the average flux incident upon one half of a loop is within 10 percent of the average flux incident upon the other half. Assumption 3 simulates a zero wind condition.

The following energy balance model is defined for spatial section s (block letters denote matrixes):

$$B = \epsilon_t \sigma T + (1-\epsilon_a)\Psi + (1-\epsilon_t)FB \quad (3a)$$

$$R = (\epsilon_t/(1-\epsilon_t))(B-\sigma T) + (1-((1-\epsilon_a)/(1-\epsilon_t)))\Psi \quad (3b)$$

$$Q = l_S L R \quad (3c)$$

where

ϵ_t = emissivity of tubes

ϵ_a = emissivity of surroundings

σ = Stefan-Boltzmann constant

l_S = length of a spatial section

and the matrixes are

$B_i \xi B$ = the flux radiated to loop partition i from other partitions in spatial section s

$L_i \xi L$ = area of the loop partition i per unit length

$R_i \xi R$ = the net flux incident upon loop partition i

$\Psi_i \xi \Psi$ = the solar flux incident upon loop i

$T_i^4 \xi T$, T_i = the fourth power of absolute temperature of the tube surface

$F_{ij} \xi F$ = the geometric view factor from loop i to loop j

$Q_i \xi Q$ = the heat energy absorbed by loop partition i.

Units of flux are watts/m^2/m (Btu/ft^2·hr/ft). Note that the element of Vector T is the fourth power of absolute temperature.

The area and view factor are defined as follows:

$$L_i = SD_{Oi} N_i \tag{4a}$$

$$F_{ij} = L_j / (\pi D_C - L_i) \tag{4b}$$

Equations (3a) and (3b) have been combined as shown below into a single matrix equation for computer solution. Thus, define I_M as an M x M identity matrix and define the matrix A as follows:

$$I_M = \begin{bmatrix} 1 & 0 & \cdots & 0 \\ 0 & 1 & & \vdots \\ \vdots & & \ddots & \vdots \\ 0 & \cdots & & 1 \end{bmatrix} \qquad \text{(dimension M x M)} \tag{5a}$$

$$A = (I_M - (1-\epsilon_t) F)^{-1} \tag{5b}$$

Rearrangement of equation (3a) yields

$$B - (1-\epsilon_t) FB = \epsilon_t \sigma T + (1-\epsilon_a) \Psi \tag{6a}$$

or $$(I_M - (1-\epsilon_t) F) B = \epsilon_t \sigma T + (1-\epsilon_a) \Psi \tag{6b}$$

which, after multiplying both sides by A yields

$$B = A (\epsilon_t \sigma T + (1-\epsilon_a)) \Psi \tag{6c}$$

Rearrangement of equation (3b) and substitution of equation (6c) into the result yields:

$$R = (\epsilon_t / (1-\epsilon_t)) \left\{ A (\epsilon_t \sigma T + (1-\epsilon_a) \Psi) - \sigma T \right\} + ((\epsilon_a - \epsilon_t)/(1-\epsilon_t)) \Psi \tag{7a}$$

Multiplication of the second term on the right hand side of equation (7a) by ϵ_t / ϵ_t and collection of terms yields:

$$R = (\epsilon_t/(1-\epsilon_t))\left\{\sigma\left[\epsilon_t A - I_M\right] T + \left[(1-\epsilon_a)A + ((\epsilon_a - \epsilon_t)/\epsilon_t) I_M\right]\Psi\right\} \quad (7b)$$

Let $$C = \sigma\left[\epsilon_t A - I_M\right] \quad (7c)$$

and $$D = \left[(1-\epsilon_a)A + ((\epsilon_a - \epsilon_t)/\epsilon_t) I_M \Psi\right] \quad (7d)$$

Substitution of equations 7c and 7d into equation 7b yields:

$$R = (\epsilon_t/(1-\epsilon_t))\left\{CT + D\right\} \quad (8)$$

The matrixes C and D are constant for a given set of design parameters and incident solar flux vectors. Equations (3c) and (8) are used to compute Q for each spatial section by assuming a set of values for tube surface temperature in each loop partition. The computed Q vectors are then used to compute the average fluid temperature t_{im} in each loop partition as follows:

Let Δp and Δh be, respectively, the change in pressure and enthalpy of the fluid in a loop partition. From fluid flow theory

$$\Delta p = 8 f_{im} m_T V_{im} l_S / \pi^2 N_i^5 D_{Ii} g_C \quad (9a)$$

where

f_{im} = the Fanning friction factor
m_T = the mass flow rate of the fluid
v_{im} = the specific volume of the fluid
g_C = the universal gravitation contact

and

D_{Ii} = the inside diameter of a tube in loop i

$$\Delta h = Q_{im} / m_T \quad (9b)$$

Let p_{im}, h_{im}, and t_{im} be the fluid pressure enthalpy and temperature at the entrance to loop i, partition m.

$$p_{im} = p_{i(m-1)} + \Delta p \tag{9c.1}$$

$$h_{im} = h_{i(m-1)} + \Delta h$$

and (9c.2)

$$t_{im} = \Phi(p_{im}, h_{im})$$

Equation set 9 is used to compute the fluid properties in each physical segment starting from values specified for pressure and enthalpy of the feedwater at the inlet of loop 1. Fluid temperature and other properties are obtained by interpolation in standard tables of thermodynamic properties of water. The fluid temperature is then used to compute a corresponding tube surface temperature as follows:

$$\Delta t_{im} = Q_{im} / U_i N_i D_{Ii} l_S \tag{10a}$$

and $$T^*_{im} = t_{im} + \Delta t_{im} \tag{10b}$$

where

U_i = the overall heat transfer coefficient based on the inside tube diameter

and T^*_{im} = the computed tube surface temperature ($T^{*4}_i \xi T^*$)

The matrix T^*_m is compared with the matrix T_m. If all matrix elements are within a convergence tolerance error δT, the solution is accepted. Otherwise, the new values for matrix T_m are assumed based on the old T_m and the new T^*_m, and the computations are repeated.

B.3 TYPICAL OUTPUTS OF MODEL

```
          solboil2 north
FLUX VECTORS FOR NORTH FIELD WILL BE USED (FILE SOLFXVNF DATA)
EXECUTION:

INPUT NEXT DATA SET. TIME IS 11.06.10 ON 28 JUL 78
> &input flow=11000,pin=1500,solday=0,flux=0,60,495,1629,3759,5944,8110,
> 11447, npo=1,ipdlt=3 &end


 200.0-FT LOOPS DIVIDED INTO  20.0-FT SECTIONS
APERTURE=  4.0 FT, WIND=  0.0 MPH, TAMB=  70.0 DEG F
EMMISIVITIES: TUBE= 0.70, SURROUNDINGS= 0.90
S= 1.183, FLOWRATE=11000.0 LBM/HR
INPUT NEW PSI,PSIO,IWN
>.9 .9
CONVERGENCE
ITERATION  4, MEAN DT=   1.61 DEG F, PSI= 0.90

                          PROPERTIES OF FLUID AT INLET

                      T       P       H       U       RE        X
   LOOP  SECTION   _DEG_F  _PSIA_  BTU/LB  FT/SEC  ______  ______
     1       1     415.1   1500.0   400.0     1.8   35950.   0.0
     2       1     427.9   1498.4   417.0     1.8   37091.   0.0
     3       1     442.9   1496.9   434.3     1.8   38522.   0.0
     4       1     466.0   1495.4   460.8     1.8   40954.   0.0
     5       1     511.6   1493.9   513.5     1.8   45252.   0.0
     6       1     595.6   1492.5   612.8     1.1   96112.   0.004
     7       1     595.5   1491.3   747.1     3.0  252806.   0.245
     8       1     595.1   1487.7   993.8     4.6  388620.   0.686

FLUID STATE ENTERING LOOP  1: T= 415.1, P=1500.0 H= 400.0, U=  1.8, X= 0.0
                              AVAILABILITY=  358.6 BTU/LBM
FLUID STATE  EXITING LOOP  8: T= 951.8, P=1485.3 H=1461.3, U= 12.1, X= 1.00
                              AVAILABILITY= 1350.6 BTU/LBM

CHANGE IN AVAILABILITY= 992.0 BTU/LBM, EFFICIENCY=  86.2%

INPUT NEXT DATA SET. TIME IS 11.08.32 ON 28 JUL 78
>/*
```

B.4 SOURCE LISTING OF MODEL

```
C   PROGRAM SOLBOIL2                                                        SOL00010
C                                                                           SOL00020
C   COMPUTES BOILER OUTPUTS TO TURBINE FOR SOLAR ENERGY LINE COLLECTOR      SOL00030
C   SINGLE TUBE RUNS IN COLLECTOR CAVITY PLACED CIRCUMFERENTIALLY           SOL00040
C   WITH RESPECT TO CAVITY RADIUS                                           SOL00050
C                                                                           SOL00060
C   SUBROUTINES STEAM, COEFF2, VIEW2, DEFLTS, FLUXS2, TTUBE2,PPTARA,       SOL00070
C   DAYTIM, AND BLOCK DATA FOR SUBROUTINE STEAM REQUIRED                    SOL00080
C   IBM SCIENTIFIC SUBROUTINE PACKAGE REQUIRED FOR MATRIX ALGEBRA           SOL00090
C                                                                           SOL00100
      REAL VELCN /183.346/, DLTPC2 /43.5476/, PI /3.141593/,                SOL00110
     A   HCTUBE(2) /2.0833,0.75/,DFTUBR/460./,SIGMA/0.1735E-8/             SOL00120
      REAL*8 STWORD(2) /'ENTERING',' EXITING'/, HTIME                       SOL00130
      INTEGER SKIP/'C   '/, NOSKIP/'    '/, IMT(2) /'MLS','STS'/,I1/1/      SOL00140
      DIMENSION QVECTR(20),AVECTR(400),LVECTR(20),CVECTR(400),              SOL00150
     A   QVECTR(20),TVECTR(20),FVECTR(400),DUMMYV(400),LAKVEC(20),          SOL00160
     B   WAKVEC(20),ESMEIV(20),AVIMES(400)                                  SOL00170
      DATA QVECTR /20*1./                                                   SOL00180
C                                                                           SOL00190
C   ARRAYS FOR NSECT AND LOOPS. CHANGE MXSECT & MXLOOP                      SOL00200
C   IF ARRAY SIZES ARE CHANGED.                                             SOL00210
C   INDEXES IN COMMON /AR/ ARE LOOPS                                        SOL00220
C   INDEXES IN COMMON /AR2/ ARE PHYSICAL SECTION,LOOP                       SOL00230
C                                                                           SOL00240
      COMMON/AR/ QIN(20),WTL(20),ENT(20),FLUX(20),QQ(20),QQN(20),FLUXFL,    SOL00250
     A   APEA(20),FIJ(20,20)                                                SOL00260
      COMMON/AR2/ TTUBES(200,20),GA(200,20),TTUBCV(200,20),QTCA(200,20)     SOL00270
C                                                                           SOL00280
      INTEGER SOLDAY,SOLHR                                                  SOL00290
      EQUIVALENCE (FIJ(1,1),FVECTR(1)), (TVECTR(1),ESMEIV(1))               SOL00300
      COMMON/INDATA/ LOOPS,SLOOP,NSECT,EPSLON,TAMB,                         SOL00310
     A   VWIND,PIN,HIN,FLOW,WAP,DELTA,GAMMA0,NPO,CORF,ROUGH,                SOL00320
     B   SOLDAY,SOLHR,CAVDIA,EPSLNS,TOUTAS,IPOLT,MAXITR,SIN                 SOL00330
      NAMELIST /INPUT/ LOOPS,ENT,WTL,SLOOP,NSECT,EPSLON,FLUX,TAMB,          SOL00340
     A   VWIND,PIN,HIN,FLOW,WAP,DELTA,GAMMA0,NPO,CORF,ROUGH,QIN,           SOL00350
     B   SOLDAY,SOLHR,CAVDIA,EPSLNS,TOUTAS,IPOLT,MAXITR,SIN                 SOL00360
C                                                                           SOL00370
      SFVFLN(A,B,C)=A + C*(B-A)                                             SOL00380
C                                                                           SOL00390
      MXLOOP=20                                                             SOL00400
      MXSECT=200                                                            SOL00410
C                                                                           SOL00420
      CALL DEFLTS                                                           SOL00430
C                                                                           SOL00440
C   READ NEXT DATA SET, INITIALIZE CONSTANTS FOR DATA SET.                  SOL00450
C                                                                           SOL00460
    5 ICASE1=1                                                              SOL00470
   10 CALL DAYTIM(NDAY,MONTH,NYR,HTIME)                                     SOL00480
      WRITE(6,1000) HTIME,NDAY,MONTH,NYR                                    SOL00490
      READ(5,INPUT,END=999,ERR=10)                                          SOL00500
      IF((NSECT.LE.0).OR.(LOOPS.LE.0)) GO TO 950                            SOL00510
      IF((NSECT.GT.MXSECT).OR.(LOOPS.GT.MXLOOP)) GO TO 950                  SOL00520
      RIMEPS=1.-EPSLON                                                      SOL00530
      ESIME=EPSLON/RIMEPS                                                   SOL00540
      FLOPS=FLOW/3600.                                                      SOL00550
```

```
      FLINV=1./FLOW                                                     SOL00560
      SECTL=SLOOP/NSECT                                                 SOL00570
      CLTFCI=CLTFCO*FLOPS*FLOPS*SECTL                                   SOL00580
      NPRINT=NPO+1                                                      SOL00590
      CRFP1=1.+COSF                                                     SOL00600
C                                                                       SOL00610
C   FLUID PROPERTIES AT INLET TO LOOP 1                                 SOL00620
C                                                                       SOL00630
      CALL STEAM(PIN,HIN,TIN,VF,VG,ENTRPY,QUALIN,VMU,TK,CP)             SOL00640
      GFLIN=VELCN*FLOPS*SPVFUN(VF,VG,QUALIN)/(DIN(1)*DIN(1)*ENT(1))     SOL00650
      IF(SIN.GT.0.) ENTRPY=SIN                                          SOL00660
      AVLBIN=HIN - TAMB*ENTRPY                                          SOL00670
C                                                                       SOL00680
C   COMPUTE OUTSIDE DIAMETERS OF TUBES IN EACH LOOP                     SOL00690
C                                                                       SOL00700
      DOUCON=CRFP1*(1. + PIN/15000.)                                    SOL00710
      SUMCON=0.                                                         SOL00720
      DO 20 J=1,LOOPS                                                   SOL00730
      DO(J)=DOUCON*DIN(J)                                               SOL00740
      DCN(J)=DO(J)*ENT(J)                                               SOL00750
   20 SUMCON=SUMCON + DCN(J)                                            SOL00760
C                                                                       SOL00770
C   COMPUTE AREA PER UNIT LENGTH, VIEW FACTOR FOR EACH LOOP             SOL00780
C                                                                       SOL00790
      CALL VIEW2(PI,SUMCON,WAP,CAVDIA,S,LOOPS,NSECT)                    SOL00800
      IF(S.LE.1.) GO TO 940                                             SOL00810
      CALL FLUXS2(SOLDAY,SOLPP,LOOPS,0.5*WAP,S,CAVDIA)                  SOL00820
      WRITE(7,1040) SLOOP,SECTL,WAP,VWIND,TAMB,EPSLON,EPSLNS,S,FLOW     SOL00830
C                                                                       SOL00840
C   COMPUTE INITIAL ASSUMPTIONS FOR TUBE TEMPERATURES,                  SOL00850
C   CONSTANT MATRICES IN ENERGY BALANCE EQUATIONS                       SOL00860
C                                                                       SOL00870
      CALL TTUBE0(ICASE1,TIN,TOUTAS,NSECT,LOOPS)                        SOL00880
      CALL ARRAY(2,LOOPS,LOOPS,20,20,FVECTR,FIJ)                        SOL00890
C                                                                       SOL00900
C   COMPUTE MATRIX A=INVERSE(I - (1-EPSLON)F)                           SOL00910
C                                                                       SOL00920
      CALL SMPY(FVECTR,R1MEPS,DUMMYV,LOOPS,LOOPS,0)                     SOL00930
      CALL MSUB(UVECTR,DUMMYV,AVECTR,LOOPS,LOOPS,2,0)                   SOL00940
      CALL MINV(AVECTR,LOOPS,DETMTA,LWKVEC,MWKVEC)                      SOL00950
C                                                                       SOL00960
C   COMPUTE MATRIX C=SIGMA(EPSLON*A - I)                                SOL00970
C                                                                       SOL00980
      CALL SMPY(AVECTR,EPSLON,DUMMYV,LOOPS,LOOPS,0)                     SOL00990
      CALL MSUB(DUMMYV,UVECTR,CVECTR,LOOPS,LOOPS,0,2)                   SOL01000
      CALL SMPY(CVECTR,SIGMA,CVECTR,LOOPS,LOOPS,0)                      SOL01010
C                                                                       SOL01020
C   COMPUTE VECTOR E=((1-EPSLNS)A + ((EPSLNS-EPSLON)/EPSLON)I)FLUX      SOL01030
C                                                                       SOL01040
      CALL SMPY(AVECTR,1.-EPSLNS,AV1MES,LOOPS,LOOPS,0)                  SOL01050
      CALL SMPY(UVECTR,(EPSLNS-EPSLON)/EPSLON,ESMEIV,LOOPS,LOOPS,2)     SOL01060
      CALL MADD(AV1MES,ESMEIV,DUMMYV,LOOPS,LOOPS,0,2)                   SOL01070
      CALL MPRE(DUMMYV,FLUX,QVECTR,LOOPS,LOOPS,0,0,1)                   SOL01080
C                                                                       SOL01090
C   COMPUTE VECTOR Q FOR EACH LOOP BY SPATIAL SECTION                   SOL01100
```

```
C                                                                       SOL01110
      NSP1=NSECT+1                                                      SOL01120
  250 REWIND 5                                                          SOL01130
      READ(5,*) (TTLBAS(I,J),I=1,NSECT)                                 SOL01140
      READ(5,*) (TTLBAS(I,J),I=1,NSECT)                                 SOL01150
      DO 310 IS=1,NSECT                                                 SOL01160
      M=NSP1 - IS                                                       SOL01170
C                                                                       SOL01180
C     DEFINE SURFACE TEMPERATURE VECTOR T IN SPATIAL SECTION IS         SOL01190
C                                                                       SOL01200
      DO 300 J=1,LOOPS,2                                                SOL01210
      TVECTR(J)=(TTLBAS(IS,J) + OFTOOR)**4.                             SOL01220
  300 IF(J.NE.LOOPS) TVECTR(J+1)=(TTLBAS(M,J+1) + OFTOOR)**4.           SOL01230
C                                                                       SOL01240
C     COMPUTE VECTOR G=(EPSLON/(1-EPSLON)) (CT + D) AND SAVE IN ELEMENTS SOL01250
C     OF MATRIX GA CORRESPONDING TO PHYSICAL TUBE SECTIONS              SOL01260
C                                                                       SOL01270
      CALL MPRD(CVECTR,TVECTR,DUMYYY,LOOPS,LOOPS,0,0,1)                 SOL01280
      CALL MADD(DUMYYY,DVECTR,GVECTR,LOOPS,1,0,0)                       SOL01290
      CALL SMPY(GVECTR,EDIME,GVECTR,LOOPS,1,0)                          SOL01300
      DO 310 J=1,LOOPS,2                                                SOL01310
      GA(IS,J)=GVECTR(J)                                                SOL01320
  310 IF(J.NE.LOOPS) GA(M,J+1)=GVECTR(J+1)                              SOL01330
C                                                                       SOL01340
C     COMPUTE FLUID PROPERTIES IN EACH LOOP AND PHYSICAL SECTION        SOL01350
C                                                                       SOL01360
      DO 90 J=1,LOOPS                                                   SOL01370
C                                                                       SOL01380
C     INITIALIZE PARAMETERS WHICH ARE CONSTANT FOR ONE LOOP             SOL01390
C                                                                       SOL01400
      DIJ=DIN(J)                                                        SOL01410
      DIJFT=DIJ/12.                                                     SOL01420
      DIJ2=DIJ*DIJ                                                      SOL01430
      DOJ=DO(J)                                                         SOL01440
      DOJFT=DOJ/12.                                                     SOL01450
      DIJ5=DIJ2*DIJ2*DIJ                                                SOL01460
      ENTJ=ENT(J)                                                       SOL01470
      DI2N=DIJ2*ENTJ                                                    SOL01480
      DLTPCN=DLTPC1/(DIJ5*ENTJ*ENTJ)                                    SOL01490
      KT=MTL(J)                                                         SOL01500
      CALL COEFF1(HCTLBE(KT),DIJFT,DOJFT)                               SOL01510
      AREALJ=AREA(J)*SECTL                                              SOL01520
      DLTCON=1./(PI*ENTJ*DIJFT*SECTL)                                   SOL01530
C                                                                       SOL01540
C     COMPUTE FLUID STATE IN EACH SECTION OF LOOP J                     SOL01550
C                                                                       SOL01560
      DO 80 M=1,NSECT                                                   SOL01570
C                                                                       SOL01580
C     STATE PROPERTIES AT INLET TO SECTION M                            SOL01590
C                                                                       SOL01600
      CALL STEAM(P,H,T,VF,VG,ENTRPY,QUAL,VMU,TK,CP)                     SOL01610
C                                                                       SOL01620
C COMPUTE SPECIFIC VOLUME, VELOCITY, REYNOLD'S NO., ETC OF FLUID        SOL01630
C                                                                       SOL01640
      SPV=SPVFUN(VF,VG,QUAL)                                            SOL01650
```

```
      LFL=VELCN*FLEPS*SPV/VISN                                          SOL01660
      IF((QUAL.LE.0.).OR.(QUAL.GT.1.)) GO TO 30                         SOL01670
C                                                                       SOL01680
C   SATURATION STATE ( TWO PHASES)                                      SOL01690
C                                                                       SOL01700
      RE=3600.*DIJFT*LFL/(VF*VFU)                                       SOL01710
      CALL COEFF2(2,RE,1.,TK,F,UINV)                                    SOL01720
      DELTAP=DLTPCN*F*SPV*SPV/VF                                        SOL01730
      GO TO 40                                                          SOL01740
C                                                                       SOL01750
C   SINGLE PHASE (LIQUID OR SUPERHEATED VAPOR)                          SOL01760
C                                                                       SOL01770
   30 RE=3600.*DIJFT*LFL/(SPV*VFU)                                      SOL01780
      CALL COEFF2(1,RE,CF*VFU/TK,TK,F,UINV)                             SOL01790
      DELTAP=DLTPCN*F*SPV                                               SOL01800
C                                                                       SOL01810
   40 GO TO(50,41,42), NPRINT                                           SOL01820
   41 IF(M.GT.1) GO TO 50                                               SOL01830
   42 WRITE(9) T,P,H,LFL,RE,QUAL                                        SOL01840
C                                                                       SOL01850
C   COMPUTE TUBE SURFACE TEMPERATURES                                   SOL01860
C                                                                       SOL01870
   50 GJ=GA(M,J)*AREAJ                                                  SOL01880
C                                                                       SOL01890
   60 DLTUBE=DLTCON*GJ*UINV                                             SOL01900
      TTUBE(M,J)=T + DLTUBE                                             SOL01910
      P=P - DELTAP                                                      SOL01920
      IF(P.LT.0.) GO TO 930                                             SOL01930
      H=H + FLINV*GJ                                                    SOL01940
      IF(H.LT.0.) GO TO 930                                             SOL01950
   80 CONTINUE                                                          SOL01960
   90 CONTINUE                                                          SOL01970
      HOUT=H                                                            SOL01980
      POUT=P                                                            SOL01990
C                                                                       SOL02000
C   DETERMINE IF COMPUTED & ASSUMED TUBE TEMPERATURES HAVE CONVERGED    SOL02010
C                                                                       SOL02020
      CALL TTUBE1(NSECT,LOOPS,DELTA,MAXITR,IPDLT,3250,$4200)            SOL02030
C                                                                       SOL02040
C   CONVERGENCE. PRINT  PROPERTIES OF FLUID                             SOL02050
C                                                                       SOL02060
 4200 REWIND 9                                                          SOL02070
      IF(NPRINT.EQ.1) GO TO 420                                         SOL02080
      WRITE(7,1010)                                                     SOL02090
      DO 410 L=1,LOOPS                                                  SOL02100
      K=NTL(L)                                                          SOL02110
      READ(9) T,P,H,UFL,RE,QUAL                                         SOL02120
      WRITE(7,1021) L,I1, T,P,H,UFL,RE,QUAL,QIN(J),QO(L),HMT(K),ENT(J),  SOL02130
     &   FLUX(J)                                                        SOL02140
      IF(NPRINT.EQ.2) GO TO 410                                         SOL02150
      DO 405 M=2,NSECT                                                  SOL02160
      READ(9) T,P,H,UFL,RE,QUAL                                         SOL02170
  405 WRITE(7,1020) L,M, T,P,H,UFL,RE,QUAL                              SOL02180
  410 CONTINUE                                                          SOL02190
  420 WRITE(7,1030) SKIP,STORED(1),I1,TIN,PIN,HIN,UFLIN,QUALIN,AVLBIN   SOL02200
```

```
      CALL STEAM(POUT,HOUT,T,VF,VG,ENTRPY,QUAL,VYU,TK,CP)                SOL02210
      AVLBOT=HOUT - TAMB*ENTRPY                                          SOL02220
      UFL=VELCN*FLRPS*SPVFUN(VF,VG,QUAL)/DI2N                            SOL02230
      WRITE(7,1070) NOSKIP,STAORD(2),LOOPS,T,POUT,HOUT,UFL,QUAL,AVLBOT   SOL02240
      DLTAVL=AVLBOT-AVLBIN                                               SOL02250
      EFFIC=100.*FLOW*(HOUT-HIN)/(SLOOP*FLUXFL)                          SOL02260
      WRITE(7,1080) DLTAVL,EFFIC                                         SOL02270
      GO TO 10                                                           SOL02280
C                                                                        SOL02290
C   ERROR PROCESSING                                                     SOL02300
C                                                                        SOL02310
  921 WRITE(6,9001) A1,AP,S,F11                                          SOL02320
      GO TO 10                                                           SOL02330
  930 WRITE(6,9030) P,H                                                  SOL02340
      CALL PRTAPA(NSECT,LOOPS)                                           SOL02350
      GO TO 4200                                                         SOL02360
  940 WRITE(6,9040)                                                      SOL02370
      GO TO 10                                                           SOL02380
  950 WRITE(6,9050) LOOPS,MXLOOP,NSECT,MXSECT                            SOL02390
      GO TO 10                                                           SOL02400
  999 STOP                                                               SOL02410
 1000 FORMAT('0INPUT NEXT DATA SET. TIME IS ',A8,' ON',I3,1XA3,I3)       SOL02420
 1010 FORMAT('0',27X'PROPERTIES OF FLUID AT INLET'//                     SOL02430
     A    25X'T',7X'P',7X'H',7X'U',6X'RE',7X'X',                         SOL02440
     B    17X'DIN',5X'DO   MTL  ENT   INPUT  FLUX'/                     SOL02450
     C    5X'LOOP  SECTION',4X'DEG F   PSIA   BTU/LB  FT/SEC',          SOL02460
     D    25X,2(6X'IN'),14X'BTU/HR-SQFT'/                               SOL02470
     E    ' ',5X'_____ _______ ',6(' ______'),                          SOL02480
     F    12X,2(' _____'),3(' ___'),10('_'))                            SOL02490
 1020 FORMAT(2I8,4X,3F8.1,F7.1,F9.0,F8.3)                                SOL02500
 1021 FORMAT(2I8,4X,3F8.1,F7.1,F9.0,F8.3,                                SOL02510
     A    12X,2F7.2,2XA3,F5.0,F12.0)                                     SOL02520
 1030 FORMAT(A1,'FLUID STATE',1XA8,' LOOP',I3,': T=',F6.1,               SOL02530
     A    ', P=',F6.1,' H=',F6.1,', U=',F8.1,', X=',F5.2,/               SOL02540
     A    31X'AVAILABILITY=',F7.1,' BTU/LBM')                            SOL02550
 1035 FORMAT('0CHANGE IN AVAILABILITY=',F6.1,' BTU/LBM, ',               SOL02560
     A    'EFFICIENCY=',F6.1,'%')                                        SOL02570
 1040 FORMAT('0',F6.1,'-FT LOOPS DIVIDED INTO',F6.1,'-FT SECTIONS'/      SOL02580
     A    ' APERTURE=',F5.1,' FT, WIND=',F5.1,' MPH, TAMB=',F6.1,' DEG F'/SOL02590
     B    ' EMMISIVITIES: TUBE=',F5.2,', SURROUNDINGS=',F5.2/            SOL02600
     C    ' S=',F6.3,', FLOWRATE=',F7.1,' LBM/HR')                       SOL02610
 9001 FORMAT(' A1=',F10.1,', AP=',F10.1,', S=',F8.4,', F11=',F8.4)       SOL02620
 9030 FORMAT(' ERROR: P=',F8.2,', H=',F8.2)                              SOL02630
 9040 FORMAT(' ERROR; S <= 1')                                           SOL02640
 9050 FORMAT(' ERROR: LOOPS=',I3,', RANGE IS 0-',I3,                     SOL02650
     A    ', NSECT=',I3,', RANGE IS 0-',I3)                              SOL02660
      END                                                                SOL02670
```

```
      SUBROUTINE COEFF1(TKTUBE,DI,DO)
C
C   COMPUTES FRICTION FACTOR, HEAT TRANSFER COEFFICIENT IN TUBE
C   THIS ENTRY IS COMPUTATION FOR EVAPORATION PHASE (CONSTANT H)
C
C   DI,DO=INSIDE, OUTSIDE TUBE DIAMETERS (FT)
C   TKTUBE=THERMAL CONDUCTIVITY OF TUBE (BTU*FT/HR*SQFT*DEF F)
C
      IF(DI.LE.0.) GO TO 900
      IF(TKTUBE.LE.0.) GO TO 910
      HISATP=(0.5*DI*ALOG(DO/DI))/TKTUBE
      UISATP=HISATP
C
C   CONSTANTS IN ALGORITHM FOR HI IN LIQUID & SUPERHEAT PHASES
C
      CHILAM=4.364/DI
      CHITRB=0.023/DI
      RETURN
C
      ENTRY COEFF2(N,RE,PR,TKFLU,F,UI)
C
C   COMPUTE FRICTION FACTOR, OVERALL HEAT TRNS. COEFF. OF FLUID
C   N=1 IS SINGLE-PHASE; N=2 IS SATURATION PHASE
C   RETURNS INVERSE OF OVERALL HEAT TRANSFER COEFFICIENT
C
      IF(RE.LE.0.) GO TO 920
      IF(RE.GT.3000.) GO TO 20
C
C   LAMINAR FLOW REGION
C
      F=64./RE
      GO TO(11,12), N
   11 HI=CHILAM*TKFLU
      UI=HISATP + 1./HI
      RETURN
   12 UI=UISATP
      RETURN
C
C   TURBULENT FLOW REGION
C
   20 F=0.316/RE**(0.25)
      GO TO(21,22), N
   21 HI=CHITRB*TKFLU*(RE**0.8)*(PR**0.4)
      UI=HISATP + 1./HI
      RETURN
   22 UI=UISATP
      RETURN
C
  900 WRITE(6,9000)
      STOP
  910 WRITE(6,9010)
      STOP
  920 WRITE(6,9020)
      STOP
  930 WRITE(6,9030)
      STOP
C
 9000 FORMAT(' TUBE ID<=0.')
 9010 FORMAT(' TUBE TK<=0.')
 9020 FORMAT(' RE<=0.')
 9030 FORMAT(' FLUID TK<=0.')
      END
```

```
      SUBROUTINE DEFLTS
C
C     SETS PROGRAM DEFAULTS
C
      COMMON/AR/ DIN(20),MTL(20),ENT(20),FLUX(20),DO(20),DON(20),FLUXPL,
     A    AREA(20),FIJ(20,20)
      COMMON/INDATA/ LOOPS,SLOOP,NSECT,EPSLON,TAMB,
     A    VWIND,PIN,HIN,FLOW,WAP,DELTA,GAMMAO,NFO,CORF,ROUGH,
     B    SOLDAY,SOLHR,CAVDIA,EPSLNS,TOUTAS,IPDLT,MAXITR,SIN
C
      INTEGER SOLDAY,SOLHR
      DELTA=10.
      GAMMAO=0.75
      EPSLON=0.7
      EPSLNS=0.7
      CORF=0.
      TAMB=70.
      VWIND=0.
      NFO=0
      IPDLT=2
      MAXITR=10
      CAVDIA=6.
      TOUTAS=1000.
      PIN=1000.
      HIN=400.
      WAP=4.
      SIN=.5911
      SLOOP=200.
      NSECT=10
      SOLDAY=1
      SOLHR=1430
      DO 10 I=1,6
      DIN(I)=1.2
   10 MTL(I)=1
      MTL(6)=2
      ENT(1)=8.
      ENT(2)=8.
      ENT(3)=12.
      ENT(4)=24
      ENT(5)=36.
      ENT(6)=36.
      LOOPS=6
      RETURN
      END
```

```
      SUBROUTINE FLUXS2(ND,NH,L,HOVER2,S,DC)                            SOL00010
C                                                                       SOL00020
C   COMPUTES AVERAGE FLUX INPUT TO EACH LOOP USING DISTRIBUTION         SOL00030
C   OF RECEIVER REFLECTED INTENSITY FOR SOLAR DAY ND, HOUR NH           SOL00040
C   MEASURED AT POINTS ON CAVITY CIRCUMFERENCE                          SOL00050
C                                                                       SOL00060
C   ND=0    :FLUX ON EACH LOOP INPUT FROM CALLING PROGRAM               SOL00070
C   ND=1,2,3: WINTER SOLSTICE, EQUINOX, SUMMER SOLSTICE                 SOL00080
C   ND=4    : INPUT FLUX DISTRIBUTION FROM TERMINAL                     SOL00090
C                                                                       SOL00100
C   INTENSITY VECTOR FOR (ND,NH) STORED IN FILE SOLFLUX2 DATA,          SOL00110
C   RECORD NUMBER=NR0(ND) + (NH-H1(ND))/100                             SOL00120
C                                                                       SOL00130
C   HOVER2=HALF-WIDTH OF APERTURE (FT)                                  SOL00140
C   DC(J) =OUTSIDE DIAMETER OF TUBE (IN)                                SOL00150
C   ENT(J)=NUMBER OF TUBES IN LOOP J (J=1,...,L)                        SOL00160
C   DCN(J)=DC(J)*ENT(J)                                                 SOL00170
C   S     =SPACING FACTOR                                               SOL00180
C   CC    =DIAMETER OF CAVITY (FT)                                      SOL00190
C   FLUXIN(J)=FLUX NORMAL TO CAVITY CIRCUMFERENCE AT CX,                SOL00200
C   WHERE CX=0.5*CC*ARCSIN(X/(0.5*CC)),                                 SOL00210
C   AND X =THE PROJECTION OF CX INTO THE APERTURE PLANE                 SOL00220
C   THE RANGE OF CX IS CJMIN FT TO CJMAX FT IN INCREMENTS OF DELTAC     SOL00230
C                                                                       SOL00240
      DIMENSION FLUXIN(50),SIGNC(2)                                     SOL00250
C                                                                       SOL00260
      DATA INMAX/50/, CJMIN,CJMAX,DELTAC/-3.6,6.2,0.2/,SIGNC/1.,-1./    SOL00270
C                                                                       SOL00280
      COMMON/AR/ DIN(20),WTL(20),ENT(20),FLUX(20),DO(20),DCN(20),FLUXFL,SOL00290
     A   AREA(20),FIN(20,20)                                            SOL00300
      INTEGER H1(3)/730,630,530/, HL(3)/1630,1730,1830/, NR0(3)/1,11,23/SOL00310
      REAL*8 DAYS(2,4) /' WINTER ',' SOLSTICE',' EQUINOX',              SOL00320
     A    ' SUMMER ',' SOLSTICE',' TERMINAL',' INPUT '/                 SOL00330
C                                                                       SOL00340
      CXFUN(X)=CAVRAD*ARSIN(X/CAVRAD)                                   SOL00350
      CKFUN(K)=DELTAC*K - CJMIN2                                        SOL00360
      KFUN(S,C) =DLTCI*(C + CJMIN2 + S*1.0E-5)                          SOL00370
C                                                                       SOL00380
      CAVRAD=0.5*CC                                                     SOL00390
      DLTCI=1./DELTAC                                                   SOL00400
      FLUXPL=0.                                                         SOL00410
      IF(ND.LT.1) GO TO 30                                              SOL00420
    1 IF(ND-4) 20,10,900                                                SOL00430
C                                                                       SOL00440
C   INPUT DISTRIBUTION FROM TERMINAL                                    SOL00450
C                                                                       SOL00460
   10 WRITE(6,1000)                                                     SOL00470
      READ(5,1010,END=999) CJ1,CJ2                                      SOL00480
      IN=1 + (1.0E-5 + DLTCI*(CJ2-CJ1))                                 SOL00490
      IF(IN.GT.INMAX) GO TO 910                                         SOL00500
      WRITE(6,1001) IN,CJ1,DELTAC                                       SOL00510
      READ(5,1010,END=999) (FLUXIN(I),I=1,IN)                           SOL00520
      IF(IN.EQ.INMAX) GO TO 30                                          SOL00530
      IN1=IN+1                                                          SOL00540
      DO 15 I=IN1,INMAX                                                 SOL00550
```

```
   15 FLUXIN(I)=0.                                                      SOL00560
      GO TO 30                                                          SOL00570
C                                                                       SOL00580
C    RETRIEVE FLUX INTENSITY VECTOR FROM FILE SOLFLUX2 DATA             SOL00590
C                                                                       SOL00600
   20 IF((RP.LT.R1(RO)).OR.(RP.GT.RL(RO))) GO TO 920                    SOL00610
      WRITE(6,1030) DAYS(1,RO),DAYS(2,RO),RH                            SOL00620
      RP=RPO(RO) + (RP-R1(RO))/100                                      SOL00630
      CALL BREAD(10,RP,FLUXIN,IFS,LRECL,8930,8930)                      SOL00640
      CJ1=CJMIN                                                         SOL00650
      CJ2=CJMAX                                                         SOL00660
      IN=INMAX                                                          SOL00670
C                                                                       SOL00680
C    COMPUTE AVERAGE FLUX INPUT TO EACH LOOP                            SOL00690
C                                                                       SOL00700
   30 CX1L=CAVRAD*(3.1415926 - ARSIN(WOVER2/CAVRAD))                    SOL00710
      CJMIN2=DELTAC-CJ1                                                 SOL00720
      SD24=S/24.                                                        SOL00730
C                                                                       SOL00740
      DO 90 J=1,L                                                       SOL00750
      WIDTHJ=SD24*DOS(J)                                                SOL00760
      IF(RO.LT.1) GO TO 90                                              SOL00770
      CX2L=CX1J                                                         SOL00780
      CX1L=CX2J - WIDTHJ                                                SOL00790
      FLUX(J)=0.                                                        SOL00800
      DO 900 IPM=1,2                                                    SOL00810
C                                                                       SOL00820
C    IPM=1: LOOP-HALF IN UPPER PORTION OF CAVITY                        SOL00830
C    IPM=2: LOOP-HALF IN LOWER PORTION OF CAVITY                        SOL00840
C                                                                       SOL00850
C                                                                       SOL00860
C    AVERAGE THE FLUX VALUES IN THE INTERVAL CX1J <= CX <= CX2J         SOL00870
C                                                                       SOL00880
      K1=KFUN( SIGNC(IPM),CX1J)                                         SOL00890
      K2=1 + KFUN(-SIGNC(IPM),CX2L)                                     SOL00900
      KDLT=1+K2-K1                                                      SOL00910
      IF(KDLT.LT.2) GO TO 940                                           SOL00920
      IF((K1.GE.IN).OR.(K2.LE.1)) GO TO 790                             SOL00930
      K2M1=K2-1                                                         SOL00940
C                                                                       SOL00950
C    ECLND VALUES AT CX1L & CX2J                                        SOL00960
C                                                                       SOL00970
   40 IF(K1.GT.0) GO TO 50                                              SOL00980
      K1P1=1                                                            SOL00990
      FLUX1J=0.                                                         SOL01000
      GO TO 60                                                          SOL01010
   50 CXK1=CKFUN(K1)                                                    SOL01020
      K1P1=K1+1                                                         SOL01030
      FLUX1J=FLUXIN(K1) + DLTCI*(FLUXIN(K1P1)-FLUXIN(K1))*(CX1J-CXK1)   SOL01040
   60 IF(K2.LE.IN) GO TO 600                                            SOL01050
      K2M1=IN                                                           SOL01060
      FLUX2J=0.                                                         SOL01070
      GO TO 610                                                         SOL01080
  600 K2M1=K2-1                                                         SOL01090
      CXK2M1=CKFUN(K2M1)                                                SOL01100
```

```
      FLUX2=FLUXIN(K2M1) +DLTCI*(FLUXIN(K2)-FLUXIN(K2M1))*(CX2-CXK2M1)SOL01110
  610 SUMFLX=FLUX1+FLUX2                                              SOL01120
      IF(KDLT.EQ.2) GO TO 80                                          SOL01130
      DO 70 K=K1P1,K2M1                                               SOL01140
   70 SUMFLX=SUMFLX+FLUXIN(K)                                         SOL01150
C                                                                     SOL01160
C   COMPLTE AVERAGE FLUX, INCREMENT TOTAL INTENSITY OVER W/2.         SOL01170
C                                                                     SOL01180
   80 FLUX(J)=FLUX(J) + SUMFLX/KDLT                                   SOL01190
  790 TEMP=CX1J                                                       SOL01200
      CX1J=-CX2J                                                      SOL01210
  800 CX2J=-TEMP                                                      SOL01220
      FLUX(J)=0.5*FLUX(J)                                             SOL01230
   90 FLUXPL=FLUXPL + FLUX(J)*WIDTHJ                                  SOL01240
      FLUXPL=2.*FLUXPL                                                SOL01250
      RETURN                                                          SOL01260
C                                                                     SOL01270
  900 WRITE(6,9000) (I,DAYS(1,I),DAYS(2,I),I=1,4)                     SOL01280
      READ(5,1020,END=999) ND                                         SOL01290
      GO TO 1                                                         SOL01300
  910 WRITE(6,9010) IN,INMAX                                          SOL01310
      GO TO 10                                                        SOL01320
  920 WRITE(6,9020) NF,DAYS(1,ND),DAYS(2,ND),H1(ND),HL(ND)            SOL01330
      READ(5,1020,END=999) NH                                         SOL01340
      GO TO 20                                                        SOL01350
  930 WRITE(6,9030) IER,NR,LRECL                                      SOL01360
      STOP                                                            SOL01370
  940 WRITE(6,9040) INMAX,K1,K2,X1J,X2J                               SOL01380
  999 STOP                                                            SOL01390
C                                                                     SOL01400
 1000 FORMAT('0INPUT MIN AND MAX CIRCUMFERENTIAL POSITIONS.')         SOL01410
 1001 FORMAT(' INPUT',I4,' FLUX VALUES FROM',F5.1,' FT IN ',          SOL01420
     A   F3.1,'-FT INCREMENTS. 10 VALUES/LINE')                       SOL01430
 1010 FORMAT(10F99.0)                                                 SOL01440
 1020 FORMAT(I99)                                                     SOL01450
 1030 FORMAT('0    FLUX DISTRIBUTION FOR',2A8,' AT',I5,' HOURS'/' ')  SOL01460
 9000 FORMAT(' INVALID INDEX FOR DAY. VALID INDEXES(ND) ARE:',        SOL01470
     A   4(/' ND=',I2,':',2A8)/' RETYPE ND')                          SOL01480
 9010 FORMAT(I4,' INPUT FLUX VALUES EXCEEDS MAX ARRAY SIZE OF',I5)    SOL01490
 9020 FORMAT(I5,' IS INVALID TIME FOR',2A8,' DAY. VALID RANGE IS ',   SOL01500
     A   I3,' TO',I5,'. RETYPE HOUR')                                 SOL01510
 9030 FORMAT(' DREAD10 ERROR',I3,', NR=',I5,', LRECL=',I5)            SOL01520
 9040 FORMAT(' SUB. FLUXS2 ERROR: INMAX,K1,K2,X1J,X2J=',3I5,2F10.1)   SOL01530
      END                                                             SOL01540
```

```
      SUBROUTINE PRTARA(NS,L)
C
C   PRINTS TUBE SURFACE TEMPERATURE MATRIXES
C
C   INDEXES IN COMMON/AR2/ ARE PHYSICAL SECTION,LOOP
C
      COMMON/AR2/ TTUBAS(200,20),QA(200,20),TTUBCM(200,20),DTCA(200,20)
C
      REAL*8 HTW(2) /'  TA    ','  TC    '/
C
      N1=1
      N=10
   10 N=MIN0(N,NS)
      WRITE(6,1000) (M,M=N1,N)
      WRITE(6,1010) (HTW(1),HTW(2),M=N1,N)
      DO 20 J=1,L
   20 WRITE(6,1020) J,(TTUBAS(M,J),TTUBCM(M,J),M=N1,N)
      IF(N.EQ.NS) RETURN
      N1=N+1
      N=N + 10
      GO TO 10
 1000 FORMAT('0',9X'TEMPERATURES',
     A    ' IN EACH SECTION (DEG F). TA IS LAST ASSUMED VALUE',
     B    ', TC IS LAST COMPUTED VALUE'//10I12)
 1010 FORMAT('  LOOP',20A6)
 1020 FORMAT(I5,1X,20F6.0)
      END
```

```
      SUBROUTINE STEAM(P1,H1,T1,VF1,VG1,S1,X,VISC,COND,CP)
C
C     THE SUBROUTINE STEAM PERFORMS LINEAR INTERPOLATIONS FROM
C     TABULATED ENTRIES OF TEMPERATURE, SPECIFIC VOLUME, ENTROPY,
C     QUALITY,VISCOSITY,THERMAL CONDUCTIVITY,AND SPECIFIC HEAT, GIVEN
C     THE STATE OF THE STEAM AT A SPECIFIC PRESSURE AND ENTHALPY.
C     THE SUBROUTINE ASCERTAINS IF THE STATE IS WITHIN THE SATURATION
C     DOME, OR IF THE STATE LIES WITHIN THE SUBCOOL OR SUPERHEAT
C     REGIONS.  IF THE FIRST CASE, THEN THE SPECIFIC HEAT IS SET TO
C     1.0.  IF THE SECOND CASE, THEN THE TEMPERATURE IS ESTIMATED
C     FROM THE DEVIATION OF ENTHALPIES, THE SPECIFIC VOLUME VG1 AND
C     THE QUALITY ARE SET TO -0.0, AND THE SPECIFIC HEAT IS SET TO 1.0.
C     IF THE THIRD CASE, THEN THE SPECIFIC VOLUME VF1 IS SET TO 0.,
C     QUALITY IS SET TO 1.0, AND THE SPECIFIC HEAT IS CALCULATED FROM
C     DELTA H/DELTA T AT CONSTANT PRESSURE.  THE SUBROUTINE ELEMENTS
C     HAVE THE FOLLOWING ENGLISH UNITS--
C
C                 P1        PSIA
C                 H1        BTU/LBM
C                 T1        DEG. F
C                 VF1       CUFT/LBM
C                 VG1       CUFT/LBM
C                 S1        BTU/LBM-DEG. F
C                 X         DECIMAL FRACTION
C                 VISC      LBM/FT-HR
C                 COND      BTU/HR-FT-DEG. F
C                 CP        BTU/LBM-DEG. F
C
C
      DIMENSION VV(38,15),HH(38,15),SS(38,15),TC(19,18),VIS(25,18)
      REAL CNVISC  /241.91E-6/, CNCOND /0.57779E-3/
C
      COMMON/STMDTA/ P(51),T(51),VF(51),VG(51),HF(51),HG(51),
     1   SF(51),SG(51),PP(38),TT(15),
     2   PCON(19),TCON(18),PVIS(25),TVIS(18),
     3  VV1(38),VV2(38),VV3(38),VV4(38),VV5(38),VV6(38),VV7(38),
     4  VV8(38),VV9(38),VV10(38),VV11(38),VV12(38),VV13(38),VV14(38),
     5  VV15(38),HH1(38),HH2(38),HH3(38),HH4(38),HH5(38),HH6(38),
     6  HH7(38),HH8(38),HH9(38),HH10(38),HH11(38),HH12(38),HH13(38),
     7  HH14(38),HH15(38),SS1(38),SS2(38),SS3(38),SS4(38),SS5(38),
     7  SS6(38),SS7(38),SS8(38),SS9(38),SS10(38),SS11(38),SS12(38),
     9  SS13(38),SS14(38),SS15(38),TC1(19),TC2(19),TC3(19),TC4(19),
     1  TC5(19),TC6(19),TC7(19),TC8(19),TC9(19),TC10(19),TC11(19),
     2  TC12(19),TC13(19),TC14(19),TC15(19),TC16(19),TC17(19),TC18(19),
     3  VIS1(25),VIS2(25),VIS3(25),VIS4(25),VIS5(25),VIS6(25),VIS7(25),
     4  VIS8(25),VIS9(25),VIS10(25),VIS11(25),VIS12(25),VIS13(25),
     5  VIS14(25),VIS15(25),VIS16(25),VIS17(25),VIS18(25)
C
      EQUIVALENCE (VV(1,1),VV1(1)), (HH(1,1),HH1(1)), (SS(1,1),SS1(1)),
     A   (TC(1,1),TC1(1)), (VIS(1,1),VIS1(1))
C
C   STEAM TABLE ARRAYS ARE INITIALIZED IN BLOCK DATA
C   NCSS FILE NAME IS SOLSTMBD FORTRAN
C
C   SPECIFCI HEAT EQUATION FOR LIQUID REGION
C   A=LIQUID TEMPERATURE (DEG F)
C   NOT GOOD FOR A<86 DEG F
C
      CPLIQF(A)=0.47739*(A**0.13915)
C
```

```
C*****TEST FOR SUPERHEAT AND SUBCOOL STATES
C
      IF(P1.LE.0.) GO TO 900
      IF(H1.LE.0.) GO TO 910
      IF(P1.GT.(3203.6)) GO TO 300
      N = 1
      IF(P1.GT.P(1)) GO TO 100
      R1=P1/P(1)
      HG1=HG(1)
      IF(H1.GE.HG1) GO TO 460
      HF1=HF(1)
      IF(H1 - HF1) 610,610,110
  100 N1=N
      N = N + 1
      IF(P(N).LE.P1) GO TO 100
      R1 = (P1-P(N1))/(P(N)-P(N1))
      HG1 = HG(N1) + R1*(HG(N)-HG(N1))
      IF(H1.GE.HG1) GO TO 300
      HF1 = HF(N1) + R1*(HF(N)-HF(N1))
      IF(H1.LE.HF1) GO TO 600
C
C*****SATURATION DOME CALCULATIONS
C
      T1 = T(N1) + R1*(T(N)-T(N1))
      CP=CPLIQF(T1)
      VF1 = VF(N1) + R1*(VF(N)-VF(N1))
      VG1 = VG(N1) + R1*(VG(N)-VG(N1))
      SF1 = SF(N1) + R1*(SF(N)-SF(N1))
      SG1 = SG(N1) + R1*(SG(N)-SG(N1))
      GO TO 120
  110 T1=32. + R1*(T(1)-32.)
      CP = 1.0
      VF1=VF(1)
      VG1=VG(1)/R1
      SF1=R1*SF(1)
      SG1=SG(1)
  120 X = (H1-HF1)/(HG1-HF1)
      S1 = SF1 + X*(SG1-SF1)
      GO TO 400
C
C*****SUBCOOL CALCULATIONS
C
  600 CP=0.5*(CPLIQF(T(N1)) + CPLIQF(T(N)))
      T1=T(N1) + R1*(T(N)-T(N1)) - ((HF1-H1)/CP)
      VF1 = VF(N1)+R1*(VF(N)-VF(N1))
      S1 = SF(N1)+R1*(SF(N)-SF(N1))
      GO TO 620
  610 T1=32. + R1*(T(1)-32.)
      CP = 1.0
      VF1=VF(1)
      S1=R1*SF(1)
  620 VG1 = 0.0
      X = 0.0
      GO TO 400
C
C*****SUPERHEAT CALCULATIONS
C
  300 IF(P1.LT.PP(1)) GO TO 460
      L = 1
      M = 1
```

```
  450 L1=L
      L = L+1
      IF((PP(L).LE.P1).AND.(L.LT.38)) GO TO 450
      HM2 = 0.0
      RP = (P1-PP(L1))/(PP(L)-PP(L1))
  451 M1=M
      M = M+1
      HM1 = HM2
      HM2 = HH((L1),M) + RP*(HH(L,M)-HH((L1),M))
      IF((HM2.LE.H1).AND.(M.LT.15)) GO TO 451
      DELTAH=HM2-HM1
      RT = (H1-HM1)/DELTAH
      VVV1= VV((L1),(M1))+RP*(VV(L,(M1))-VV((L1),(M1)))
      VVV2= VV((L1),M)+RP*(VV(L,M)-VV((L1),M))
      VG1 = VVV1 + RT*(VVV2-VVV1)
      SSS1= SS((L1),(M1))+RP*(SS(L,(M1))-SS((L1),(M1)))
      SSS2= SS((L1),M)+RP*(SS(L,M)-SS((L1),M))
      GO TO 460
  460 RP=P1/PP(2)
      DO 465 M=2,15
      IF(HH(2,M).GT.H1) GO TO 470
  465 CONTINUE
      M=15
  470 M1=M-1
      L=2
      HM1=HH(2,M1)
      HM2=HH(2,M)
      DELTAH=HM2-HM1
      RT=(H1-HM1)/DELTAH
      SSS1=SS(2,M1)
      SSS2=SS(2,M)
      VVV1=VV(2,M1) + RT*(VV(2,M)-VV(2,M1))
      VG1=VVV1/RP
  480 DELTAT=TT(M)-TT(M1)
      T1 = TT(M1) + RT*DELTAT
      VF1=0.0
      S1 = SSS1 + RT*(SSS2-SSS1)
      X = 1.0
      IF((HM1.GT.902.5).OR.(P1.GT.3203.6)) GO TO 490
      CP=(HH(L,M+1)-HM2)/(TT(M+1)-TT(M))
      GO TO 400
  490 CP=DELTAH/DELTAT
C
C*****VISCOSITY CALCULATION
C
  400 L = 1
      IF(P1.LT.PVIS(1)) GO TO 4500
      M = 1
  410 L1=L
      L = L+1
      IF((PVIS(L).LE.P1).AND.(L.LT.25)) GO TO 410
      IF(T1.LE.TVIS(1)) GO TO 4505
  411 M1=M
      M = M+1
      IF((TVIS(M).LE.T1).AND.(M.LT.18)) GO TO 411
      RP = (P1-PVIS(L1))/(PVIS(L)-PVIS(L1))
      RT = (T1-TVIS(M1))/(TVIS(M)-TVIS(M1))
      VS1 = VIS((L1),(M1))+RP*(VIS(L,(M1))-VIS((L1),(M1)))
      IF((X.GE.1.).OR.(X.LE.0.)) GO TO 412
      PVLF1=PVIS(L+1)
```

```
      VISLP1=VIS(L+1,M)
      DVISDP=(VIS(L+2,M)-VISLP1)/(PVIS(L+2)-PVLP1)
      VS2=VISLP1 - DVISDP*(PVLP1-P1)
      GO TO 415
  412 VS2 = VIS((L1),M)+RP*(VIS(L,M)-VIS((L1),M))
  415 VISC = (VS1 + RT*(VS2-VS1))
      GO TO 416
 4500 IF(T1.GT.TVIS(1)) GO TO 4510
 4505 VISC=VIS(L,1)
      GO TO 416
 4510 DO 4520 M=2,18
      IF(T1.LE.TVIS(M)) GO TO 4530
 4520 CONTINUE
      M=18
 4530 M1=M-1
      VISC = VIS(1,M1) +
     A       (VIS(1,M)-VIS(1,M1))*(T1-TVIS(M1))/(TVIS(M)-TVIS(M1))
  416 VISC=CNVISC*VISC
C
C*****THERMAL CONDUCTIVITY CALCULATION
C
      L = 1
      IF(P1.LT.PCON(1)) GO TO 500
      M = 1
  420 L1=L
      L = L+1
      IF((PCON(L).LE.P1).AND.(L.LT.19)) GO TO 420
      IF(T1.LE.TCON(1)) GO TO 505
  421 M1=M
      M = M+1
      IF((TCON(M).LE.T1).AND.(M.LT.18)) GO TO 421
      RP = (P1-PCON(L1))/(PCON(L)-PCON(L1))
      RT = (T1-TCON(M1))/(TCON(M)-TCON(M1))
      CC1 = TC((L1),(M1))+RP*(TC(L,(M1))-TC((L1),(M1)))
      CC2 = TC((L1),M)+RP*(TC(L,M)-TC((L1),M))
      COND = CNCOND*(CC1+RT*(CC2-CC1))
      RETURN
  500 IF(T1.GT.TCON(1)) GO TO 510
  505 COND=CNCOND*TC(L,1)
      RETURN
  510 DO 520 M=2,18
      IF(T1.LE.TCON(M)) GO TO 530
  520 CONTINUE
      M=18
  530 M1=M-1
      COND=TC(1,M1) +
     A    (TC(1,M)-TC(1,M1))*(T1-TCON(M1))/(TCON(M)-TCON(M1))
      COND=CNCOND*COND
      RETURN
C
  900 WRITE(6,9000)
      STOP
  910 WRITE(6,9010)
      STOP
 9000 FORMAT(' SUBROUTINE STEAM ERROR: PRESSURE<=0')
 9010 FORMAT(' SUBROUTINE STEAM ERROR: ENTHALPY<=0')
      END
```

```
      SUBROUTINE TTUBE0(ICASE1,TI,TO,NS,L)
C
C     COMPUTES INITIAL ASSUMPTIONS FOR TUBE SURFACE TEMPERATURES
C     TI & TO ARE INLET & ASSUMED FINAL TEMPERATURES (DEG F)
C     L=NUMBER OF LOOPS, NS=NUMBER OF SECTIONS/LOOP
C
C     ARRAYS FOR LOOPS AND SECTIONS
C     INDEXES IN COMMON/AR/ AND VECTOR TSECT ARE LOOPS
C     INDEXES IN COMMON/AR2/ ARE PHYSICAL SECTION,LOOP
C
      DIMENSION TSECT(20)
      COMMON/AR/ DIN(20),MTL(20),ENT(20),FLUX(20),DO(20),DON(20),FLUXPL,
     A    AREA(20),FIJ(20,20)
      COMMON/AR2/ TTUBAS(200,20),DA(200,20),TTUBCM(200,20),DTCA(200,20)
C
C
      PSI=0.
      PSI0=0.
      IC=0
      GO TO(1,15),ICASE1
    1 ICASE1=2
      PLNS=L*NS
      DT=(TO-TI)/PLNS
      TSJM1=TI-DT
      DO 10 J=1,L
      IF(J.GT.1) TSJM1=TTUBAS(NS,J-1)
      DO 10 M=1,NS
      DTCA(M,J)=1.E+5
   10 TTUBAS(M,J)=TSJM1 + M*DT
   15 RETURN
C
      ENTRY TTUBE1(NS,L,DT,NC,IW,*,*)
C
C     TEST FOR CONVERGENCE OF COMPUTED TUBE TEMPERATURE MATRIX
C     WITH ASSUMED VALUES, DT IS CONVERGENCE ERROR (DEG F).
C     PSI IS CONVERGENCE ADJUSTMENT PARAMETER
C     NC IS MAX NUMBER OF CONVERGENCE TRIES ALLOWED.
C
      K=1
      IC=IC+1
      IF(IC.GT.NC) GO TO 50
      SUMDLT=0.
      DO 30 J=1,L
      DO 30 M=1,NS
      DTCA(M,J)=TTUBCM(M,J)-TTUBAS(M,J)
      DELTA=ABS(DTCA(M,J))
      GO TO (21,30),K
   21 IF(DELTA.LE.DT) GO TO 30
      K=2
   30 SUMDLT=SUMDLT + DELTA
      AVDLT=SUMDLT/PLNS
      IF(IW.LT.3) WRITE(6,1000) IC,AVDLT,PSI
      IF(K.EQ.1) GO TO 40
      IF(IW.EQ.1) CALL PRTARA(NS,L)
      IF(PSI0.GT.0.) GO TO 250
      WRITE(6,1052)
      READ(4,1051,END=95) PSI,PSI0,IWN
      IF((IWN.GT.0).AND.(IWN.NE.IW)) IW=IWN
  250 DO 300 J=1,L
      DO 300 M=1,NS
```

```
  300 TTUBAS(N,J)=TTUBAS(N,J) + PSI*DTCA(M,J)
C
C    SORT NEW TA'S INTO ASCENDING ORDER WITHIN SECTION
C
      DO 350 M=1,NS
      IS=NS+1-M
      DO 310 J=1,L,2
      TSECT(J)=TTUBAS(M,J)
  310 IF(J.NE.L) TSECT(J+1)=TTUBAS(IS,J+1)
      J=L
  320 JP1=J
      J=J-1
      IF(J.EQ.0) GO TO 340
      TEMP=TSECT(JP1)
      DO 330 JJ=1,J
      IF(TEMP.GE.TSECT(JJ)) GO TO 330
      TSECT(JP1)=TSECT(JJ)
      TSECT(JJ)=TEMP
      TEMP=TSECT(JP1)
  330 CONTINUE
      GO TO 320
  340 DO 350 J=1,L,2
      TTUBAS(M,J)=TSECT(J)
  350 IF(J.NE.L) TTUBAS(IS,J+1)=TSECT(J+1)
      RETURN 1
C
C    CONVERGENCE OF TTUBAS & TTUBCM VECTORS TO WITHIN DT DEG F.
C
   40 IF(IW.EQ.4) GO TO 45
      WRITE(6,1001)
      WRITE(6,1000) IC,AVDLT,PSI
   45 IC=0
      IF(IW.LE.2) CALL PRTARA(NS,L)
      RETURN
C
C    MAX. NUMBER OF ITERATIONS EXCEEDED. RETURN TO INPUT STATEMENT
C
   50 WRITE(6,1010)
      IF(IW.LE.2) GO TO 55
      WRITE(6,1000) IC,AVDLT,PSI
      RETURN 2
   55 CALL PRTARA(NS,L)
      RETURN 2
   95 REWIND 4
  100 RETURN 2
 1000 FORMAT(' ITERATION',I3,', MEAN DT=',F7.2,' DEG F, PSI=',F5.2)
 1001 FORMAT(' CONVERGENCE ')
 1010 FORMAT('0MAX. NUMBER OF ITERATIONS EXCEEDED')
 1050 FORMAT(' INPUT PSIO,PSI')
 1051 FORMAT(2F99.0,I99)
 1052 FORMAT(' INPUT NEW PSI,PSIO,IWN')
      END
```

```
      SUBROUTINE VIEW2(PI,SDN,W,D,S,L,NS)
C
C   COMPUTES CHARACTERISTIC LOOP AREAS AND VIEW FACTORS
C   FOR LOOPS DISTRIBUTED RADIALLY IN BOILER CAVITY.
C
C   PI =3.141593
C   SDN=SIN(SDN)  (IN)
C   W  =APERTURE WIDTH (FT)
C   D  =DIAMETER OF CAVITY (FT)
C   S  =SPACING FACTOR
C   L  =NUMBER OF LOOPS
C   NS =NUMBER OF SECTIONS/LOOP
C   DON=TUBE O. D. * NUMBER OF TUBES IN LOOP (IN)
C
      COMMON/AR/ DIN(20),MTL(20),ENT(20),FLUX(20),DO(20),DON(20),FLUXPL,
     A   AREA(20),FIJ(20,20)
C
      PID=PI*D
      CMAX=D*(PI - ARSIN(W/D))
      SD12=CMAX/SDN
      S=12.*SD12
      DO 10 I=1,L
   10 AREA(I)=SD12*DON(I)
      DO 20 I=1,L
      FDEN=1./(PID-AREA(I))
      DO 20 J=1,L
      FIJ(I,J)=FDEN*AREA(J)
   20 IF(I.EQ.J) FIJ(I,I)=0.
      RETURN
      END
```

THIS PAGE

WAS INTENTIONALLY

LEFT BLANK

Appendix C

HELIOSTAT FIELD EXPERIMENT PLAN

THIS PAGE

WAS INTENTIONALLY

LEFT BLANK

Appendix C

HELIOSTAT FIELD EXPERIMENT PLAN

This appendix contains a description of the field experiment planned for the Central Receiver Research Study. Construction of the experiment at a site near the ESD facility was started in October 1978. Construction was stopped by the Department of Energy in January 1979 due to funding constraints, and the field experiment was deleted by DOE from the project scope of work.

C.1 OBJECTIVES

There were three prime objectives for the heliostat field experiment:

1. Demonstrate feasibility of heliostat control logic.
2. Measure the distribution of flux within the image from the heliostat.
3. Estimate overall heliostat collection efficiency.

A half-section of an FMC Line Focus Heliostat Module was to be tested to demonstrate that the heliostat can focus incident solar radiation to within a 4-foot vertical image, to measure the fraction of incident radiation within this concentrated image, to measure the distribution of solar flux within the image, and to verify heliostat control logic.

The test heliostat consisted of an 18.3 meter by 3.05 meter (60 feet by 10 feet) section (approximately 55 square meters (590 square feet) of glass area) with elevation and focus controls. A description of the controls can be found in Section 5. The control logic to be used in the test heliostat simulated that which would be used in a line focus system.

The heliostat was to be tested at each of three positions (Figure C-1). The reflected image from the heliostat was to be focused upon a motorized target (Figure C-2). A photocell was to move across the face of the target to make a sawtooth scan of the image.

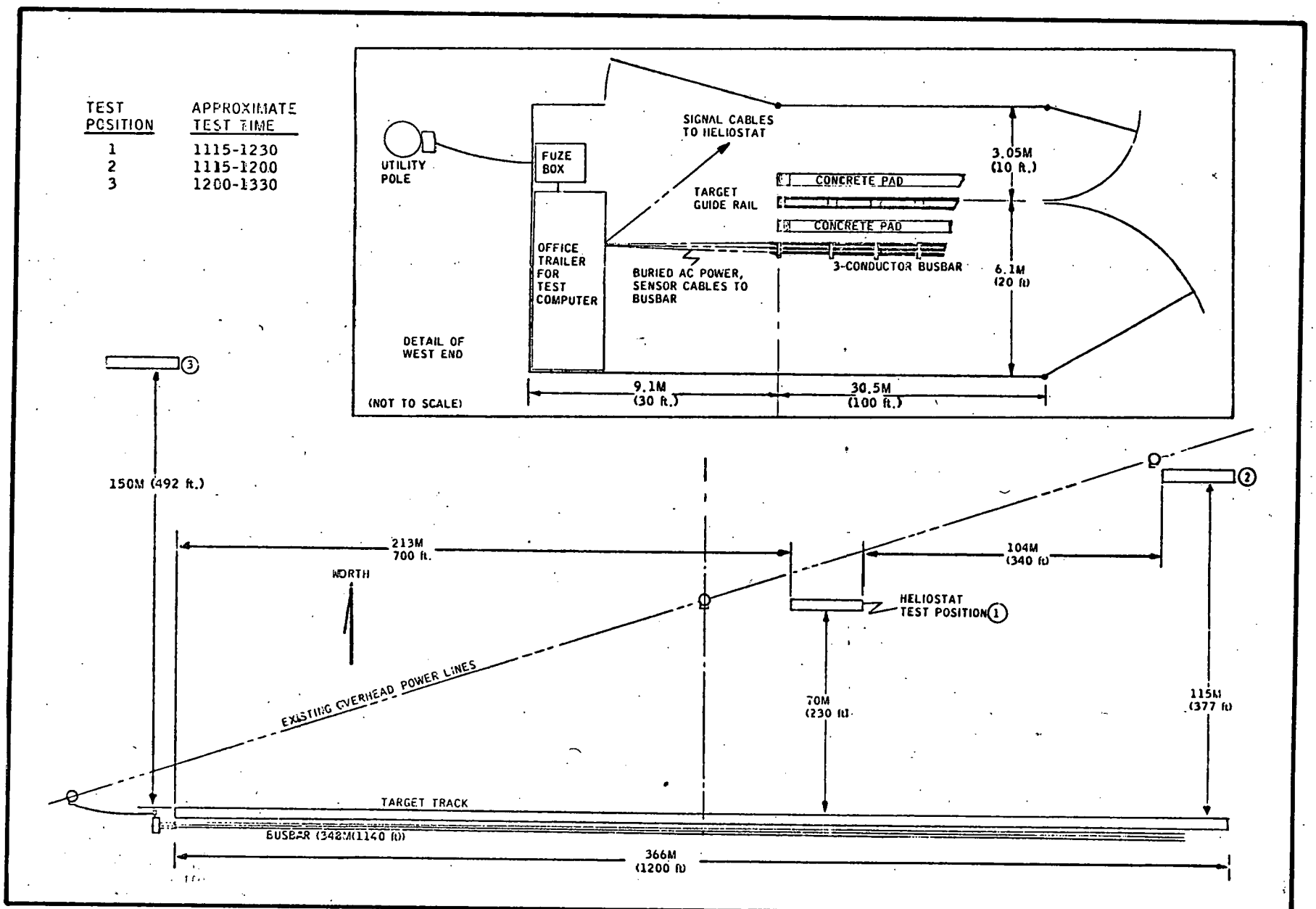

Figure C-1 TEST FIELD LAYOUT

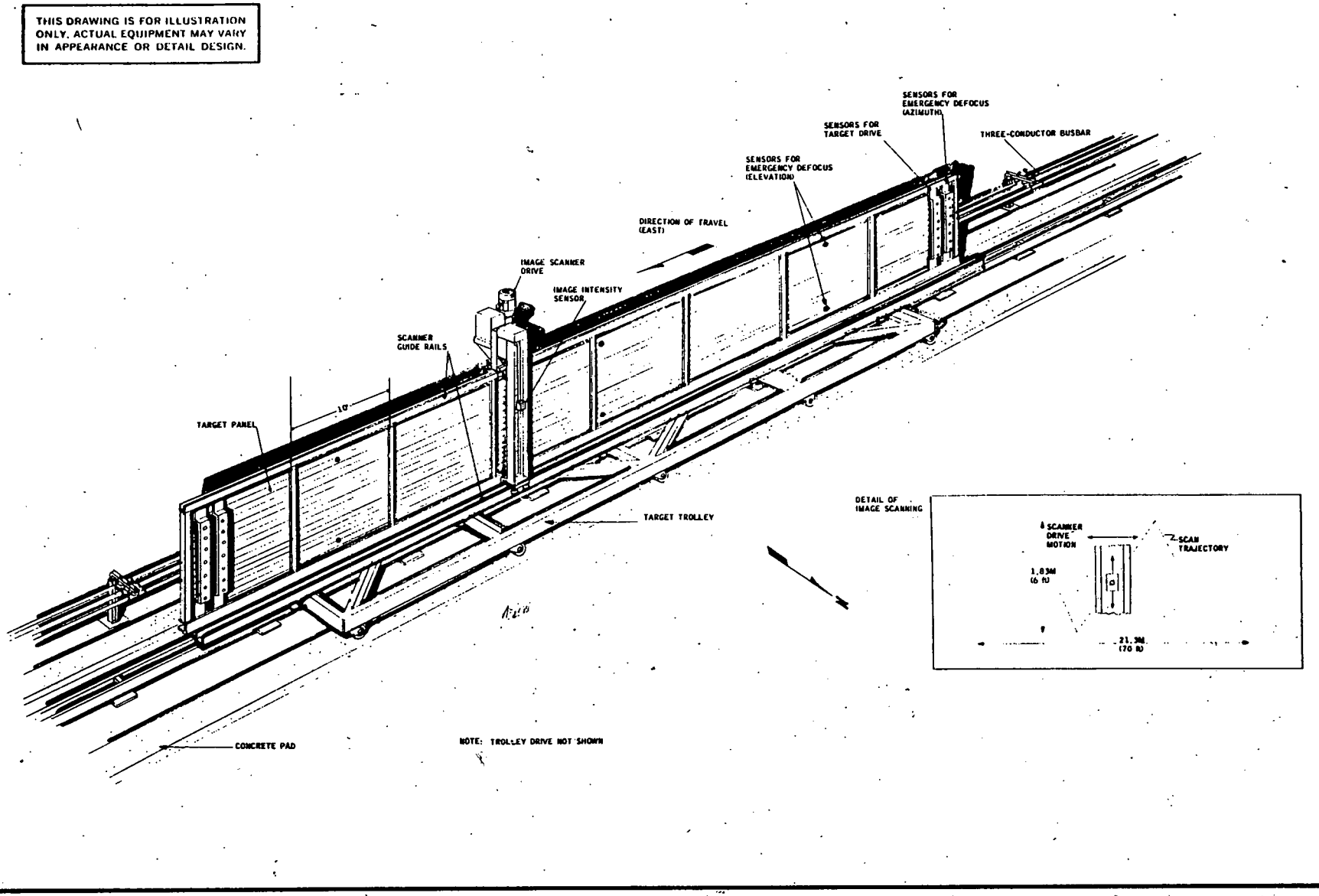

Figure C-2 LAYOUT OF TARGET AND GUIDANCE TRACK

Figure C-2 shows the target vehicle mounted on the guidance track. The view shown in Figure C-2 is from the heliostat side. Figure C-3 shows part of the completed guidance track, looking West. The test site was constructed on a City of Santa Clara landfill located six miles from the ESD facility.

The target (Figure C-4) was composed of eight louvered panels, each 3.05 meters (10 feet) square. A panel consists of a steel frame which supports aluminum louvers. The louver angle is 30 degrees, to reflect some of the incident image from the heliostat down and in front of the target.

The target trolley was to ride on steel casters along two concrete pads, as shown in Figure C-2. The trolley was driven by engagement of a sprocket gear with a drive chain mounted on the south side of the center guide rail. The drive assembly (Figures C-5 and C-6) was to be mounted on the west end of the trolley. The drive sprocket is opposed by a spring-loaded guide wheel. Two guide wheels bear against each side of the guide rail at the east end of the trolley to restrict lateral motion.

The heliostat module was installed aboard a flat-bed trailer, as shown in Figure C-7. The trailer was to provide the means for transporting the heliostat to the test site and was to serve as the foundation platform for the heliostat during testing. The use of a flat-bed trailer as the heliostat foundation reduced the technical and logistic problem of moving the heliostat to a new test position and eliminated the requirements for constructing (and dismantling) three concrete foundations. Leveling jacks on the trailer were to be used for sighting the heliostat at the target plane.

Scanning of the image from the heliostat was to be accomplished by a sensor which was mounted on a moving scanner assembly. The scanner assembly (see Figure C-8) was mounted vertically in front of the louver panels. Horizontal traverse of the assembly is accomplished by driving a set of wheels mounted at the top and bottom of the assembly. Each set of wheels rides in a channel mounted on the louver panels.

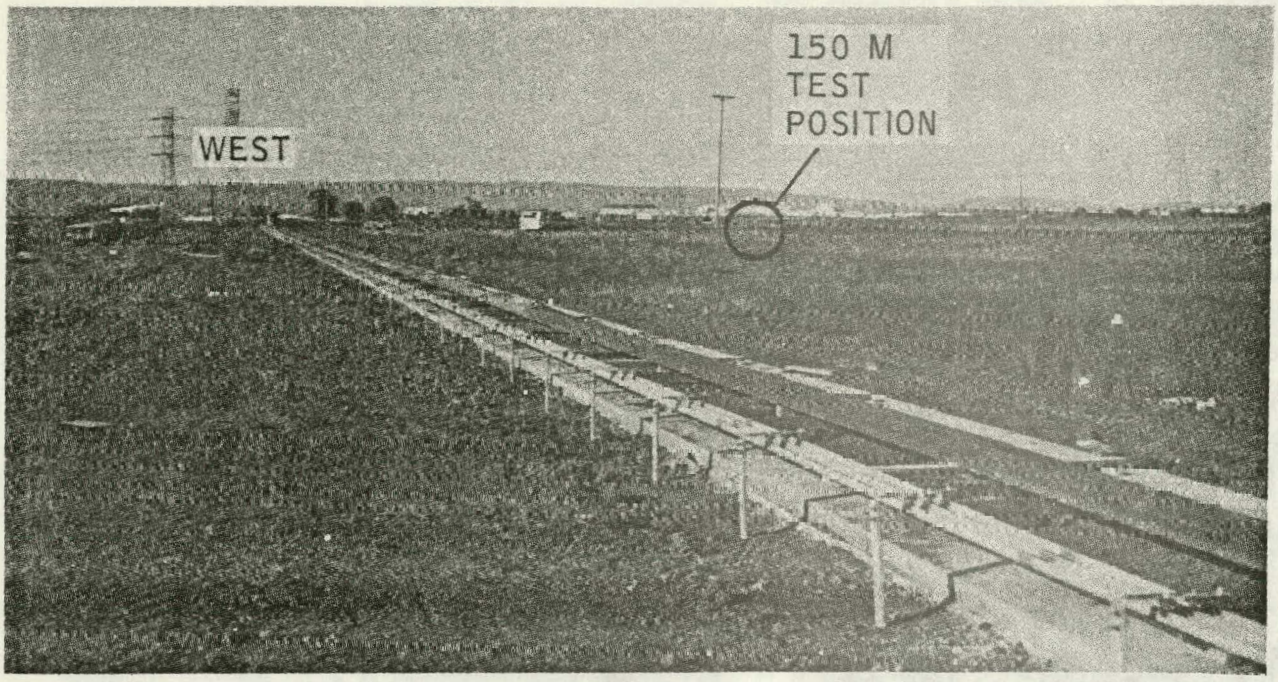

Figure C-3 COMPLETED GUIDANCE TRACK

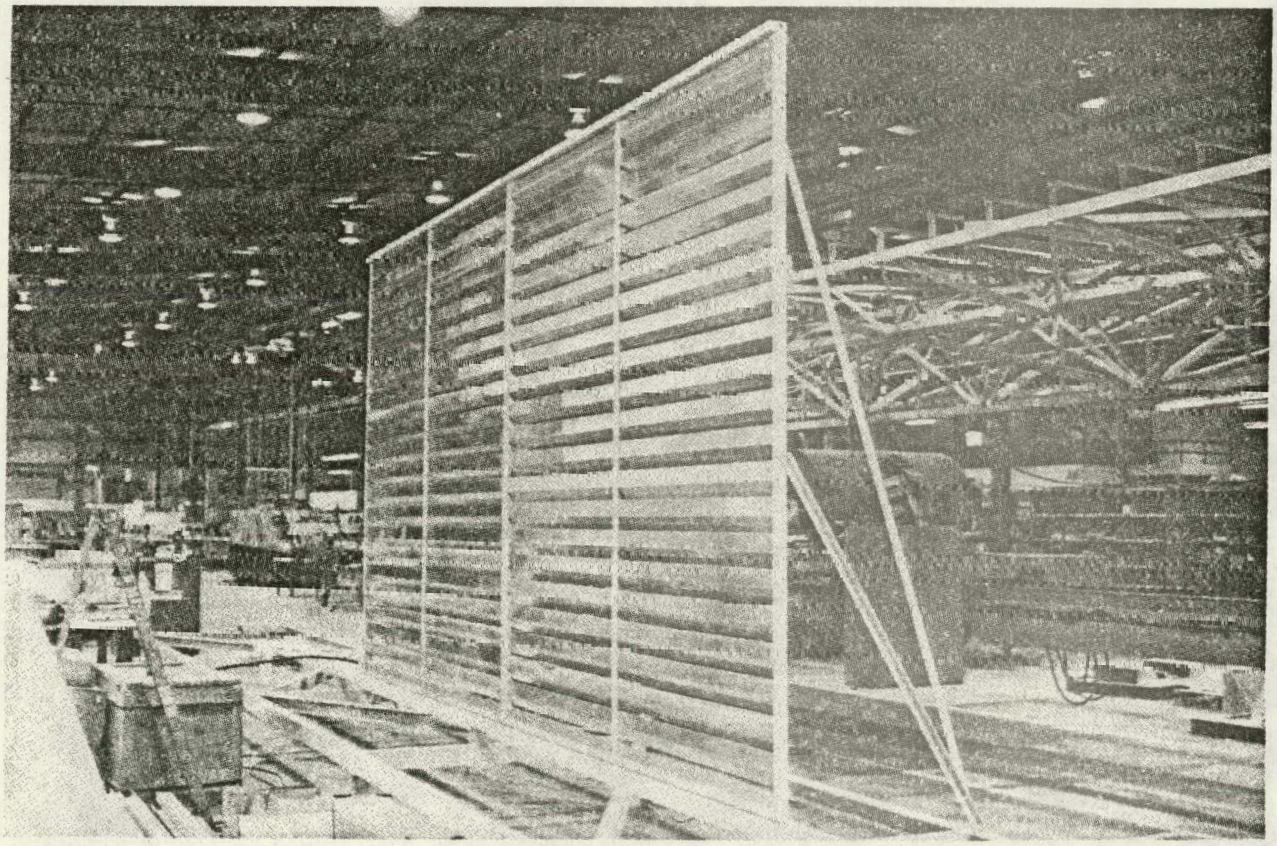

Figure C-4 TARGET ASSEMBLY READY FOR TRANSPORT TO TEST SITE

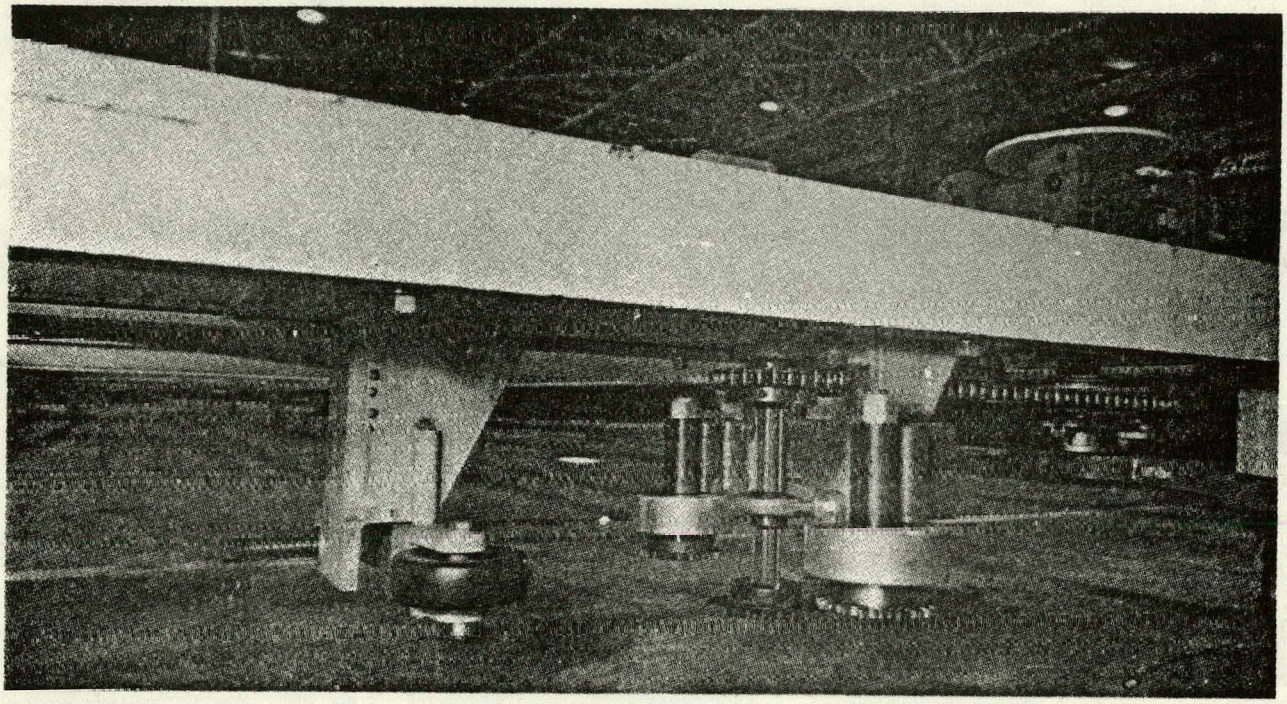

Figure C-5 TARGET DRIVE, BOTTOM VIEW

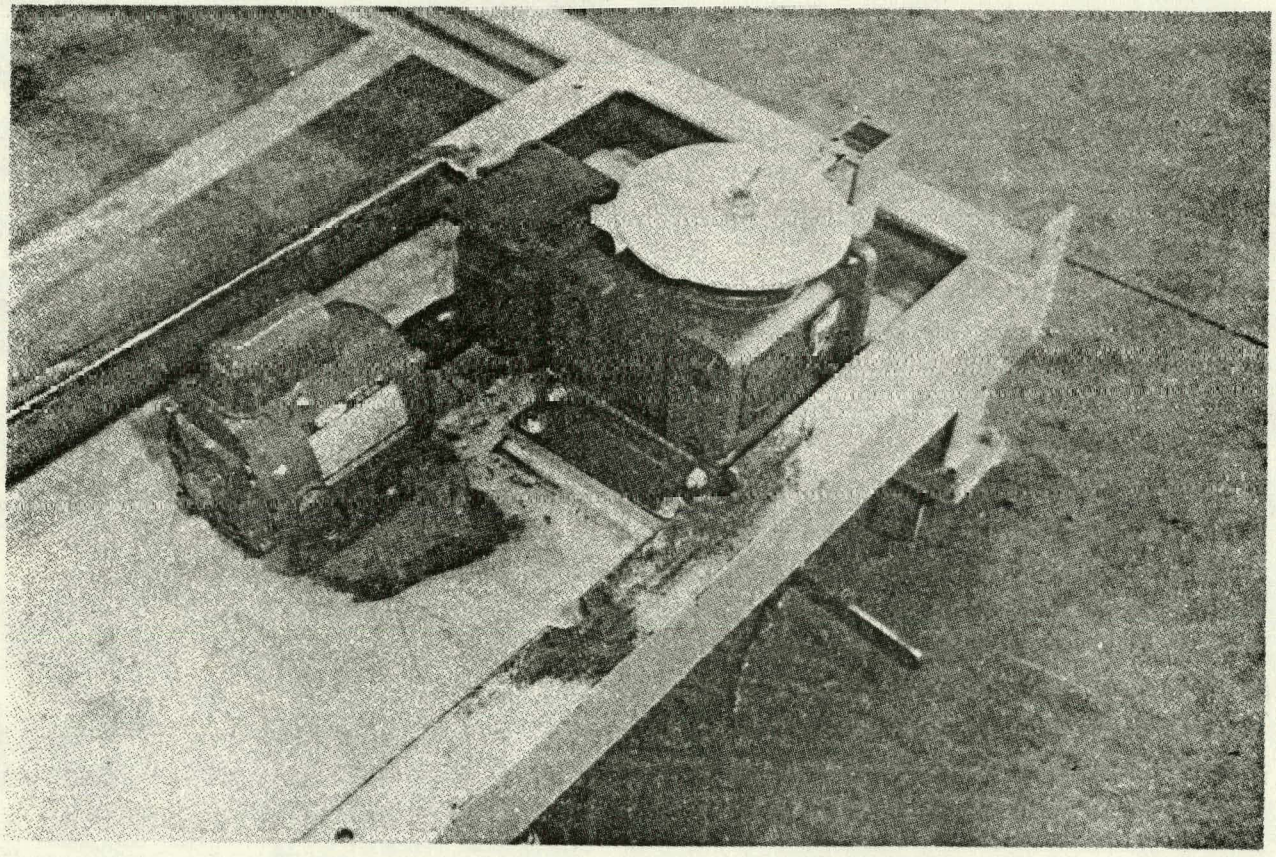

Figure C-6 TARGET DRIVE, TOP VIEW

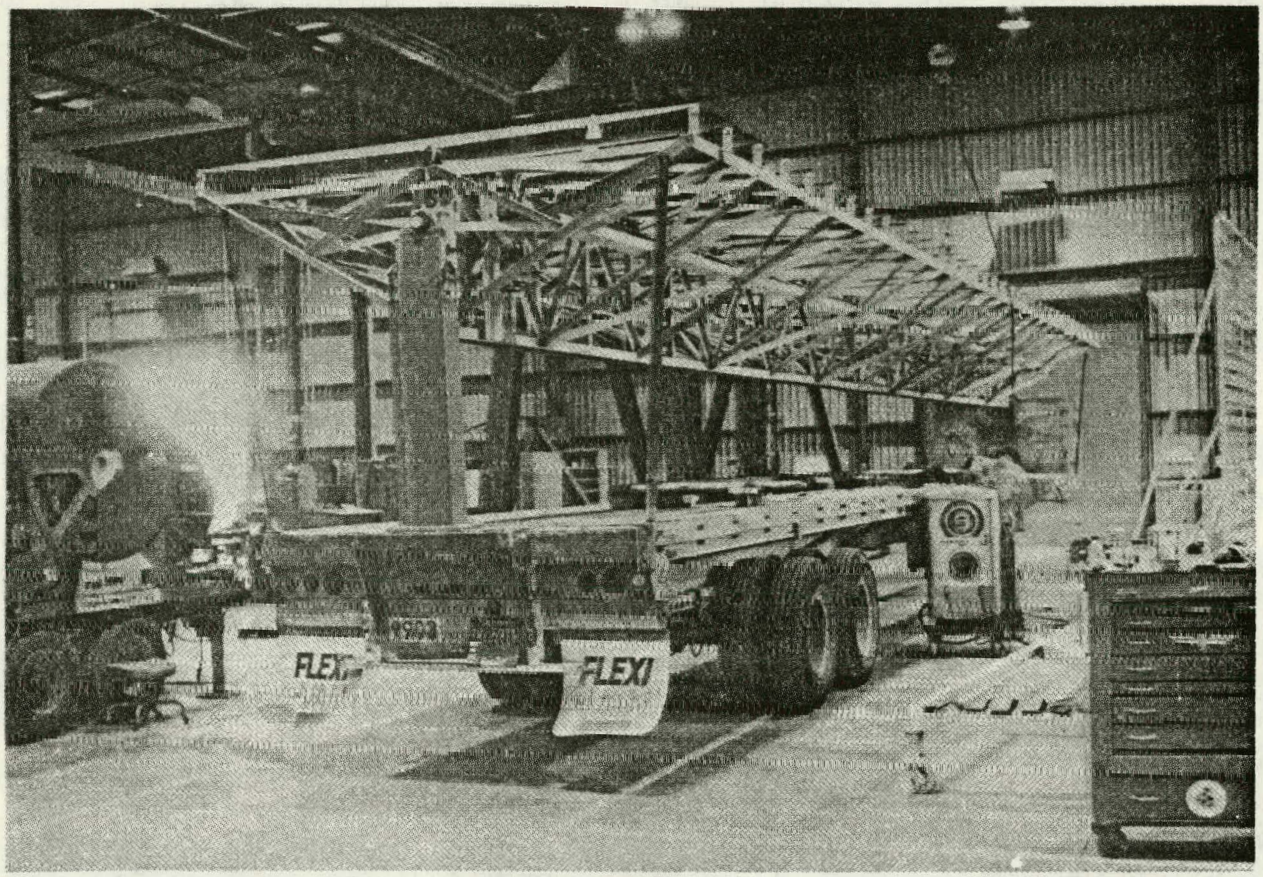

Figure C-7 TEST HELIOSTAT MOUNTED ON TRAILER

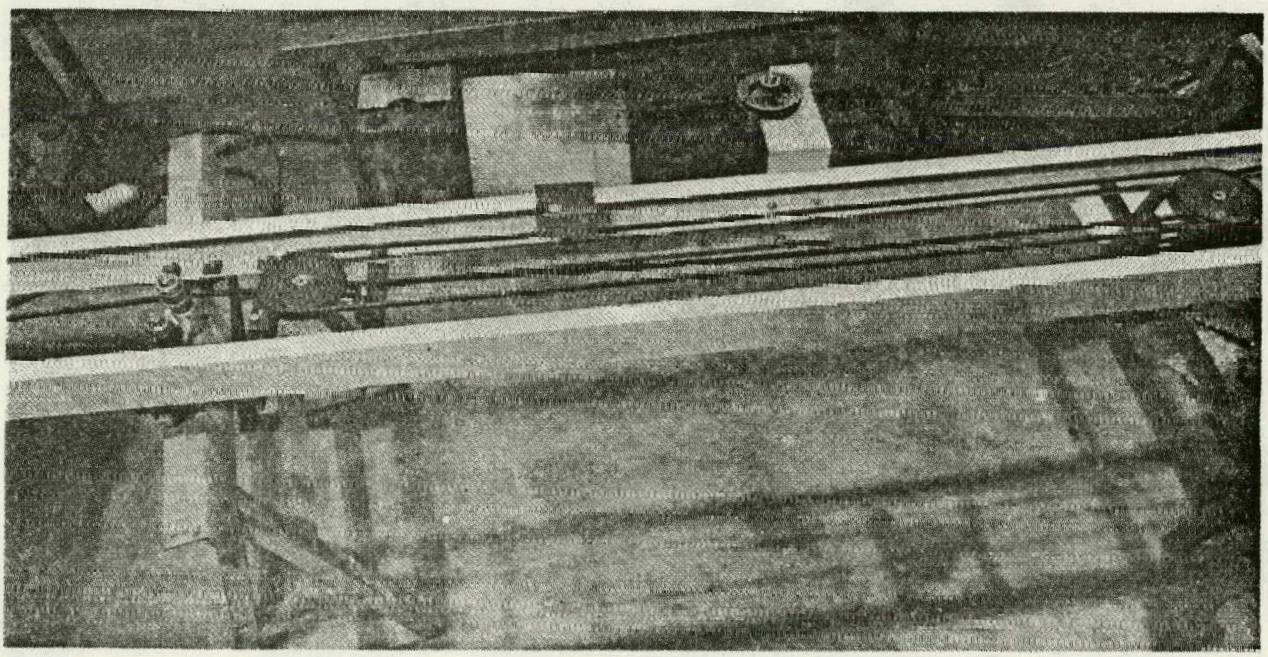

Figure C-8 SCANNING SENSOR DRIVE ASSEMBLY

The drive system was designed to simultaneously drive the assembly horizontally at a speed of 3.94 cm/s (1.55 in/s), and the photocell vertically at a speed of 28.4 cm/s (11.2 in/s). The photocell travels 1.83 meters (6 feet) vertically (full top-to-bottom travel) during 25.4 cm (10 in) of horizontal travel. One complete scan (22.9 meters (75 feet) of horizontal travel takes about 10 minutes. The scanner assembly operated within 1 percent of design requirements during tests performed in the ESD shop.

A three-channel busbar was to be used to supply power to the trolley and to transmit all sensor signals to the test computer in the instrument van. Slide contacts mounted on the trolley ride in the busbar channels. The busbar was installed on the south side of the track. Figure C-9 shows a detail view of the installation.

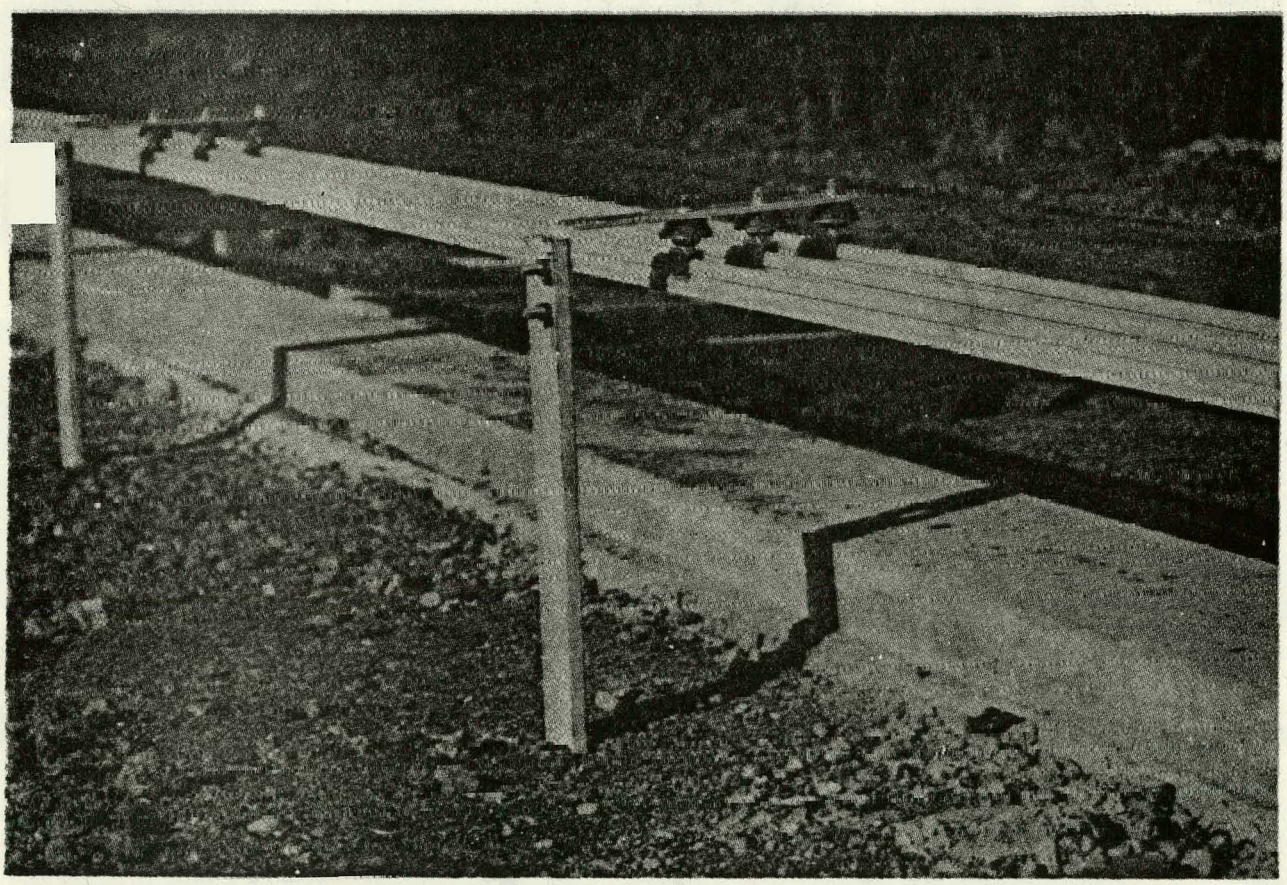

Figure C-9 DETAIL OF BUSBAR INSTALLATION AT TEST SITE

A four-channel chart recorder was to be mounted on the target to record the following on a continuous basis for the duration of a test run:

- Scanning photocell output.
- Photocell position (cam actuation of relay every 6 inches of vertical travel of scanner.)
- Horizontal travel of target (cam actuation of relay every 12 inches of target travel.)
- Time synchronization pulse from recorder.

A chart digitizer located at ESD was to be used to convert the chart tracings to digital form for subsequent computer processing.

Output of the photocell was to be calibrated against readings from a pyroheliometer to obtain factors to convert the photocell output to flux intensity. A computer program was written to process the digitized chart tracing to generate flux distribution and compute integrated image intensity.

An instrument van was to be located at the West end of the test track to contain the following instrumentation:

- PDP 11/03 computer to communicate with the heliostat local controller for elevation and focus control, collect data on tracking performance, and to perform emergency defocus control.
- Tracking pyroheliometer (mounted outside of van.)
- Strip chart recorder with time synchronization pulse to record pyroheliometer output.
- Weather station with visual display to measure ambient temperature, wind speed and direction, and relative humidity.

C.2 TEST PLAN

Five specific tests were planned. Section 5 describes the associated control logic to be examined and verified in these tests.

Stowing/Destowing

Purpose: To demonstrate that stowing/destowing control strategy works as planned.

Procedure: With the heliostat module operating with mirrors temporarily defocused, the test computer will alternately stow and destow the heliostat. Tests will be conducted for several different wind vectors (if possible.)

Expected Results: Correct performance will be determined by observation. Motion picture coverage will document the test.

Emergency Defocus

Purpose: To demonstrate that the emergency defocus logic and controls perform as required.

Procedure: (Command Control). The heliostat will be commanded to focus and track the sun. A simulated emergency defocus command will be issued via the test computer.

Expected Results: If the emergency defocus is operating, the mirror will defocus (i.e., return to a convex curvature) within 0.25 second. The change in image intensity will be recorded by the scanning sensor on the target.

Procedure: (Target Horizontal Tracking Control). The inboard set of vertical image sensors will be commanded to focus and track.

Expected Results: If the emergency defocus system is operating properly, power to the heliostat will be automatically cut off when the outboard set of vertical sensors detect the image. This will cause the heliostat to defocus and stow within 20 seconds (design goal).

Procedure: (Target Vertical Tracking Control.) The heliostat will be commanded to focus and track. After manual tracking is established, the heliostat will be commanded to rotate (increase elevation angle with respect to target center) until the upper row of sensors detect the image.

Expected Results: In normal operation, the heliostat will immediately defocus and stow. The test will be repeated for the lower row of sensors.

Focus Performance

Purpose: Verify correct operation of mirror focus control.

Procedure: The defocused heliostat will be commanded to track. The focus motor will be commanded to run through its entire range under control from the test computer. The scanning sensor will record the change in image size and intensity.

Expected Results: The focus motor will cause the heliostat to focus the image on the target to within a four-foot vertical height at all test positions and for varying wind conditions.

Tracking Performance

Purpose: Verify correct operation of mirror tracking system, and examine long-term tracking stability during an operating day.

Procedure: The heliostat will be commanded to track. The test computer will collect and record signals from the elevation encoder output and stepper motor input. The data will be subsequently processed to compute deviation between actual and reference parameters.

Expected Results: The deviations between measured tracking parameters and reference parameters should not exceed system design requirements (Section 5.2).

Image Intensity

Purpose: Measure the distribution of flux at points within the solar image concentrated upon the target by the heliostat when operating normally.

Procedure: A normally operated heliostat (all tests described above are successful) will be commanded to track the sun. The position of the sun will be pre-computed for 6-minute intervals over the duration of a test run. One run will last for 60-90 minutes, depending on the time of year and heliostat position (see Figure C-1). The geometry of the test site is such that the solar image will be incident upon the target between 1030 and 1430. The specific period again depends upon the time of year and heliostat position.

The target will be positioned at the West end of the track. The heliostat will be initially commanded to the defocused position, and will be commanded to begin elevation tracking a short time prior to the time at which the solar image is predicted to be incident upon the target.

The heliostat will track in defocused mode until the full image from the heliostat is incident upon the target. The heliostat will then be commanded to focus the image to within a four-foot vertical span on the target face. The test computer will issue a new solar position message to the local controller every six minutes. All recording instrumentation will operate during the test run.

Expected Results: The solar image should remain concentrated upon the target with a vertical height of 2-4 feet, depending upon the mirror curvature and heliostat-target distance. Predicted maximum intensity is approximately 2 times normal incident flux (suns) at 4-foot concentration, and 4 to 5 suns at 2-foot concentration. Predicted collection efficiency is 0.7-0.9, depending upon time of day and heliostat position. Detailed predicted performances corresponding to specific test conditions will be computed during the test period.

C.3 STATUS OF CONSTRUCTION

At the time FMC was instructed by the Department of Energy to eliminate the field experiment from the scope of work, construction of the test site was complete, except for (1) connection of power cables from the fuse box to the trailer, and from the trailer to the busbar, and (2) installation of the test computer and other equipment in the trailer.

Grading of access roads from the enclosure to each heliostat test position was completed. Each test position had been graded and leveled. Surveying of alignment markers for the heliostat had been completed. The markers defined reference lines to align the long axis of the heliostat with the target track.

Elevation sightings from reference points at each test position to the North concrete pad had been completed. Sightings were taken at 18.3 meter (60 foot) intervals along the length of the track. The average and maximum elevation difference between any of the reference points and the pad surface were, respectively, 2.5 cm (1.0 in) and 5.7 cm (2.25 in). The overall change in elevation from the West to East end of the track was 2.5 cm (1.0 in). These measurements were well within the tolerances specified by FMC to the construction subcontractor.

In accordance with the revised scope of work, dismantling of the site was started in early January and was scheduled for completion by early February.

THIS PAGE

WAS INTENTIONALLY

LEFT BLANK

Appendix D

SIZING AND PERFORMANCE ESTIMATES FOR BASELINE PLANT CONCEPTS

THIS PAGE

WAS INTENTIONALLY

LEFT BLANK

Appendix D

SIZING AND PERFORMANCE ESTIMATES FOR BASELINE PLANT CONCEPTS

This appendix contains the computations performed to size baseline concepts for electric generation plants using the FMC line focus heliostat and once-through receiver concept. Two concepts were generated. The concepts, a 10 MWe pilot plant and a 100 MWe commercial plant, were based on (1) requirements used by Phase I contractors for the Point Focus Central Receiver Solar Thermal Power System, and (2) the thermal-to-electric power conversion cycles evolved by the McDonnell Douglas Astronautics Company (MDAC). The MDAC power conversion cycle was selected because the flow rates and steam conditions required by the MDAC thermal storage and electric power generating subsystems best matched the FMC receiver concept.

Performance data for the once-through receiver (Section 4.1) were used for all sizing computations. These data were generated early in the project, using an assumed system operating pressure of 6.9 MPa (1000 psia) and the following operating temperatures:

- feedwater to receiver inlet at 216°C (422°F)
- steam at receiver outlet at 538°C (1000°F).

The conditions vary from the MDAC operating requirements, which were published after the analysis phase of our project was completed. The MDAC requirements are:

- feedwater to receiver at 250°C (401°F) and 13.8 MPa (2000 psia)
- receiver steam to turbine at 510°C (950°F) and 10.1 MPa (1465 psia).

The project budget did not permit general re-computation of receiver performance data, so only performance data at specific design points were re-computed with the MDAC requirements to permit realistic plant sizing. All other performance data were generated with the original receiver data (enthalpy of 838 kg-cal/kg at 538°C steam). Since the

MDAC turbine requires steam at a somewhat lower available energy content (enthalpy of 810 kg-cal/kg at 510°C), the use of the original receiver data allows, in effect, for a 3 percent heat loss in the piping between the receivers and turbine.

D.1 10 MWe PILOT PLANT

Two concepts were evaluated. The first concept was based on North and South collector fields, optimized for 2:00 p.m. winter solstice design point (Section 2.2). The second concept contained only optimized North collector fields.

Field sizing was based on preliminary data for the MDAC 10 MWe concept (1) which specified turbine operation at 477°C (890°F) 10 MPa (1450 psia) input steam, 56.7°C (135°F) 0.16 MPa (2.5 psia) exhaust steam, and operation from thermal storage for 6 hours at 7 MWe. These conditions differ from the final MDAC specifications (2). The original sizing and performance computations are presented in the following paragraphs because time did not permit recalculation with the final specifications. However, note that fewer receivers would be required, as shown by the following computations:

MDAC 2:00 p.m. winter solstice design point, 10 MWe power to busbar
0.7 MWth/kg

- absorbed thermal energy from receiver (3) = 32.6 MWth
  $= 28 \times 10^6$ kg-cal/hr
- flow rate to turbine (4) 46,467 kg/hr (102,440 lb/hr)
- turbine inlet steam conditions (5) = 510°C (950°F), 10.1 MPa (1465 psia)

Under these conditions, design point sizing is as follows, using 538°C (1000°F) steam from a North receiver section, and 3 percent heat losses between receivers and turbine:

- flow rate from north receiver (Figure D-1) = 2550 kg/hr (5620 lb/hr)
- enthalpy of steam to turbine = (0.97) (838) = 810 kg-cal/kg

- enthalpy of feedwater to receiver = 222 kg-cal/kg
- number of receiver sections required = 46,467/2550 = 18.2
- net absorbed energy by 19 receivers = (19) (2550) (810-222)
  $= 28.5 \times 10^6$ kg-cal/hr
  = 33.2 MWth

Thus, 10 North/South receiver units are still sufficient to meet the design point requirements. The remainder of this section contains the performance estimates based on the preliminary MDAC data.

D.1.1 North and South Fields

North and South collector fields, optimized for 2:00 p.m. winter solstice were used. Table D-1 shows the field characteristics for 10 MWe sizing.

Table D-1 NORTH/SOUTH FIELD SIZING FOR 10 MWe PLANT CONCEPT

Field	Number of heliostat rows	610-meter (2,000-foot) length		Butterfly area $[m^2(10^3 ft^2)]$	Total number of heliostats (Note 1)
		Average number per row	Number of mirror sections		
North	21	33-1/3	700	9,105 (98)	432
South	29	33-1/3	967	10,590 (114)	578

Note 1: Two mirror sections (3.05 meters by 18.3 meters) per heliostat.

The following parameters were used to compute receiver performance with the simulation model described in Appendix B:

- Receiver 61 meters (200 feet) long, containing North and South receiver cavities. Each cavity contains eight banks of tubes distributed about the cavity circumference (Section 4.1).
- Feedwater introduced into the outermost bank of tubes at 6.9 MPa (1000 psia) and 216°C (422°F).
- Emissivity and absorptivity of the tubes, respectively, 0.7 and 0.9.

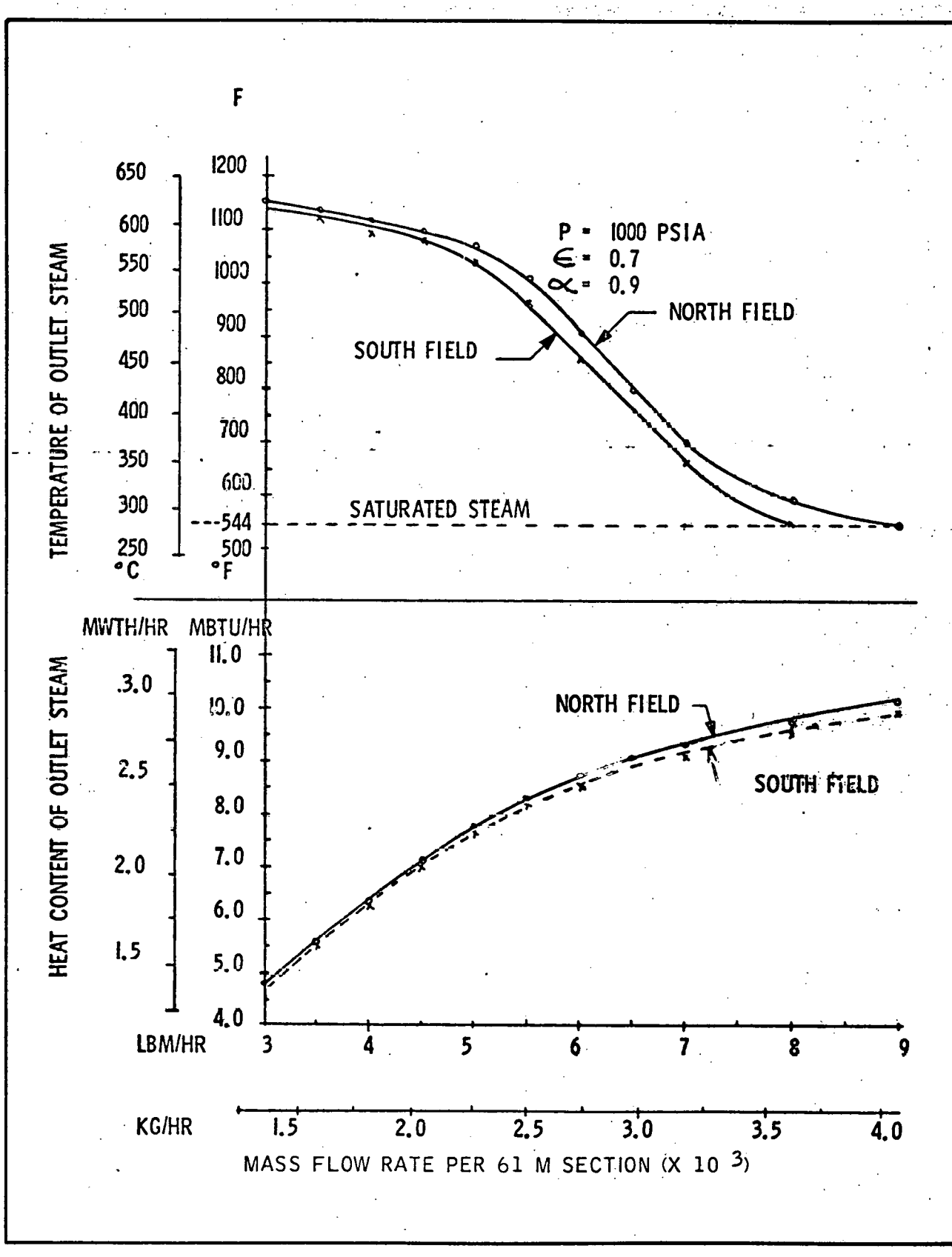

Figure D-1 COMPARISON OF OUTPUT FROM NORTH AND SOUTH BOILER SECTIONS AT 2 P.M. ON WINTER SOLSTICE

- Superheated steam extracted from the innermost bank of tubes where the flux density is highest for transmission to the turbine or to storage.

Performance of a North boiler section was computed for a range of feedwater flow rates at hourly intervals for winter solstice, equinox, and summer solstice insolation. The computer programs developed for collector field optimization were used to generate the circumferential distribution of solar flux intensity from an optimized flat North field (Appendix A).

Peformance of a South field receiver section was simulated only for the baseline design point to minimize expenditures for computer time. South receiver performance for other times was estimated from North receiver performance data with a set of scaling factors. The scaling factors were derived from the relative performance of each section at the baseline design point and the relative solar flux intensities incident on the two sections at other times and days. Figure D-1 shows the performances of the North and South receiver sections at 2:00 p.m. winter solstice for a nominal operating pressure of 6.9 MPa (1000 psia).

The number of receiver sections required to produce 10 MWe net at the baseline design point was computed as follows:

- Total steam to turbine (6) = 51,400 kg/hr (113,000 lb/hr).
- Flow rate from North section for steam at 477°C, 10 MPa =2700 kg/hr (5950 lb/hr).
- Number of receiver sections required = 51,400/2700 = 19.04
- Enthalpy of steam at turbine inlet = 792 kg-cal/kg (1425 Btu/lb).
- Enthalpy of steam at turbine outlet*=514 kg-cal/kg (925 Btu/lb).
- Net power input to turbine=51,400 (792-514) = 14.3 x 10^6 kg-cal/hr. =16.6 MWth

---

*Isentropic expansion assumed. Exhaust steam at 5m Hg (6). Estimated final steam quality = 0.8 for isentropic expansion.

Thus, 10 double-receiver sections (one North receiver and one South receiver per section) were selected for the baseline design point, with the output of 10 North receivers and nine South receivers routed to the turbine and the output of the remaining South receiver routed to thermal storage. Because the above computations are based on steam from North receivers and because the performance of South receivers is different at the same flow rate (see Figure D-1), performance was recomputed as listed in the following paragraphs for a flow rate of 2700 kilograms per hour from North and South receivers.

Properties of steam from North receiver:

- Temperature: 496°C (925°F)
- Enthalpy: 803 kg-cal per kg (1,446 Btu/lb).

Properties of steam from South receiver:

- Temperature: 465°C (870°F)
- Enthalpy: 784 kg-cal per kg (1,412 Btu/lb).

Net power input to turbine:

10 North section x 2,700 kg/hr x (803 - 514 kg-cal/kg)
+ 9 South section x 2,700 kg/hr x (784 - 514 kg-cal/kg)
= 14.4×10^6 kg-cal/hr = 16.7 MWth.

Thus, the steam from 10 North receivers and nine South receivers each 61 meters (200 feet) long will produce 10 MWe net power at the baseline design point.

The output of one South receiver is routed to thermal storage at the design point. The following assumptions were made to compute gross thermal input to thermal storage:

- Steam input at 343°C (650°F) and 6.9 (1,000 psia)
- Steam condenses to saturated liquid at 250°C (480°F), the average temperature of thermal storage (6).

Thus, at the baseline design point:

- Flow rate from the South receiver (Figure D-1) = 3,200 kg/hr (7,050 lb/hr).
- Enthalpy of input steam = 725 kg-cal/kg (1,305 Btu/lb).
- Enthalpy of output liquid = 280 kg-cal/kg (505 Btu/lb).
- Net input to thermal storage = 3,200 kg/hr (725 - 280 kg-cal/kg)
  = 1.4×10^6 kg-cal/hr (5.6×10^6 Btu/hr)
  = 1.6 MWth.

The following operating schedule was assumed to compute daily power output:

- The plant operates between the morning and afternoon hours at which a receiver section can generate steam at 343°C (650°F) or greater.
- All receiver sections generate steam at 343°C between the startup time and the time at which a receiver section can generate steam at turbine operating temperature (morning storage period). During the morning storage period, output of all sections is routed to thermal storage.
- When the receivers are capable of generating steam at turbine operating temperature, enough receivers are used to produce 10 MWe net power output to the turbine. Output of the remaining sections is routed to thermal storage.
- When the receivers cannot generate steam at turbine operating temperature, all output is routed to storage at 343°C until steam at that temperature can no longer be produced (afternoon storage period).
- Steam at 275°C (525°F) and 2.7 MPa (385 psia) is generated from the energy in thermal storage to run the turbine at 7 MWe net power output.

The morning and afternoon storage periods for each of the three solar days were estimated from a time-based plot of maximum attainable steam temperature (no-load stagnation temperature). Table D-2 shows the operating schedule used for each solar day. Figure D-2 shows the time-based plot.

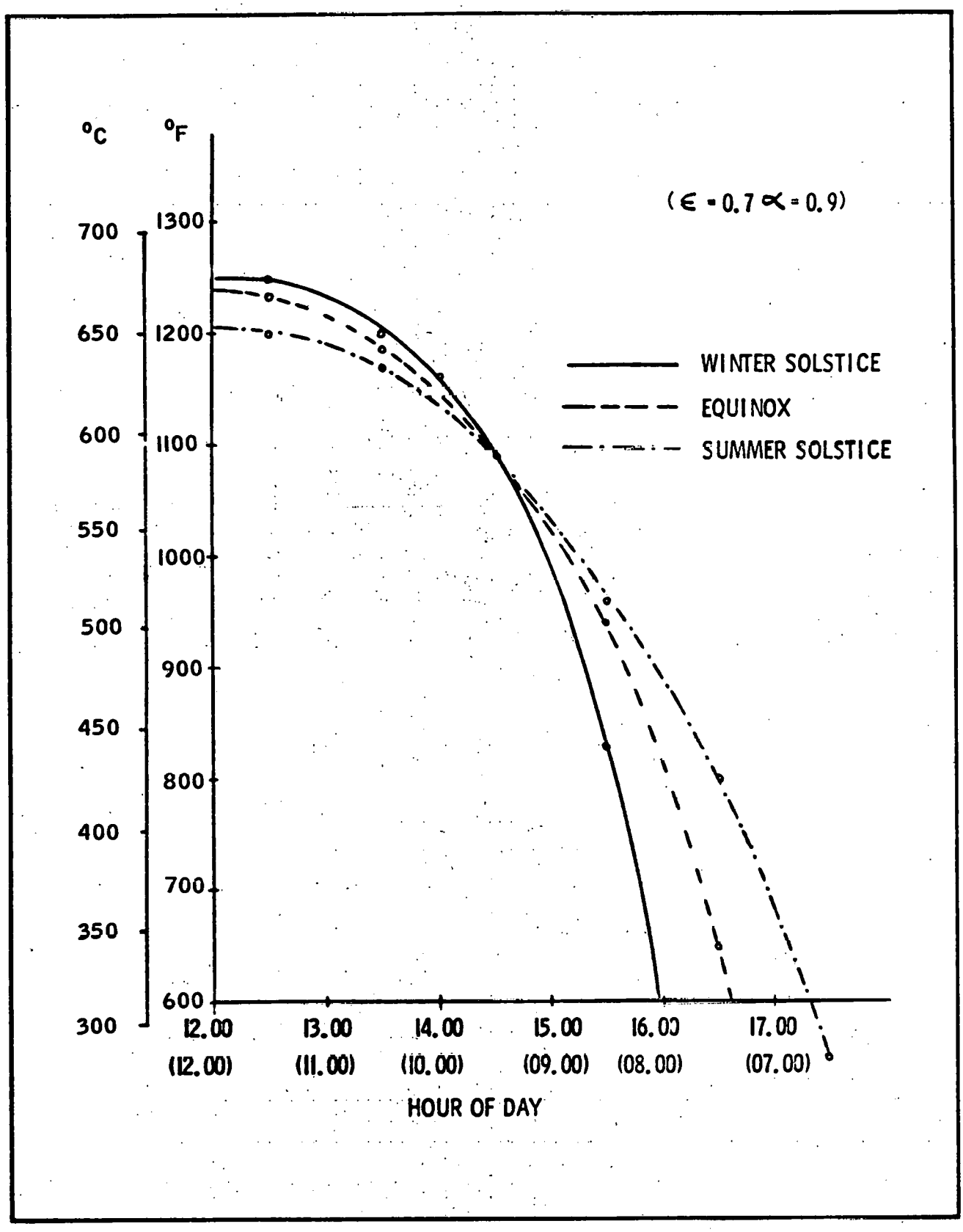

Figure D-2 ESTIMATED MAXIMUM TEMPERATURE OF OUTLET STEAM FROM 61-METER SECTION IN NORTH FIELD

Table D-2 OPERATING SCHEDULE FOR PERFORMANCE COMPUTATIONS

Solar day	Morning storage	Direct turbine operation	Afternoon storage
Winter solstice	0800 - 1000	1000 - 1400	1400 - 1600
Equinox	0730 - 0900	0900 - 1500	1500 - 1630
Summer solstice	0700 - 0900	0900 - 1500	1500 - 1700

Each period was divided into intervals of one-half hour or one hour and the properties of receiver steam at the midpoint were used to make the following computations.

Number of Sections Required to Operate Turbine (N_T)

$$N_T = Q_{TG} / m_T (h_T - h_{ext}) \quad \text{(D1)}$$

where Q_{TG} = gross energy input required to generate 10-MWe net power
= 16.6 MWth (14.3×10^6 kg-cal/hr)

m_T = mass flow rate in one receiver section (kg/hr)

h_T = average enthalpy of steam from North and South receiver sections

h_{ext} = enthalpy of exhaust steam from turbine = 514 kg-cal/kg.

Mass flow rate in one receiver section (m_T) was selected so that the average temperature of the steam from North and South sections was equal to the operating temperature of the turbine.

Net Electric Energy Generated by Direct Turbine Operation (E_T)

The value of N_T from Equation D1 was used to select the number of North and South receiver sections to be used for direct turbine operation. E_T was then computed as follows:

$$P_T = (1.163 \times 10^{-6}) \eta m_T [N_{TN}(h_{TN} - h_{ext}) + N_{TS}(h_{TS} - h_{ext})] \quad \text{(D2)}$$

where N_{TN} = number or North receiver sections to the turbine

N_{TS} = number of South receiver sections to the turbine

h_{TN} = enthalpy of steam from North receiver section

h_{TS} = enthalpy of steam from South receiver section

η = thermal cycle efficiency of turbine = 10 MWe net/16.6 MWth ideal
= 0.6

and the units of P_T are MWe.

Net energy generated during the time period is given by:

$$E_T = (\Delta H)\ (P_T)\ \text{MWhe} \qquad \text{(D3)}$$

where ΔH = time period.

Gross Energy Input to Thermal Storage (Q_s)

The operating characteristics described in the MDAC report for the thermal storage subsystem were used to compute the gross energy charging rate and net energy output.

$$Q_s = (1.163 \times 10^{-6})\ (\Delta H) m_s \left[(10 - N_{TN})\ (h_{SN} - h_{exs}) + (10 - N_{TS})\ (h_{SS} - h_{exs})\right] \qquad \text{(D4)}$$

where m_s = mass flow rate from a receiver section (kg/hr)

h_{SN} = enthalpy of steam from a North receiver section (kg-cal/kg)

h_{SS} = enthalpy of steam from a South receiver section (kg-cal/kg)

h_{exs} = enthalpy of exhaust from thermal storage
= 280 kg-cal/kg (saturated water at 250°C)

and Q_s = gross energy input to storage (MWhth) during time period ΔH.

As in Equation D], the value of m_s was chosen so that the average temperature of steam from North and South sections was 343°C.

Net Daily Energy Output from Thermal Storage (E_s)

The MDAC data (7) indicates that 187 MWhth are required from thermal storage to generate 42 MWhe net (7 MWe for 6 hours) for an overall thermal efficiency of 42/187 = 0.225. This efficiency was used in the calculations. Thus:

$$E_s = (1.163 \times 10^{-6})\ (0.225)\ \Sigma Q_s \text{ MWhe net from storage.} \qquad \text{(D5)}$$

The duration of operation from thermal storage at 7 MWe net output is given by:

$$H_S = E_S/7 \text{ (units of hours.)} \qquad (D6)$$

Equations D1 through D6 were used to compute the performance for each time period during each of the three solar days. Performance calculations were made for direct turbine operation at 371, 427, 482, and 538°C (700, 800, 900, and 1000°F). Table D-3 shows the daily performance summaries for direct turbine operation at 482°C.

Table D-3 SUMMARY OF DAILY PERFORMANCE FOR DESIGN POINT SIZING

Parameter		Winter solstice	Equinox	Summer solstice
Direct operation of turbine	Net power (MWe)	10.0	10.3	10.2
	Net energy (MWhe)	40.0	62.0	61.0
	Hours of operation per day	4.0	6.0	6.0
Operation from thermal storage	Gross energy input (MWhth)	123.0	114.0	147.0
	Maximum charging rate (MWhth)	27.0	29.0	21.0
	Net energy (MWe)	28.0	26.0	33.0
	Hours of operation @ 7 MWe/day	3.9	3.7	4.7
Daily summary	Net energy (MWhe)	68.0	88.0	94.0
	Hours of operation/day	7.9	9.7	10.7
	Load factor*	0.28	0.37	0.39
	Mean power output** (MWe)	8.6	9.0	8.8

* Load factor = net energy/24 hours x 10 MWe net capacity.
**Mean power output = net energy/hours of operation/day.

D.1.2 North Fields Only

The second 10 MWe plant concept contained optimized North fields only. This alternative was evaluated following a review of the FMC concept by Aerospace Corporation (8). Table D-4 shows the optimized design point field sizing. To maintain the same basis for comparison, a design containing 20 North receiver sections is used.

Table D-4 NORTH-ONLY FIELD SIZING FOR 10 MWe PLANT CONCEPT

Field	Number rows	610-meter (2,000-foot)length		Butterfly area $[m^2(10^3 ft^2)]$	Total number of heliostats
		Number per row	Number of mirror sections		
North	21	33-1/3	1,400	9,105 (98)	782

The assumptions and equations used in Section D.1.1 were used with the exception that the terms for South receiver sections are dropped from Equations D1 through D4, and enthalpies and flow rates are for North receiver sections at turbine operating temperature. The modified equations are as follows:

$$N_T = Q_{TG}/m_T(h_T - h_{ext}) \quad (D7)$$

$$P_T = (1.163 \times 10^{-6})\,\eta\, m_T\, N_T\, (h_T - h_{ext}) \quad (D8)$$

$$E_T = (\Delta H)(P_T) \quad (D9)$$

$$Q_S = (1.163 \times 10^{-6})(\Delta H)m_s(20 - N_T)(h_s - h_{exs}) \quad (D10)$$

Where m_t, m_s, h_t, and h_s are mass flow rates and enthalpies from a North receiver section. Table D-5 shows the daily performance summaries at the baseline design day for direct turbine operation at 482°C (900°F).

D.1.3 Cost/Performance Comparison

Annual generating capacity and total investment cost were estimated for the two pilot plant concepts. Table D-6 shows the comparison of system characteristics.

D.1.3.1 Annual Generating Capacity

Annual generating capacity for each system was estimated from the daily outputs computed for 3 solar days, as shown in Table D-7. The annual

Table D-5 DAILY PERFORMANCE FOR NORTH-FIELD-ONLY DESIGN

Mode	Parameter	Winter solstice	Equinox	Summer solstice
Direct operation of turbine	Net power (MWe)	10.0	10.2	10.2
	Net energy (MWhe)	49.6	61.2	60.8
	Hours of operation per day	5.0	6.0	6.0
Operation from thermal storage	Gross energy input (MWhth)	106.6	109.4	114.0
	Maximum charging rate (MWhth)	33.4	25.4	19.5
	Net energy (MWe)	24.0	24.6	25.7
	Hours of operation @ 7 MWe/day	3.4	3.5	3.7
Daily summary	Net energy (MWhe)	74.0	85.8	85.5
	Hours of operation/day	8.4	9.5	9.7
	Load factor*	0.31	0.36	0.36
	Mean power output** (MWe)	8.4	9.1	8.9

*Load factor = net energy/(24 hours x 10 MWe net capacity.)
**Mean power output = net energy/hours of operation/day.

Table D-6 CHARACTERISTICS OF 10-MWE BASELINE SYSTEMS

Subsystem characteristic	North/south system	North-only system
Number of heliostats	1,010	782
Number of 61-m receivers	10 (double)	20 (single)
Number of 61-m towers	11	21
Collector area (km^2)	0.121	0.094

capacities, shown in Table D-8, were computed by linear interpolation between the solar days to estimate monthly capacity for January-June, and then assuming symmetry about summer solstice to estimate capacities for July-December.

Table D-7 DAILY PERFORMANCE FOR DESIGN POINT SIZING

Solar day		Winter solstice		Equinox		Summer solstice	
System		North/ south	North only	North/ south	North only	North/ south	North only
Direct operation of turbine	Net power (MWe)	10.0	10.0	10.3	10.2	10.2	10.2
	Net energy (MWhe)	40.0	49.6	62.0	61.2	61.0	60.8
	Hours of operation/day	4.0	5.0	6.0	5.6	6.0	5.2
Operation from thermal storage	Gross energy input (MWhth)	123.0	106.6	114.0	109.4	147.0	114.0
	Maximum charging rate (MWhth)	27.0	33.4	29.0	25.4	21.0	19.5
	Net energy (MWe)	28.0	24.0	26.0	24.6	33.0	25.7
	Hours of operation @ 7 MWe/day	3.9	3.4	3.7	3.5	4.7	3.7
Daily summary	Net energy (MWhe)	68.0	74.0	88.0	85.8	94.0	85.5
	Hours of operation/day	7.9	8.4	9.7	9.5	10.7	9.7
	Load factor[1]	0.28	0.31	0.37	0.36	0.39	0.36
	Mean power output[2] (MWe)	8.6	8.4	9.0	9.1	8.8	8.9

1. Load factor = net energy/24 hours x 10 MWe net capacity.
2. Mean power output = net energy/hours of operation/day.

Table D-8 COMPARISON OF ANNUAL GENERATING CAPACITY FOR BASELINE SIZING

		Electric energy output, 10^6 kWH		Mean daily power, MWe		Mean annual load factor	
Turbine operating temperature °C (°F)		North/ south	North only	North/ south	North only	North/ south	North only
371	(700)	29.8	27.2	8.9	8.4	0.34	0.31
427	(800)	30.4	30.1	9.0	8.9	0.35	0.34
482	(900)	31.1	30.5	8.9	9.3	0.36	0.35
538	(1,000)	30.9	31.0	8.8	8.9	0.35	

D.1.3.2 System Investment Costs

Subsystem investment costs were estimated to compute the total plant investment cost (TIC) in 1976 dollars. Subsystem costs for the receiver, collector, and control subsystems were based on automated production of 1,000 heliostats. Appendix E contains the details of the cost estimations. Costs of the thermal storage and electric generation subsystem were based on those estimated by McDonnell Douglas for their 10 MWe point central receiver system (9).

Table D-9 summarizes the subsystem costs and TIC for each system. The lower TIC of the North-only system is due to the requirement of fewer heliostats to achieve equivalent annual generating capacity of the North/South system. The numbers in parentheses are the cost per unit area (m^2) of collector surface.

Table D-9 INVESTMENT COSTS FOR BASELINE SYSTEMS

	Investment cost, millions of 1976 dollars			
Subsystem	North/south system		North-only system	
Collector	6.4	($52/m^2$)	4.9	($53/m^2$)
Receiver	1.8	(15)	2.3	(25)
Control	4.5	(37)	4.3	(46)
Storage	4.3		4.2	
Generating	6.9		6.9	
Other	5.2		4.3	
System cost	29.1	(241)	26.9	(286)

Busbar energy costs were computed for each baseline system. The Aerospace Corporation Power Plant Economic Model (PPEM) was used to make the computations.

Subsystem investment costs (1976 dollars) for the 10 MWe plant using a 482°C (900°F) turbine were used to compute investment costs per KWe.

The default values in the PPEM program were used for the input data parameters, with the exception of the following:

- Investment Cost Year (YRD): 1976
- Year of Constant Dollars (YRO): 1976
- Plant Capacity Factor (PCF): 0.36
  North field only 0.35
- Annual Operating Expenses (OPEX): $100/KWe
- Annual Inflation Rate (XINF): 0.05 (5 percent per year)

Table D-10 contains the results.

Table D-10 SUMMARY OF PPEM OUTPUTS

Plant size	10 MWe	
System	North/south	North only
Total capital investment to year 1 of commercial operation (dollars/kw)	5,648	5,295
Busbar costs in 1976 dollars (mils/kwh) • Year 2 of commercial operation (1991)	139	136
Net cash flow in 1976 dollars (mils/kwh) • Year 2 of commercial operation	63	61

The data in Table D-10 shows that the North-system only 100 MWe baseline design reduces total capital investment by 6 percent. The principal reason for the decreases is the reduction in the size of the collector field required to achieve baseline performance.

Table D-11 summarizes net busbar costs (1976 dollars) as a function of turbine operation temperature for North-only (20 single boiler sections) and North/South (10 double boiler sections) concepts. The numbers in the columns titled MIN are the minimum number of boiler/superheat sections required to operate at 10 MWe using turbine inlet steam at 6.9 MPa and 482°C.

Table D-11 NET BUSBAR COST IN YEAR 2 OF OPERATION (Mils/Kwh)

Plant size	10 MWe		MIN	
Turbine operating temperature °C(°F)	North/south system	North-only system	North/south system	North-only system
371 (700)	146	153	22	22
427 (800)	142	139	20	20
482 (900)	139	136	20	19
538 (1,000)	143	137	19	18

D.2 100 MWe COMMERCIAL PLANT CONCEPT

D.2.1 Selection of Design Points

A limited trade study of energy collection versus field size was conducted to establish a reasonable (but not necessarily optimum) plant configuration. Initially, a design point corresponding to the day of maximum energy collection (summer solstice) was selected. However, it was found that the number of heliostats in an optimally sized summer solstice field was larger than that for an optimal equinox field, but the incremental energy collected by the summer solstice field was not proportionally greater. Table D-12 shows the comparison.

Table D-12 COMPARISON OF EQUINOX AND SUMMER SOLSTICE DESIGN POINTS

Design point	Summer solstice, 3:00 p.m. point relative to equinox, 3:00 p.m.
Number of heliostats	1.07
Energy at receivers (mwh-th)	
• Equinox	0.96
• Summer solstice	1.08
• Winter solstice	1.00
• Annual	1.04

It is possible to size both the field and the plant for the design point day, which is summer solstice. However, our analysis indicated a better heliostat utilization factor and lower busbar cost if the field is configured in a layout cptimized for an equinox design day.

Analysis of field sizing indicated that an acceptable balance could be achieved by combining the spacing between rows of heliostats corresponding to an equinox design point with a plant configured for maximum output on summer solstice. When operating over the year, this configurtion, which contains 7.4 percent fewer heliostats than the summer solstice field sizing, achieves the 100 MWe/420 MWhe requirements, while collecting 97 percent of the energy collected by a field sized for summer solstice.

D.2.2 Plant Sizing

The number of receiver sections required for the commercial concept was based on the performance at 3:00 p.m. summer solstice of a North-only collector field optimized for 3:00 p.m. equinox; reciver performance with an equinox field was not generated, because of funding constraints, so the performance data for the once-through receiver (Section 4) was used to estimate performance at the new design point.

Energy at the receiver aperture was computed from Figures 4-7 through 4-10 and replotted as a function of flow rate for final steam temperatures of 343°C (650°F) and 538°C (1000°F). Figure D-10 shows these plots, which were used to determine the equivalent flow rate required for an equinox field. A check of receiver performance for noon equinox was made, assuming a receiver working pressure of 10.3 MPa (1500 psia) to verify that the performance of the baseline loop configuration was reasonably close to the performance required by the MDAC EPGS.

Table D-13 lists the computed values of fluid state exiting each receiver loop (average of upper and lower loop halves) and the average incident flux across each loop. Appendix B contains the corresponding output from the computer model for the once-through concept.

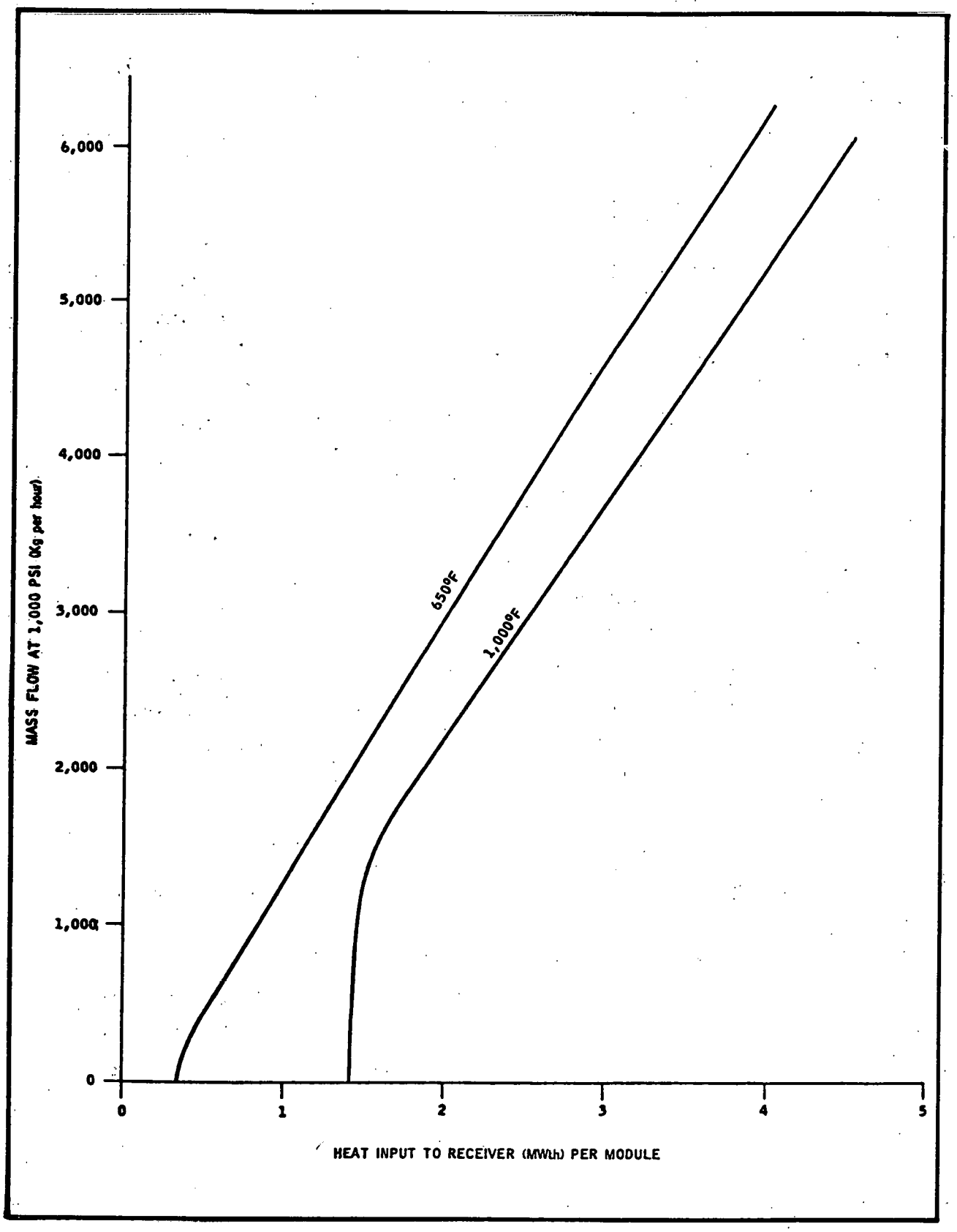

Figure D-10 HEAT INPUT PER RECEIVER SECTION VERSUS FLOW RATE

Table D-13 FLUID STATE IN BASELINE RECEIVER CONCEPT AT LOOP EXITS

Loop		Temperature °C (°F)	Pressure MPa (psia)	Flow rate m/s (ft/s)	Average incident flux kw/m^2 (btu/hr-ft^2)
1		212 (415)	10.3 (1,500)	0.55 (1.8)	0 (0)
2	Preheat	220 (428)	10.3 (1,498)	0.55 (1.8)	0.20 (60)
3		228 (443)	10.3 (1,497)	0.55 (1.8)	1.62 (495)
4		241 (466)	10.3 (1,495)	0.55 (1.8)	5.34 (1,629)
5		267 (512)	10.3 (1,494)	0.55 (1.8)	12.33 (3,759)
6	Boiling	313 (596)	10.3 (1,493)	0.34 (1.1)	19.50 (5,994)
7		313 (596)	10.3 (1,491)	0.91 (3.0)	26.60 (8,110)
8	Superheat	313 (596)	10.2 (1,488)	1.40 (4.6)	37.55 (11,447)

Notes:
1. At noon equinox
2. Mass flow rate = 1.39 kg/s (3.06 lbs/s)
3. Net energy absorbed by working fluid = 550 kg cal/kg (992 btu/lb)
4. Receiver efficiency = 0.86
5. Final steam conditions: 511°C (952°F), 10.2 mPa (1,485 psia), 3.7m/s (12.1 ft/s) flow rate
6. Maximum flux incident on loop 8 = 42.9 kw/m^2 (13,068 Btu/hr-ft^2).

Let the output of the receiver be superheated steam at 1,000°F and 1,000 psi for direct power generation. Let the output be 650°F, 1,000 psi for operation into storage, and let the return water to the receiver be 400°F. Let the turbine be multistage with an outlet of 110°F into 1 psi, and steam quality, x = 0.8 (isentropic expansion to saturation assumed):

Enthalpies:

Steam at 1,000°F, 1,000 psi, h_{IN} = 1.504 Btu per pound

Steam at 650°F, 1,000 psi, h_t = 1,288 Btu per pound

Steam at 110°F, 1 psi, h_o = 1,109 Btu per pound

Water at 440°F, 1,000 psi, h_R = 420 Btu per pound

If a multistage turbine is used which bleeds a small fraction of superheated steam between stages to preheat the return water to 440°F, this quantity of heat is constant in the system and is deducted from the total heat used to calculate the turbine efficiency, η_t

$$\eta_t = \frac{h_{IN}-h_o\,(x)}{h_{IN}-h_R} = \frac{1,504-1,109\,(0.8)}{1,504-420} = 0.569$$

If 0.75 mechanical and 0.9 electrical efficiency is assumed, the total generating efficiency, η_e, is

$$\eta_e = 0.569\,(0.75)\,(0.9) = 0.385.$$

This efficiency is high because of losses involved in the bleeding stages, however, the number compares well with the 0.377 figure reported for the MDAC commercial plant specifications (10). The 0.377 efficiency value will be used.

Let piping losses be 5 percent of sensible heat, then

$$\Delta T = (h_{IN} - h_R - h_{UAP})\,(0.05)/C_P$$

$$= (1,504-420-660)\,(0.05)/0.51$$

$$= 41°F \text{ (between receiver outlet and turbine inlet)}$$

At turbine input, T = 960°F, 1,000 psi, h_T = 1,483Btu/lb.

Using the parasitic loss value of 0.89 reported by MDAC (10), the mass flow, w_g, for 100 MWe is:

$$w_g = 3.413\,(10^8)/\left[0.89\,(0.377)\,(1,483-420)\right]$$

$$= 956,900 \text{ lb/hr } (434,042 \text{ kg/hr})$$

The heat input at 3:00 p.m. summer solstice is 2.265 MWth per module. Receiver steam flow for 2.265 MWth input (Figure D-10) is 2,550 kg/hr (5,620 lb/hr).

Thus, the number of receiver modules, N, is

$$N = 956,900/5,620 = \underline{170}$$

At solar noon, the power in P_I, is 3.742 MWth per module and W_M = 4,870 kg/hn (10,736 lb/hr) and the total field output is

$$P_F = W_M - (h_T \cdot h_R)(\eta_e)(\eta_P)(N)(0.293)$$

$$= 10,736\ (1,483-420)(0.377)(0.89)(170)(0.293)(10^{-6})$$

$$P = 190.7\ MW$$

Power factor = $\underline{1,9}$

The charging rate to thermal storage is computed as follows:

Superheated steam (960°F, 1,000 psi, or 650° F, 1,000 psi) is input to the desuperheater and output at 650° F, 1,000 psi. The steam is condensed in the thermal storage heater; outlet is water at 480° F, 1,000 psi (h = 465 Btu/lb). The efficiency of the TSU is 0.98 (10).

Assuming the heat in the 480° outflow water is conserved and can be recovered to regenerate the 440° return water, the thermal storage efficiency, η_{TS}, is:

$$\eta_{TS} = \frac{(h_T - h_O)\ \eta_{TSH}}{h_T - hr}$$

$$= \frac{(1,483-465)(0.98)}{1,483-420}$$

$$\eta_{TS} = 0.94$$

Calculation of hourly heat partition

1. Determine input power flux for one receiver module on a particular day and hour from Figures 4-7 through 4-10 (use half-hour curve as average value over the hour.)

2. If $P < 2.265$ MWth /module, read W_M from 650°F curve of Figure D-10.
If $P > 2.265$ MWth /module, read W_M from 1,000°F curve.

3a. If $P_I < 2.265$, calculate heat to storage

$$P_S = N(\eta_{TS})(h_{650}-h_{480})(0.293) \times 10^{-6} W_M$$

$$P = \underline{0.040461\ W_M} \quad (W_M \text{ in lb/hr})$$

Mass flow to storage

$$W_S = 170\ (W_M)$$

3b. If $P_I > 2.265$ MWth /module, calculate flow to storage,

$$W_S = 170(W_M) - 956,900 \text{ (lb/hr)}$$

Heat to storage

$$P_S = W_S(\eta_{TS})\ (h_T-h_{420})\ (10^{-6})\ (0.293)$$

$$= W_S\ (0.94)(1,063)(0.293)(10^{-6})\ W_M$$

$$P_S = \underline{\underline{(0.000293)}}\ W_M \quad (W_M \text{ in lb/hr})$$

Typical Calculations for Summer Solstice

Assume symmetry about 1200 to use curves in Figures 4-7 through 4-10.

0800-0900 (use curves for 1530, Figures 4-9 and 4-10.)

$P_I = 1.554$ MWth at 650°F

$W_M = 2,230$ kg/hr = 4,916 lb/hr

$P_S = 4,916\ (0.040641) = \underline{199.8}$ MW

W_S = 2,230 (170) = 379,100 kg/hr

900-1000 (use curves for 1430)

P_I = 2.423 MWth at 1,000°F,

W_M = 2,850 kg/hr = 6,283 lb/hr

W_S = 170 (6,283) - 956,900 = 111,210 lb/hr = 50,444 kg/hr

P_S = 111,210 (0.000293) = 32.6 MWth

W_g = 434,042 kg/hr

P_o = 100 MWe

1000-1100 (use curves for 1330)

P_I = 3.094 MWth at 1,000°F

W_M = 3,870 kg/hr = 8,532 lb/hr

W_S = 170 (8,532) - 956,900 = 493,500 lb/hr = 223,850 kg/hr

P_S = 493,500 (0.000293) = 144.5 MWth

W_g = 434,042 kg/hr

P_o = 100 MWe

Other hours are similarly calculated. The estimates for the three solar days are shown in Table D-14. Figure D-12 shows the estimated daily plant output over July through December.

Table D-14 HOURLY PERFORMANCE, NORTH FIELD SIZED FOR 3:00 PM EQUINOX

Summer Solstice

Hour	W_S x 10^3kg/hr	P_S MWth	W_g x 10^3kg/hr	P_o MWe	Total Output	
7	147	77.5	0	0	Direct	600 MWeH
8	390	199.8	0	0	Storage	454 MWeH
9	50	32.6	434	100	Total	1,054 MWeH
10	224	144.5	434	100		
11	348	224.6	434	100		
12	396	259.3	434	100		
13	348	224.6	434	100		
14	217	140.1	434	100		
15	569	300.1	0	0		
16	335	176.5	0	0		
17	116	60.9	0	0		
		1,840.5 MWthH		600 MWeH		

Equinox

Hour	W_S x 10^3 kg/hr	P_S MWth	W_g x 10^3kg/hr	P_o MWe	Total Output	
8	174	91.7	0	0	Direct	550 MWeH
9	557	293.9	0	0	Storage	426 MWeH
10	234	151.1	434	100	Total	976 MWeH
11	396	255.3	434	100		
12	450	290.4	434	100		
13	387	249.8	434	100		
14	231	148.9	434	100		
15	196	126.6	217	50		
16	226	119.2	0	0		
		1,726.9 MWthH		550 MWeH		

Winter Solstice

Hour	W_S x 10^3 kg/hr	P_S MWth	W_g x 10^3 kg/hr	P_o MWe	Total Output	
8	190	100.3	0	0	Direct	500 MWeH
9	330	173.8	0	0	Storage	218 MWeH
10	568	20.9	434	100	Total	718 MWeH
11	152	98.4	434	100		
12	209	134.6	434	100		
13	158	101.7	434	100		
14	568	20.9	434	100		
15	328	172.9	0	0		
16	190	100.3	0	0		
		883.8 MWthH		500 MWeH		

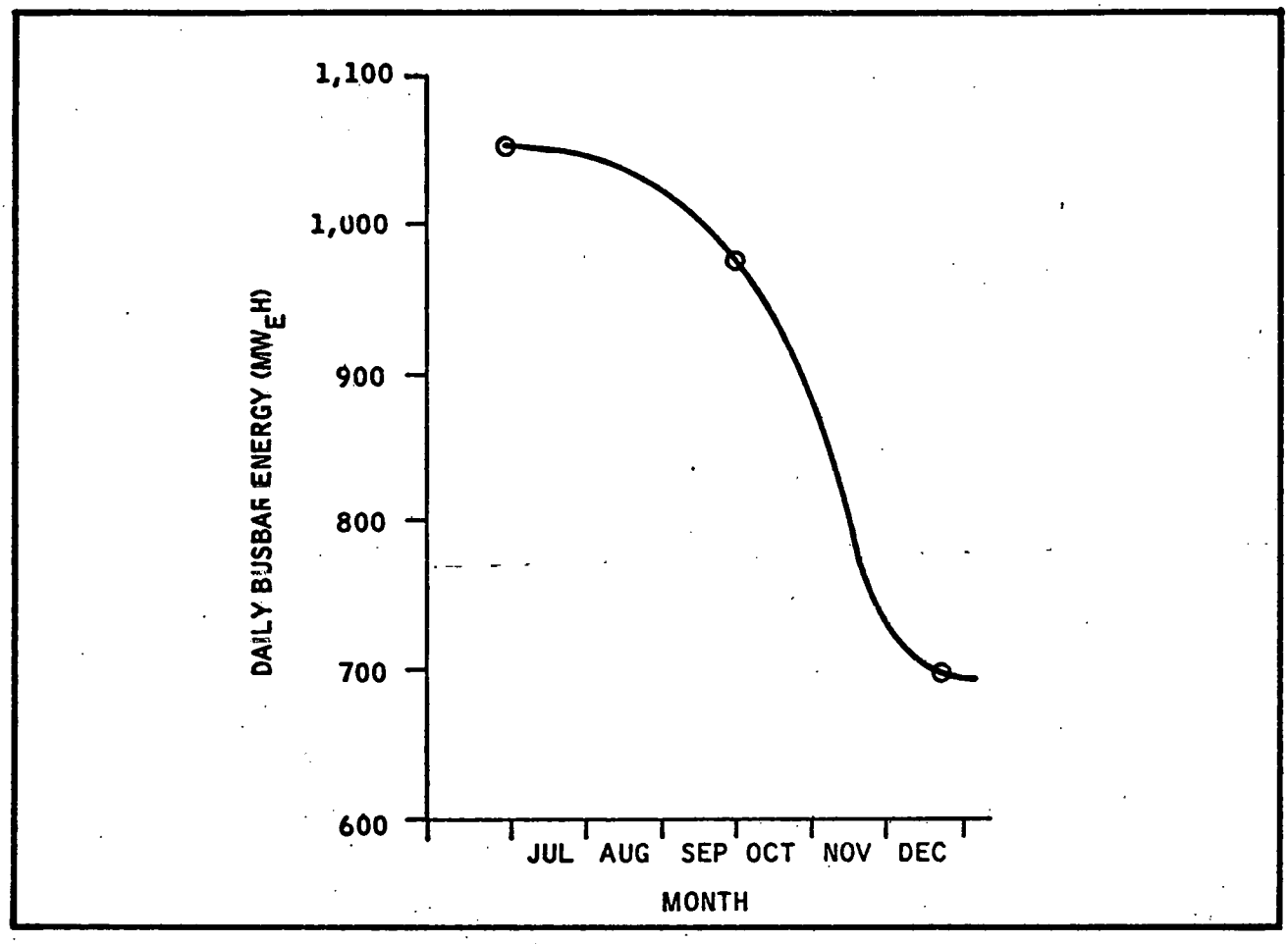

Figure D-12 ANNUAL BUSBAR POWER OF BASELINE CONFIGURATION

Appendix E

COST ESTIMATES FOR 100 MWe BASELINE PLANT CONCEPT

THIS PAGE

WAS INTENTIONALLY

LEFT BLANK

Appendix E

COST ESTIMATES FOR 100 MWe BASELINE PLANT CONCEPT

This appendix contains supporting data used to develop estimates of subsystem costs for the first 100 MWe plant configuration using the FMC line focus concept.

Cost estimates for the heliostat, heliostat controller, receiver, and receiver support towers are based on actual costs of parts and materials used to fabricate the test heliostat section and heliostat controller, and estimated costs of fabricating 1,000 heliostat units (two sections plus a controller) and 20 once-through receiver sections. These estimates were made in late 1976 for an economic evaluation of the FMC concept in a 10 MWe plant configuration.

Inflation and discount factors were applied to the 1976 estimates to re-estimate the costs in 1978 dollars, and account for the much larger quantities required for a 100-MWe configuration. These factors are noted where applied.

The cost of the receiver support towers is based on the tower configuration shown in Section E.4.2. A detailed estimate was made for the thermal transport subsystem based on the conceptual piping network described in Section E.5.2.

Costs for the remaining subsystems (energy storage, electric power generation, master control, balance of plant, etc.) were taken from published data for the McDonnel-Douglas concept for a 100 MWe point focus system.

E1 CONCENTRATOR EQUIPMENT

BASES: ACTUAL COSTS OF PARTS & MATERIALS FOR TEST HELIOSTAT
ESTIMATED FABRICATION & TOOLING COSTS FOR 1000 UNITS

FACTORS: ADD 20% TO 1976 COSTS FOR INFLATION
REDUCE INFLATED COSTS BY 50% FOR PARTS & MATERIALS
TO REFLECT VOLUME DISCOUNTS FOR 3806.5 UNITS

(A) PARTS & MATERIALS

ITEM	1976 COST BASIS QUANTITY	1976 COST BASIS UNIT COST	ADJUSTED UNIT COST	100 MWe PLANT ONE UNIT QUANTITY	100 MWe PLANT COST
MIRROR ASSEMBLY PER EMC DRAWING 5132761	120,000 ft²	$1/ft²	$0.50/ft²	1200 ft²/UNIT	$ 720
MIRROR SUPPORT FRAME (5132702)					
- 3×3×3/16 STEEL ANGLE	360 ft	$0.74/ft	$0.44/ft	720 ft	$ 320
- 2×2×1/8 " "	600 ft	$0.33/ft	$0.20/ft	1200 ft	$ 238
- END JOURNALS	2/UNIT	$25/UNIT	$15/UNIT	4 UNITS	$ 60
- END SUPPORTS	1/UNIT	$50/UNIT	$30/UNIT	2 UNITS	$ 60
- BRIDLE	10/UNIT	$15/UNIT	$ 9/UNIT	20 UNITS	$ 180
SUB TOTAL MIRROR SUPPORT					$ 858
DRIVE UNIT					
- FOCUS MECH. (5132727 5132705)	1/UNIT	$260/UNIT	$156/UNIT	2 UNITS	$ 312
- FOCUS MOTOR	"	$100/UNIT	$ 60/UNIT	2 UNITS	$ 120
- ELEVATION MECH-MOTOR (5132703)	"	$525/UNIT	$315/UNIT	1 UNIT	$ 315
SUBTOTAL DRIVE UNIT					$ 747
TOTAL PARTS & MATERIALS					$2325

(B) FABRICATION + ASSEMBLY LABOR

- MIRROR INSTALLATION	2 HOURS	$15.88/HR	$19.06/HR	4 HOURS	$ 76
- MIRROR SUPPORT	28 "	"	"	56 "	$1067
- DRIVE UNIT	14 "	"	"	28 "	$ 534
TOTAL LABOR					$1677
(C) TOOLING COST	2000 UNITS	$50/UNIT	$30/UNIT	2 UNITS	$ 60
SUBTOTAL, HELIOSTAT FAB. & ASSEMBLY					$4 2

(D) HELIOSTAT CONTROLLER (8831 CONTROLLERS)

PART	1976 COST (1 UNIT) QTY	UNIT COST	ADJUSTED UNIT COST
- ELEVATION STEPPER MOTOR	1	$150	
- FOCUS " "	1	150	
- STOW MOTOR, 220 VAC, ½HP	1	50	
- LIMIT SWITCHES	3	40	
- STEPPER TRANSLATOR	2	50	
- STOW MOTOR STARTER	1	85	
- DISCONNECT SWITCH	1	30	
- POWER SUPPLY	1	85	
- ENCLOSURE	1	150	
- SHAFT ENCODER	1	500	
- MPROCESSOR, PLS-441	1	230	
- INPUT-OUTPUT CARDS	3	132	
- CARD CAGE	1	80	
- RELAYS	5	30	
PARTS SUBTOTAL		$2276	
ADJUSTED 1978 COST			$1365
CONTINGENCIES			135
SUBTOTAL, PARTS/CONTROLLER			$1500
ASSEMBLY LABOR	8 HRS	15.88/HR	19.06/HR
INSTALLATION "	5.75 HRS	"	
CHECKOUT+TEST "	2 "	"	
SUBTOTAL, LABOR	15.75 "	"	$ 300

(E) FIELD INSTALLATION

CONCRETE PADS, 2 yd³/UNIT	2 PADS	$80/PAD	$160
INSTALL HELIOSTAT UNIT,	4 HRS	$15.88/HR	$19.06/HR
LEVEL, TEST	4 HRS	$15.88/HR.	"
SUBTOTAL, FIELD INSTALLATION			$312

ESD 7 (8-74)

(F) FIELD MODULE CONTROL EQUIPMENT

ITEM	QTY	ESTIMATED UNIT COST (1978 $)	COST FOR 100 MW$_e$ BASELINE PLANT
- PDP 11/03 COMPUTER	7	$12,000	$84,000
- INTERFACE TO HELIOSTAT CONTROLLER	8831	$50	441,550
SUBTOTAL, EQUIPMENT			525,550
LABOR FOR INSTALLATION, CHECKOUT (100%)			525,550
ESTIMATED TOTAL COST			$1,051,100
COST PER HELIOSTAT UNIT (8806.5 UNITS)			$119

SUMMARY OF COSTS FOR CONCENTRATOR EQUIPMENT

COST CATEGORY	1ST PLANT UNIT COST	% OF TOTAL UNIT COST	
REFLECTIVE UNIT (110 m^2)	$ 796	11%	2 EACH, 18M x 3.05M SECTIONS
DRIVE UNIT	1281	18	
CONTROL EQUIPMENT	1754	24	LOCAL CONTROL + FIELD CONTROL
SUPPORT STRUCTURE	1925	27	INCLUDES TOOLING COST
FIELD INSTALLATION, CHECKOUT	342	5	(E) + 50% OF (F) LABOR
CONTINGENCIES	1102	15	$135 FROM (D)+21.5%(A)+(B)+(C)+(E)+(F)
TOTAL 1ST PLANT UNIT COST	$7200	100%	

1ST PLANT COST, CONCENTRATOR SUBSYSTEM = (8806.5)($7200)
= $63.4 x 10^6
= $65 / m^2 REFLECTING AREA

E.2 RECEIVER EQUIPMENT

BASIS: COST ESTIMATE MADE IN 1976 AND 1977 FOR 12 EACH, 61M SECTIONS
MATERIAL UNIT COST QUOTES FROM LOCAL VENDORS
LABOR COST TAKEN AS ESD SHOP GRADE 8 + 90% FOR INDIRECT COSTS

FACTOR: ALL UNIT COSTS ESCALATED BY 20% FOR INFLATION

E.2.1 ONCE-THROUGH CONCEPT

(A) MATERIALS & PARTS — 1977 COST BASIS — ONE 61M RECEIVER SECTION

ITEM	QUANTITY	UNIT COST	QUANTITY	COST
0.5"I.D. STEEL TUBE (3/8"-SCHEDULE 40)	360,000 ft	$0.25/ft	30,000 ft	$9000
0.9"I.D. " " (1"-SCHEDULE 40)	86,400 ft	$0.35/ft	7,200 ft	3030
0.9"I.D. STAINLESS " (1"- " ")	72,000 ft	$1.21/ft	6,000 ft	8726
LOOP MANIFOLDS (3", SCHEDULE 40)	2,400 ft	$5.75/ft	200 ft	1380
SUBTOTAL, RECEIVER/ABSORBER				$22136 *
INSULATION, CELO-WOOL (6" THICK)	230,400 ft^3	$0.75/ft^3	19,200 ft^3	17280
RECEIVER SHELL, 1/4" STEEL, 10#/ft^2	38,400 ft^2	$1.80/ft^2	3,200 ft^2	6912
INSULATION STUDS,	48,000 ea	$0.25/each	4,000	120
TUBE HANGERS (200#'s ea)	240 ea	$40 ea	20	960
ADDITIONAL PARTS & MTLS	A/R	$5000	A/R	500
SUBTOTAL, STRUCTURAL SUPPORT (SHELL ONLY)				$25772 *
INSTRUMENTATION & CONTROL SENSORS, MOUNTS, ETC				2000 *

(B) FABRICATION & ASSEMBLY LABOR

PREPARE, SETUP STEEL FOR WELDING	240 HRS	$16.09/HR	20 HRS	$ 386
WELDING OPERATIONS (512,000 ft, 25,800 WELDS)	2580 "	"	215 "	4151
INSTALL INSULATION STUDS (48000)	1200 "	"	100 "	1930
" MANIFOLDING, TUBES	100 "	"	8.33	161
FINAL PIPE CONNECTIONS, PAINTING	384 "	"	32 "	618
SUBTOTAL, LABOR				7246 *

(C) OTHER RECEIVER COSTS

ITEM	1977 COST BASIS QUANTITY	UNIT COST	ONE 61M RECEIVER SECTION QUANTITY	COST
JIGS, FIXTURES FOR WELDING	A/R	$50,000	A/R	$353
DESIGN & ENGINEERING	A/R	$150,000	A/R	1059
ERECTION, INSTALLATION SUPPORT	2400ft	$20/ft	200ft	5000
SUBTOTAL, OTHER COSTS				6412 *

E.2.2 NATURAL CONVECTION CONCEPT (1976 ESTIMATES BASED ON 12 SECTIONS)

DIFFERENCES BETWEEN CONCEPTS ARE REQUIREMENTS FOR BOILER/SUPERHEAT MATERIALS & WELDING, AS FOLLOWS

(A) MATERIALS & PARTS (ABSORBER/RECEIVER TUBES)

ITEM	3 NOV 76 COST BASIS QUANTITY (ft)	UNIT COST/ft	ONE 61M RECENER QUANTITY (ft)	COST
BOILER OUTLET (8"-SCHED 40)	500 ft	$22.02	42	1110
SUPERHEAT PLENUM (6" " ")	640	$14.63	53	930
" " 5"	600	$11.32	50	679
" " 4"	600	$ 8.32	50	499
" " 3"	600	$5.75	50	345
" OUTLET HEADER (2")	2400	$2.31	200	554
" SUPPLY " (2", .125)	2400	$2.31	200	554
" DRUM RISER " "	960	$ 2.31	80	222
" TUBES (3/8", .0625" WALL, 5'L)	84000	$0.25	7000	2100
STEAM SEPERATION DRUMS (8"-SCH. 40)	816	$22.02	68	1797
BOILER LOWER HEADER (2", .125 WALL)	2400	$2.31	200	554
CIRCULATION DOWNCOMER (1.9", .08 WALL)	74448	$ 1.38	6204	10250
BOILER UPPER HEADER (3" SCH 40)	1728	$ 5.75	144	994
DRUM INLETS "	1728	$ 5.75	144	994
BOILER TUBES (3/8", .062 WALL, 5'L)	96000	$0.25	8000	2400
EQUALIZER LINE (1", .08 WALL)	900	$ 0.35	75	32
ATEMPORATOR LINE (")	480	$ 0.35	40	17
BOILER FEED (3"-SCH 40)	1800	$5.75	150	1035
SUBTOTAL, RECEIVER/ABSORBER MATERIALS				$25,067 *

(B) FABRICATION & ASSEMBLY LABOR				
PREPARE, SETUP FOR WELDING	768 hrs	$16.09/HR	64 hrs	$1,235
WELDING (40,800 WELDS)	6800 "	"	566.67 hrs	10941
OTHER (SAME AS ONCE-THROUGH)	1684 hrs	"	140.33 hrs	2709
SUBTOTAL, LABOR				$14885 *

E.2.3 SUMMARY OF RECEIVER COSTS (LESS SUPPORT TOWERS)

COST ITEM	1ST PLANT UNIT COST	NATURAL-CONVECTION CONCEPT (SEE SEC. E.2.3)
RECEIVER/ABSORBER MTLS	$22136	$25067
CAVITY, SHELL MTLS	25772	25772
INSTRUMENT, SENSORS	2000	2000
FABRICATION, ASSEMBLY LABOR	7246	14885
OTHER COSTS	6412	6412
SUBTOTAL	63566	74136
CONTINGENCY (10%)	7134	7414
TOTAL 1ST PLANT UNIT COST	$70700	$81550
COST/METER	$1159	$1337

E.3 RECEIVER SUPPORT STRUCTURE (EXCLUDING CAVITY ABOVE)

	1977 COST BASIS		ONE 61 M RECEIVER SECTION	
ITEM	QUANTITY	UNIT COST	QUANTITY	COST
8"x8"x3/4" STEEL BEAMS (39.6 lb/ft)	9600 ft	$8.17/ft	800 ft	$7843
12"x10"x1" " " (50 lb/ft)	7700 ft	$12.31/ft	642 ft	9484
4"x4"x1/2" " " (12.3 lb/ft)	9600 ft	$2.30/ft	800 ft	2208
LABOR FOR ERECTION, INSTALLATION	2940 hrs	$15.88/hr	245 hrs	4519
SUBTOTAL, RECEIVER SUPPORT STRUCTURE				$24054

E.4 SUPPORT TOWERS

A TOTAL OF 177 TOWERS ARE REQUIRED FOR THE BASELINE PLANT. THE FOLLOWING COSTS ARE BASED UPON THE TOWER CONFIGURED IN THE FOLLOWING PAGES. THE CONFIGURATION WAS DEVELOPED TO SUPPORT THE NATURAL CONVECTION RECEIVER, BUT IS ADEQUATE TO SUPPORT THE ONCE-THROUGH CONCEPT, SINCE THE ONCE-THROUGH CONCEPT HAS COMPARABLE STRUCTURE AND FLUID WEIGHTS.

E.4.1 COST ESTIMATE

ITEM	1977 COST BASIS (PER TOWER) QUANTITY	UNIT COST	ONE TOWER QUANTITY	COST
6"x6"x5/8" STEEL BEAMS (24.2 lb/ft)	560 ft	$5.10/ft	560 ft	$3427
4x4x1/2 " " (12.8 lb/ft)	2200 ft	$2.30/ft	2200 ft	6083
3x3x7/16 " " (7.2 ")	1900 ft	$1.30/ft	1900 ft	2954
5x5x1/2 " " (6.2 lb/ft)	240 ft	$3.00/ft	240 ft	864
GUSSETS (10% OF $13328)	A/R	—	A/R	1333
EXCAVATION & FORMS	A/R	$2000	A/R	2400
RE-BARS & CONCRETE	40 yd^3	$125/yd^3	40 yd^3	6000
SUBTOTAL, MATERIALS				$23061 *
LABOR, ERECT & INSTALL	573 hrs	$15.88/hr	573 hrs	$10921 *
TOTAL COST PER TOWER				$33982

E.4.2 TOWER SIZING

Weight analysis - Receiver

Shell : 58" dia - 1/4" wall
245° Arc - steel ——— 105.4 lb/ft

Insulation : 5" thick
6 lb/ft^3 (w/skin) ——— 34.7 "

Doors : 1" thick x 24" wide
(2pc) composit structure ——— 51. "

Drum : 9" dia x 1/2" thick ——— 45.4 "
Liquid in drum, half full. ——— 10.9 "

SH Header : 4 1/2" dia x 1/4" thick ——— 11.3 "

SS Upper header :

6" dia x $\frac{3}{8}$" thick ——— 22.5 "

Liquid in header, half full ——— 4.7 "

SS Lower header :

$2\frac{1}{2}$" dia x $\frac{3}{16}$" thick ——— 4.6 "

SS Tube : $\frac{1}{2}$" dia x .052" thick
45" long @ 2" c/c — 7.1 lb/ft

SH Tube : $\frac{3}{4}$" dia x .10 " thick
33" long @ 2" c/c — 11.4 lb/ft

SH to header
Drum to SH
Drum to header
} return lines + liquid — 5. lb/ft

Supporting brackets, internal — 12. lb/ft

Total receiver weight — 326 lb/ft

Contingency 25. % — 82 lb/ft

---

408 lb/ft

Receiver Support Beam LL & DL

LL: 816 lb/ft DL: 400. lb/ft (Est.)

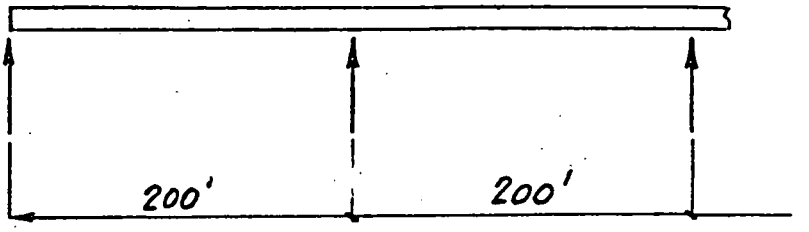

Maximum moment

$$M_{max} = \frac{WL^2}{8} = \frac{(816+400)(200)^2}{8}$$

$$= 6,080,000 \text{ ft-lb}$$

$$= 72,960,000 \text{ in-lb}$$

Using HSLA steel (SAE-J410-950D or equiv)

Yield strength $\sigma_y = 50,000$ psi (min)

Tensile strength $\sigma_u = 70,000$ psi (min)

Allowable stresses per AISC

tension $F_t = 30,000$ psi

shear $F_v = 20,000$ psi

Required section modulus (beam)

$$Z = \frac{M}{\sigma_{allow}} \approx \frac{72,960,000}{30,000} = 2432\ in^3$$

Wind load

height	Wind velocity
3 m	25 m/sec
50 m	45 m/sec
66 m	47 m/sec

At 200 ft (60.96 m) the wind velocity is 103.7 mph (46.37 m/sec)

$$p_{Wind} = C_D \frac{\rho}{2} V^2$$

$$= 0.8 \left(\frac{0.00234}{2}\right)(103.7 \times 1.467)^2 = 21.7\ psf$$

Design wind pressure 25 psf

Wind load $5(25) = 125 \frac{lb}{ft}$

Moment due to wind load

$$M_{Wind} = \frac{WL^2}{8} = \frac{125(200)^2}{8}$$

$$= 625,000\ ft\text{-}lb$$

$$= 7,500,000\ in\text{-}lb$$

Overturning moment at base of columns

$M_{of} = 200(125)\,200 = 5,$

$= 5{,}000{,}000$ ft-lb

$= 60{,}000{,}000$ in-lb

Required section modulus (column)

$$Z = \frac{M}{\sigma_{allow}} = \frac{60{,}000{,}000}{30{,}000} = 2000 \text{ in}^3$$

Support Truss

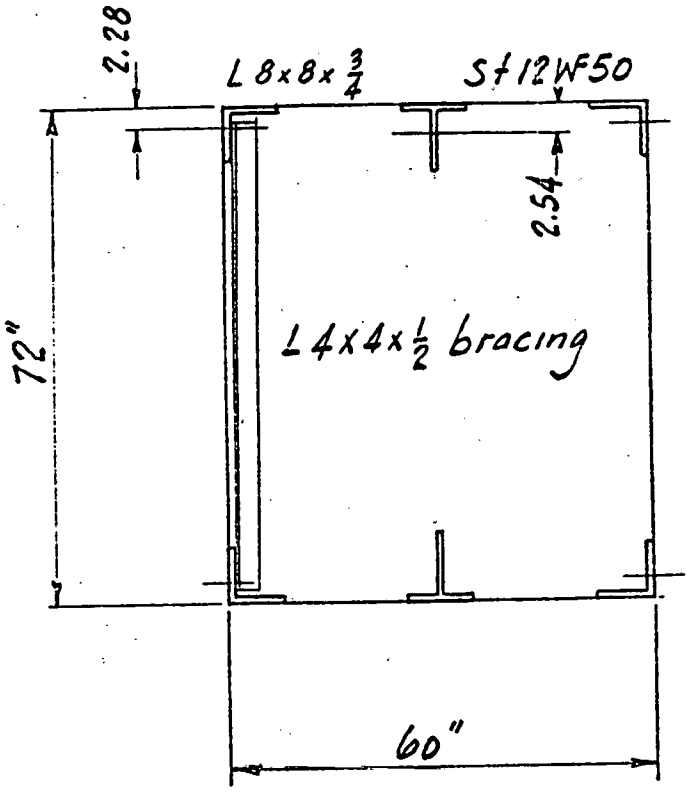

$$Z = \frac{I}{36} = \frac{4[69.7 + 11.44(36-2.28)^2] + 2[176.7 + 14.72(36-2.54)^2]}{36}$$

$$Z = \frac{85,623}{36} = 2378 \text{ in}^3$$

Weight : $4(38.9) + 2(50) + 4(12.8) = 307 \frac{\text{lb}}{\text{ft}}$

Support Tower

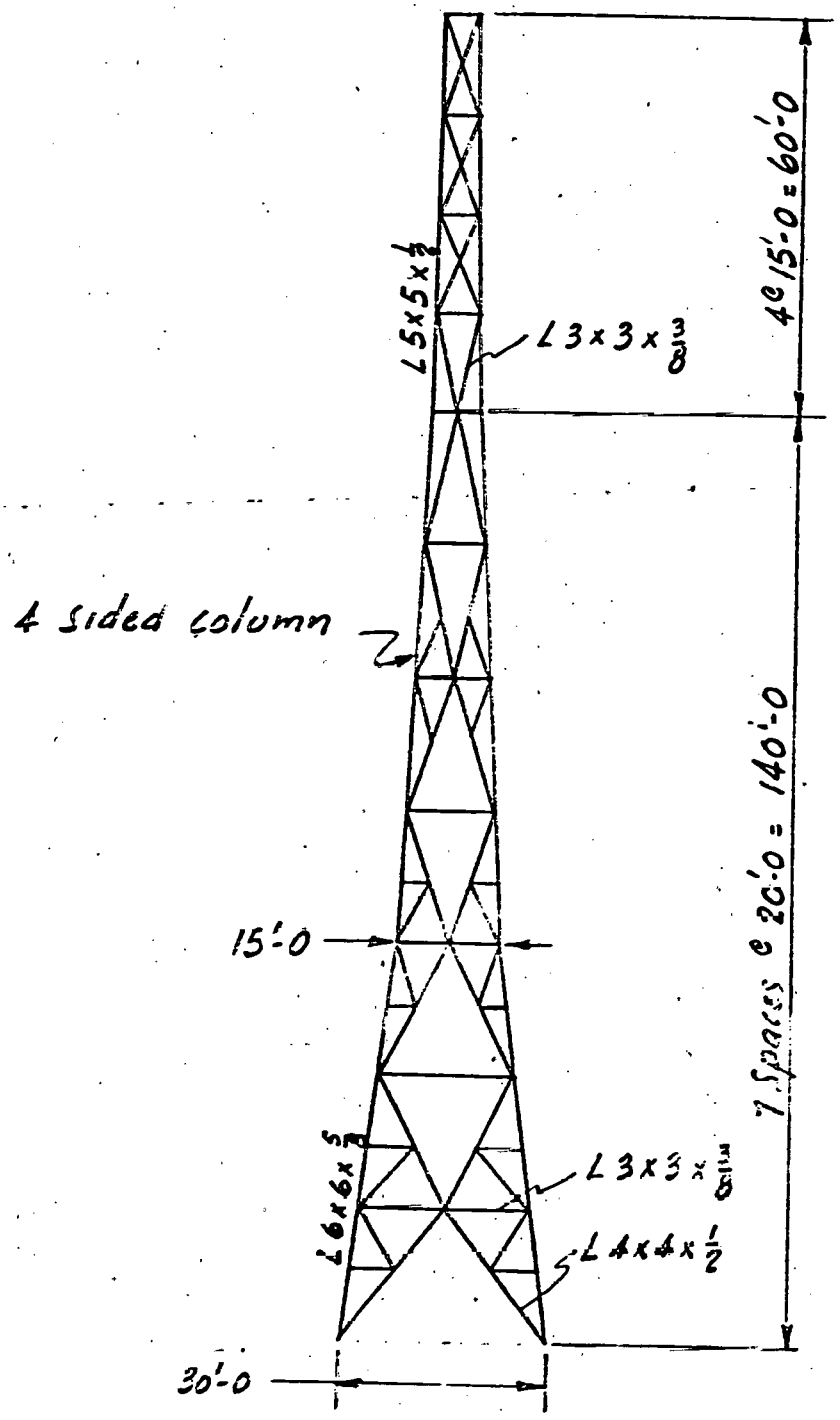

Footings

Overturning moment

Wind on collector	5,000,000 ft-lb
Wind on column	2,000,000 ft-lb
Total	7,000,000 ft-lb

Lift load at column leg

$$P_{lift} = \frac{7,000,000}{2(30)} = 233,000 \text{ lb}$$

Less column and beam wt = 75,000 lb

Total lift load 158,000 lb.

Yards of concrete in column footing

$$\frac{158,000}{4000} = 40 \text{ cu-yards}$$

E.5 THERMAL TRANSPORT SUBSYSTEM

E.5.1 COST ESTIMATE

(ALL PIPING BETWEEN RECEIVERS AND POWER PLANT)

BASIS: ACTUAL 1978 ESTIMATES INCLUDING FIELD ERECTION AND INSTALLATION.

ITEM	QUANTITY	INSTALLED UNIT COST	100 MWE PLANT COST
GATE VALVES: 1000° F / 1500 PSI STEAM SERVICE, WEDGE GATE, WELDING END			
SIZE			
1"	172	$300	$51,600
1¼"	172	400	68,800
1½"	2	450	900
2	10	600	6,000
2½"	16	650	10,400
3	10	300	3,000
3½"	4	900	3,600
5"	8	1500	12,000
6"	4	1800	7,200
8"	6	3000	18,000
10"	6	4300	25,800
14"	2	7000	14,000
16"	1	10,000	10,000
CHECK VALVE: WELD ENDS 1000° F / 1500 PSI W.P. STEAM SERVICE 1"	170	300	51,000

ITEM		QUANTITY	INSTALLED UNIT COST	100 MWE PLANT COST
SAFETY VALVE - WELD-ENDS 1000°F/1500 P.S.I. W.P. STEAM SERVICE	1 1/4"	170	$450	76,500
ELBOWS: WELDENDS SCHED. 160	SIZE			
	1"	28	3	84
	1 1/4"	28	4	112
TEES: WELDEND				
SCHED	SIZE			
160	1" X 1 1/4" X 1"	26	6	156
160	1 1/4" X 1 1/2" X 1"	26	10	260
160	1 1/4" X 2" X 1 1/4"	26	10	260
160	1 1/2" X 2" X 1"	24	10	240
160	2" X 2" X 1"	48	16	768
160	2" X 2 1/2" X 1"	14	16	224
160	2" X 2 1/2" X 1 1/4"	28	20	560
160	2 1/2" X 3" X 1 1/4"	26	20	520
160	3" X 3" X 1 1/4"	24	30	720
160	3" X 3 1/2" X 1 1/4"	14	30	420
160	2" X 2 1/2" X 3 1/2"	4	30	120
120	10" X 10" X 14"	2	400	800
120	14" X 14" X 16"	1	700	700
120	6" X 6" X 8"	2	100	200

ITEM		QUANTITY	INSTALLED UNIT COST	100MWE PLANT COST
CROSSES: WELDENDS SCHED 120	SIZE			
	5"	4	$300	1,200
	6"	4	400	1,600
	8"	4	650	2,600
	10"	6	900	5,400
	12"	1	1,300	1,300
	14"	2	1,800	3,600
	16"	1	2,200	2,200
REDUCERS: WELDENDS				
SCHED.	SIZE			
160	2" X 5"	4	40	160
160	2½" X 5"	4	40	160
160	3½" X 5"	4	40	160
120	1½" X 6"	6	60	360
120	2½ X 6"	6	60	360
120	5" X 6"	4	60	240
120	5" X 8"	4	120	480
120	6" X 8"	4	120	480
120	3" X 8"	4	120	480
120	3½" X 8"	4	120	480
120	2½" X 10"	2	210	420
120	3" X 10"	4	210	840
120	3½" X 10"	6	210	1,260

ITEM	QUANTITY	INSTALLED UNIT COST	100 MWE PLANT COST

PIPE: ASTM SPEC. A155
GRADE 1, TYPE 1 2¼
CR - 1 MO
- OR -
ASTM SPEC. A387
GRADE 22 TYPE 1
OR 2 2¼ CR - 1 MO

SCHED	SIZE	FEET		
160	1"	7,000	$ 3	21,000
160	1¼"	14,000	4.50	63,000
160	1½"	7,000	6	42,000
160	2"	19,000	7.60	144,400
160	2½"	10,000	10	100,000
160	3"	12,000	15	180,000
160	3½"	6,000	16	96,000
120	5"	4,500	20	90,000
120	6"	2,500	28	70,000
120	8"	5,500	44	242,000
120	10"	2,500	56	140,000
120	12"	200	70	14,000
120	14"	3,000	82	246,000
120	16"	150	110	16,500

ITEM	QUANTITY	INSTALLED UNIT COST	100 MWE PLANT COST
INSULATION:			
JOHNS MANSVILLE			
THERMO - 12			
CALCIUM SILICATE			
PIPE SIZE / INSUL. THICK.	FEET		
1" / 2½"	7,000	$5	35,000
1¼" / 3"	7,000	6.50	45,500
1¼" / 6"	7,000	13	91,000
1½" / 3"	7,000	7	49,000
2" / 3½"	12,000	8	96,000
2" / 6½"	7,000	16	112,000
2½" / 4"	4,000	28	112,000
2½" / 7"	7,000	29	203,000
3" / 7½"	12,000	35	420,000
3½" / 4½"	2,500	24	60,000
3½" / 8"	3,500	54	189,000
5" / 5"	2,250	34	76,500
5" / 9"	2,250	74	166,500
6" / 5"	2,500	31	77,500
8" / 5½"	3,000	38	114,000
8" / 10"	2,500	69	172,500
10" / 10½"	2,500	106	270,000
12" / 6"	200	66	13,200
14" / 10½"	3,000	125	375,000
16" / 10½"	150	156	23,400
SUPERVISION AND OVERHEAD:			368,600
TOTAL			4,876,324

REFERENCE: GUTHRIE, KENNETH M. 'PROCESS PLANT ESTIMATING EVALUATION & CONTROL' CRAFTSMAN BOOK

E.5.2 PIPE SIZING

Line Sizing

System lines were sized for a maximum steam velocity of 150 feet per second and a feedwater velocity of 7 to 10 feet per second.

The maximum flow rate is 5,000 kilograms (11,000 pounds) per hour through a receiver section.

Inlet conditions: 10.99 MPa (1,600 psi) and 216°C (421°F) at 859 kilograms per square meter (53.5 lb/ft^3)

Outlet conditions: 10.3 MPa (1,500 psi) and 508°C (946°F) at 31.8 kilograms per square meter (1.98 lb/ft^3).

At 11,000 pounds per hour, the volume flow is

$$\frac{11,000}{53.5 \times 3,600} = 0.057 \text{ ft}^3/\text{sec inlet}$$

$$\frac{11,000}{1.98 \times 3,600} = 1.543 \text{ ft}^3/\text{sec outlet.}$$

and the required feedwater line flow area is:

$$\frac{0.057 \times 144}{7} = 1.173 \text{ in}^2 \text{ minimum per unit}$$

$$\frac{0.057 \times 144}{10} = 1.675 \text{ in}^2 \text{ maximum.}$$

The required minimum steam line flow area per unit is:

$$\frac{1.543 \times 144}{150} = 1.481 \text{ in}^2.$$

Check of Pipe Wall Thickness, Feedwater

Estimated pipe span between supports is 25 feet.

For 10"-80 pipe the weight per foot is 64.33 pounds.

Calcium silicate insulation at recommended thickness of 5.5 inches; insulation weight per square foot:

$$\left[(21.75)^2 - (10.75)^2\right] \times \frac{\pi \times 13}{4 \times 144} = 25.3416.$$

Water weight per foot = 31.1 pounds.

Total pipe loading:

64.33 + 25.34 + 31.1 = 120.78 pounds per foot.

Estimated maximum bend moment from thermal stress:

120,000 pound-inches.

Static pad bend moment:

$$\frac{\omega l^2}{12} = \frac{120.78 \times (25 \times 12)^2}{12 \times 12} = 75.488 \text{ pound-inches.}$$

From ASME piping code:

$$\frac{P\ Do}{4t_h} + \frac{0.75\ i\ M_A}{Z} \leq 1.0\ S_h$$

where

P = Internal design pressure, psig

D = Pipe outside diameter, inches

t_h = Nominal wall thickness

M_A = Resultant moment bending loading on cross section due to weight, etc., in pounds.

Z = Section modulus

i = Stress intensification factor (2.1)

S = Basic material allowable stress at maximum temperature.

$$\frac{1,600 \times 10.75}{4 \times 0.593} + \frac{0.75 \times 2.1 \times (75,488 + 120,000)}{45.6} = 14,003 \text{ psi.}$$

Seamless carbon steel pipe, ASTM A1063, has an allowable stress value of 15,000 psi for service to 650°F.

Steam:

10"-120 pipe

Weight per foot Pipe = 89.20 pounds

Water = 28.0

$$10.5\text{" insulation} = \left[(31.75)^2 - (10.75)^2\right] \times \frac{\pi \times 13}{4 \times 144} = 63.3$$

Total weight per foot = 180.5 pounds.

Maximum bend moment:

$$120,000 + \frac{180.5 \times (25 \times 12)^2}{12 \times 12} = 232,813 \text{ pound-inches.}$$

$$\text{Maximum stress in pipe} = \frac{1,500 \times 10.75}{4 \times 0.843} + \frac{0.75 \times 2.1 \times 232,813}{60.3}$$

$$= 10,862 \text{ psi.}$$

Seamless alloy steel tubing ASTM A213 T22 (2-1/4 percent cr, 1 percent mo) has an allowable stress of 11,000 psi at 950°F and 7,800 psi at 1,000°F. This is acceptable, but marginal. Temperatures higher than 950° C will require heavier piping.

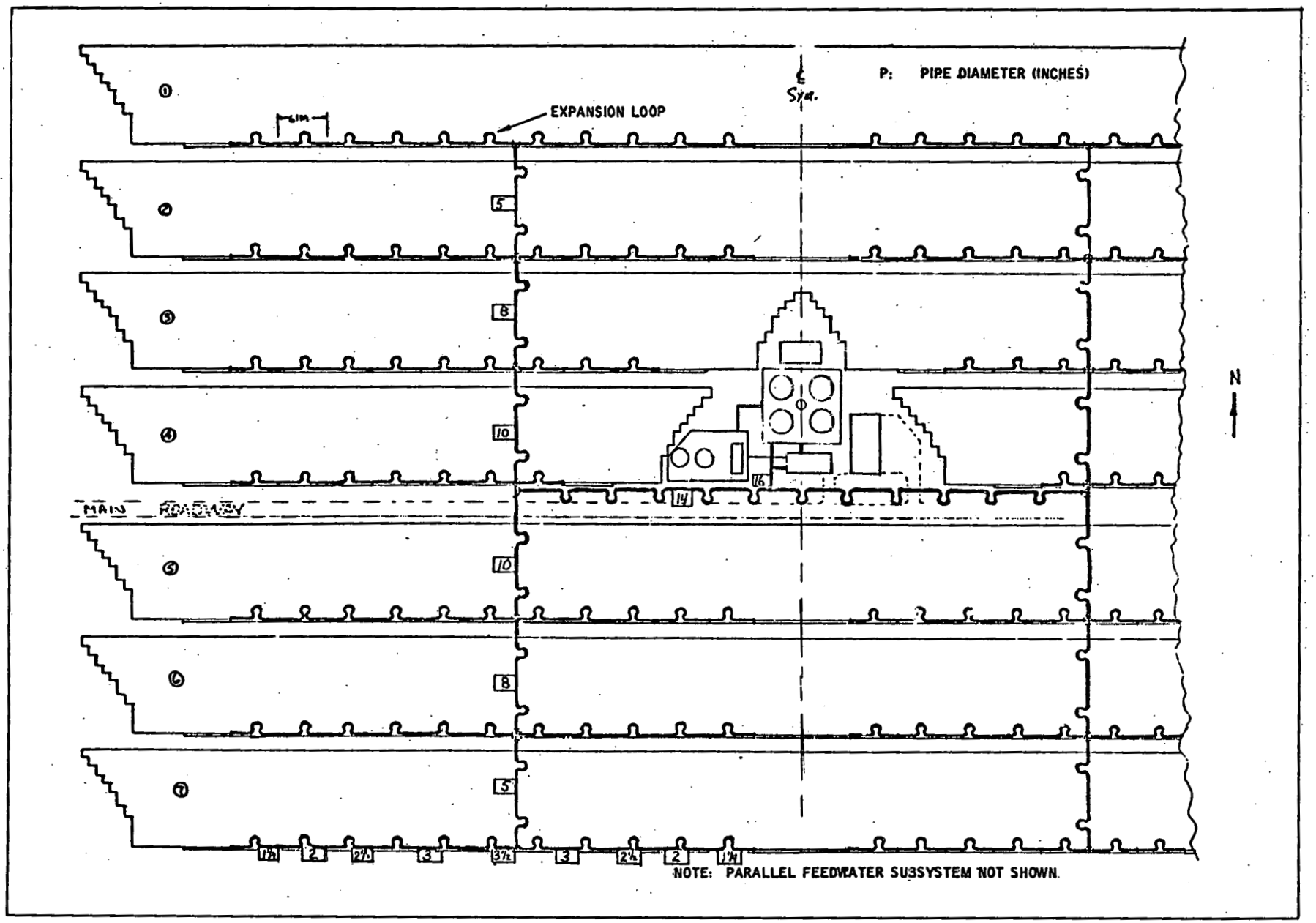

Figure E-1 SCHEMATIC, STEAM TRANSPORT SUBSYSTEM

Appendix F

RESULTS OF MIRROR REFLECTANCE MEASUREMENTS

THIS PAGE

WAS INTENTIONALLY

LEFT BLANK

Appendix F

RESULTS OF MIRROR REFLECTANCE MEASUREMENTS

F.1 SUMMARY

This appendix contains the results of measurements made by Sandia Laboratories at Albuquerque on one sample mirror panel. The measurements were made during January 1979 by R.B. Pettit, J. Freese and B. Hansche. The sample consisted of one panel selected at random from the panels fabricated by Mechanical Mirror Works, Inc., for use in the field experiment model heliostat. The overall dimensions of the panel were 152.4 cm by 50.8 cm (60 m by 20 in). Section 3.1 contains a description of the panel construction.

During the testing, the Sandia investigators observed "grayish" areas in the sample. As noted below, these areas exhibited lower specular reflectance than "clear" areas of the sample. These gray areas were not present when the panels were received from the manufacturer. However, recent inspection of other mirror panels at FMC revealed that some panels had similar areas. No attempt has been made to determine the origin of the gray appearance, however, it is possible that the phenomenon is an effect of ageing. The mirror panels were fabricated in July 1977, and have been stored in the FMC/ESD shop since that time. The panels have spent all but a few hours of their life in the shipping crate, so deterioration from exposure to light can be ruled out.

In summary, the Sandia investigaters estimated a specular reflectance of 0.85, and an RMS surface shape dispersion error of 1.2 mrad in the long dimension of the panel (the dimension that is deformed by the heliostat focus mechanism.) For comparison, the performance studies discussed in the body of this report were based on assumed values of 0.9 and 2 mrad for, respectively, heliostat reflection efficiency and surface dispersion error.

The lower dispersion error should balance the lower reflectance because with a tighter beam spread, a greater fraction of reflected solar flux will be focused within the receiver aperture. Figure A-1 in Appendix A illustrates the effect. Curve C in Figure A-1 is the dispersion distribution that was used in the performance analyses. A distribution based on 1.2 mrad surface error and 2 mrad focus and tracking errors, peaks about a third of the way between Curves B and C. Since the integrated beam intensity at the aperture plane is about 15 percent higher with Curve B than Curve C, it is reasonable to conclude that most or all of the lower-than-assumed reflectance would be compensated for.

It should be noted that the Sandia investigators estimated that RMS surface dispersion would be less than 0.5 mrad with a mirror mounted flat. In fact, mirror panels are supported along their entire long dimension by a rigid framework when emplaced in a heliostat, so the compensation of reflectance by increased accuracy is further supported. Thus, it is concluded that the results of the performance analyses would not be significantly affected by the changes to mirror performance.

F.2 MEASUREMENT OF SURFACE FIGURE

A 61 cm by 51 cm (24 in by 20 in) section of the panel was used to measure surface figure with laser ray trace instrumentation. It was observed that because the glass was so thin, it appeared to be critical for the laser ray trace measurements how the mirror was supported (see Figure F-1.) The results suggested that when the measurements were taken the mirror was slightly bent, which may have been due entirely to the way it was supported. The maximum slope error compared to a flat surface was only 5 milli-radians (mrad). A parabolic fit to the surface shape was unsuccessful because the effective focal length was very large. When the results were analyzed assuming that the mirror should be flat, then the root mean square (RMS) slope errors were calculated to be 2.4 mrad across the short dimension (20 inches) and 1.2 mrad across the long dimension (24 inches). Obviously, the way in which this mirror is mounted in the final heliostat assembly may strongly affect its shape and thus its focal properties. The investigators estimated that the RMS slope errors would be below 0.5 mrad with the mirror mounted flat.

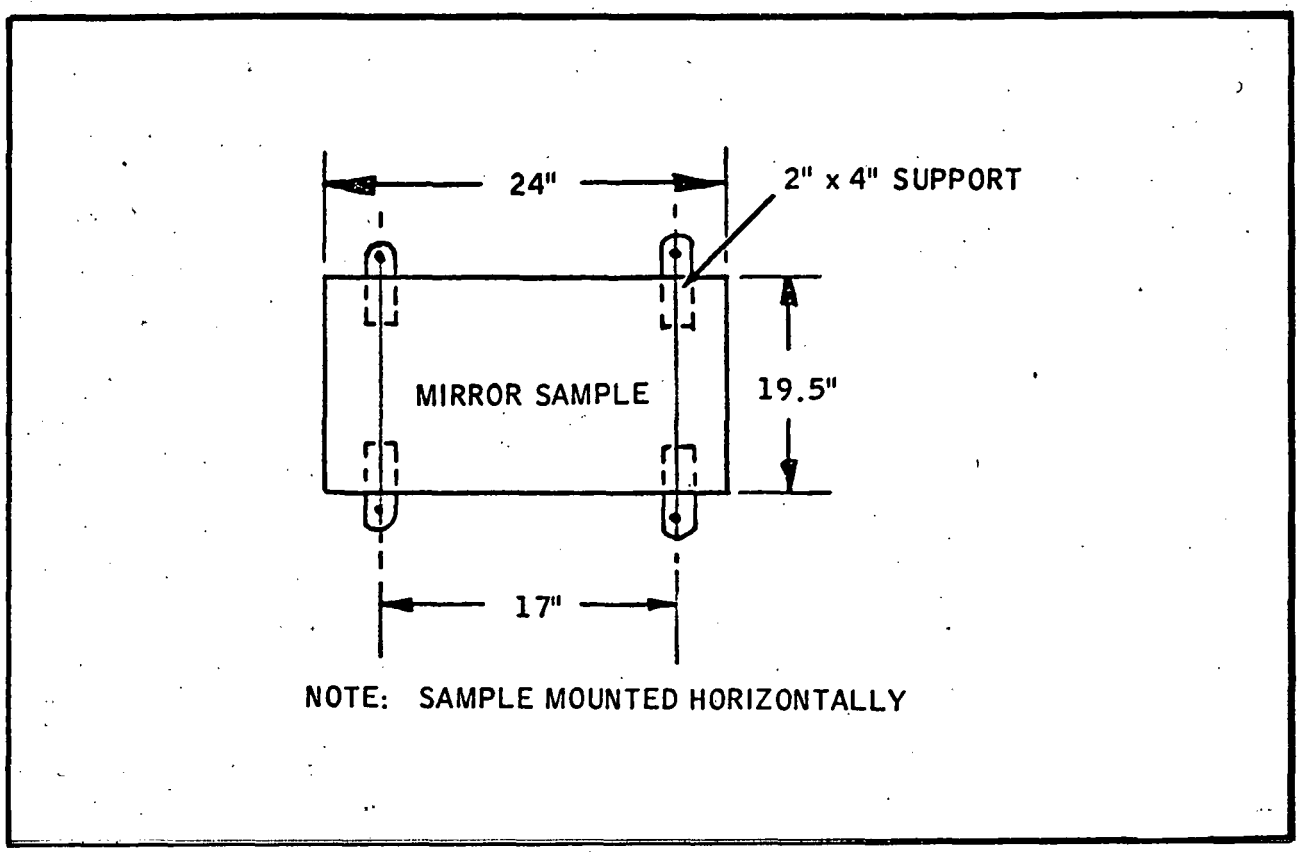

Figure F-1 MIRROR SAMPLE SUPPORT FOR LASER RAY TRACE

F.3 MEASUREMENT OF REFLECTANCE PROPERTIES

The spectral hemispherical reflectance properties from 450 nm to 2500 nm were measured using an integrating sphere reflectometer while the specular reflectance properties at 500 nm were measured using a specially constructed bi-directional reflectometer (see Solar Energy Vol. 19, pp. 733-741, 1977). When viewing the mirror with a dark background, it was noticed that there was a "grayish" appearance on some areas of the mirror while other areas were "clear". The grayish appearance was associated with the silver glass interface, not the outer glass surface or internal to the glass. The reflectance properties were measured from areas within both regions.

The hemispherical reflectance properties, which include both specular and scattered radiation, were identical for both regions. The solar averaged hemispherical reflectance (for an air mass 1.5 spectrum) was 0.85 ± 0.01. This value is typical of silvered float glass of this thickness.

The specular reflectance properties were measured using a small incident beam (7 mm diameter) in order to isolate the properties of the gray and clear areas. On a clear area, the specular reflectance at 500 nm was within 0.5 percent of the hemispherical reflectance value at the same wavelength. Thus there appears to be no appreciable scattering in the clear areas. On the grayish areas, the specular reflectance was 2 to 4 percent lower than the specular reflectance from a clear area. Thus the solar average specular reflectance from the gray areas would be 2 to 4 percent below the solar average hemispherical reflectance of 0.85 (i.e., 0.83 to 0.81). No attempt was made to determine the fractional area covered by the gray regions nor the origin of the gray appearance.

Appendix G
REFERENCES

THIS PAGE

WAS INTENTIONALLY

LEFT BLANK

Appendix G
REFERENCES

G.1 SECTION 3.0

1. McDonnell Douglas Astronautics Co., Central Receiver Solar Thermal Power System, Phase I Report, Volume 3, Book 1, p. 2-19.

2. Ibid., pp. 4-187 through 4-191.

3. California Energy Commission, California Solar Data Manual, Sacramento, Ca., March 1978, p. 263.

4. Department of Energy, On the Nature and Distribution of Solar Radiation, DOE Report HCP/T2552-01, March 1978, pp. 20-21.

G.2 SECTION 4.0

1. McDonnell Douglas Astronautics Company, Central Receiver Solar Thermal Power System, Volume 4, Receiver Subsystem, November 1977, p. 3-7.

2. Perry, J. H., Chemical Engineers Handbook, Third Edition, McGraw-Hill, 1950, pp. 1600, 1604-1605.

G.3 SECTION 6.0

1. McDonnell Douglas Astronautics Company (MDAC), Central Receiver Solar Thermal Power System, Volume 5. Thermal Transport Subsystem, November 1977.

2. MDAC, Ibid, Volume 2, System Description and System Analysis, pp. 2-14, 2-38.

3. Jet Propulsion Laboratory, The Cost of Energy from Utility-Owned Solar Electric Systems, report ERDA/JPL-1012-76/3, June 1976.

4. Department of Energy, "Line Focus Solar Central Power System", Request for Proposals ET-78-R-03-2073, June 1978.

5. MDAC, Volume 2, p. 3-60.

6. Ibid, Figure 1-3, p. 1-10.

7. MDAC, Volume 3, Book 2, (a) pp. 6-180 through 6-189; (b) pp. 4-96, 4-124; (c) pp. 4-112, 4-126; (d) pp. 4-47, 4-124.

8. Berg, R.S., "Heliostat Dust Buildup and Cleaning Studies", Sandia Laboratories Report SAND 78-0510, March 1978.

G.4 APPENDIX A

1. Abette, G., The Sun, D. Van Nostrand Co., 1938, p. 316.

2. Jose, P.D., Journal of Solar Energy Science and Engineering, Vol. I, No. 4, p. 19-22 (1957).

3. Levi, L., Applied Optics, Vol. I, J. Wiley & Sons, 1968, p. 235.

4. Evans, R.P., The Atomic Nucleus, McGraw Hill, 1955, p. 768.

G.5 APPENDIX D

1. McDonnell Douglas Astronautics Company, Preliminary Cost Estimate for Central Receiver Solar Thermal Power System 10 MWe Pilot Plant, 1 March 1976. This reference is subsequently referred to as MDAC-1.

2. Ibid, Central Receiver Solar Thermal Power System, Phase I Report, Volume 2. System Description and System Analysis, October 1977. This reference is subsequently referred to as MDAC-2.

3. MDAC-2, Figure 2-21, p. 2-31.

4. MDAC-2, pp. 2-38, A-13.

5. MDAC-2, p. 4-23.

6. MDAC-1, p. 3-9.

7. MDAC-1, p. 3-8.

8. Aerospace Corporation, An Evaluation of the FMC Line Cavity Central Receiver Concept, Aerospace Report ATR-77(7523-21-1), April 1977.

9. MDAC-1, Figure 2-2.

10. MDAC-2, Figure 3-18, p. 3-60.

* U.S. GOVERNMENT PRINTING OFFICE: 1979—640-189/ 1337